AD NUMBER

AD841562

NEW LIMITATION CHANGE

TO

Approved for public release, distribution
unlimited

FROM

Distribution authorized to U.S. Gov't.
agencies and their contractors;
Administrative/Operational Use; 23 Jun
1973. Other requests shall be referred to
Department of the Air Force, Washington,
DC.

AUTHORITY

USAF ltr, 27 Jun 1973

AFAL-TR-68-97

THE U. S. A. F. AVIONICS LABORATORY

GEORGIA INSTITUTE OF TECHNOLOGY

SYMPOSIUM ON ELECTROMAGNETIC WINDOWS

PROCEEDINGS
VOL. I

MATERIALS RESEARCH, DEVELOPMENT,

TESTING AND EVALUATION

(PART I AND PART II)

JUNE 1968

AD841562

OCT 23 1968

89

DISCLAIMER NOTICE

THIS DOCUMENT IS BEST QUALITY PRACTICABLE. THE COPY FURNISHED TO DTIC CONTAINED A SIGNIFICANT NUMBER OF PAGES WHICH DO NOT REPRODUCE LEGIBLY.

NOTICES

When Government drawings, specifications, or other data are used for any purpose other than in connection with a definitely related Government procurement operation, the United States Government thereby incurs no responsibility nor any obligation whatsoever; and the fact that the Government may have formulated, furnished, or in any way supplied the said drawings, specifications, or other data, is not to be regarded by implication or otherwise as in any manner licensing the holder or any other person or corporation, or conveying any rights or permission to manufacture, use, or sell any patented invention that may in any way be related thereto.

Copies of this report should not be returned to the Research and Technology Division unless return is required by security considerations, contructual obligations, or notice on a specific document.

BLANK PAGE

PROCEEDINGS OF THE USAF AVIONICS LABORATORY/GEORGIA INSTITUTE OF TECHNOLOGY
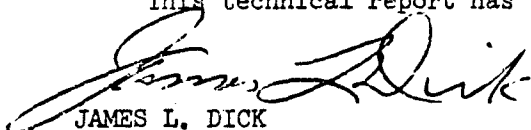SYMPOSIUM ON ELECTROMAGNETIC WINDOWS

June 1968

Volume I

MATERIAL RESEARCH, DEVELOPMENT
TESTING AND EVALUATION
(PART I AND PART II)

FOREWORD

The proceedings are contained in four volumes, three of which are unclassified and one classified Confidential. Volumes I through III, were reproduced by the Georgia Institute of Technology, directly from the manuscripts submitted by the authors. Volume IV was reproduced by the U. S. Air Force at Wright-Patterson Air Force Base, Ohio. The papers presented in these volumes were submitted for the USAF Avionics Laboratory/Georgia Institute of Technology Symposium on Electromagnetic Windows held on the Georgia Tech Campus, Atlanta, Georgia, 12, 13, and 14 June 1968. Volumes I through III were compiled by Nick E. Poulos, Engineering Experiment Station, Georgia Institute of Technology under USAF Contract No. F33615-67-C-1594. This contract was initiated under BPSN: 7-63416103, AFAL, ASD, and is administered under the direction of the AVWE, Wright-Patterson Air Force Base, Ohio with Gene Tarrants acting as Project Engineer. Volume IV was compiled by Mr. Richard A. Ireland, AFAL/AVWE, Wright-Patterson Air Force Base, Ohio.

This technical report has been reviewed and is approved.

JAMES L. DICK
Colonel, USAF
Director

TABLE OF CONTENTS - VOLUME I

SESSION I

MATERIALS RESEARCH, DEVELOPMENT, TESTING AND EVALUATION (PART I)

SESSION II

MATERIALS RESEARCH, DEVELOPMENT, TESTING AND EVALUATION (PART II)

PAPERS NOT PRESENTED

TABLE OF CONTENTS - VOLUME I (Continued)

PAPERS NOT PRESENTED

ANTENNA WINDOWS FOR HYPERSONIC AND REENTRY VEHICLES

B. Poulin
R. J. McHenry
A. J. Patrick, Jr.
Avco Space Systems Division
Lowell, Massachusetts 01851

ABSTRACT

Hypersonic and reentry vehicles require the use of a heat shield to protect the basic missile structure and components from the aerodynamic heating developed during flight. The use of radar for guidance and fusing requires that a portion of the heat shield be electrically transparent during missile operation. This requirement has forced the development of a new class of antenna window materials.

The current materials which were available for radome use and the basic heat shield material were unacceptable for antenna window use because of high electrical losses due to charring of the ablator in the case of organic materials and poor shock properties and ablation compatibility with the surrounding heat shield material in the case of ceramics. The materials which were needed were non-charring, good ablators which were compatible with available heat shield materials. Because of the large number of missions possible for missiles (hypersonic to reentry) several materials had to be developed to meet the different heat protection requirements.

This paper will discuss in detail the specific requirements, from an electrical and ablation standpoint, for antenna windows for hypersonic and reentry vehicles. In addition to defining the requirements, the different materials developed by Avco for hypersonic and reentry vehicles will also be discussed. Electrical transmission and ablation data for the materials discussed will be presented.

INTRODUCTION

Hypersonic and reentry vehicles require the use of a heat shield to protect the basic missile structure and components from the aerodynamic heating developed during flight. The use of radar for guidance and fusing requires that a portion of the heat shield be electrically transparent during missile operation. Currently, there are two classes of materials which can meet this requirement: high temperature ceramics and ablative composite materials. High temperature ceramics such as alumina have several limitations including poor thermal shock resistance, poor ablation performance if heated beyond their melting point and the handling and design properties inherent in a ceramic. For these reasons, ceramics other than silica-based materials have found limited use as antenna windows.

Although silica still possesses the mechanical limitations of ceramics, its thermal shock characteristics are better than those of other ceramics because of its low coefficient of thermal expansion. Silica ablation performance is superior because its melt has a very high viscosity and is therefore not removed under most aerodynamic shear conditions.

The second class of antenna window materials is comprised of various ablative plastics and plastic composites. The ablative material must be compatible in ablation with the surrounding heat shield and still remain electrically transparent. Normal ablative heat shield materials form a carbonaceous char during ablation and are therefore not electrically transparent.

This paper discusses in detail the specific electrical and thermal requirements for ablative antenna windows for hypersonic and reentry vehicles. In addition to defining these requirements, the properties of various materials developed by Avco for hypersonic and reentry vehicles are also discussed.

ELECTRICAL REQUIREMENTS

In the electrical design of a non-ablative antenna window, the properties of dielectric constant and loss tangent are conventionally considered. In particular, it is required that the loss tangent remain low over the operating temperature limits and that the dielectric remain relatively constant with temperature. In the design of an ablative antenna window, additional factors must be considered because of the change in the physical nature and dimensions of the ablated material.

The absolute magnitude as well as the temperature insensitivity of the dielectric constant is important in the design of a half wave ablative window. That is, there is a premium in having the dielectric constant as low as possible because of the antenna window thickness change due to ablation. As the window ablates, the front surface regresses and the overall thickness of the window decreases. This thickness change has an effect on transmission due to the change of thickness from the ideal half wave design. With low dielectric materials the change in transmission is less pronounced for a given thickness change than for a higher dielectric constant material.

The charring characteristic of the ablative antenna window is very important from a transmission standpoint. Standard heat shield materials depend on the formation of a carbonaceous char to obtain their excellent ablation properties. This char is very conductive and would reduce a transmitted signal below tolerable antenna window limits. In the development of ablative composite antenna windows, the elimination of char or the prevention of char formation while maintaining adequate ablation performance is the main problem area. The specific areas of effort in the reduction of char will be covered in the discussion of each of the individual material covered by this paper.

2

A note should be made as to how the electrical performance of the antenna window materials under ablation conditions can be determined. The antenna window material is mounted in a water cooled copper frame and a transmitting horn is placed in back of the antenna window. A transmission check is made before ablation. After this check, a plasma arc is used to ablate the sample. It is impossible to make a meaningful transmission measurement during actual ablation because of the electrical characteristics of the plasma but a measurement is made immediately after the arc is shut off. This represents the transmission properties at temperatures reached during ablation and in most cases is pro bly a good approximation of performance under actual ablation condi rs.

ABLATIVE REQUIREMENTS

The basic ablation requirement for the antenna window is mai nance of low back face temperature during flight. This can be thermodyr ically achieved by several routes depending on the particular requirements of the vehicle. For a short time-high velocity vehicle such as a high performance reentry body, the surface temperature of the ablative surface is extremely high and a significant thickness of material is removed through ablation. Since the flight time is short, relatively little unablated material is required to limit the amount of heat transferred to the structure through thermal conduction. It has been noted before that current heat shield material forms a conductive char. The function of this high temperature char is two-fold: to reduce the net heating to the material through reradiation and to prevent mechanical erosion of the heat shield. In an antenna window, the use of a carbonaceous char is eliminated because of its effect on the transmission properties; however, a silica residue can perform to some extent the same function without excessive electrical loss. In the development of antenna windows for reentry vehicles, the effort was directed toward developing a matrix which would not char under ablation conditions for use with a silica reinforcement in a plastic composite.

In certain non-reentry hypersonic vehicles or in a lower performance blunt reentry vehicle such as Apollo, the ablative conditions are somewhat reduced in heat flux but the flight times have increased so that the total integrated heating is still large. This means that the ablative material must have a low thermal conductivity to prevent heat transfer during the long flight time. As was noted for the reentry vehicle material, the formation of some type of non-carbonaceous residue is necessary to limit the amount of material removal.

In other hypersonic, non-reentry vehicles, the total range and hence heating times are much shorter although the velocity, heat flux and aerodynamic shear forces may be higher. Since the total integrated heating is low, less efficient ablators can be used without excessive mass loss. Such ablators often ablate without forming a char (e.g., Teflon) and hence have a low surface temperature with resultant relatively low ablation efficiency. Since the shear forces are often so high that a char would be removed by mechanical erosion without having

performed its function, such a noncharring ablator may actually be more efficient than a normally charring ablator which has its char removed by shear. The low surface temperature also reduces the driving force for conduction and permits, for these short times, the use of thin coatings of relatively high thermal conductivity materials such as Teflon.

A second aspect of the problem of an ablative antenna window is that of ablation compatibility with the surrounding heat shield material. If the window ablates faster or slower than the heat shield, turbulence will be set up around the window causing an accelerated erosion of the faster ablating material. This aspect of the problem can be investigated by use of a plasma arc to determine the ablative performance of various materials under turbulent and laminar flow conditions. Figures 1 and 2 give a comparison of the ablation performance of a Teflon quartz antenna window with a typical reentry body heat shield material. The heat shield material is a silica fabric-phenolic resin tapewrapped composite. This material is a char former. Figure 1 gives the ablation performance under laminar conditions and Figure 2 gives the performance under turbulent conditions. From these data, it would be predicted that the two materials would be fairly compatible. Figure 3 is a picture of a specimen in which a Teflon quartz window material was inserted into a silica phenolic heat shield material and ablated under turbulent conditions. This sample shows very little difference in erosion, perhaps less than would have been predicted based on Figure 2. As a comparison, Figure 4 shows the effect of ablation incompatibility on silica phenolic into which a boron nitride window material was inserted. The boron nitride has an ablation rate much lower than the silica phenolic which caused turbulence to be created around the window and ablated the silica phenolic faster than normal around the window. The boron nitride window sheared off toward the end of the test and hence appears to be at the same level as the silica phenolic. In reality, the window actually protruded above the silica phenolic throughout most of the run.

In summary, the ablation requirement is to maintain a required backface temperature with a material which is a non-char former and which is compatible in ablation with the surrounding heat shield material.

DEVELOPED ANTENNA WINDOW MATERIALS

1. Antenna Windows for Reentry Vehicles

In the development of ablative antenna windows for reentry vehicles, two possible paths were open: to develop a material which inherently does not char under ablation conditions or to develop some method for eliminating the char in a normally char-forming material. Avco's first attempt involved the fabrication of a Teflon quartz composite since Teflon was not known as a char former upon thermal degradation. The basic electrical properties of the composite is shown in Table II. Hot transmission tests were conducted as described previously. Visual observation of the sample indicated that the initial degradation product

Figure 1

ABLATION PERFORMANCE VERSUS ENTHALPY
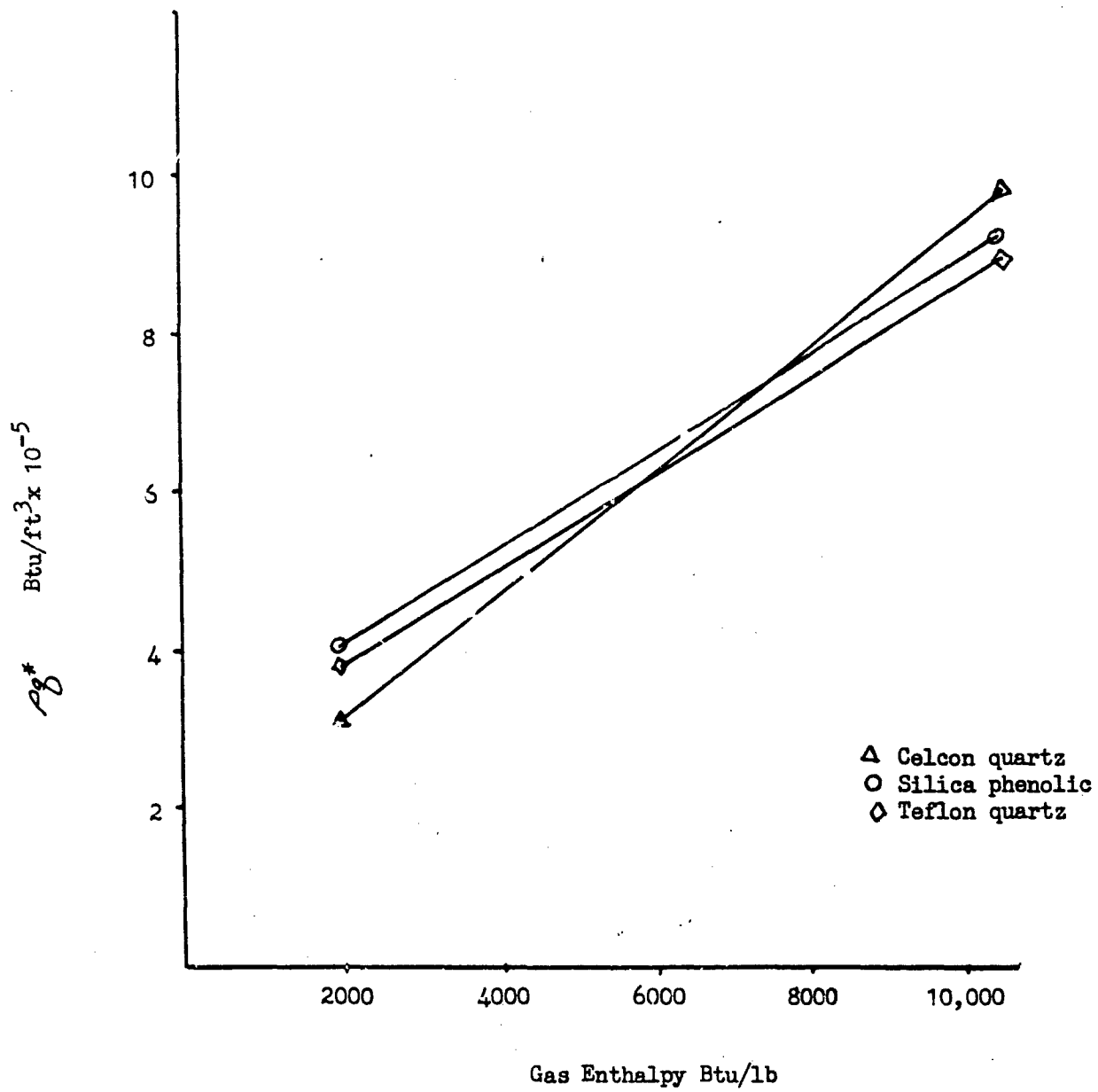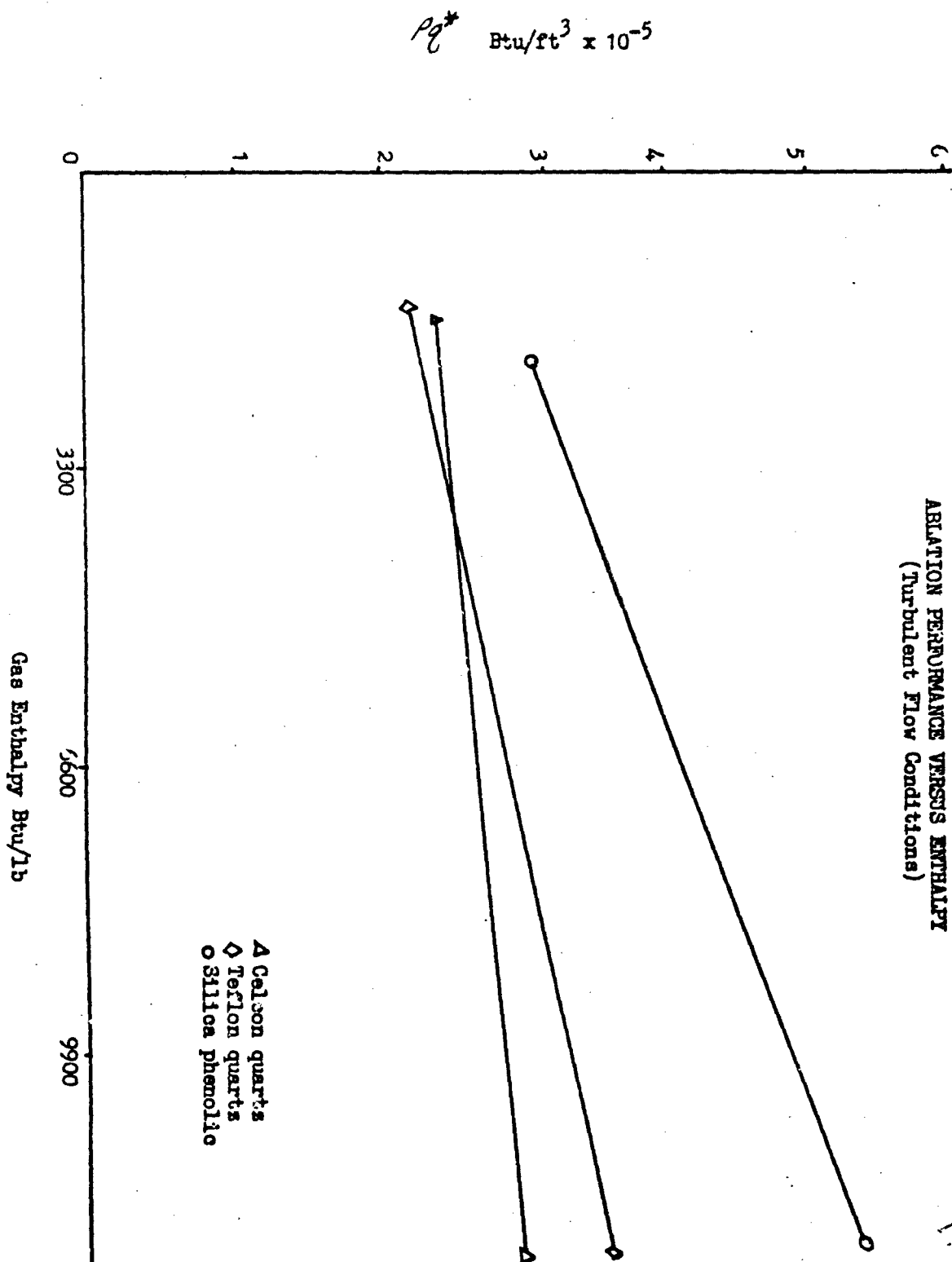(Laminar Flow Conditions)

ρq^* Btu/ft^3 x 10^{-5}

Figure 2
ABLATION PERFORMANCE VERSUS ENTHALPY
(Turbulent Flow Conditions)

Gas Enthalpy Btu/lb

△ Carbon quartz
◇ Teflon quartz
○ Silica phenolic
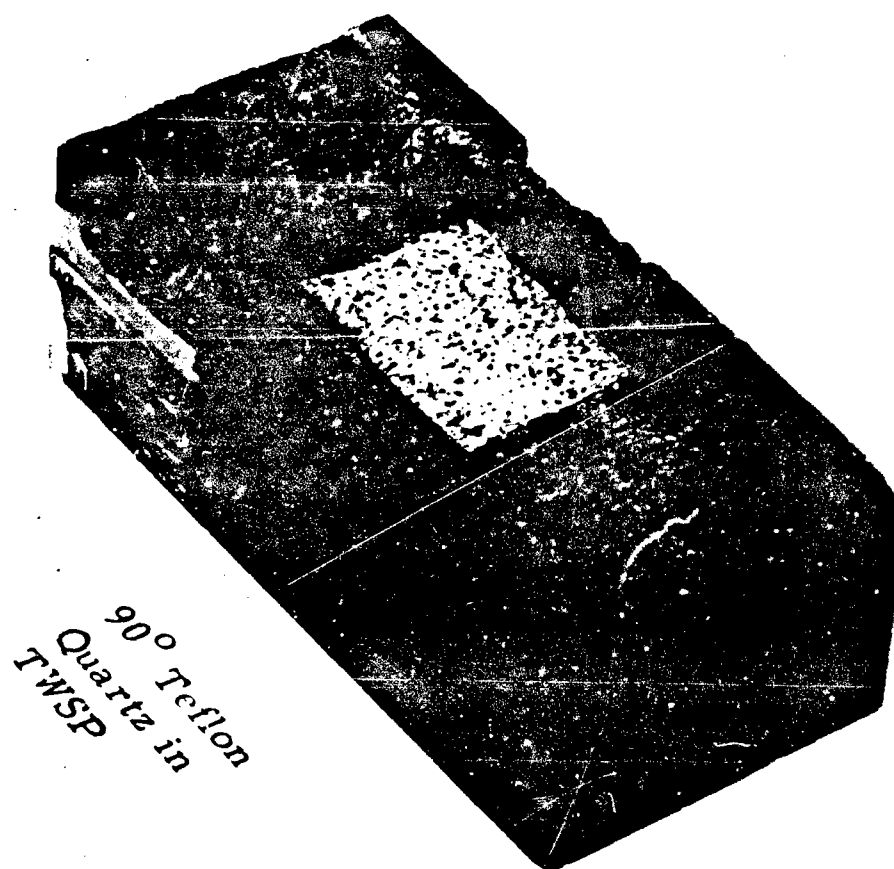
90° Teflon
Quartz in
TWSP

Figure 3.

Figure 4.

of Teflon underwent further reaction as it passed over the very hot
silica fibers to form a slight carbon layer to deposit on the fibers.
The results shown in Table III indicated that the Teflon did indeed char
and this had a pronounced effect on the electrical properties. In order
to remove the char, an oxidizing additive was added to the Teflon quartz
during composite fabrication. The initial amount of additive added was
small but had a pronounced effect on the amount of char present. Table
III indicates that the loss was reduced from 7.5 db to 1.5 db. The
sample had changed color from black to light gray. A second sample with
7% additive was made and ablated and the char was white. No electrical
transmission tests were made of the second sample. It was concluded,
however, that the char could be eliminated and satisfactory transmission
achieved with Teflon quartz with an oxidizing additive.

A second approach to the development of a reentry antenna window
was to use a material which has as many oxygen atoms as carbon atoms in
the structure. One such material is a polyformaldehyde resin (Celcon)
which has the following structure:

$$- \overset{\overset{\textstyle H}{|}}{\underset{\underset{\textstyle H}{|}}{C}} - O - \overset{\overset{\textstyle H}{|}}{\underset{\underset{\textstyle H}{|}}{C}} - O -$$
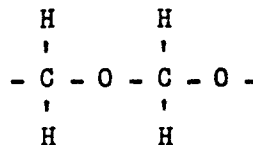
There is one oxygen atom for each carbon atom and when this material
degrades, it first forms formaldehyde and then carbon monoxide and
hydrogen. The temperatures of the antenna windows under ablation favors
the formation of the CO and H_2 and there is no apparent tendency to form
a char. Tables II and III give the electrical properties and performance
of the polyformaldehyde-quartz antenna window material. From the results,
it was concluded that the material did not char and would be acceptable
for use as an antenna window material. Table I gives the mechanical and
thermal properties of the Teflon-quartz and polyformaldehyde quartz
antenna window materials. As indicated earlier in Figures 1 and 2,
Teflon quartz and polyformaldehyde quartz are compatible with the heat
shield materials.

2. Antenna Windows for Hypersonic Vehicles

As was indicated in the ablative requirements section, there are two
types of materials, either of which might be required depending on the
specific environment. The first is a low density material. Avco has
developed such a material (480-1B) for use in low shear-long time environ-
ments. This material has not shown a conductive char under the ablation
conditions for which it is normally considered. The basic electrical
properties are shown in Table I. No electrical transmission tests have
been made but it is expected to be low loss during ablation. The example
in the ablative requirements section demonstrates the value of a low
thermal conductivity ablator.

TABLE I

MECHANICAL AND PHYSICAL PROPERTIES OF
TEFLON QUARTZ AND CELCON QUARTZ

Tensile Strength, psi	Teflon Quartz	Celcon Quartz
Prop. Limit	6,000	6,580
Yield Stress	22,000	23,975
Ultimate Stress	30,030	37,200
Modulus x 10^{-6}	3.02	2.52
% Total Strain	2.23	2.23
Compressive Strength, psi	3,380	9,200
Core Shear, psi		
Interlaminar	950	2,200
Warp/Fill	10,800	17,400
Coefficient of Thermal Expansion		
Perpendicular (in/in-°F)	5.2×10^{-5}	7×10^{-5}
Parallel (in/in-°F)	2.4×10^{-6}	2×10^{-6}
Density (gm/cm^3)		
(60/40 composite)	2.2	1.88

TABLE II

DIELECTRIC PROPERTIES OF VARIOUS ANTENNA WINDOW MATERIALS

MATERIAL	UHF		3KMC		5KMC		10KMC	
	K	TAN	K	TAN	K	TAN	K	TAN
8021*	2.65	.02	2.65	.02	2.65	.02	2.65	.02
AVCOAT II	2.84	.022	2.73	.02	2.72	.02	2.72	.02
TEFLON	1.99	.0006	2.15	.002	2.04	.003	2.2	.003
CELCON	3.05	.05	2.96	.03	2.9	.03	2.9	.023
FUSED SILICA	3.55	.0004	3.7	.004	3.7	.014	3.7	.004
TEFLON QUARTZ	--	--	--	--	--	--	3.4	.01
CELCON QUARTZ	--	--	--	--	--	--	3.8	.02
480-1B	--	--	--	--	--	--	1.58	.01

*REPRESENTATIVE VALUES

TABLE III

ANTENNA WINDOW TRANSMISSION TEST*

8021	300MC	900MC	2.5KMC	10KMC
AVCOAT II**	.6	2	—	—
TEFLON**	.6	2	—	—
FUSED SILICA	0.3	0.3	0.3	0
TEFLON QUARTZ	ACCEPTABLE		7.5	13.8
TEFLON QUARTZ/ADD.	ACCEPTABLE		1.5	4.0
CELCON QUARTZ	—	—	0.3	—

*ONE WAY ATTENUATION IN DECIBELS
**DATA OBTAINED FROM NASA REPORT - DATA FOR TEFLON IS HIGHER THAN
ANTICIPATED AND MAY BE THE RESULT OF EXPERIMENTAL UNCERTAINTY.

For short time applications, such materials as Teflon and certain epoxy-urethane materials are available. These materials degrade at a relatively low temperature and do not form a char. Their main drawback is the amount of material needed to provide the thermal protection to the substrate. Avco has developed an epoxy-urethane material (8021) which does not char and provides adequate thermal protection. This material was developed to replace Teflon. This replacement was desired because of the difficulty in working with Teflon. 8021 is a castable material and easily applied to irregular shapes. The electrical properties of 8021 are shown in Tables II and III. In Table II, no actual data are available but 8021 has the same chemistry of degradation as does AVCOAT II on which data are available. Therefore, AVCOAT II data are presented in Table III. The ablated samples of 8021 do not show a char and remain transparent after ablation. The physical and mechanical properties of 480-1B and 8021 are presented in Table IV. Neither of these materials has an ablation compatibility problem since the whole vehicle can be coated with the material to provide the basic heat shield. In fact, the materials were originally developed as heat shield materials and are superior in ablation performance to other heat shield materials currently considered for such environments.

Materials Selection

In the selection of an antenna window material, several factors have to be considered including speed, flight time and operating frequency. It should be pointed out that some materials will be acceptable at one frequency and not at others. One example is Teflon quartz. The material forms a carbonaceous char. At the lower frequencies, this char does not greatly affect transmission because the char is very thin compared to a wavelength. As the frequency increases, the losses become too large and an oxidizing additive must be added. This effect can be seen in Table III.

The final selection of the material must include the thermal environment, shear loads, transmission performance and the desired flight time. Knowing these, the various materials available can be reviewed and the proper antenna window material selected.

SUMMARY

The wide range of missile applications has required the development of many missiles with many flight profiles. This has required the development of thermal protection systems for a wide range of applications. Accompanying this development has been the development of a number of antenna window materials which are compatible with the thermal protection systems. Knowing the requirements of a given system, a suitable thermal protection system and antenna window material can be selected.

TABLE IV

MECHANICAL AND PHYSICAL PROPERTIES OF
480-1B AND 8021

Tensile Strength, psi	480-1B	8021
-150°F	338	15,600
75°F	152	2,940
400°F	131	300

Elastic Modulus (psi x 10^{-6})		
-150°F	.019	.52
75°F	.0083	.01

Thermal Conductivity		
Btu/hr-ft-°F	.053	.1

Specific Heat		
Btu/lb-°F	.275	.41

Density (gm/cm^3)	.28	1.1

BALLISTIC IMPACT RESISTANCE OF SILICA RADOMES

Richard D. Rocke
Antenna Department   and
Hughes Aircraft Company
Fullerton, California 92634

Louis E. Gates, Jr. and
Charles J. Bahun
Materials Technology Department
Hughes Aircraft Company
Culver City, California 90230

ACKNOWLEDGEMENT

ABSTRACT

This work represents an effort to identify the seriousness of debris impact on ceramic radomes. Testing methods, results and data analysis are presented for determination of fracture behavior of one foot square by 0.7 inch thick silica plates under impact of ceramic projectiles simulating impact of high velocity rock debris. Nominal projectile sizes were one and three millimeter diameter rods and one, two, five and ten centimeter diameter spheres. Nominal velocities attained were between 100 and 3200 ft/sec for the smaller projectiles and between 60 and 170 ft/sec for the largest projectiles. Impact tests were conducted for single and multiple particle impacts. Plate damage varied from surface erosion to total destruction. Correlation with results obtained by other investigators on wave mechanics and impact phenomena is discussed.

1.0 INTRODUCTION

One of the primary uncertainties with respect to the effects of the nuclear environment on hardened radars is the potential erosion and cracking of the radome or thermal shield through impact of debris ejected by explosions in the vicinity of the earth's surface. Surveys of data on impact phenomenology indicate little evidence of applicable experimentation to enable an analysis of radome damage due to impinging debris.

Hertz (1) was one of the first to form a theory of impact and the French(2) as early as 1884 investigated and performed tests on the penetration of spherical cannon balls into masonry walls and ship hulls. In the early 1940's many experiments were conducted by Division 2 of the National Defense Research Committee (3) on the penetration of concrete by bombs and metal projectiles. The emphasis in this work was to substantiate relationships for predicting the projectile penetration, perforation, and back face scabbing for concrete slabs. In addition, Tolch and Bushkovitch (4) have conducted extensive penetration and cratering tests on granite, diabase, quartzite, oolitic limestone, and sandstone.

Further background into the mechanics of penetration and impact can be gained from two other extensive fields of endeavor, i.e., hypervelocity impact and rain erosion. A comprehensive survey of hypervelocity impact information has been compiled by Hermann and Jones (5). Others who have contributed in this area are Kornhauser (6), Huth, Thompson and Van Valkenburg (7), Reinhart (8), and others (9-13). Supporting the hypothesis of the hypervelocity work is that of Engel (14) and others (15-16), who have studied the rain erosion behavior of many materials.

Although the reference material is quite broad and plentiful, all of the previous work mentioned does not really consider the case of interest, i.e. a brittle rock-like projectile impacting a brittle ceramic radome plate. It will be shown, however, that the same general forms of relationships for depth of penetration versus velocity of impact, etc., which have evolved from the above referenced work can be used with high correlation to describe these same types of behavior for ejecta material impacting a ceramic radome.

As an initial effort to identify the seriousness of the debris impact problem, Hughes Aircraft Company conducted a Study Task (17) which was sponsored by the Ballistic Systems Division of the Air Force Systems Command and included limited testing of the response of fused silica radome material to the impact of particles. This test program, as reported herein, was to provide data over the spectrum of particle size and velocities that might be expected from bursts in the vicinity of a hardened radar. In addition, the test data were analyzed to obtain expressions defining penetration, cratering, and back face spallation as a function of the impact parameters.

2.0 IMPACT TEST PROCEDURES

2.1 TASK OBJECTIVES

The objectives of this program were to provide impact data over a spectrum of particle sizes and impact velocities and to examine the results for correlation of descriptive variables. The particle size/density/velocity spectrum employed was one that could be easily achieved in the laboratory and is shown in Table 2-I. Slip-cast fused silica was selected for the sample radome material as it has been chosen in several preceding programs as a leading radome material because of its superior thermal and dielectric characteristics. The dielectric constant and loss tangent factor are substantially insensitive to temperature and frequency variations. Less important factors were its low cost, ease of fabrication, and ready availability.

The fused silica plates used were one foot square and approximately 3/4 inch thick. The plate size was chosen from the viewpoint that large radomes would most likely be constructed in a tile fashion to minimize crack propagation and catastrophic radome failure from a few high energy impacts. The size chosen may not be the most optimum for any particular application, but it represents a reasonable size for laboratory testing and general design usages. In addition to the test radome plates, backup plates of the same material and same area but two inches in thickness were used. This was to represent a continuous support of the radome plates which could be indicative of plugged radiating element antennas or slab antennas.

TABLE 2-I. DEBRIS IMPACT CONDITIONS

Object Size Diameter cm	Number of Impacts Per Unit Area	Velocity ft/sec
	(impacts/cm^2)	
0.1	1, 10, 100	100, 300, 1000, 2500, 3500
0.3	0.1, 1, 10	100, 300, 1000, 2500
	(impacts/ft^2)	
1.0	1, 10	100, 300, 1000
2.0	1, 5	100, 300, 1000
5.0	1	100, 300
10.0	1	100, 300

2-1

17

2.2 RADOME PLATE AND PROJECTILE SPECIMENS

Slip cast fused silica* test plates were fabricated by open slip-casting, drying, and firing to 1210°C. A kiln heating rate of 300°C per hour was used. The plates were not soaked at maximum temperature in order to keep cristobalite formation in the silica to a low level. The plates were then ground to a specified thickness with parallelism tolerances of ±0.01 inch and surface finish of 64 rms or better. Density of the fired material was 1.94 g/cc consistently. Several plates were made double or triple thickness to act as heavy backup slabs. Radome test plates were bonded onto these thick slabs with 3M adhesive Number EC-1300-L, a strong elastomeric contact adhesive. The plates were coated with graphite to provide photographic contrast.

To simulate rock-like projectiles, fused silica spheres and quartz rods were utilized. Quartz rods (density 2.6 g/cc) of one and three millimeter diameter were used to manufacture one and three millimeter projectiles. These were cylindrical rather than spherical. For the high density shots of one millimeter particles, sand was screened and weighed. The larger projectiles, 410-caliber balls (approximating one centimeter diameter), 20-mm cannon balls and the 2- and 4-inch mortar balls (approximating 5 and 10 centimeter diameters, respectively), were made of slip-cast fused silica by solid casting. Balls were finished round and smooth by hand in the unfired state, then were fired to 1210°C to full hardness. The four inch balls were reground in the fired state in a sphere lapping machine to improve sphericity and to assure a good fit in the mortar barrel.

2.3 TEST EQUIPMENT AND PROCEDURES

For a single impact of one and three millimeter projectiles, a pneumatic launcher was constructed with interchangeable barrels having the required bores. This launcher consisted of a six-inch diameter pressure accumulator tank and a fast-acting electric solenoid valve operated by remote control. Air pressures up to 1500 psi provided 850 ft/s for one mm projectiles and 1200 ft/s for three mm projectiles. Pressure limitation of the system prevented achieving higher velocities. However, by performing high density multiple impact tests with the shotgun launcher at higher velocities, it was determined that high velocity single impact tests were not warranted for these small projectiles; i.e., insignificant damage resulted from high velocity, multiple impacts.

The action of a 410 gauge shotgun was used as the one centimeter projectile launcher, Figure 2-1. Balls were loaded directly into shotgun shell casings with a sufficient number of wads to develop the chamber pressure necessary for each velocity test point. Generally, a thicker wad column was used for the higher powder charges. Velocities in excess of 2500 ft/s were obtained with one centimeter diameter balls. Two test points with shells containing 1000 grains of one mm diameter quartz sand particles were also obtained with the shotgun launchers at velocities in excess of 3000 ft/s.

---

*Made from Teco-sil, fine, Tennesse Electro-Minerals Corp., Decatur, Georgia, 30033.

A 20 mm smooth bore cannon was used to launch two centimeter diameter projectiles, Figure 2-2. Powder charges were held in place in 20-mm cartridges with tightly packed tissue paper wadding, and balls were seated into the cartridges with several thicknesses of tissue. Wider scattering of velocity points was observed with this launcher than with the shotgun launcher, but fracture data obtained were satisfactorily correlated. This spread was undoubtedly caused by a less controllable loading procedure with the 20 mm shells.

For 5 and 10 centimeter diameter projectile launchers, two mortars were constructed, Figures 2-3 and 2-4. After the 1-centimeter tests were concluded, the barrel of the 410-gauge shotgun was cut off at a point just forward of the shell chamber section and threaded externally to fit matching threaded holes in the two breech blocks. In this way, standard shotgun shells were used to accelerate these larger projectiles. Tight fitting teflon sabots were machined to fit the bore of each mortar. Maximum velocities obtained with the mortars were 212 ft/s with the 2-inch projectile and 137 ft/s with the 4-inch projectile. These velocities totally destroyed the ceramic plates so that higher velocities were not investigated.

For all test shots, ceramic test plates were bolted tightly into a heavy steel angle framework backed by 3/4-inch thick plywood as shown in the previous figures. The framework was either set into or clamped onto a massive backing structure (a permanent fixture at the test site) to provide both good support and protection of personnel and equipment from laterally scattered, high velocity debris.

Velocities were measured as the projectiles penetrated two conductive silver serpentine patterns (silk screened onto thin paper targets) spaced one foot apart. The conductive silver used was duPont No. 4929, thinned with Cellosolve acetate. A Hewlett-Packard Model 722-B decade counter was used to record the time interval of the projectile passing between the two paper targets. To check the retardation effect of the targets on small diameter, low velocity projectiles, a third sheet of paper was inserted between the first and last sheets, and a negligible effect resulted at the lowest velocities.
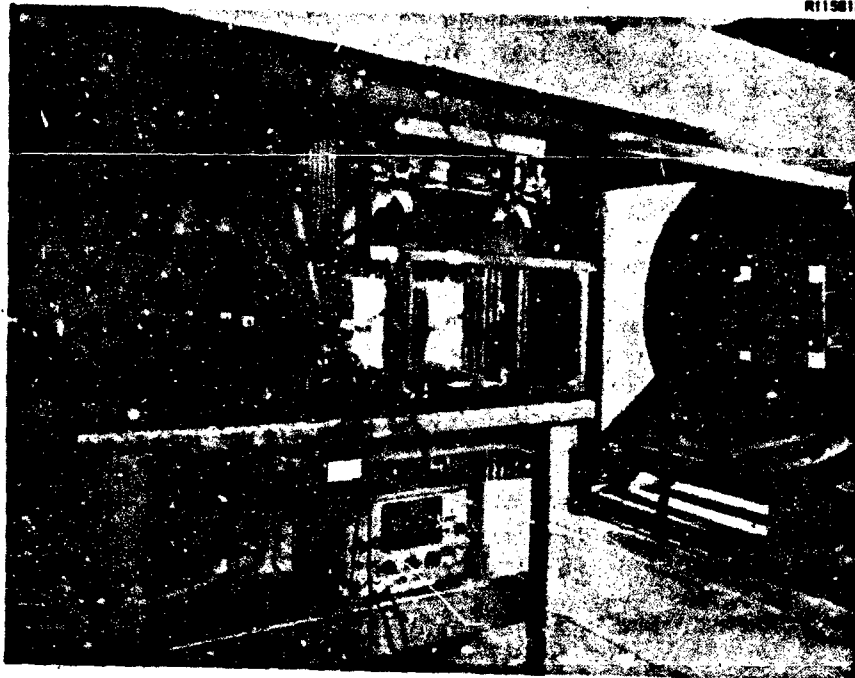
Figure 2-1. Remote Test Site Setup for 410-Gauge Launcher

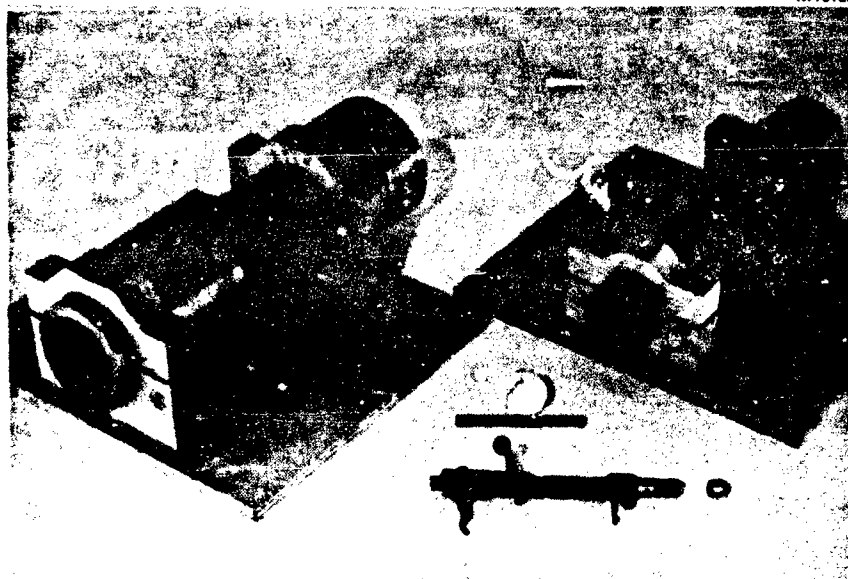Figure 2-2. Remote Test Site Setup for 20-mm Launcher

Figure 2-3. Launchers for 5 and 10-cm Projectiles

Figure 2-4. Remote Test Site Setup for 5 and 10-cm Mortar Launchers

3.0 IMPACT TEST RESULTS

A summary of the impact shots performed and a qualitative description of the resulting damage is given in Table 3-I. Included in this table are fourteen columns giving the projectile properties (number, diameter, mass, impacting kinetic energy), the plate properties, and the target (radome plate) damage. The plate damage has been divided into front and rear surface characteristics, as back face spallation was a common occurrence. Figures 3-1 and 3-2 show the front and back surfaces, respectively, of a typical test plate. In some cases a front crater occurred, but was so small in size that neither the depth nor volume could be accurately measured. Therefore, several of these dimensions are missing in the table, but these points were deemed insignificant compared to more gross damage impacts. It will also be noted that in some cases the 2-inch backup plate was not used. In tests where only front face damage was anticipated single plates were used to conserve time and expense.

The basic data from the impact tests are given in Table 3-I. By inspection of the columns marked target damage, one can obtain a general sense of the thresholds of damage, i.e., the particles sizes and their velocities which initiate damage. The number of tests were not sufficient to allow a large variation in parameters in order to closely define these thresholds, but the general qualitative values are apparent. Figures 3-3 through 3-22 present a clear visualization of the ramification of these impact tests. These photographs are the results of representative tests shown in order of increasing severity of damage. All plates were painted with a graphite solution to give a high contrast in order to emphasize the crater damage.

Figure 3-3 shows the damage inflicted by one and three millimeter projectiles for single and multiple impact conditions. The bottom row shows the small craters formed by single 3 mm particles at velocities in the range of 130 to 300 ft/s. The third row illustrates the 1 mm particle damage. These four shots were at approximately 350 ft/s. The two patterns on the left edge of the plate were caused by ten consecutive shots in each instance. The far left entry of the second row shows the results of a single 1 mm particle impact at 876 ft/s. The other three patterns of this row resulted from ten consecutive shots, each of 3 mm particles, with the second from the left resulting from velocities of 120 ft/s, and the latter two patterns from velocities of 300 ft/s. The top row shows two single 3 mm impacts at 1200 ft/s (two craters toward the left edge), one pattern from ten consecutive shots of 1 mm particles at 885 ft/s (third from left), and one almost undetectable crater from a single 1 mm particle at 840 ft/s (top right corner of the plate). Several size/velocity test combinations were eliminated when it was determined that little or no effect could be discerned. Thus the 1 mm/100 ft/s and 3mm/100 ft/s were eliminated. To confirm that small particles at high velocities do very little damage, one shot, using the 410 gauge launcher, was made containing 1000 particles of 1 mm sand at 3200 ft/s. The results of this shot are shown in Figure 3-4. From a calibration shot, the intensity was approximated to be in excess of 200 particles per square centimeter at the center of the impact area. The surface indicated a sand blasting effect, but the plate was relatively undamaged.

3-1

22

Figure 3-5 shows the damage from two multiple impact tests. Both craters resulted from 10 consecutive shots each of 3 mm particles at 1190 ft/s. Figure 3-6 shows the back side of this plate where rear face spallation has just initiated (test plate was not backed up).

Figures 3-7 and 3-8 show the front and rear crater damage (radome plate with backing) caused by a 1 cm projectile at approximately 2500 ft/s. Note that the rear crater is substantially larger than the front. This phenomena is discussed in greater detail in a later section. Figures 3-9 and 3-10 indicate the damage under nearly identical conditions as the previous photograph, except only a single plate was used. The damage is more extensive, the plate being severely cracked and completely penetrated.

Figures 3-11 through 3-14 show the results of using a steel sphere as the projectile (mass approximately 28 times that of a 1 cm fused silica ball) at velocities of 76 and 117 ft/s, respectively. It is interesting to note from the curve in Figure 4-13 that the steel spheres, upon impact, cause a larger front crater (and also rear crater) per unit of impacting energy. This is to be expected since steel balls do not shatter upon impact and impart all the available impact kinetic energy to the plate. In nearly all cases, no evidence could be found after impact that the ceramic balls did not fracture. In fact, several 1 cm projectiles were dyed and attempts were made after impact tests to locate fragments identifiable to the projectile. These attempts failed in each instance.

Two of the 5 cm projectile tests at velocities of approximately 170 ft/s are shown in Figures 3-15 through 3-19. These two tests indicate several interesting phenomena and are discussed in greater detail below. Figures 3-20 and 3-21 show the devastating damage which can occur from impacts of 2 cm rocks at a relatively high velocity of 1060 ft/s. This test plate is very interesting as it very nearly depicts a radome plate (0.71 inch thick) bonded to a 2-inch backup plate to simulate plugged waveguides of a representative Phased Array Radar system. An impact of this magnitude would undoubtedly remove nearly half of a radome plate and spall several, if not totally demolish, 4 to 6 backup plugs. Figure 3-22 shows the rear face of a test panel constructed of 4 bonded plates, each 0.71 inches thick, which has been impacted by a 10 cm projectile at a velocity of 89 ft/s. It is of interest to note that this represents a velocity well below the predicted 350 ft/s free-fall velocity for a 10 cm sphere.

As illustrated by the photographs in the preceding figures, the lower threshold for radome damage caused by impinging debris is 3 mm projectiles at velocities in excess of 1000 ft/s. Moreover, the damage at this level of impact is quite minor for single impact. At the other extreme is the severe damage level by high velocity (500 to 1000 ft/s), 2 cm projectiles and low velocity (150 ft/s), 5 cm particles (see Figure 3-15).

23

3-2

TABLE 3-1. TEST DATA SHEETS

| Test No. | | Projectiles | | | | Target | | Target Damage | | | | | | |
| | | | | | | | | Front Crater | | | | Rear Crater | | |
Test No.	Number ①	Diameter, mm	Mass, $\frac{\text{lb-sec}^2}{\text{in}} \times 10^{-7}$	Impact Velocity, ft/sec	Impact Energy, in-lbs	Number of Plates, in	Plate Thickness, in	Depth, in	Diameter, in	Volume, in³ $\times 10^{-4}$	Depth, in	Diameter, in	Volume, in³ $\times 10^{-4}$	Number of Cracks
1	1	1	0.33	346	0.79	1	0.71	-	0.043	-	0	0	0	0
2		1	0.29	411	0.35	1	0.71	-	0.035	-	0	0	0	0
3	10c	1	0.34	345	2.88	1	0.71	Same as T7 and T8						0
4	10c	1	0.34	345	2.88	1	0.71	Same as T7 and T8						0
5	1	1	0.33	876	1.83	1	0.71	0.005	0.015	0.61	0	0	•	0
6		1	0.29	840	1.45	1	0.71	-	-	-	-	-	•	0
7	10c	1	0.34	345	2.93	1	0.71	0.020	0.250 ⑤	3.27	0	0	•	6
8	1000s	1	90.63	2562	42.83	1	0.71	0.018	6.5 ⑤	69.45	0.213	1.286	1877	6
9	1000s	1	94.62	3230	7108	2	1.43	0.100	7.0 ⑤	248.20	0	0	•	0
10	1	1	5.14	127	0.60	1	0.71	-	0.058	-	0	0	•	0
11		1	5.10	124	0.58	1	0.71	-	0.040	-	-	-	•	0
12	100	1	51.87	120	5.38	1	0.71	Same as T9 and T10						•
13	1	3	4.80	304	3.19	1	0.71	0.004	0.125	0.434	-	-	•	•
14	1	3	5.04	309	3.47	1	0.71	0	0.090	0.332	-	-	•	0
15	10c	3	52.33	300	33.91	1	0.71	0.025	0.330	10.08	-	-	•	0
16	10c	3	50.79	300	32.91	1	0.71	0.030	0.275	5.54	-	-	•	0
17	1	3	5.23	1202	54.41	1	0.71	0.048	4.290	7.51	-	-	•	0
18	1	3	6.19	1190	63.11	1	0.71	0.063	0.312	16.62	-	-	•	•
19	10c	3	51.87	1190	528.9	1	0.71	0.173	0.962	364.50	-	-	•	0
20	10c	3	51.58	1190	546.3	1	0.71	0.203	1.135	395.30	0.030	1.22	0.56	0
21	10s	3	29.94	2270	1111	1	0.71	0.065	1.688 ⑤	127.50	-	2.555	34.06	0
22	10s	3	24.34	1850	599.8	1	0.71	0.080	1.88 ⑥	214.50	No Damage			0
23	1	10.4	58.66	291	35.76	1	0.71	-	-	-	No Damage			0
24		10.4	66.86	269	34.83	1	0.71	-	-	-	-	-	-	0
25	10c	10.4	587.60	343	497.7	1	0.71	0.030	0.710	21.12	0.055	1.485	85.94	1
26	10c	10.4	585.50	283	336.8	1	0.71	0.012	1.038	1.51	-	-	-	0
27	1	10.4	59.84	1110	530.8	1	0.71	0.023	0.358	10.21	-	-	-	•

TABLE 3-1. TEST DATA SHEETS (Continued)

Test No.	Projectiles					Target		Target Damage						
								Front Crater			Rear Crater			
	1 Number ①	2 Diameter, mm	3 Mass, lb-sec²/in X 10⁻⁷	4 Impact Velocity, ft/sec	5 Impact Energy, in-lbs	6 Number of Plates, in	7 Plate Thickness, in	8 Depth, in	9 Diameter, in	10 Volume, in³ X 10⁻⁴	11 Depth, in	12 Diameter, in	13 Volume, in³ X 10⁻⁴	14 Number of Cracks
28	1	10.4	59.58	1390	828.8	1	0.71	0.115	2.065	185.90	0.039	1.378	54.36	0
29	1	10.4	41.54	1492	665.8	1	0.71	0.069	0.472	60.00	0.023	1.596	30.28	0
30	5c ②	10.4	283.00	1018	2111	2	1.42	0.255	2.552	2150.1	0.316	3.505	11000	4
31	6c ③	10.4	367.40	1110	3215	2	1.42	0.249	4.122	4790.1	·	·	·	5
32	1	10.4	59.65	2380	2433	1	0.71	0.203	1.342	729.0	0.410	3.490	11500	5
33	1	10.4	63.78	2562	3014	2	1.42	0.241	1.195	872.00	0.561	3.870	18600	2
34	1	10.4	59.35	2700	3115	1	0.71	0.260	1.325	946.00	0.450	3.612	12800	6
35	8c	10.4	436.50	2318	16650	2	2.91	0.625	4.525	21900	·	·	·	8
36	1	20	361.60	1.6	35.03	1	0.71	0.006	0.316	7.251	·	1.928	50.00	1
37	1	20	361.20	70	12.74	1	0.71	0.001	·	·	·	·	·	0
38	1	20	385.70	107	31.79	2	1.42	0.003	0.242	0.714	No Back Damage		·	0
39	1	20	361.80	104	28.18	2	1.42	0.002	0.235	0.204	No Back Damage		·	0
40	1	20	365.70	394	408.7	2	1.42	0.004	0.339	0.868	·	·	·	0
41	1 ② ④	19	1596.00	117	156.0	1	0.71	0.095	2.375	7410.1	0.615	5.375	66200	11
42	1	19	1596.	76	66.37	1	0.71	0.135	0.550	450.30	0.575	3.065	1260	3
43	5c	20	1800	209	566.1	1	1.475	0.095	1.145	198.30	0.290	3.02	3690	0
44	5c	20	1840	529	3707	4	2.84	0.670	3.125	8370.1	·	·	·	12
45	1	20	365	1300	441	2	1.42	0.115	0.9975	233.00	0.642	4.278	28000	8
46	1	20	354	812	1683	2	1.42	0.062	1.345	269.00	0.690	4.490	34000	16
47	5c	20	1900	848	9837	4	2.86	·	·	Completely Destroyed	Completely Destroyed	·	·	·
48	5c	20	1870	1060	15130	2	2.86	·	·	Completely Destroyed	Completely Destroyed	·	·	·
49	1	54.0	8260	164	1590	4	2.84	·	·	Completely Destroyed	Completely Destroyed	·	·	·
50	1	54.0	7980	172	1690	2	1.42	·	·	Completely Destroyed	0.668	4.875	50000	0
51	1	54.0	8710	62	241.1	4	1.42	·	·	Completely Destroyed	Completely Destroyed	·	·	·
52	1	101.6	36600	89	3206	2	2.77	·	·	Completely Destroyed	Completely Destroyed	·	·	·
53	1	101.6	58100	102	4327	4	3.28	·	·	Completely Destroyed	Completely Destroyed	·	·	·
54	1	101.6	48300	137	6548	2	2.80	·	·	Completely Destroyed	Completely Destroyed	·	·	·

① ~ C - Consecutive and S - Simultaneous Shots
② ~ Out of 10 shots, 2 split and 3 pulverized before striking target
③ ~ Out of 10 shots, 3 split and 1 pulverized before striking target
④ ~ Steel ball
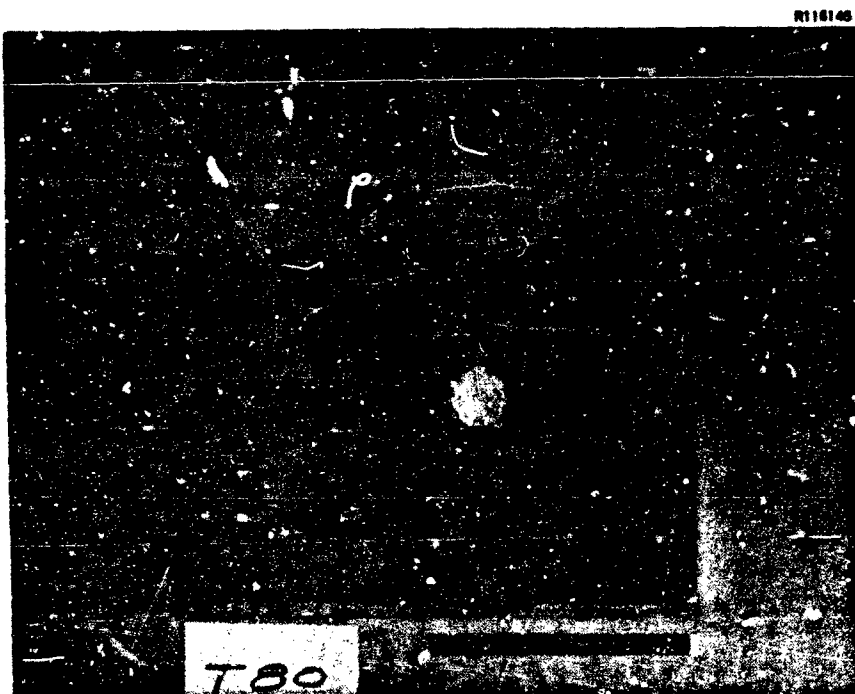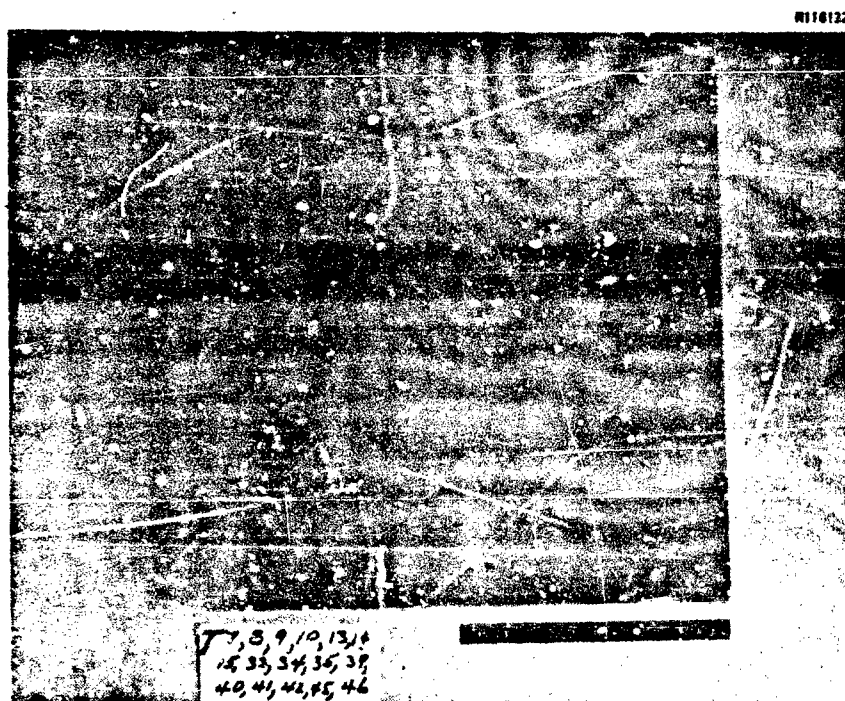⑤ ~ Mean diameter of total scatter area, damaged and undamaged

3-4

Figure 3-1. Results of Impact Test No. 46 (Front Face) (2-cm Projectile at 812 ft/s)

Figure 3-2. Results of Impact Test No. 46 (Back Face) (2-cm Projectile at 812 ft/s)

NO.	TEST NO.	PARTICLES		
		DIA (MM)	VELOCITY FT/SEC	NO.
1	17	3	1200	1
2	18	3	1200	1
3	7	1	885	10
4	5	1	840	1
5	6	1	876	1
6	12	3	120	10
7	15	3	300	10
8	16	3	300	10
9	3	1	350	10
10	4	1	350	10
11	1	1	350	10
12	2	1	350	1
13	10	3	127	1
14	11	3	126	1
15	13	3	304	1
16	14	3	309	1

Figure 3-3. Results of Impact Tests (Test Nos. 1 Through 7 and 10 Through 18).
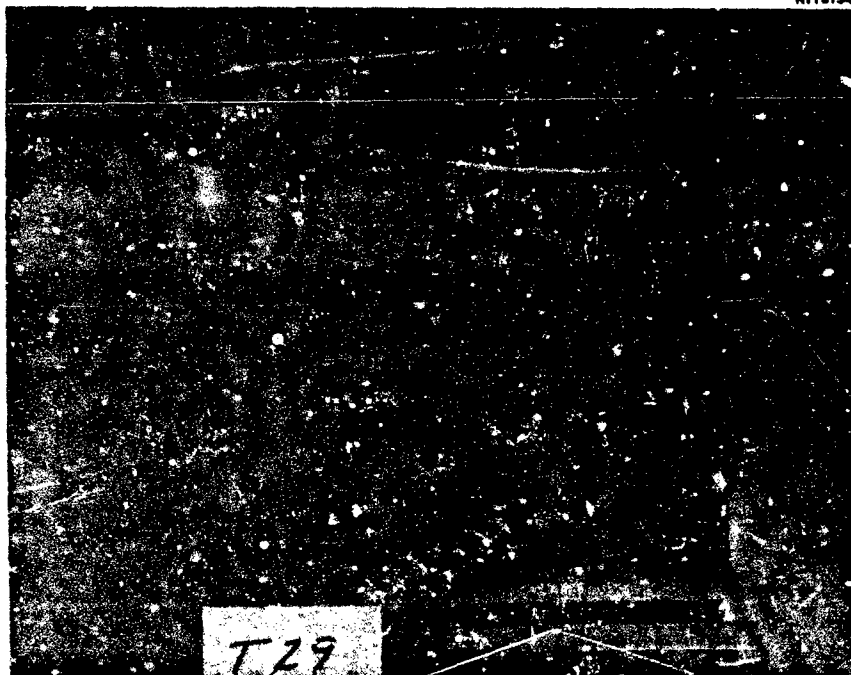
Figure 3-4. Results of Calibration Impact Test No. 9
(1000-1 mm Particles at 3200 ft/s)

Figure 3-5. Results of Impact Test Nos. 19 and 20 (Front Face)
(10-3 mm Particles at 1190 ft/s)
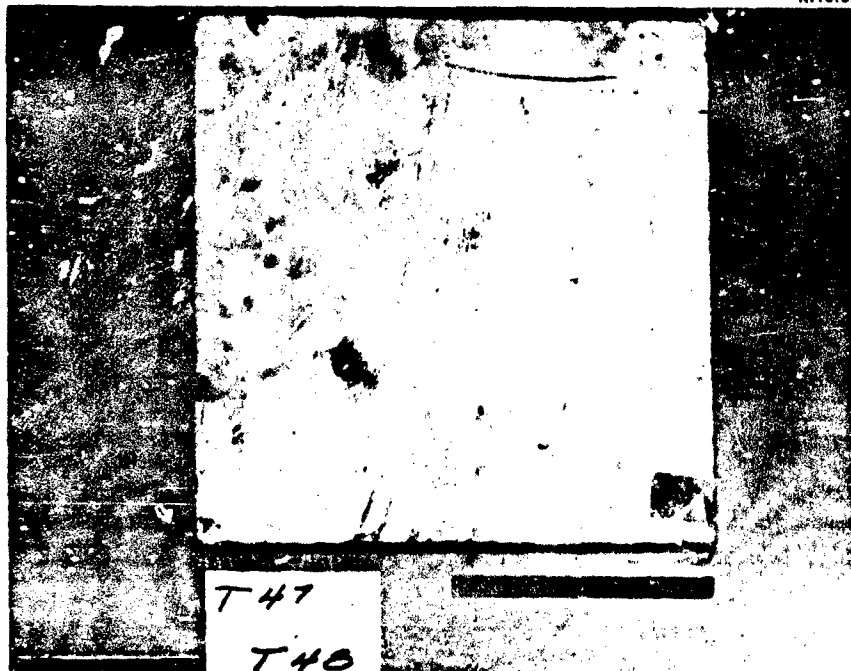
Figure 3-6. Results of Impact Test Nos. 19 and 20 (Back Face)
(10-3 mm Particles at 1190 ft/s)
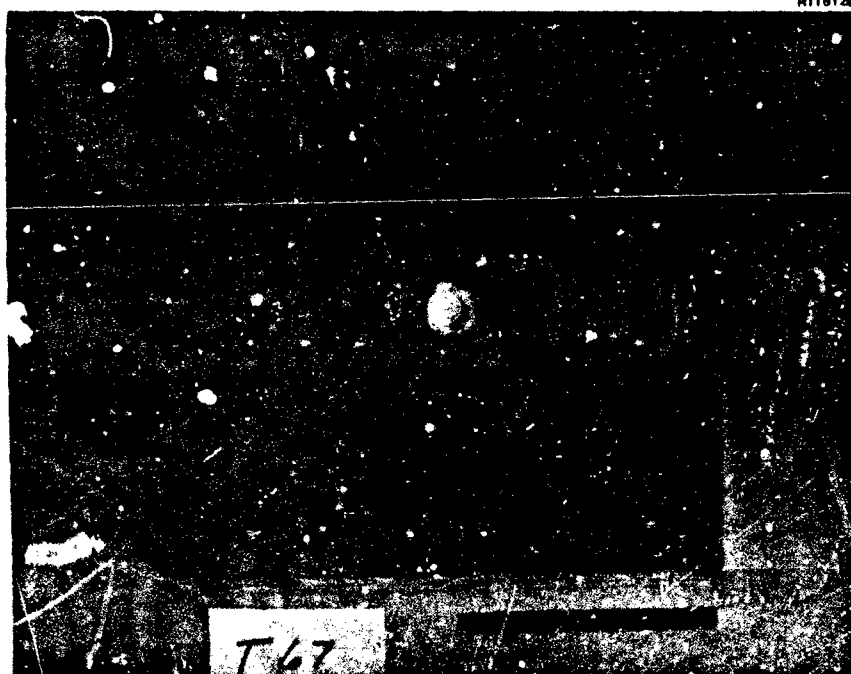
Figure 3-7. Results of Impact Test No. 33 (Front Face)
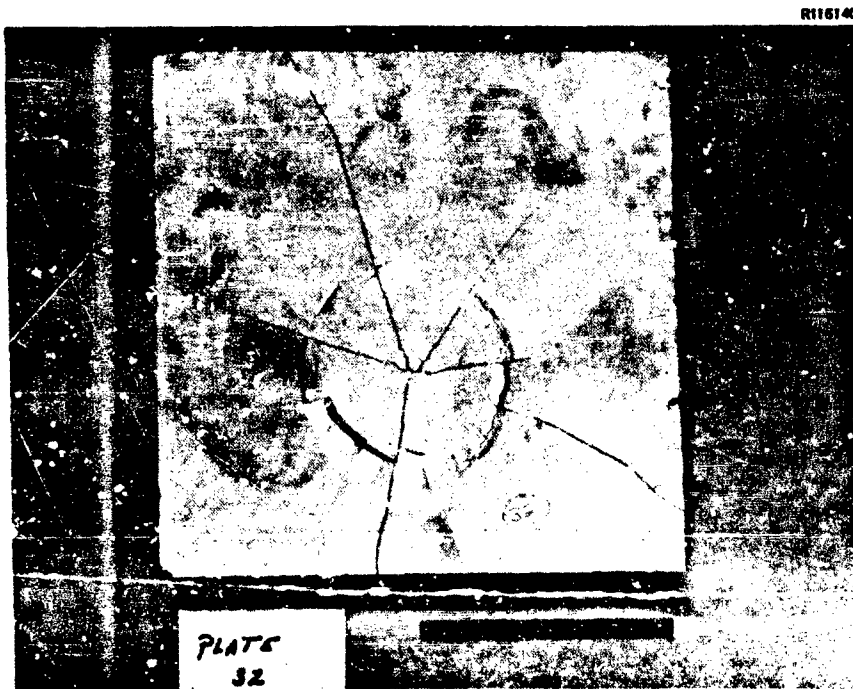(1-1 cm Projectile at 2562 ft/s)

Figure 3-8. Results of Impact Test No. 33 (Back Face)
(1-1 cm Projectile at 2562 ft/s)
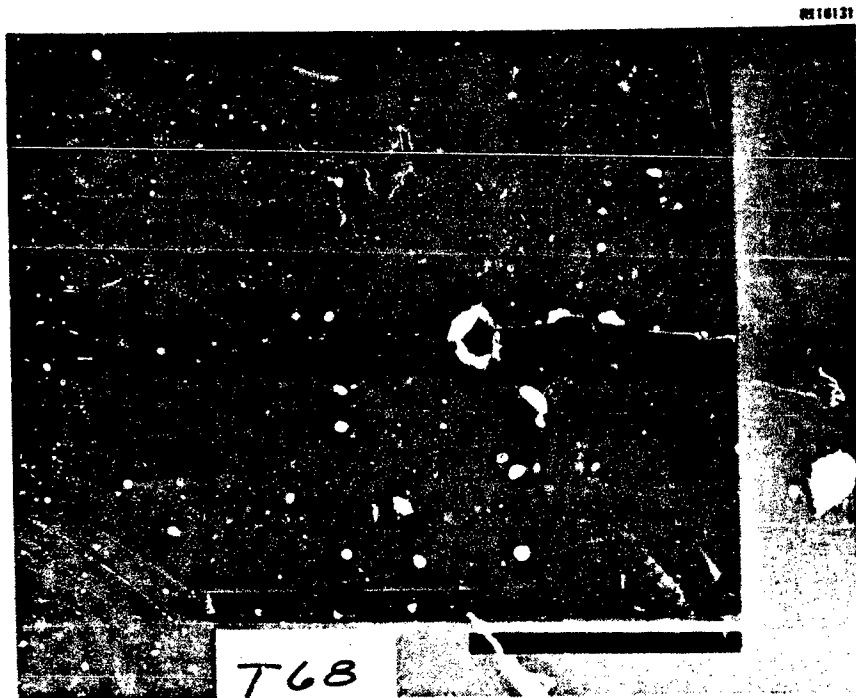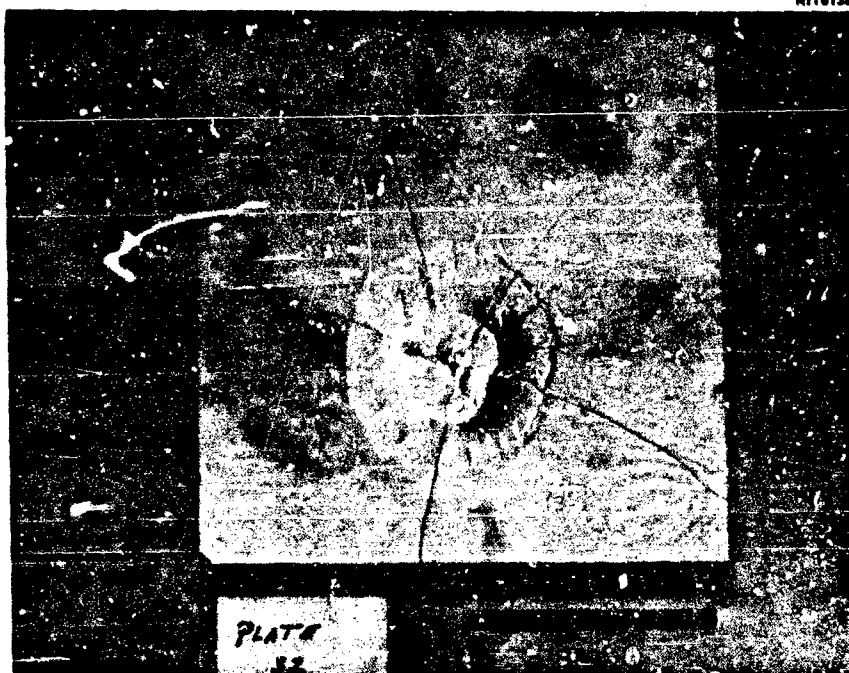
Figure 3-9. Results of Impact Test No 34 (Front Face, No Back Up) (1-1 cm Projectile at 2700 ft/s)

Figure 3-10. Results of Impact Test No. 34 (Back Face, No Back Up) (1-1 cm Projectile at 2700 ft/s)
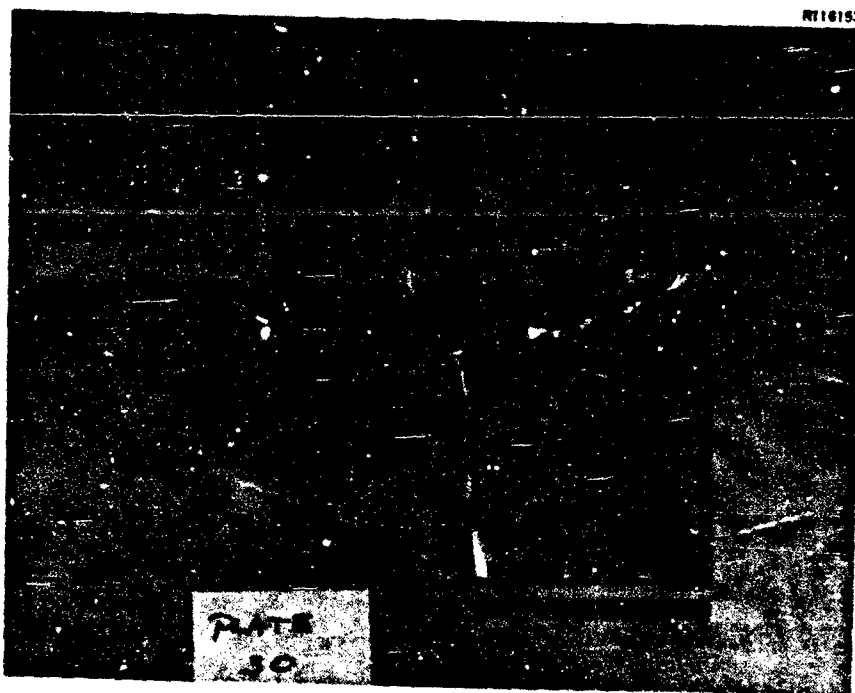
Figure 3-11. Results of Impact Test No. 42 (Front Face)
(Steel Sphere at 76 ft/s)
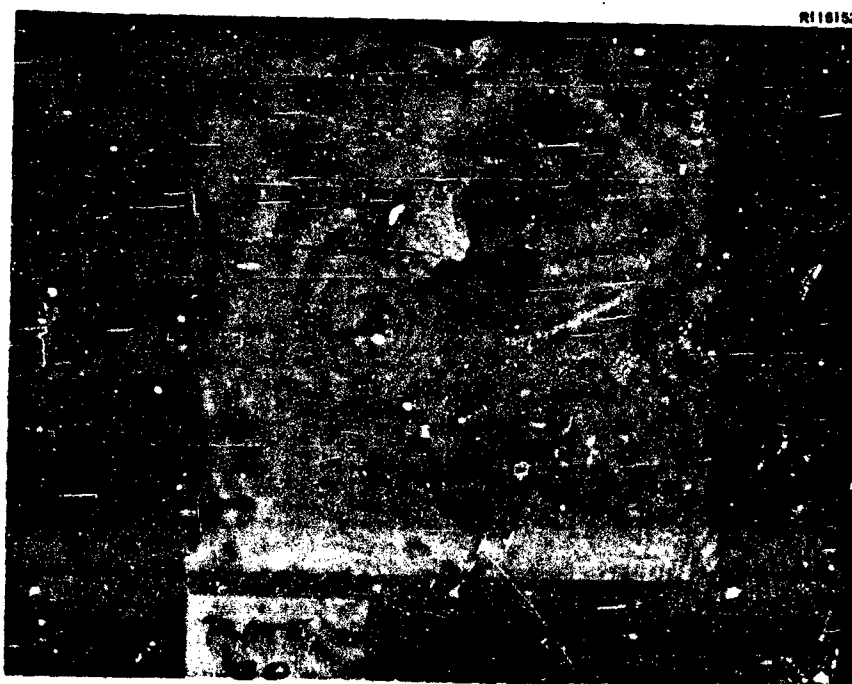
Figure 3-12. Results of Impact Test No. 42 (Back Face)
(Steel Sphere at 76 ft/s)

RI16154

Figure 3-13. Results of Impact Test No. 41 (Front Face)
(2 cm Steel Sphere at 117 ft/s)

RI16155

Figure 3-14. Results of Impact Test No. 41 (Back Face)
(2 cm Steel Sphere at 117 ft/s)

Figure 3-15. Results of Impact Test No. 49 (Front Face)
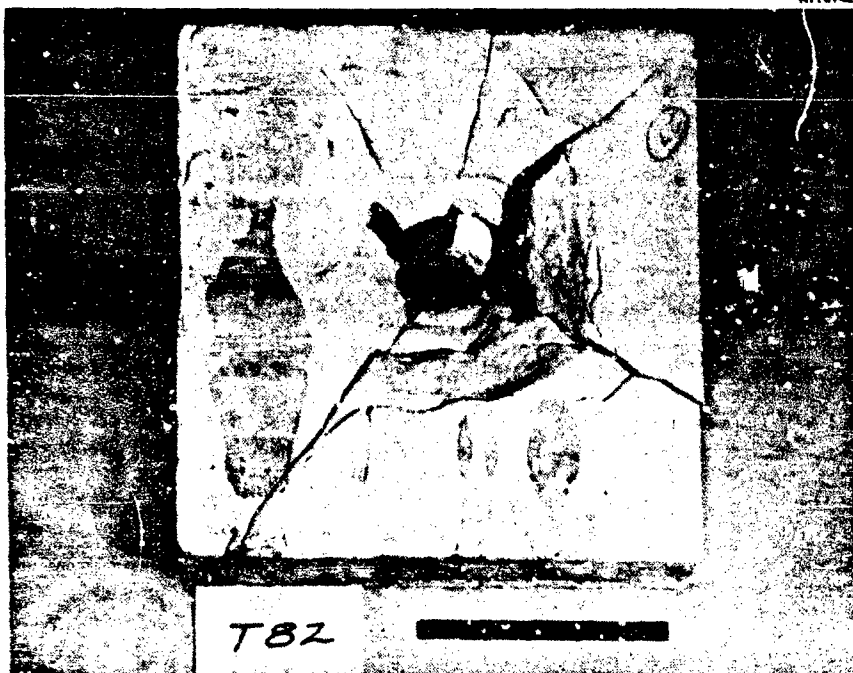(5 cm Projectile at 164 ft/s)
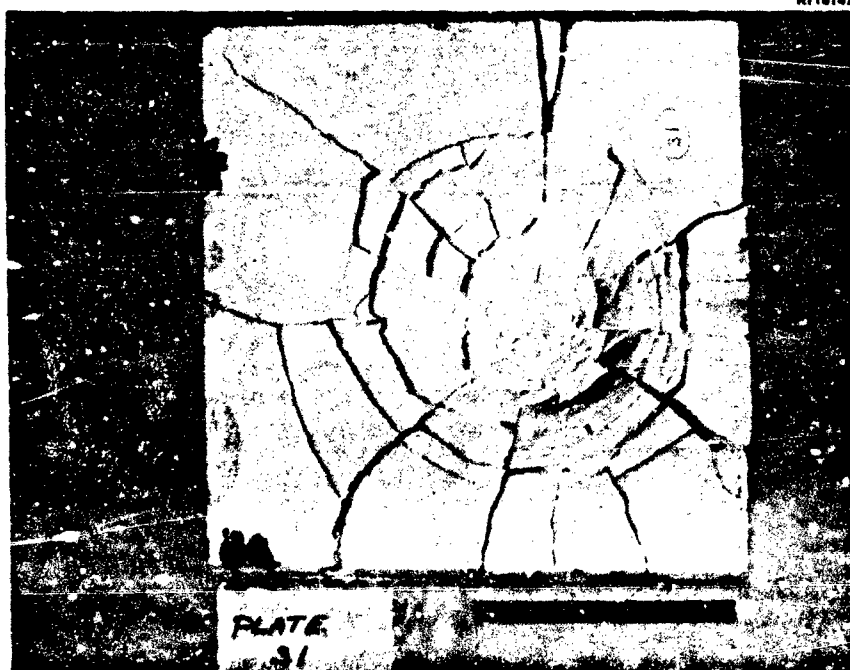
Figure 3-16. Results of Impact Test No. 49 (Rear Face)
(5 cm Projectile at 164 ft/s)

Figure 3-17. Results of Impact Test No. 50 (Front Face)
(5 cm Projectile at 172 ft/s)

Figure 3-18. Results of Impact Test No. 50 (Back Face)
(5 cm Projectile at 172 ft/s)

Figure 3-19. Results of Impact Test No. 50 (Back Face, Crater Material Removed) (5 cm Projectile at 172 ft/s)

Figure 3-20. Results of Impact Test No. 48 (Front Face) (2 cm Projectile at 1060 ft/s)

Figure 3-21. Results of Impact Test No. 48 (Back Face)
(2 cm Projectile at 1060 ft/s)

Figure 3-22. Results of Impact Test No 52 (Back Face)
(10 cm Projectile at 89 ft/s)

4.0 ANALYSIS OF TEST DATA

4.1 CORRELATION OF RELATED PARAMETERS

In order to assess quantitatively the significance of the impact test shots, descriptive variables must be chosen to specify the damage. From a review of the literature it is seen that the standard description has been the depth and the volume of the crater formed from impact. In addition to describing the front face crater by these two parameters, the rear face crater formed by spallation has similarly been described in the following table and figures. Table 4-I summarizes the dependent parameters, i.e., volumes, depth, etc., and the independent variables used to statistically describe the test data. Using the literature review as a guideline, the data has been examined to determine if any dependencies, similar to those found by former workers investigating penetration of concrete, rocks, etc., are apparent.

Dependencies of the following forms were anticipated:

$$p \propto C_p (V)^n \text{ and}$$

$$S \propto C_s (V)^m$$

where

$\qquad$ p = crater depth (inches)

$\qquad$ S = crater volume (inches^3)

$\qquad$ C_p = penetration constant

$\qquad$ C_s = volume constant

The test data are presented on log-log graphs where the exponents n and m in the above equations are simply the slope of the resulting straight line. Figures 4-1 through 4-14 show the test data plotted according to the parametric form summarized in Table 4-I. The data in each figure has been statistically processed to determine the "best fit" curve of the form:

$$\ln Y = B + M \ln x$$

by a least squares method. These curves are plotted in the figures as solid lines.

38

TABLE 4-I. TEST DATA CORRELATION ANALYSIS

| Figure No.	Dependent Variable, Y	Independent Variable, X	Intercept, B	Slope, M	Correlation Coefficient	Significant Level	Comment
4-1	Front Crater Volume	Velocity	-7.16	+2.21	+0.799	0.001	Single Impact
4-2	Front Crater Volume	Impact Energy	+2.07	+1.04	+0.885	0.001	Single Impact
4-3	Front Crater Diameter	Front Crater Depth	+0.839	+0.431	+0.710	0.01	Single Impact
4-4	Front Crater Volume	Velocity	-17.1	+4.08	+0.950	0.001	Multiple Impacts
4-5	Front Crater Volume	Impact Energy	+2.77	+1.12	+0.838	0.01	Multiple Impacts
4-6	Front Crater Diameter	Front Crater Depth	+1.58	+0.321	+0.808	0.01	Multiple Impacts
4-7	Rear Crater Volume	Velocity	-62.3	+9.72	+0.977	0.05	Single Impact, Single Plate, Only 2 Degrees of Freedom
4-8	Rear Crater Volume	Impact Energy	-19.8	+4.26	+0.992	0.01	Single Impact, Single Plate, Only 2 Degrees of Freedom
4-9	Rear Crater Diameter	Rear Crater Depth	+1.52	+0.316	+0.967	0.05	Single Impact, Single Plate, Only 2 Degrees of Freedom
4-10	(Front Crater Vol)$^{1/3}$ + Projectile Dia.	Velocity	-5.60	+0.896	+0.865	0.001	Single Impact
4-11	Front Crater Volume + Kinetic Energy	Velocity	-2.16	+0.655	+0.493	Not Significant	Single Impact
4-12	Front Crater Depth	Velocity	-13.3	+1.46	+0.887	0.001	Single Impact
4-13	Front Crater Volume	Momentum + Area	+10.0	+2.06	+0.638	0.01	Single Impact
4-14	Rear Crater Volume	Momentum + Area	+12.2	+1.42	+0.287	Not Significant	Single Impact

4-2

39
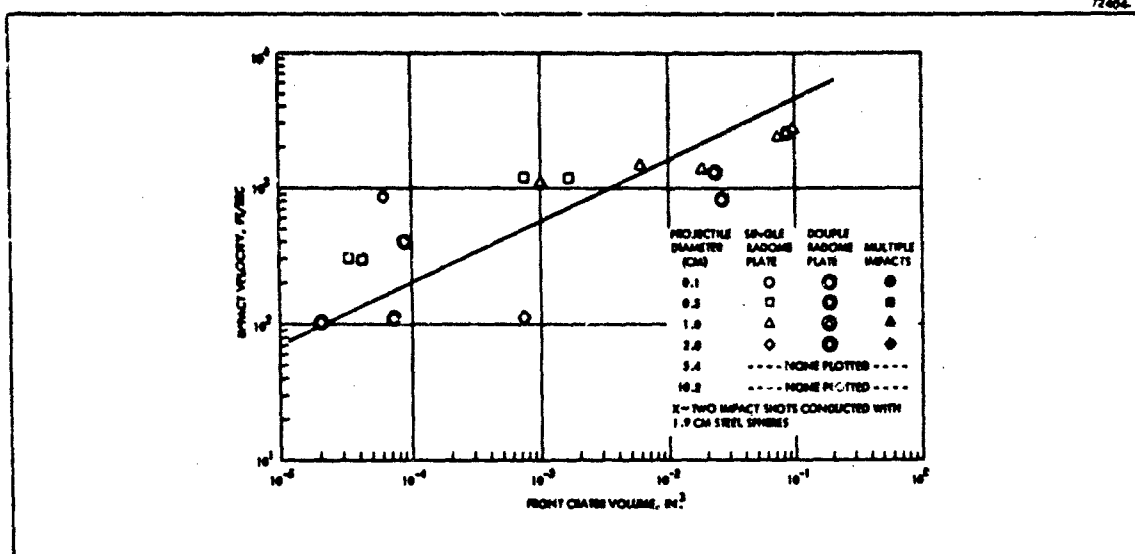
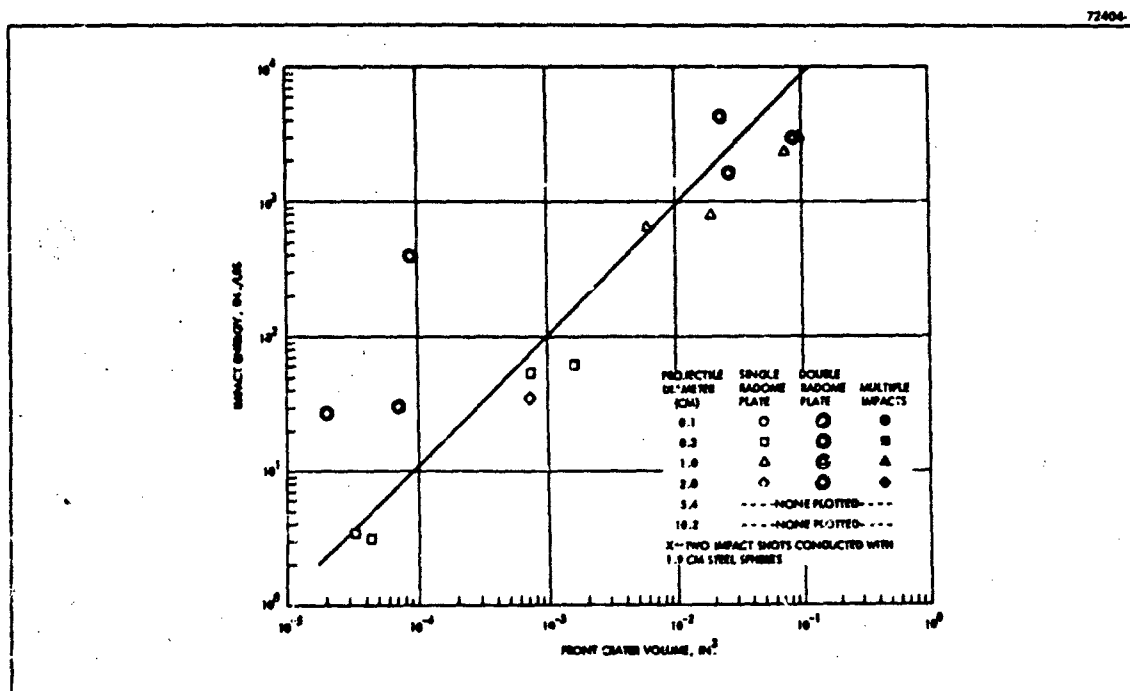Figure 4-1. Front Crater Volume Versus Particle Impact Velocity (Single Impact).

Figure 4-2. Front Crater Volume Versus Impact Kinetic Energy (Single Impact).
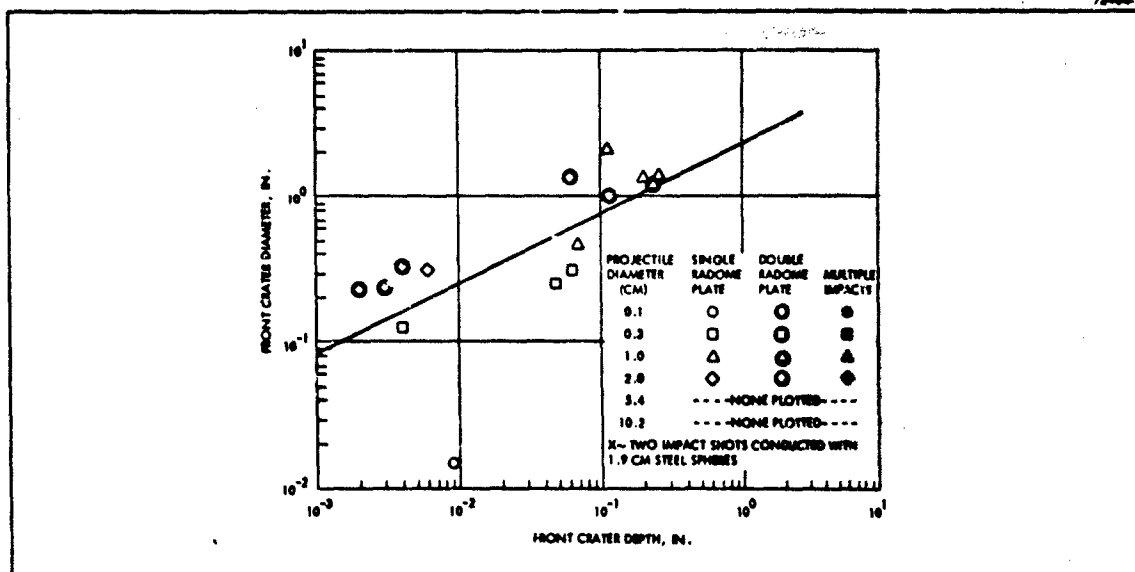
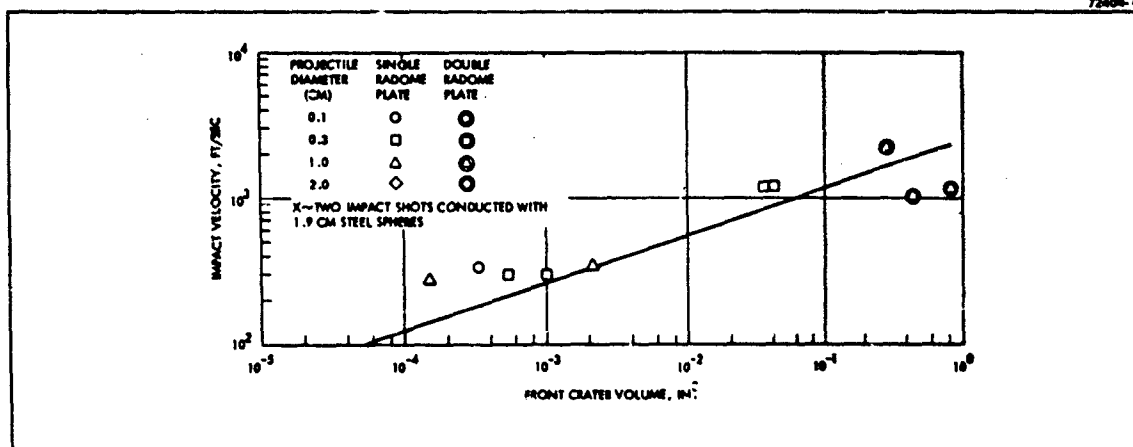Figure 4-3. Front Crater Depth Versus Front Crater Diameter (Single Impact).

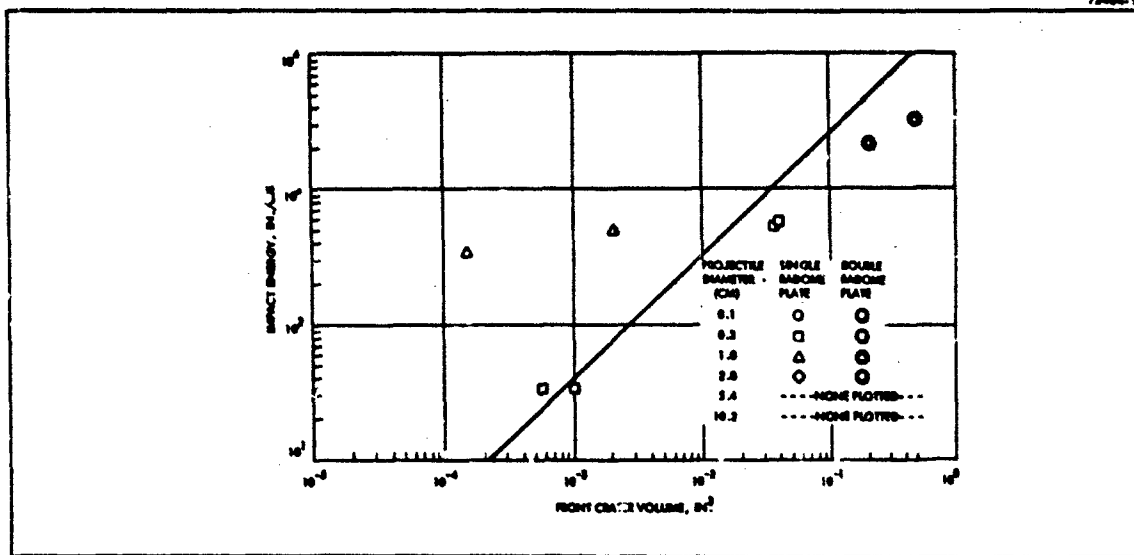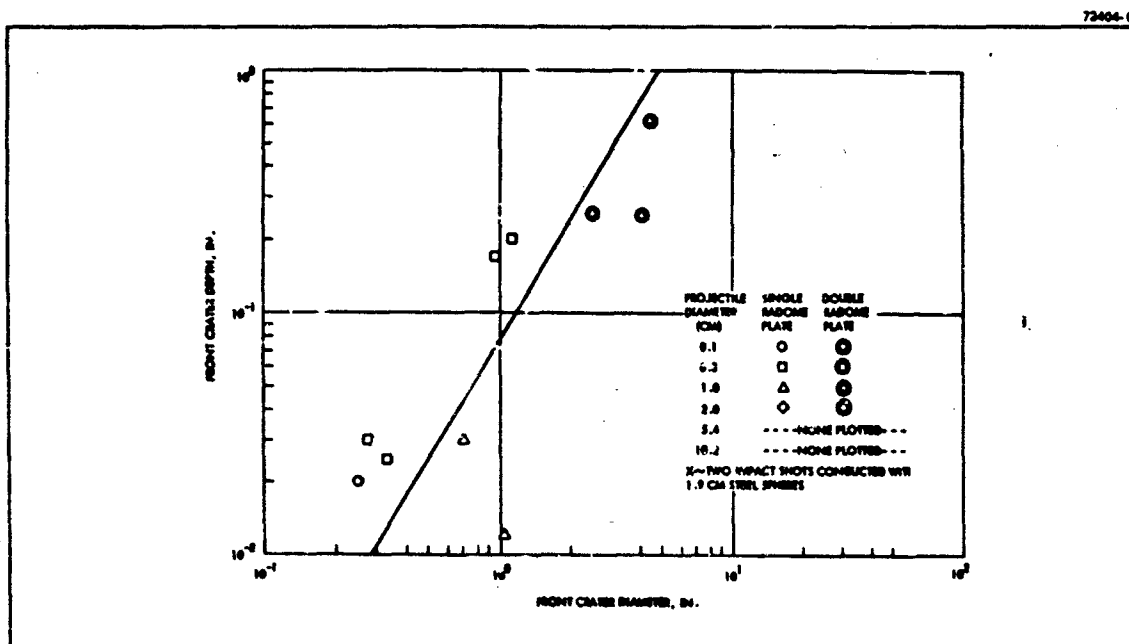Figure 4-4. Front Crater Volume Versus Particle Impact Velocity (Multiple Impacts).

41

4-4

Figure 4-5. Front Crater Volume Versus Impact Kinetic Energy (Multiple Impacts).

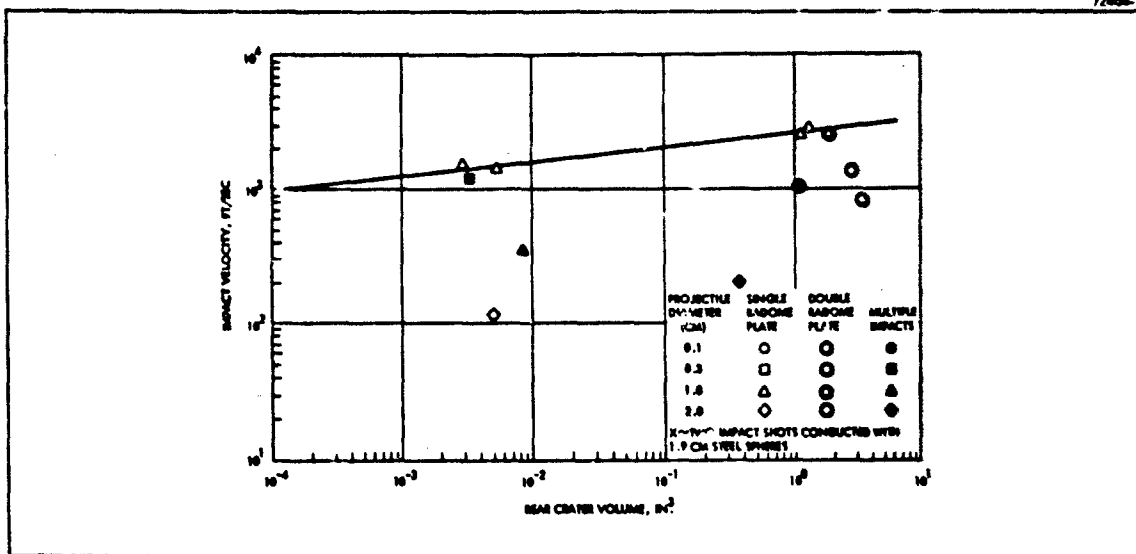Figure 4-6. Front Crater Depth Versus Front Crater Diameter (Multiple Impacts).

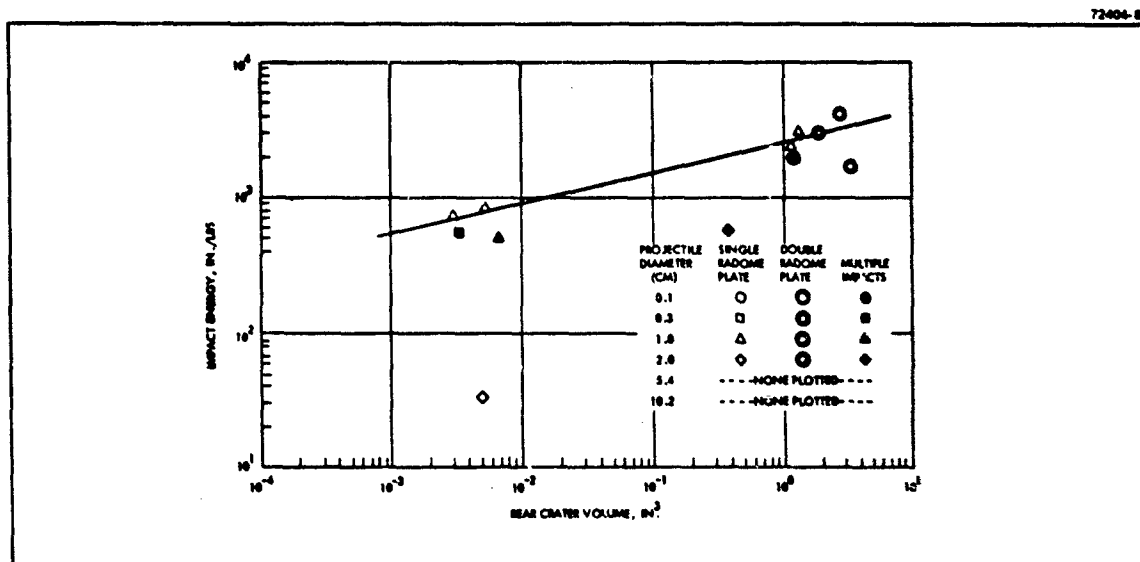Figure 4-7.   Rear Crater Volume Versus Impact Velocity (Single Impact and Multiple Impact).

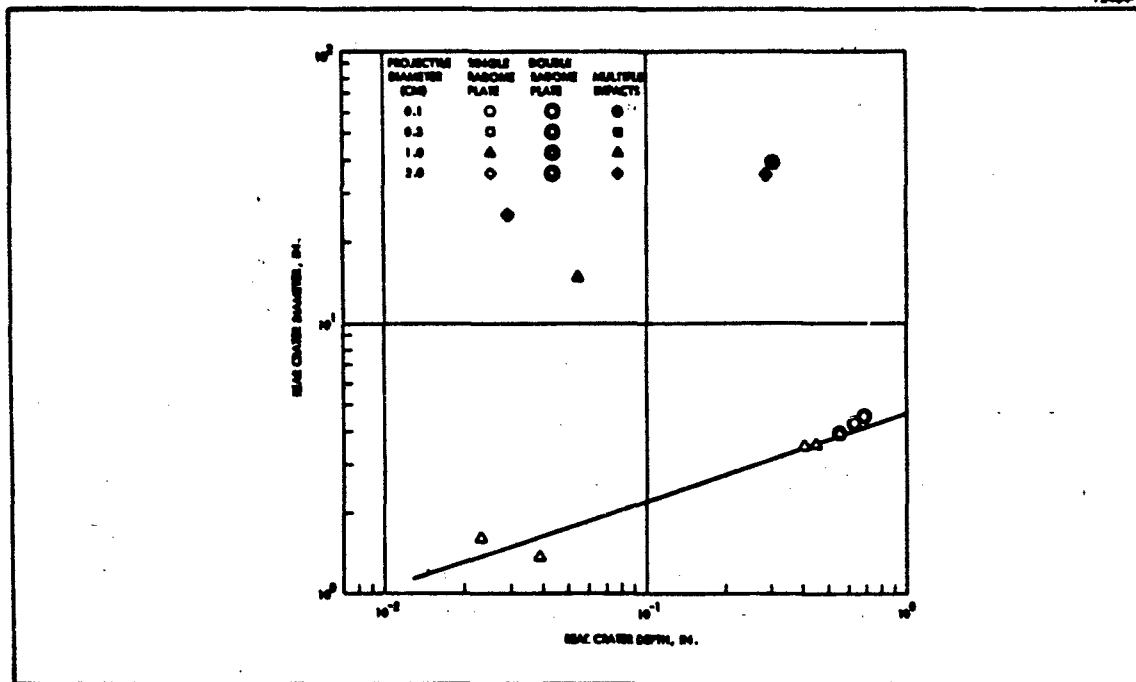Figure 4-8.   Rear Crater Volume Versus Impact Kinetic Energy (Single Impact and Multiple Impact).

4-6

Figure 4-9. Rear Crater Depth Versus Rear Crater Diameter (Single Impact and Multiple Impact).
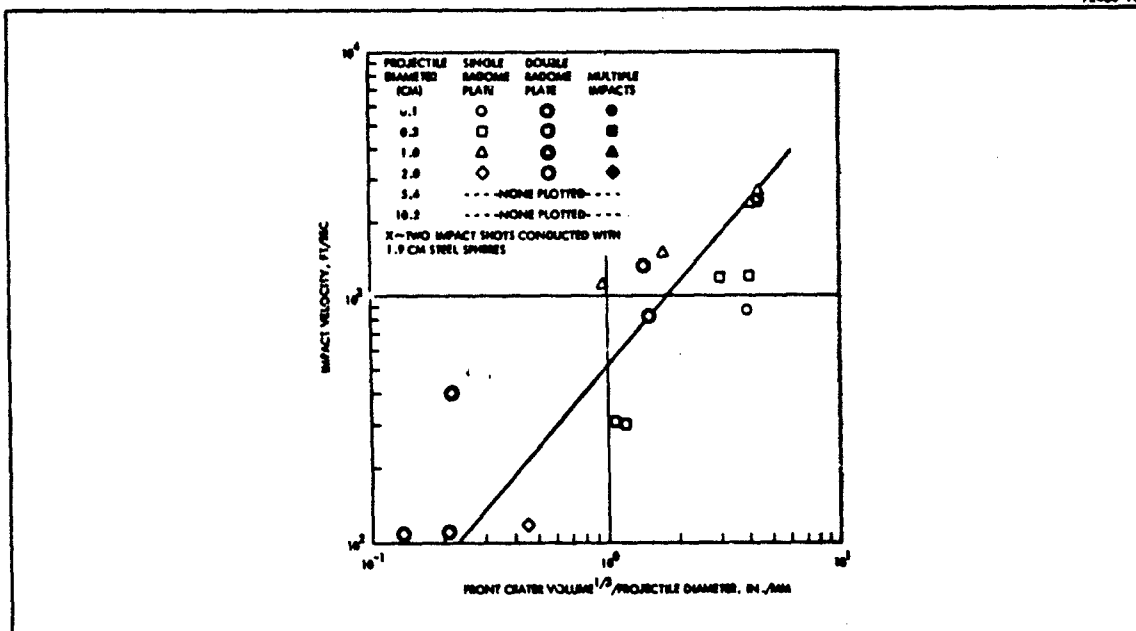
Figure 4-10. (Front Crater Volume)$^{1/3}$ (Diameter) Versus Impact Velocity (Single Impact).
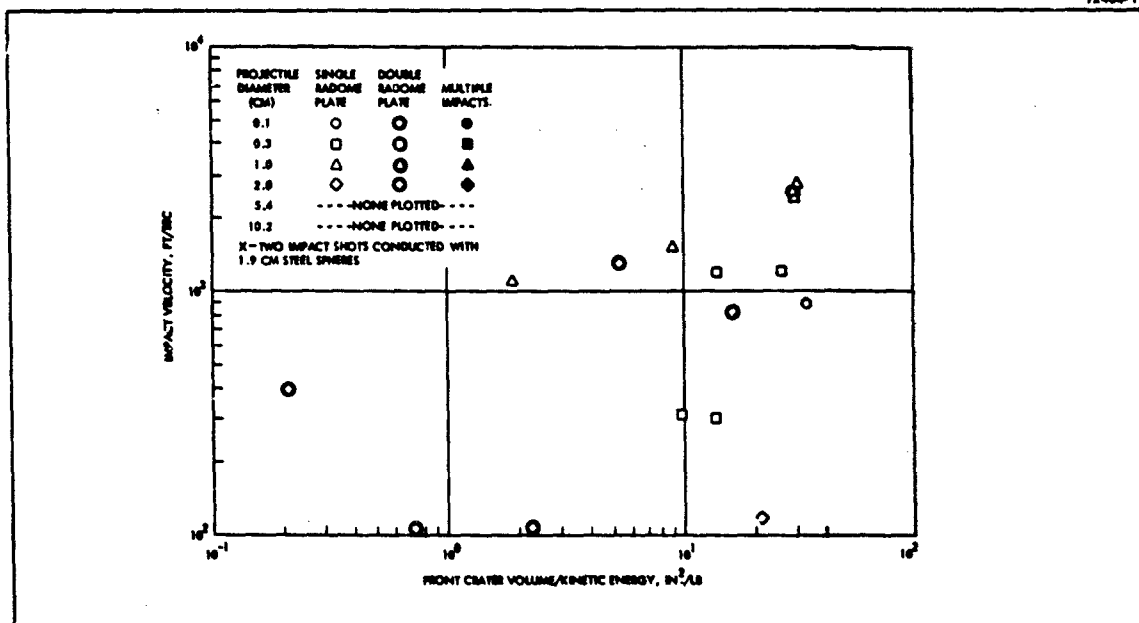

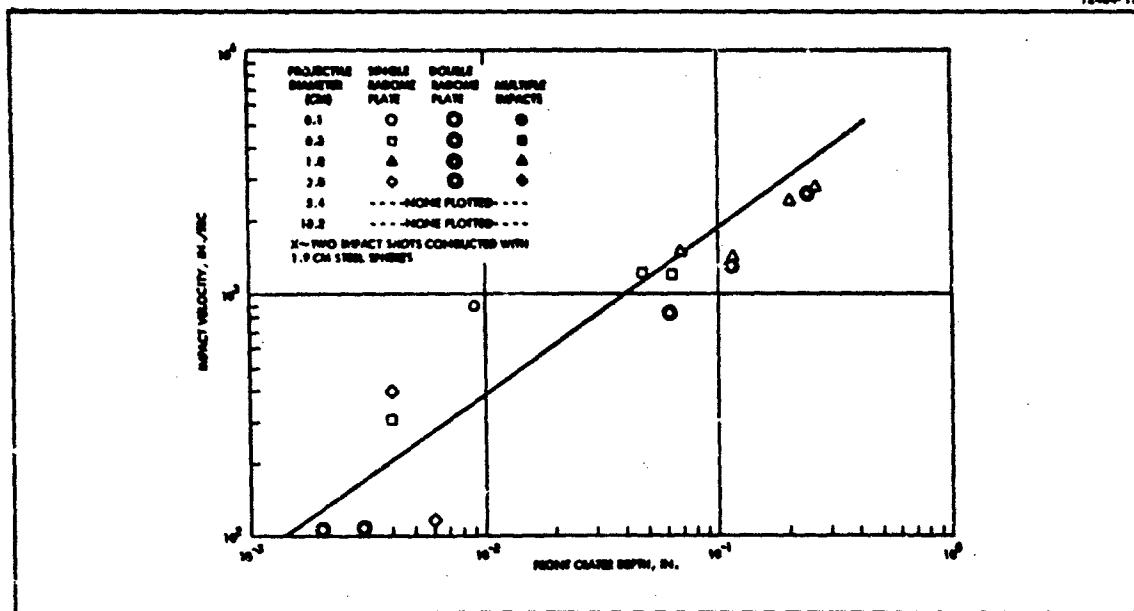Figure 4-11. Front Crater Volume/Kinetic Energy Versus Impact Velocity (Single Impact).

4-8

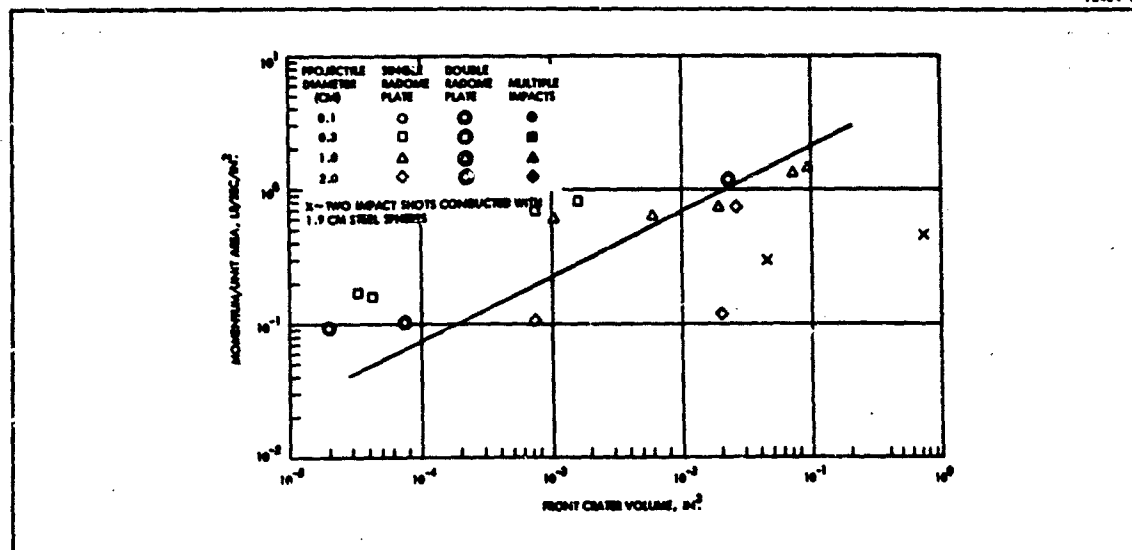Figure 4-12. Front Crater Depth Versus Impact Velocity (Single Impact).

Figure 4-13. Front Crater Volume Versus Impact Momentum/Unit Area (Single Impact).
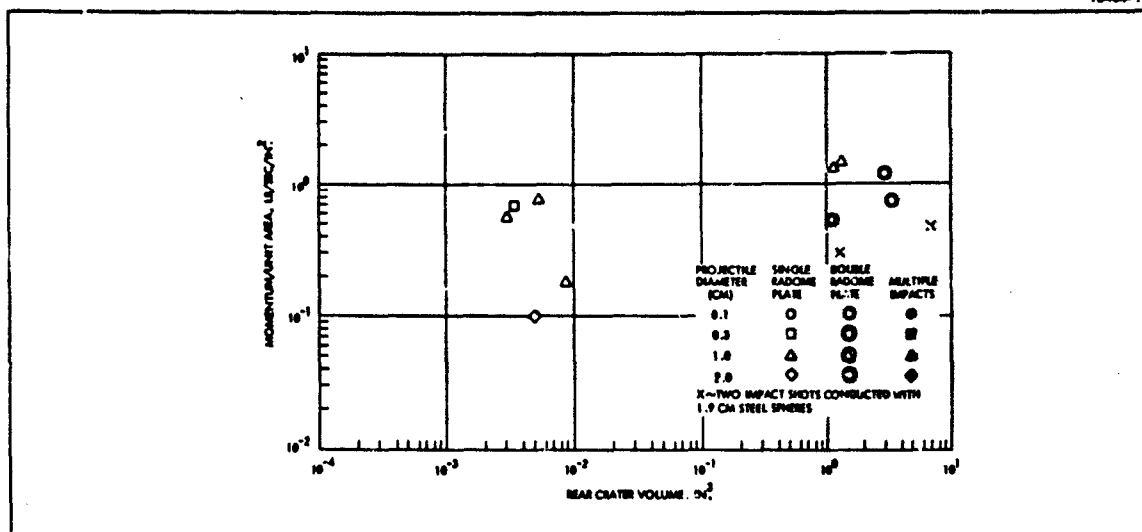
46

Figure 4-14. Rear Crater Volume Versus Impact Momentum/Unit Area (Single Impact).

The strength of the relationship between the variables is estimated by the coefficient of correlation between their logarithms and its significance level (≤ 0.05) which is also a function of the number of data points available.

Of the fourteen curves or combinations of variables used, only two had such a wide scatter of points as to have little correlation. The first of these was Figure 4-11

$$\left(\frac{\text{front crater volume}}{\text{kinetric energy}} \text{vs impact velocity}\right) \text{ and the second was Figure 4-14}$$

$$\left(\text{rear crater volume vs} \frac{\text{momentum}}{\text{unit ares}}\right). \text{ A discussion of the probable reason for this}$$

behavior is given in the following section. In addition, there are several more data points included in Figures 4-7 through 4-9 than were used to determine the best fit functions. These data points are shown in these figures by the solid symbols and stand for multiple impact test shots. While there were too few of these data points to treat separately, they are nevertheless included for comparison purposes.

Although many relationships have been formed it does not necessarily imply that there are twelve independent, significant relationships. In fact if one has:

S = crater volume

V = particle impact velocity

m = particle mass

E = impacting kinetic energy

then for Figures 4-1, 4-4, and 4-7:

$$\ln S = B_1 + M_1 \ln V \tag{4-1}$$

For the curves in Figures 4-2, 4-5, and 4-8:

$$\ln S = B_2 + M_2 \ln E \tag{4-2}$$

and for Figure 4-11:

$$\ln (S/E) = B_3 + M_3 \ln V \tag{4-3}$$

However, since $E = 1/2 \, mV^2$ it follows that above equations reduce to:

$$\ln S = B_1 + M_1 \ln V \tag{4-4}$$

$$\ln S = (B_2 - M_2 \ln 2) + M_2 \ln m + 2M_2 \ln V \tag{4-5}$$

$$\ln S = (B_3 - \ln 2) + \ln m + (M_3 + 2) \ln V \tag{4-6}$$

Therefore, all of the relationships, except the correlation of crater diameter to crater depth, are of the general form:

$$\ln S = A_1 + A_2 \ln m + A_3 \ln V \tag{4-7}$$

which holds for Figures 4-13 and 4-14 also.

4.2 COMPARISON OF TEST RESULTS TO IMPACT MECHANICS

In general, the impact damage occurred as anticipated. Very small particles shattered or rebounded elastically with no visual pitting or penetration of the ceramic plates. The next larger particles (3 mm) inflicted front face craters upon impact, but the rear face did not experience spallation. As the particles and velocities (impact energy) increased the front craters became appreciably larger (see Figure 3-7) and rear face spallation began to occur. Both the front and rear face craters were cupshaped and several diameters larger than the impacting particle. This is the expected failure mode for a ceramic, or any brittle material, where the allowable tensile stress is much lower than the compressive stress. Figure 4-15 (a) shows a simplified representation of an impact, where C_1, C_2, and C_R are the longitudinal, transverse, and Rayleigh surface wave velocities, respectively. It is well known that, when a body is dynamically loaded, the disturbance is transmitted throughout the body by longitudinal (dilatational) and transverse (distortional) waves. Bowden and Field[14] have also shown the Rayleigh surface wave to be of importance in this problem. Figure 4-15(b) shows diagrammatically the effects that occur. The impact point is P at the top of the plate. At impact, a stress distribution, similiar to that given by Hertz[2] for a static point load, is impressed. The lines of principal stress for this condition are shown in Figure 4-16, where the solid lines represent compression and the dashed lines tension. Note that near the point of impact the principal stress is compression. A little further away only the very central region is compression and still further away there is tension throughout. This distribution and shape, inconjunction with surface flaws, etc., account for the front crater phenomena evidenced in this impact study.
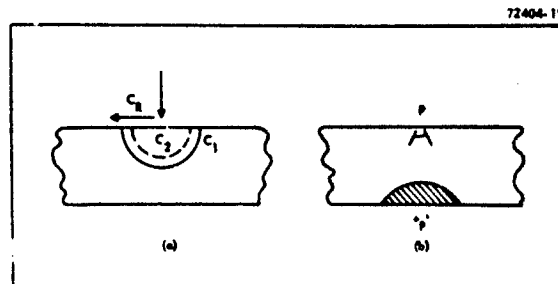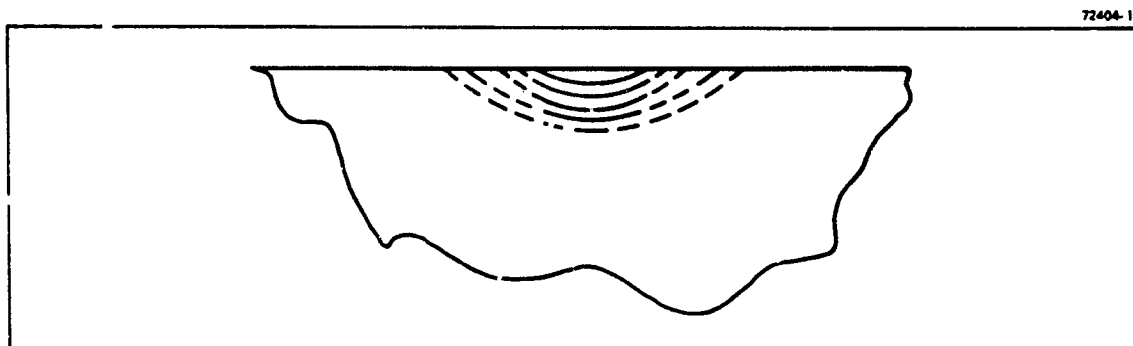
Figure 4-15. Impact Representation.

Figure 4-16. Lines of Principal Stress.

In addition to some fracture forming the front crater, a spherical compressive wave propagates through the plate as shown in Figure 4-15(a), and is reflected at the rear face, which is a free surface. In the region immediately beneath the point of impact, the wave is reflected entirely as a tension wave; farther out it will approach the rear face at oblique incidence and a reflected, distortional (transverse) wave will be generated in addition to the tension wave. A dilatational wave is always reflected at an angle equal to the angle of incidence, so it appears to be diverging from an image point of the point of contact, (see Figure 4-15(b)). During the reflection process, the reflected tension pulse must pass through the oncoming compressive wave, so that the resultant stress in the plate is the sum of stresses due to the incident and reflected pulses. Therefore, appreciable tension will be first set up at some distance from the free edge and it is at this line that fracture occurs. The region in which fracture occurs is shown in the shaded region of Figure 4-15(b), and is limited to the area where the tensile stress in the reflected wave exceeds the tensile strength of the material. The fact that fused silica is much weaker in tension than in compression and the geometry of the problem contribute to the fact that the spallation crater, in general, is greater than the front crater formed at the point of impact.

There are two other very interesting results which describe the plate damage as shown in Figures 3-15 and 3-17. Considering the tests to progress from smaller particles to larger ones, one might expect the front crater volume to continue to increase as the diameter increases (with a constant velocity, kinetic energy also increases) until the large particles give very large front craters. The functional relationships in Figures 4-2 and 4-8 would substantiate this trend, if only the data

points of particles up through 1 cm diameter are examined. In the actual tests, however, the front crater nearly disappeared from test shots of 2 cm projectiles for which the kinetic energy level would predict large craters on the basis of the curve in Figure 4-2. In addition, the plate did crack and the rear spallation was nearly as expected from the impact. This occurrence can be explained by examining the data plotted in Figure 4-13. This figure shows front crater volume as a function of the maximum available momentum per unit area in the impact. The area used to obtain this relationship is the maximum projected area of the fused silica balls, which is not completely realistic as the actual impact area. However, as the ball diameter increases so will the contact area, such that the normalizing factor is consistent. Examination of Figure 4-13 indicates that there is a lower threshold (momentum per unit area ≈ 0.1) at which the front crater volume data shows variations of three orders of magnitude. This would indicate that there is a level below which the energy and force intensity resulting from impact is such that a front crater will not be formed and the formation is quite sensitive to other factors, i. e., surface flaws on the plate, etc. It could also be postulated that the fracture mechanics of the ball shattering is instrumental in this case, but this is discounted because of one or two tests with large particles at higher levels of momentum. Figure 3-17 illustrates the case just discussed, where the front face is appreciably cracked, but not cratered, while Figures 3-18 and 3-19 show the resulting rear crater. Note in Figure 3-18 how the spallation crater material is intact, but can be easily removed as shown in Figure 3-19 to reveal a crater as previously discussed and shown in Figure 4-15(b). It is also noteworthy that the cracks are probably a result of plate bending where the back face is in tension. This has been substantiated by other workers in similar tests.

The second phenomenon that should receive comment is the occurrence of circumferential cracks in some instances. Figures 3-18 through 3-19 show this action at two extremes. In the first figures the damage is noticeably greater than in the test plate shown in the latter two figures. However, the projectile was of the same diameter and impacted at approximately the same velocity. The difference in the level of damage is attributed to the two different plate structures. In Figure 3-15 there are two plates (each 0.71 inch thick) bonded together and in Figure 3-17 there are four plates of the same type bonded together. The mechanics of the fracture are identical to those found and discussed by Bowden and Field. This primarily concerns the interference and reinforcement between Rayleigh surface waves and longitudinal and transverse waves reflected from the rear face of the plate. Figure 4-17 shows schematically how the wave relationships exist. Figure 4-17(a) indicates an impact, which occurs over a finite area, denoted by ΔY and shows how the dilational wave can reflect to reinforce the Rayleigh surface wave. Likewise, Figure 4-17(b) shows how the incident longitudinal and transverse waves reflect both types of waves at the free surface and lead to another band of reinforcement on the front surface. Note that Figure 3-17 does show clearly several bands of circumferential cracks. Figures 3-15 and 3-16 also indicate circumferential cracks on both the front and rear crater. However, with only two bonded plates, the energy intensity from the rear face reflection was much greater than the other case, resulting in substantially more front face damage.
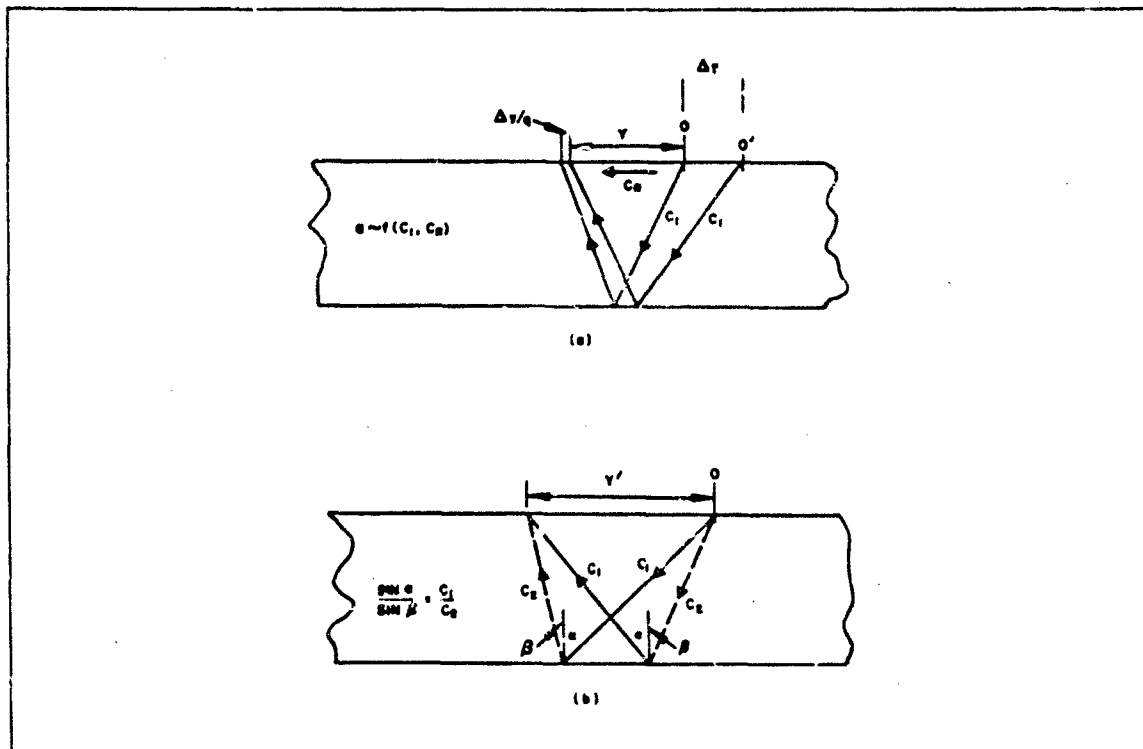
50

Figure 4-17.   Stress Wave Relationships.

5.0 SUMMARY AND CONCLUSIONS

Impact tests were performed using one foot square, 0.71 inch thick fused silica plates and silica projectiles accelerated by launchers capable of providing nominal projectile diameter and velocity profile ranges of 0.1-10 cm and 100-3500 ft/s respectively.

Test results showed fused silica to be subject to severe cratering and spallation. Damage may be classified as follows: particles of 1 mm diameter or smaller at velocities up to 3500 ft/s and densities up to 250 impacts per square centimter cause only a slight sand blasting effect on the plate surface. Particles of 1 cm diameter or smaller at free-fall velocity, i.e., the terminal velocity of a spherical particle in a standard atmospheric environment, do no damage under single impact conditions. Gross damage to the sample plates was experienced from single impacts of 2 cm particles at velocities of 800 ft/s or 5 cm particles at velocities of 175 ft/s.

Analysis of the cratering and spallation data at levels between the two extreme thresholds shows the existence of relationships between crater volumes, impact kinetic energy, impact velocity, and impact momentum per unit area. More study into wave and fracture mechanics of point impact is required to extrapolate the results for fused silica to other ceramics. Qualitatively, it can be stipulated that crater volumes would decrease and the spallation threshold increase (damage decrease for given impacts) as the ultimate tensile strength of the ceramic increases. Depending upon the size of debris expected for any given radar hardening application, fused silica may be inappropriate as a radome material due to low impact resistance. Recent research into fiber reinforced ceramics may prove to be useful in improving impact characteristics of ceramics, however, and should be one area of further investigation for developing better impact resistant radome materials.

6.0 REFERENCES

1. Love, A.E.H., A treatise on the Mathematical Theory of Elasticity, 4th Ed., Dover Publications, New York, pp 198-200.

2. Helie, F., Portions of Traite de Balistique Experimentale Which Deal with Terminal Ballistics, Chap. III, IV, V, and XIV, Paris (1884) Translated by J.S. Rinehart 0 NOTS Tech. Memo RRB-75, 1 May 1950.

3. Effects of Impact and Explosion, Summary Technical Report of Division 2, NDRC, Vol. 1, 1946, AD 221586, Chapter 7.

4. Tolch, N.A., and Bushkovitch, A.V., Penetration and Crater Volume in Various Kinds of Rocks as Dependent on Caliber, Mass, and Striking Velocity of Projectile, Ballistic Research Laboratories Report No. 641, AD 617267, October 1947.

5. Herrmann, W. and Jones, H.A., Survey of Hypervelocity Impact Information, ASRL Report No. 99-1, AD267-290, October 1961, pp 59-66.

6. Kornhauser, M., Prediction of Cratering Caused by Meteroid Impacts, the Journal of the Astronautical Sciences, Vol. V, 19 pp 58-63.

7. Huth, J.H., Thompson, J.S., and VanValkenburg, M.E., Some Data on High-Speed Impact Phenomena, Journal of Applied Mechanics, 24, 1957, pp 65-68.

8. Rinehard, J.S., Some Observations on High-Speed Impacts, NOTS Technical Memo RRB-50, 1 November 1950.

9. Collins, Rufus D., Jr., and Kinard, William H., The Dependency of Penetration on the Momentum per Unit Area of the Impacting Projectile and the Resistance on Materials to Penetration. NASA TN D-238, 1960.

10. Collins, Rufus D., Jr., and Kinard, William H., Investigation of High-Velocity Impact Cratering into Nonmetallic Targets and Correlation of Penetration Data for Metallic and Nonmetallic Targets. NASA TN D-726, 1961.

11. Hancox, N.L., and Brunton, J.H., The Physics of Impact and Deformation: Multiple Impact, Philosophical Trans. A, Vol. 260, pp 121-152.

12. Rostoker, M., The Formation of Craters by High-Speed Particles, Meteoritics, Vol. 1, No. 1, 1953, pp 11-27.

13. Bowden, F.P. and Field, J.E., The Brittle Fracture of Solids by Liquid Impact, Solid Impact, and by Snock, Royal Society Proceedings, Series A, Vol. 282, November 1964, pp 331-352.

14. Engel, Olive G., Pits in Metals Caused by Collision with Liquid Drops and Soft Metal Spheres, NBS Journal Research, Vol. 62, No. 6, June 1959, pp 229-246.

15. Hurd, Donald E. and Holmes, Roy F., "A Study of Rain Erosion Testing Methods for Supersonic Speeds," WADC TR 53-173, Part VI, January 1960.

16. Walton, J.D., Gorton, C.W., and Harris, J.N., A Hydrosonic Rain Erosion Test Program, Engr. Experiment Station, Georgia Institute of Technology, AFAL (AVWE-3), Wright-Patterson AFB, Ohio.

17. (U) Radar Hardening Studies, Defense System Interaction Study, Effects of Impinging Debris on Radome, May 1967, BSD TR67-41, P67-97, HAC Ref. No. B0787, SDN A-59861/22, Secret-Restricted Data.

18. Kolsky, H., Stress Waves in Solids, Dover Publications, Inc., New York, 1963, pp 183-196.

SINGLE IMPACT STUDIES OF RAIN EROSION MECHANISMS

by

A. A. Fyall and P. A. Smith
Royal Aircraft Establishment
Farnborough, England

ABSTRACT

Theories of the process of rain erosion have hitherto depended on a number of fundamental assumptions regarding the impact sequence. This paper is concerned with an examination of the validity of such assumptions by the use of high speed photography of the collision process and of photomicrography and profilometry of the impact damage, caused by a single drop. Correlation is shown between observed radial flow phenomenon and the nature of the subsequent damage site, including the effect of obliquity of impact.

Photoelastic studies of impact show that pre-stressing of the target surface may occur prior to collision. The implications of such a phenomenon for high altitude flight are discussed.

Collision with particles other than waterdrops are featured in a discussion of the validation of simulation techniques. These include high speed impact sequences of collisions with spheres of polymeric materials, such as cellulose acetate, poly(ethylene), poly(styrene), nylon and poly(tetra-fluoroethylene), of inorganic materials such as a ceramic aggregate, and of metals such as mecury or lead.

A short film (16mm- no sound track) will show animated sequences of these collisions, taken from camera speeds of up to 8,000,000 pictures per second.

INTRODUCTION

Research aimed at an elucidation of the phenomenon of rain erosion, has hitherto been severely limited by lack of information regarding the high speed collision of a material surface with a single raindrop. Theoretical considerations of the fundamental mechanisms have, of necessity, been based on certain assumptions whose validity has been unresolved by practical demonstration.

It is the purpose of this paper to discuss a series of single impact studies aimed at the establishment of some of the basic parameters of the impact sequence.

The results of high speed photography of the event and of profilometry and photomicrography of the impact damage caused by a single drop are used to describe the collision process and its consequences. Correlation is shown between the observed radial flow phenomenon and the nature of the damage site, including the effect of obliquity of impact.

Photoelastic studies of impact indicate that pre-stressing of the target surface may occur prior to collision and the implications of this phenomenon for high high altitude flight are discussed.

Collision with particles other than waterdrops are features in an examination of the validity of simulation techniques. These include high speed impact sequences of collisions with polymeric, ceramic and metallic spheres with particular reference to the case of lead.

TEST METHOD

A schematic representation of the equipment is shown in Figure 1. The material to be impacted forms part of the nose section of a light-weight bullet. When the turbine-driven camera mirror reaches the required speed, the projectile is fired from a compressed gas gun at a droplet or sphere, which is suspended on an artificial web. Before impact, the bullet actuates a photocell which triggers high intensity, short duration flashes to light the event. The projectile is arrested by passing through a series of rubber rings, which retard it without damaging the impacted surface.

TEST SPECIFICATIONS

The specimen is usually a truncated cone with a frontal diameter of, typically, 1.18 cm. The bullet is made of magnesium and weighs approximately 13 grams. Projectiles and specimens are shown in Figure 2. A wide variety of materials may be tested, including metals, ceramics, polymers, ect. Because of the high deceleration forces imposed by the arrester system, the technique may not be suitable for certain glasses and ceramics, particularly in thin section.

The rotating mirror camera has a range of 2×10^5 to 8×10^6 pictures per second (p.p.s.). Typically, at the top speed, matched lenses, arranged in an arcuate path, give a consecutive sequence of 117 pictures of 8.23 mm diameter on 35 mm film, the exposure time being 0.12 μs. The Xenon flash tubes are discharged at 2.8 kilovolts, and emit approximately 180 joules; the rise time of the pulse is 1-2 μs and the duration 80-90 μs. This pulse length is less than the time for a half revolution of the double-sided steel mirror and thus multiple exposure of the film is obviated. To assist in data reduction and to enhance qualitative detail, the 35 mm film negative is processed as a continuous roll of enlarged positive print. The mirror turbine is usually driven by compressed nitrogen at approximately 50 lb/in^2 pressure. The gas gun has a capability of approximately sonic velocity using compressed air or nitrogen as propellant while the use of hydrogen will extend the velocity to 1500 ft/s. Gun discharge pressure for a projectile velocity of 1000 ft/s is 1000 lb/in^2, with a triggering pressure of 300 lb/in^2.

The web is fabricated by drawing out filaments from a solution of poly(methylmethacrylate), (hereafter designated Perspex), in aniline and stretching them over a supporting frame. Such webs have supported targets of spheres of water, mercury, poly(ethylene), poly(styrene), poly(tetrafluror-ethylene) or P.T.F.E., cellulose acetate, nylon, plasticine, tungsten
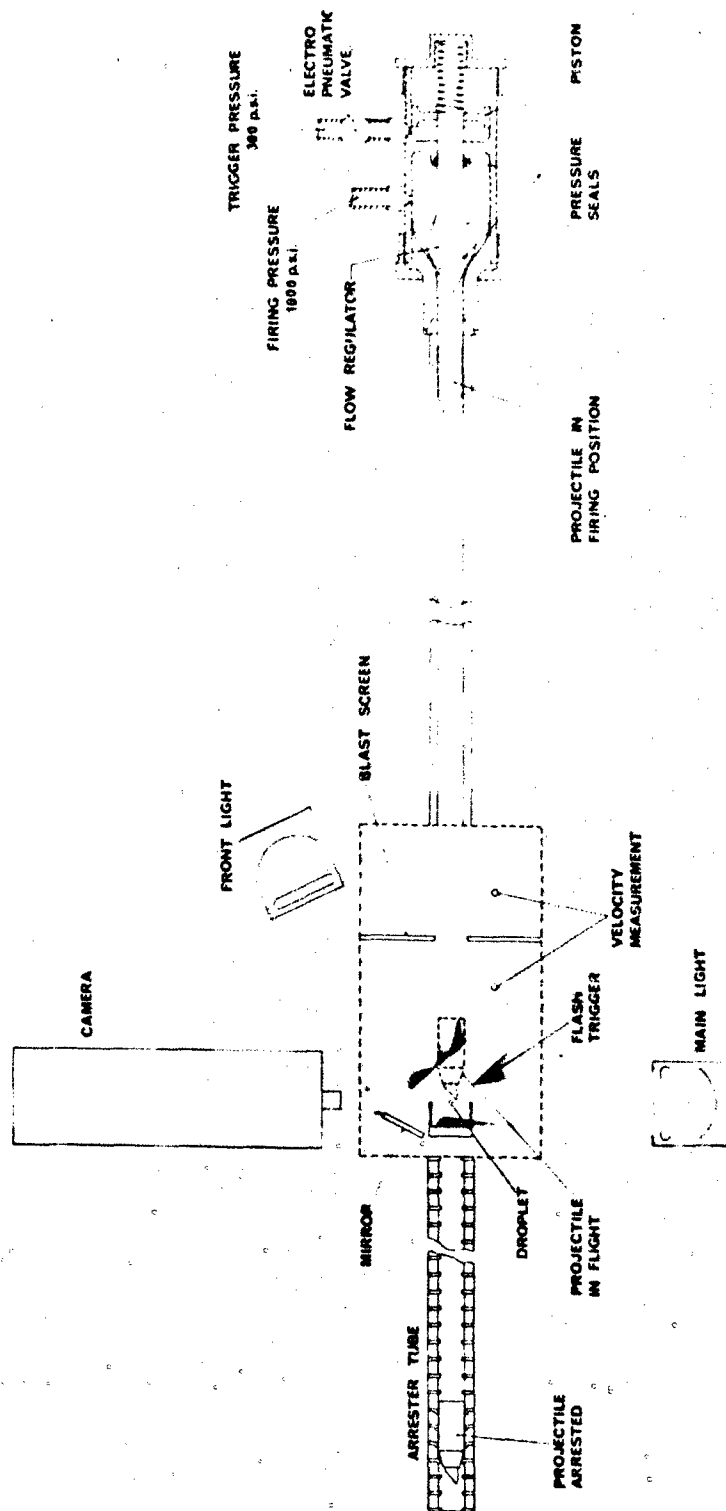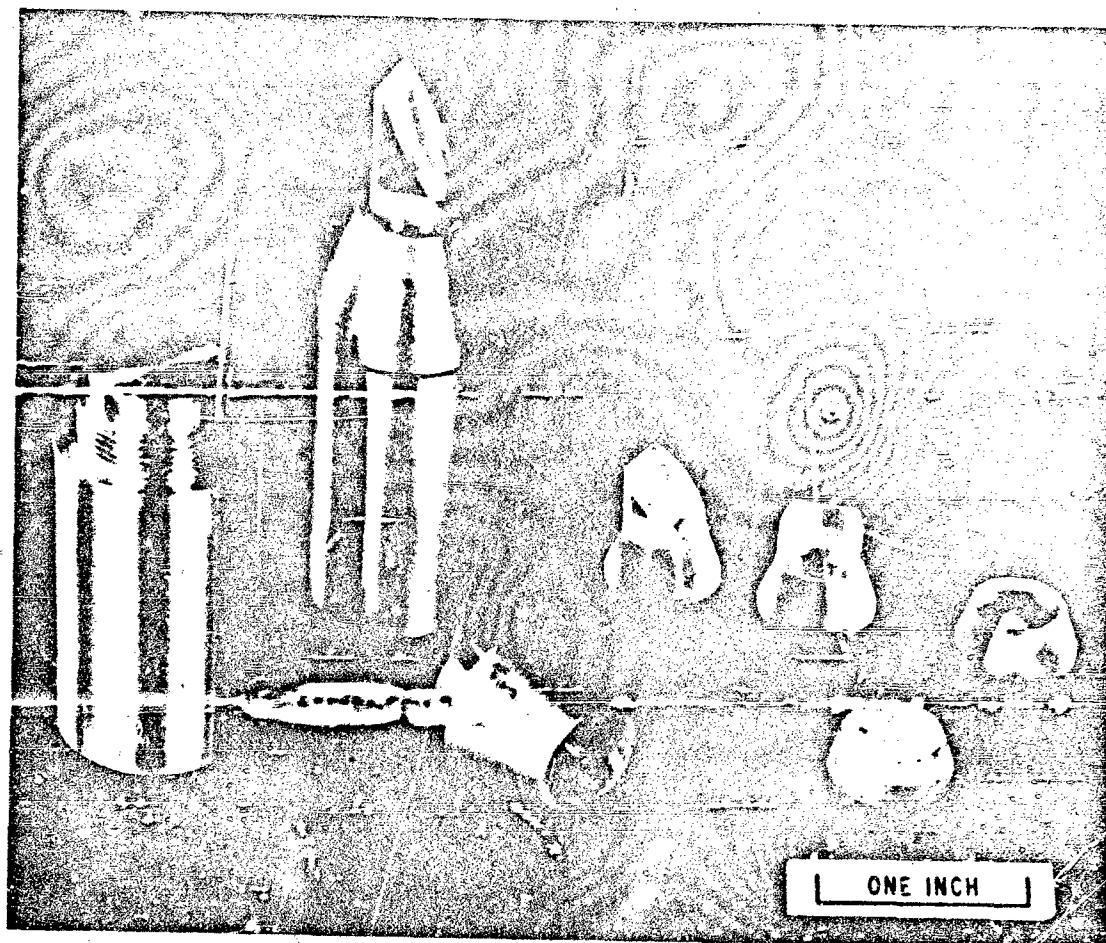
Figure 1. Schematic Arrangement of Apparatus.

Figure 2. Projectile and Specimens for Gas Gun.

carbide, steel, lead, synthetic sapphire (α alumina) and light-weight ceramic aggregate.

As Perspex shows excellent damage sites when impacted against waterdrops at ~1000 ft/s, it is used as a standard material. This material has also been well characterised in multiple impact experiments, takes a fine polish and its photoelastic properties are also useful.

Initial experiments showed that the combined techniques of high speed photography, photomicrography and profilometry gave a very adequate description of the collision processes and resultant damage. In particular, the last technique gave an excellent measurement of damage, as the results were very reproducible.

IMPACT WITH WATERDROPS

The impact process with waterdrops is an extremely rapid event and to examine its various features in detail, the camera was first used at speeds up to 1.0×10^6 p.p.s., giving a sequence of 28 pictures (Figure 3). There was sufficient detail in these pictures to estimate radial velocity and to observe the general progress of the impact.

RADIAL FLOW

Preliminary results indicated that the radial velocity had an initial high value for ~2 µs, reducing to a steady value for the next 6-8 µs.

Various authorities, notably Engel [1] and Bowden and Field [2] have shown that the pressure (P) generated on impact is given by the "water-hammer" equation of Gibson [3] and Rich [4]: -

$$P = \rho \, C \, V$$

where ρ is the density of the liquid, C the velocity of a compression wave in the liquid and V the velocity of impact. Bowden and Brunton [5] postulate that the high radial velocity results from the jetting action of the water between the confines of the drop and the impacting surface. A more reasonable explanation may be that the radial wash originates as steady incompressible Bernoulli flow, resulting from the release of the high pressure generated at impact. This view is supported by the correlation of the radial velocity and the calculated water-hammer pressure.

It is apparent from Figure 3 that in the first microsecond after impact, a considerable movement of water has occurred. The impact pressure has been released and the radial wash is already jetting over the surface. This is supported by Bowden and Brunton's [5] measurements of a time of ~1 µs to achieve peak impact pressure. To examine the initial stages of impact in more detail, the camera was fitted with an alternative bank of 117 lenses, thus extending its maximum rate of 8×10^6 p.p.s. Measurements of radial velocity agreed with those made as 10^6 p.p.s. although a more detailed description was possible (Table I). The behavior of the drop in the earliest stages of impact
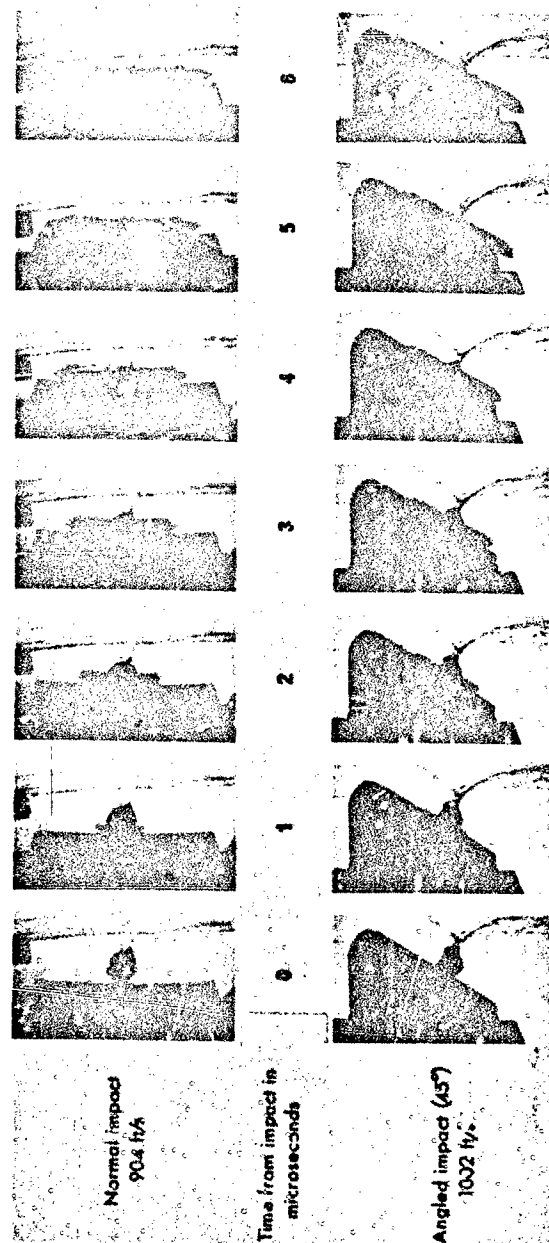
Figure 3. Single Impact with 2 mm. Waterdrop.

Normal impact
904 ft/s

Time from impact in
microseconds

Angled impact (45°)
1002 ft/s

TABLE I

RADIAL VELOCITY OF 2 mm WATERDROPS ON IMPACT WITH PERSPEX

Velocity of Impact (ft/s)	Camera Rate (pictures per sec)	Time from Impact (μs)	Radial Velocity (ft/s)
904	1×10^6	$\frac{3}{8}$ - 8 $\frac{3}{8}$ - 13	2660 2075
908	5.1×10^6	0.6 - 6.7 6.7 - 13.5	2625 1925
907	5.8×10^6	0 - 2 2 - 3.3 3.3 - 8	3360 3301 2240
987	8.0×10^6	0.8 - 2.9 2.9 - 3.9 3.9 - 5.6 5.6 - 12.9	3056 2650 2610 1820

showed that no sideways flow of water was apparent for at least 0.25 μs.
Close-up pictures (field of view ~X3 diameter of drop) give further refinement
of the radial wash measurement and observation of the initiation of flow. The
measured reduction of the diameter of the drop over this period agreed very
closely with that calculated for the movement of the target surface through the
drop at the velocity of impact. This observation further substantiates the
theory that the first stage of the process is that of pressure build-up. In
the high speed photography of waterdrop collision, no evidence of any spalling
on the back surface has been found. Such waves as are generated may be
attenuated within the drop.

SHEARING ACTION OF RADIAL FLOW

In many papers on rain erosion, the importance of the shearing action
resulting from the high speed radial flow across the surface is often stressed.
This is possibly correct for surfaces containing asperities against which the
flow may generate high local pressures. However, for a smooth surface, it
would appear inadmissible that the so-called "scouring action" has much signif-
icance at the impact velocities examined. Damage sites on Perspex (Figure 4)
are characterised by an annular depression, the centre of which is an undamaged
plateau. Beyond the depression lies circumferential cracking, usually to the
extent of approximately the diameter of the drop. There is only limited
evidence of shearing action witnessed by the removal of very small amounts of
material, although with impact on certain solid spheres, extensive shearing

may be witnessed. Photographs of waterdrop impact show the drops to disintegrate rapidly into a spray of much smaller droplets which appear to travel with at least the velocity of the moving target surface or even to rebound from it. Radial flow continues well outside the area of circumferential cracking and thus the damage may be almost entirely ascribed to the primary impact process.

Perhaps one of the most important features of any possible shearing effect of the radial flow may be in determining at what stage in the process the water ceases to flow as a sheet and commences to move as a spray of discrete droplets. Derivation of formulae describing radial flow have usually assumed that the flowing water existed as a discrete sheet and not as a spray.

PHOTOMICROGRAPHY OF DAMAGE

As illustrated in Figure 4, the damage sites can best be examined qualitatively in a projection microscope, suitable for subsequent photography. Oblique illumination with reflected light is used and the surface may be lightly silvered to enhance detail. The annular ring and circumferential cracking are quite evident.

PROFILOMETRY

The quantitative extent of the damage is best measured by a profilometer. Longitudinal magnifications of X100 are usual while, vertically, magnifications up to 50000 times are possible, although rarely necessary. A typical trace is shown as part of Figure 4.

EFFECT OF ANGLE OF IMPACT

Waterdrop impact at various angles of impact have also been studied using this technique. Figure 3 shows a typical sequence of impact at 45°. Photomicrography of the damage sites (Figure 4) of angles specimens show considerable asymmetry. The hypothesis that the erosion rate at a given angle of impact is governed by the normal component of velocity, an observation which does not really permit of physical interpretation, appears to be confounded by this view. Analyses of the radial velocities occurring on angled specimens show, that as indicated by the asymmetry of the damage sites, the maximum pressure is generated on the upper sides of the point of contact. Typically, for impact of a 2 mm diameter waterdrop with a 45° angled Perspex wedge at 1002 ft/s the radial velocities are: - 3050 ft/s upslope and 1960 ft/s downslope.

CORRELATION OF SINGLE IMPACT DATA WITH MULTIPLE IMPACT STUDIES

It has been shown 6/ that although the extents of the annulus and central plateau areas do not apparently correlate with the angle of impact, yet if the extent of the circumferential cracking is estimated, a correlation with multiple impact data is possible. If it is postulated that erosion occurs as a result of t   overlapping and interaction of the circumferential crack areas from many impacts, then the "cracked" area of an individual impact may be related to the multiple erosion characteristics of the target material.
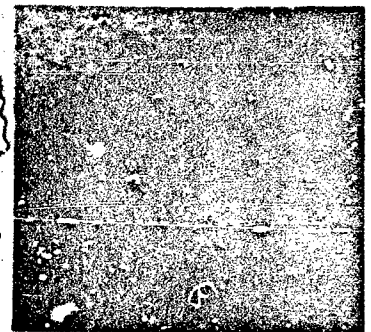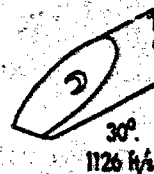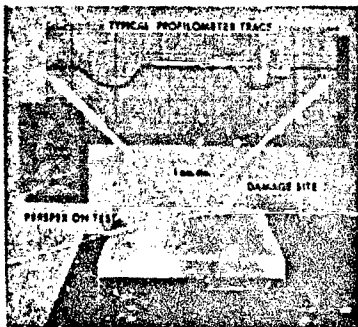
2mm. water droplet

60°. 984 ft/s

90°. 904 ft/s

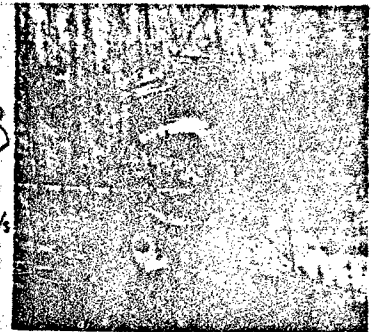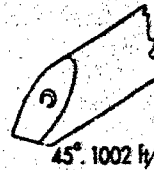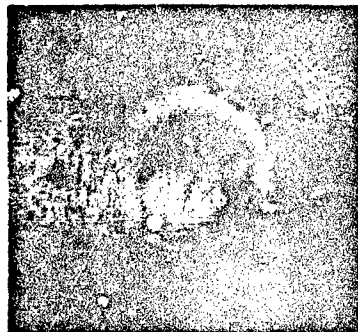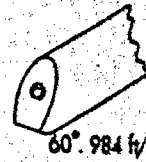45°. 1002 ft/s

30°. 1126 ft/s
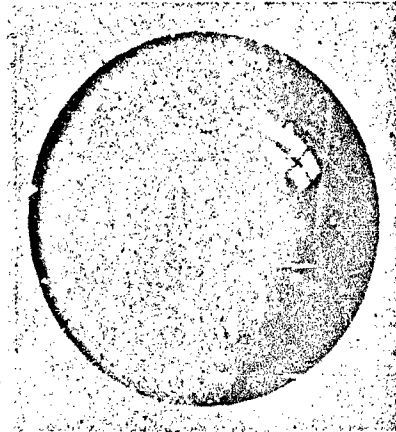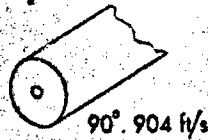
Figure 4.   Typical Damage Sites at Various Angles of Incidence.

"HEAD-ON" PHOTOGRAPHY

The pictures of impacting drops discussed thus far were taken across the test surface i.e. in profile. The flow patterns resulting from pressure release are obscured by the resulting spray of droplets. Plan views of the flow on angled surfaces were obtained by suitable disposition of camera and specimen at impact. A technique for "head-on" viewing of surfaces impacted at normal incidence using expendable plastic mirrors (0.0005 inch thick) has been developed but not yet perfected to give adequate resolution.

Plan-view pictures of flow on angled surfaces allow the deformation of a drop to be followed in its entirety. Flow is first manifest by the appearance from beneath the drop of a very fast primary radial flow, following the release of the "water-hammer" pressure. By the principle of conservation of energy, the entire drop cannot flow at speeds higher than that of collision. Thus, if the subsequent or secondary flow from the drop is slower than the primary jetting of pressure release, a discontinuity of flow with time should be observed as the relative velocity becomes apparent. This is illustrated in Figure 5, in which the widening gap between the two flow systems is clearly seen. The secondary flow appears approximately one µs after impact and, initially, has approximately half the impact velocity. Table II shows some values of the two flows as measured along the upslope axis of the impacted surface. The shape of the primary radial flow pattern, of the secondary flow and of the resultant intervening gap also indicate the asymmetry of pressure, already shown in the damage sites of Figure 4. The crescent-shaped separations measured at their maximum upslope widths at 7.6 µs and 10.1 µs from impact indicate a relative velocity of ~700 ft/s. The differences of the weighted means of Table II is 580 ft/s. The maximum breadth of the primary spray pattern at 10 µs is approximately 1.6 mm.

TABLE II

RADIAL VELOCITIES OF PRIMARY AND SECONDARY FLOWS FOR 30° INCIDENCE

Time From Impact (µs)	Primary Radial Velocity (ft/s)	Secondary Radial Velocity (ft/s)
1.9	2987	427
6.0	1083	467
7.6	1073	537
10.1	994	470
Mean	1055	475

NOTE: Impact velocity 928 ft/s; 2 mm diameter waterdrop.

+5μs.

+7μs.

+10μs.
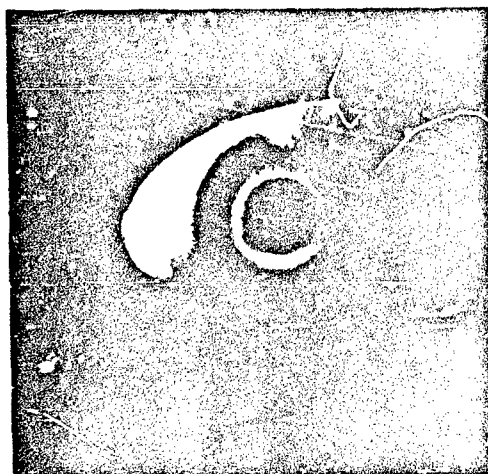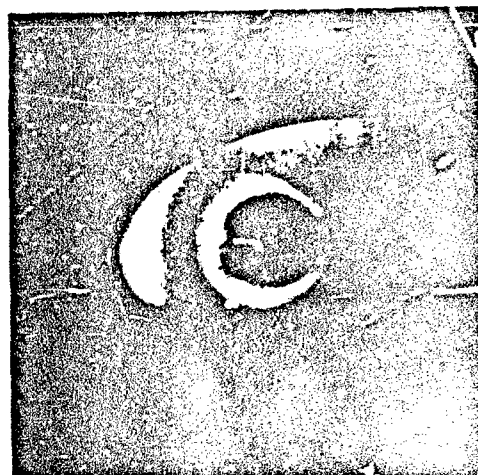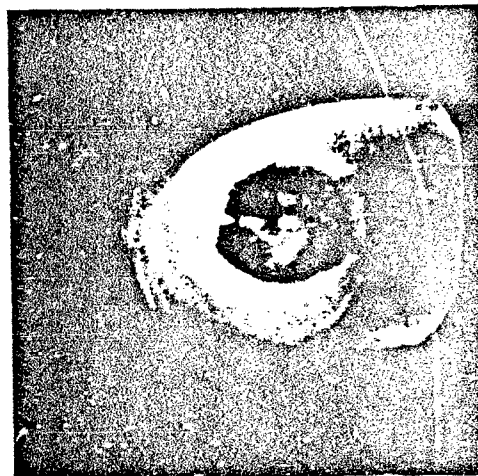
+12.5μs.

Head-on view

1,000ft/s. 30°

Figure 5. Primary and Secondary Flow Patterns at 30° Incidence.

65

Pictures of the last stages of the collision indicate that subsequent flow is such that the back of the drop finally rests on the test surface. This is substantiated in that on recovery of the projectile from the arrester tube, small waterdrops are usually present on the impact surface. In summary, the evidence points to the following sequence of events in the collision of a surface, moving at high speed, with a waterdrop: -

1. progress of surface through drop at impact speed without flow with consequent pressure build-up over ~0.25 µs followed by

2. its release as primary high speed radial flow (after Bernoulli) with a velocity of several times that of impact; then follows

3. an area of flow separation with then

4. a secondary radial flow at, initially, approximately half the impact speed and

5. a gradual decrease of flow velocity until the back of the drop comes to rest on the moving target surface.

It should be noted that the flow consist of small droplets and is not a discrete sheet.

Future experiments will be aimed at mapping the asymmetric collision pressure as witnessed by the radial flow.

PHOTOELASTIC STUDIES

Preliminary studies to determine the shock wave pattern and stress distribution in a material, resulting from high speed collision with a single waterdrop, indicated that pre-stressing of the target surface may occur prior to collision. Figure 6 shows that a shock wave pattern is generated before impact. Table III shows the wave velocities measured for three such experiments. The longitudinal or compressional wave velocities agree with the value of 8137 ft/s for Perspex at 20° C given by Wada and Yamamoto [7]. The effect of the Rayleigh or surface waves on fracture at higher impact speeds is discussed by Bowden and Field [2]. They give values of $c_R/c_T = 0.8743$ to 0.9554 for Poisson ratio values of 0 to 0.5 and note that "fractures are initiated by a disturbance travelling out with a velocity between those limits", i.e. between c_T and c_R. The photographs of Figure 6 show a fine structure of the shock pattern, discriminating between the Rayleigh and transverse or distortional wave, the ratio of c_R/c_T being 0.907 (Poisson ratio for Perspex is 0.4). Other workers have reported, for higher test speeds, the occurrence of a light flash at impact. This has been variously ascribed to adiabatic compression of the air between the drop front and the advancing surface [8,9] or to the separation of charges resulting from the sudden dissociation of the water upon impact [10]. However, no observation appears to have made of the implications of these forces on the subsequent damage to the surface. Figure 6 seems to favour the explanation of adiabatic compression for the light flash phenomenon. The extent and magnitude of the initial pressure wave

66
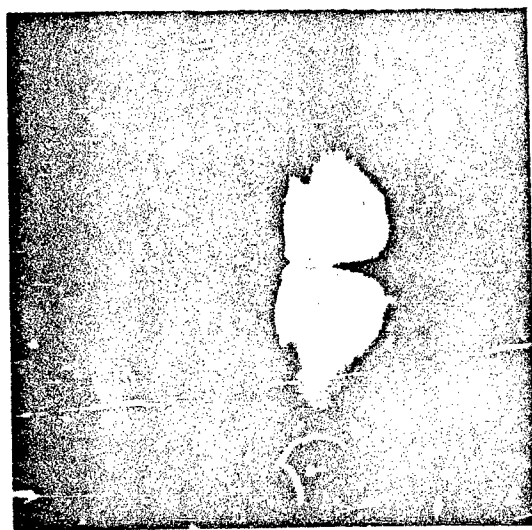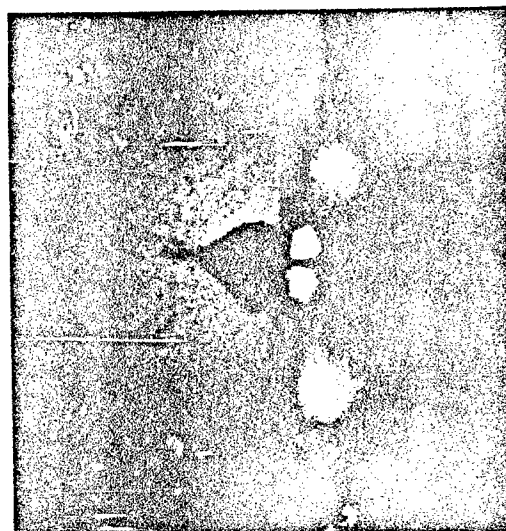
Impact at 1,000ft/s.
Intervals 1μs.

Figure 6. Shock Wave Pattern in Perspex.

TABLE III

WAVE VELOCITIES FOR IMPACT OF 2 mm DIAMETER WATERDROPS AGAINST PERSPEX

Velocity of Impact (ft/s)	Velocity of Longitudinal Wave c_L (ft/s)	Velocity of Transverse Wave c_T (ft/s)	Velocity of Rayleigh Wave c_R (ft/s)
930	7694	5624	5102
933	7718	5630	5106
978	7760	5656	5130

must be assessed in relation to the total pressure, built up during the collision process. If this adiabatic compression effect is significant then the pre-stressing of the impacted surface may play an important role in the ultimate damage pattern. Smith et al. [11], discussing the erosion of steam turbine blade materials, note that "the maximum weight loss can be reduced by a factor of seven if the pressure inside the chamber is raised from 2 to 5 inches inches mercury by the "cushioning" effect of the increased steam density. It should be noted that droplet sizes ranged up to 800 μm and that the test speed was 1730 ft/s. The implication is that erosion rates for aircraft and missile materials may increase with altitude. From Smith's [11] erosion rates for 50 hours exposure of a standard metal specimen at various chamber pressures, with the reservation that there may be drop size effects, it may be calculated that, equivalently, erosion rates will increase by a factor of 7 between 42000 and 62000 ft altitude and by a further factor of 1.5 between 62000 and 69000 ft.

Also, Nicholson [12] has shown in discussing drop break-up by airstream impact that alleviation of erosion damage by this mechanism is reduced with increased altitude. Typically, at Mach number of 2, he indicates that a 2 mm diameter waterdrop may break up in a distance of 4 inches at sea level but may require 10.5 inches for the same degree of disintegration at 50000 ft altitude. The implications of the combination of these two features of the erosion process must obviously be a serious consideration for supersonic transport operation, particularly in view of the evidence offered by Kantor and Grantham [13] regarding the occurrence of precipitation-bearing clouds at supersonic aircraft altitudes. The provision of vacuum conditions for the new whirling arm facility of Bell Aerosystems [14] may thus have more significant advantages than the original intentions of minimisation of power and of cooling requirements.

IMPACTS WITH SOLIDS

There are three main reasons for studying the impact of surfaces on solid particles: -

1. in flight, aircraft and missiles encounter foreign bodies other than waterdrops e.g. a helicopter may produce its own sandstorm during hover;

2. to help to understand the mechanisms of collision processes more completely;

3. to examine the merits and limitations of simulation techniques, in which the waterdrops are substituted by solid particles.

The technique already described for water impact is readily adaptable to that of solids. Webs have supported a variety of metallic, polymeric, glassy and ceramic particles.

RESULTS

Results for collision with a variety of solid spheres have already been reported 6/. Table IV summarizes the characteristics of those materials which show no radial flow characteristics while Table V deals with those which do. It should be noted that none of these materials in the first category can satisfactorily simulate water impact, not only because of the difference in time scale of the impact but also because none, in fact, disintegrate at all.

TABLE IV

DURATION OF CONTACT OF SOLIDS AFTER COLLISION
AND THEIR VELOCITIES OF SEPARATION 6/

Material of Sphere	Velocity of Impact (ft/s)	Duration of Contact (μs)	Velocity of Separation (ft/s)
Poly(ethylene)	1018	52	115
Nylon	957	6.7	240
Cellulose Acetate	985	5	250
Sapphire	1075	8.5	373

Poly(tetrafluoroethylene) or P.T.F.E., and plasticine (modelling clay) most closely resemble water flow characteristics. Examination of the photomicrographs of the damage sites show, however, an important defect in simulation of waterdrop erosion viz. excessive scouring across the surface, as happens with the non-disintegrating polymeric spheres. For other target materials, which are harder than the impacted spheres, this may of course, result in sphere material being transferred, which may minimise the effect of subsequent impact.

TABLE V

RADIAL VELOCITIES OF DISINTEGRATING SOLIDS ON A PERSPEX SURFACE 6/

Material of Sphere	Velocity of Impact (ft/s)	Camera Rate (p.p.s.)	Time From Impact (μs)	Radial Velocity (ft/s)
Plasticine	873	1.1×10^6	$0 \to 12$	1839
	930	1.02×10^6	$0 \to 12$	2250
P.T.F.E.	965	1×10^6	$0 \to 4$	1680
			$4 \to 5$	1121
			$5 \to 31$	596
Light-weight Ceramic Aggregate	1011	5.1×10^6	$0 \to 8$	226
	1045	5.1×10^6	$0 \to 8$	183
	1133	5.1×10^6	$0 \to 8$	226

Since the publication of this data a more detailed study has been made of impacts with lead spheres, this being pertinent to the "shot-gun" technique used by the High Temperature Materials Group of the Georgia Institute of Technology 15/. In preliminary studies, only impacts against Perspex surfaces were examined. These showed that although lead belonged to the category of Table V, its apparent radial velocity was approximately that of impact. This arose from lack of definition caused, to some extent, by the deep penetration of the lead into the Perspex surface. This has now been reappraised and impact studies have also been made with titanium and fused silica targets. Table VI shows a summary of the flow characteristics of lead on various target materials and of water. A "lifting" component of velocity i.e. normal to the surface, was measured as approximately half the impact velocity. If the radial flow of lead on fused silica is examined at further intervals after the first microsecond from impact there appears to be an initial decrease of radial velocity after the primary high speed jetting action. This however is followed by an increase in velocity about 3-4 μs from collision. A smear of lead showing evidence of radial flow was left on the impacted surface; the diameter corresponded to a contact time of this magnitude. Thus, the apparent acceleration of the lead after 3-4 μs is probably due to the release of energy to the disintegrating sphere as the lifting component of velocity enables it to move off the surface, over which it has been shearing with a consequent frictional reduction of velocity.

The effect of the scouring action of the lead in relationship to erosion simulation will be further examined. While the lead technique may have relevance to evaluation of ceramics, it should however be noted that it will not be suitable for soft target materials e.g. pure aluminum, in which it embeds without flow.

TABLE VI

SUMMARY OF LEAD SPHERE IMPACTS

Materials	Impact Velocity (ft/s)	Radial Velocity for First Microsecond (ft/s)
Lead on Perspex	991	2936
Lead on Fused Silica	1056	3807
Lead on Titanium 130	1000	3535
Water on Perspex	1070	2806

CONCLUSIONS

Various aspects of rain erosion have been examined by observation of single impact collisions using high speed photography. A description has been given of the collapse of a waterdrop, which has been struck by a fast moving surface. The effect of obliquity of impact on the subsequent damage has been outlined. The results of photoelastic experiments in relation to their relevance to high altitude flight are discussed. Finally, the validity of simulation techniques using solid spheres is examined.

REFERENCES

1. O. G. Engel, Mechanism of Rain Erosion, Journal of Research, National Bureau of Standards, Vol. 54, No. 281 (1955).

2. F. P. Bowden and J. E. Field, The Brittle Fracture of Solids by Liquid Impact, by Solid Impact, and by Shock, Proceedings of the Royal Society, Vol. 282A, pp. 331-352 (1964).

3. A. H. Gibson, The Mechanical Properties of Fluids, Blackie, London, (1923).

4. G. R. Rich, Hydraulic Transients, McGraw-Hill, New York (1951).

5. F. P. Bowden and J. H. Brunton, The Deformation of Solids by Liquid Impact at Supersonic Speeds, Proceedings of the Royal Society, Vol. 263A, pp. 433-450 (1961).

6. A. A. Fyall, Single Impact Studies with Liquids and Solids, Proceedings of the Second Meersburg Conference on Rain Erosion and Allied Phenomena. Ed. A. A. Fyall and R. B. King, Royal Aircraft Establishment.

7. Yasaku Wada and Keiji Yamamoto, Temperature Dependence of Velocity and Attenuation of Ultrasonic Waves in High Polymers, Jnl. of Phys. Soc. of Japan Vol. 11, No. 8 (1956).

8. J. H. Brunton, The Deformation of Solids Under High Speed Liquid Impact, Proc. of the Rain Erosion Conference held at Meersburg, West Germany (1965) Ed. A. A. Fyall and R. B. King, Royal Aircraft Establishment

9. S. M. De Corso and R. E. Kothman, Luminous Phenomena, A.S.T.M. Materials Research and Standard, p. 525 (1965).

10. G. Hoff and G. Langbein, Resistance of Materials Towards Various Types of Mechanical Stress, As Ref. 6.

11. A. Smith, R. P. Kent and R. L. Armstrong, Erosion of Steam Turbine Blade Shield Materials, A.S.T.M. STP408, Am. Soc. Testing Mats. pp. 125-158, (1967).

12. J. E. Nicholson, Drop Break-up by Airstream Impact, As Ref. 6.

(Continued)

REFERENCES (Continued)

13. A. J. Kantor and D. D. Grantham, Distributions and Composition of Clouds at Supersonic Aircraft Altitudes, As Ref. 6.

14. N. E. Wahl, Study and Design of Supersonic Rotating Arm Rain Erosion Apparatus, As. Ref. 6.

15. J. D. Walton, C. W. Gorton and J. N. Harris, Rain Erosion at High Mach Numbers, As Ref. 6.

BLANK PAGE

ELECTRICAL DESIGN OF THE C5A NOSE RADOME

Arthur J. Thompson
Brunswick Corporation
Technical Products Division
Marion, Virginia

ACKNOWLEDGEMENTS

ABSTRACT

This paper presents the principle aspects of the C5A Nose Radome electrical design. The radome/antenna geometry and functions are described and the ray analysis results summarized. Development of the wall configuration and the subsequent performance evaluation based on the ray analysis, the material selection and empirical correlation is also outlined. Attention is directed toward the lightning protection, weight, and structural loads requirements which rendered the radome electrical specification quite stringent.

INTRODUCTION

The U.S. Air Force Lockheed C-5 Galaxy is the world's largest airlifter with a payload of up to 265,000 pounds and a cargo compartment volume of 34,734 cubic feet. The aircraft's uniqueness extends to the most forward region of the fuselage where a number of advanced radar systems are enclosed by the largest single piece aircraft radome ever produced. The radome - approximately 16 feet in base diameter and 10 feet in length - is shown in Figure 1 and in Figure 2 with the primary system antennas sketched in their respective locations. Uppermost in the radome is the X-band phase interferometer, a 3.6" x 20.0" array operating in X-band which provides the primary terrain following/terrain avoidance function. Immediately below is an X-band parabolic antenna which is designed for high altitude ground mapping, weather mapping, and contour mapping, using a 34" x 43" polarization sensitive reflector surface. The Ku-band phase interferometer shown in Figure 2 handles primary radar approach to landing and consists of a 2" x 24" aperture using horizontal polarization. The Ku-band parabolic antenna provides the
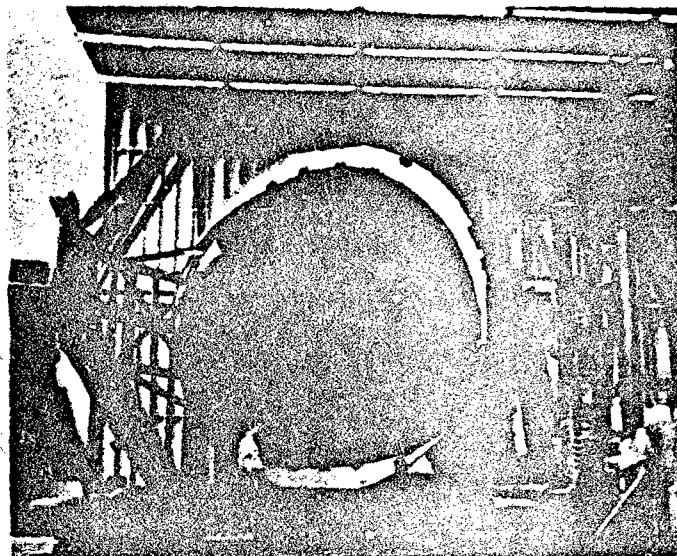
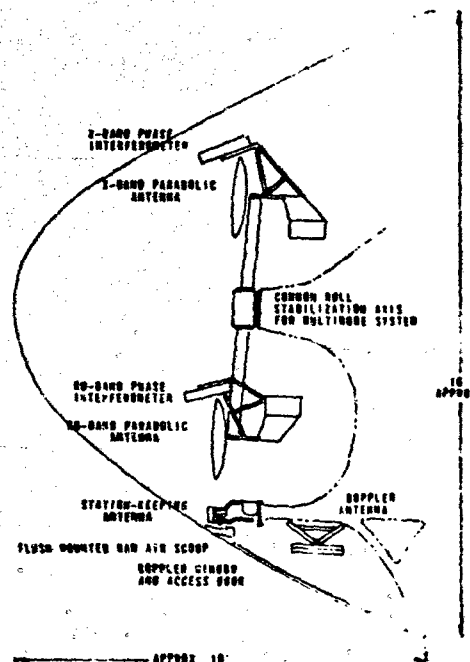**Figure 1.** C5A Nose Radome on Electrical Test Fixture.

Figure 2. C5A Nose Radome Cross-Section Depicting Enclosed Antenna System.

primary lcw-altitude ground mapping function using either horizontal or vertical polarization in conjunction with a 30" x 62" reflector. These four apertures, which also possess back-up function capabilities, then constitute the multimode radar system. Scan and stabilization limits combine to yield angular movements of +110° in azimuth, +25° to -30° in elevation (+15° for the phase interferometer), and +45° about the common roll axis. A station keeping antenna is located in the bottom forward region of the radome, this 4" x 6" array operating at C-band (5.090 GHz) with vertical polarization and having azimuth scan limits of +90° azimuth.

Additionally a doppler antenna is located aft of the station keeping antenna, however it utilizes a separate window area in the radome which also serves as an access door. This antenna is a planar array (16" x 12") operating at 13.325 GHz with horizontal polarization and having angular movements of +15° pitch, +30° roll, and +30° drift.

System requirements necessitated high levels of performance in all radome electrical characteristics. Transmission efficiency objectives were set at 90% average and 85% minimum for all antennas except the X-band interferometer which was assigned values 80% average and 75% minimum. Directional accuracy requirements were:

  X-&Ku-Parabolas – 3 milliradians maximum – 1 milliradian RMS
  X-Phase Interferometer – 6 milliradians maximum – 2 milliradians RMS
  Ku-Phase Interferometer – 5 milliradians maximum – 2 milliradians RMS
  Station Keeping Array – 0.5° maximum
  Doppler Antenna – 1 milliradian maximum – 0.5 milliradian average

Pattern requirements placed on the multimode system antennas included main lobe conformance to +1 db, beamwidth changes limited to 5%, and maximum side lobe increases of 3 db. The maximum power reflection permitted was 2% except in the case of the doppler antenna where the maximum cross coupling (between transmit and receive ports) was not to exceed -40 db.

The objective then, in essence, was to develop a radome wall configuration capable of satisfying these stringent electrical requirements at C-band (5.090 GHz), X-band (9.20 - 9.66 GHz), and Ku-band (16.0 - 17.0 GHz) over all of the relative antenna-radome scan orientations specified while also assuring adherence to stringent weight, structural, and lightning protection requirements.

RAY STUDIES

The first phase of the electrical design was of course to determine the geometrical relations between the various antenna apertures, the radiated energy, and the radome wall. The purpose of the ray analyses was to obtain the incidence and polarizing angles for energy of representative rays (from each of the antenna apertures) impinging on the radome wall. This was accomplished utilizing conventional graphical techniques coupled with computerization of certain phases utilizing equations (1), (2), and (3).

Two important criteria which determine the refinement or accuracy of the ray study results are proper selection of the number and location of the representative rays for each antenna operational mode and the number and location of the scan positions to be evaluated for each system mode. The C5A Radome size and shape coupled with the antenna shapes yielded minimum incidence and polarizing angle changes across the aperture, while the antenna power weighting expressions were smooth continuous functions, consequently a relatively large spacing between rays was acceptable. A rectangular grid was employed. The location and proximity of look positions to be used for each antenna is determined by the rate of change of incidence angle and polarization weighting (represented by ξ) as a function of antenna scan position. Again the radome shape precluded the necessity of closely spaced look positions. In particular it was noted that minimal variation occurred at most azimuth offsets, a noteable exception being around zero degrees. Accurate representation was then obtained by limiting the study to 27 scan positions for each multimode system antenna and a somewhat lesser number for the station keeping and doppler apertures.

This work provided the necessary incidence and polarizing angle data while also indicating that most radome window area was illuminated by virtually all of the antenna apertures thus precluding sectionalized design of the wall for specific frequencies, incidence angles, etc. Results showed an incidence angle range of 0° to 75° for X-band, 0° to 55° in Ku-band, 0° to 75° at C-band, and 0° to 65° in the doppler door radome.

ANTENNA-INCIDENCE ANGLE WEIGHTING DEVELOPMENTS

With each antenna mode defined in terms of the characteristics of representative rays at a number of scan positions, the relative importance or weighting of (1) each antenna look position and (2) each representative ray must be determined. Item (1) was simplified since identical angular increments of scan had been considered, thus equal weighting may reasonably be assigned to each look position. Only when flat panel and/or performance evaluation results indicated significant degradation changes at a particular scan position was this area given primary consideration.

Item (2) was derived in the conventional manner from the illumination taper or power distribution across the effective antenna aperture.

With the establishment of the antenna ray weighting factors coupled with the ray analysis results [incidence (θ) and polarizing (ξ) angles], it was possible to determine the relative importance of incidence angle and polarization for each antenna operational mode and scan area.

Substitution of equation (15) into equation (16) yields

$$T_{AV}^2 = \sum_{i=1}^{n} W_i T_{e_i}^2 = \sum_{i=1}^{n} W_i (T_{\perp i} \sin^2 \xi_i)^2 + \sum_{i=1}^{n} W_i (T_{\parallel i} \cos^2 \xi_i)^2 +$$

78

$$\sum_{i=1}^{n} 2 W_i T_{\perp i} T_{\parallel i} \sin^2 \xi_i \cos^2 \xi_i \cos (\Delta_{\perp i} - \Delta_{\parallel i})$$

where
$$W_i = \frac{A_i S_i}{\displaystyle\sum_{i=1}^{n} A_i S_i}$$

The polarizing angles (ξ) derived in the antenna ray study indicated that in many cases, the polarization was heavily weighted either toward perpendicular or parallel for the various multimode apertures and the station keeping antenna. The predominance of course depended on the antenna polarization, horizontal yielding primarily perpendicular and vertical corresponding generally to principally parallel polarization. This trend was most pronounced with the X-band apertures and station keeping antenna due simply to their well "off-center" locations within the radome. Consequently either the first or second term in the above expression becomes dominant, the third term being of minimum importance. For the ith ray the first term is

$$W_i (T_{\perp i} \sin^2 \xi_i)^2 \quad \text{or}$$

$$T^2_{\perp i} (W_i \sin^4 \xi_i).$$

Now, for a small incidence angle increment, $T^2_{\perp i}$ is essentially constant, hence we may sum over all rays (at a given antenna look position) in the jth incidence angle increment to obtain

$$T^2_{\perp j} \sum(j) (W_i \sin^4 \xi_i).$$

The quantity $\sum(j) (W_i \sin^4 \xi_i)$ now represents closely the perpendicularly polarized power impinging on the radome surface at an incidence angle increment, θ_j. Obtaining these summations for increments over the entire incidence angle range then provides a measure of the relative incident power (perpendicularly polarized) as a function of incidence angle.

A similar argument applies to the second term and yields the summation term $\sum(j) (W_i \cos^4 \xi_i)$ which is then a measure of the parallel polarization component of power impinging at an incidence angle increment, θ_j. These summations over all scan positions were obtained and plotted as shown in Figure 3 for both perpendicular and parallel polarization using
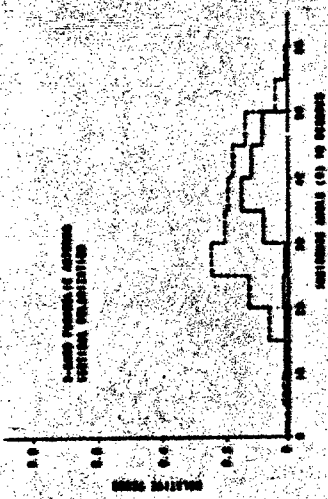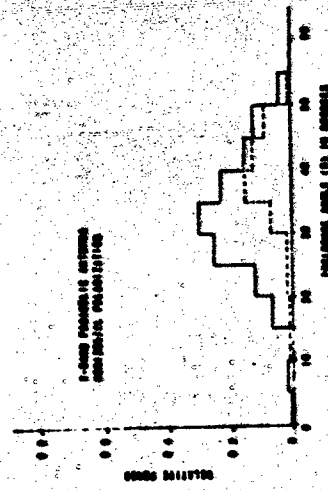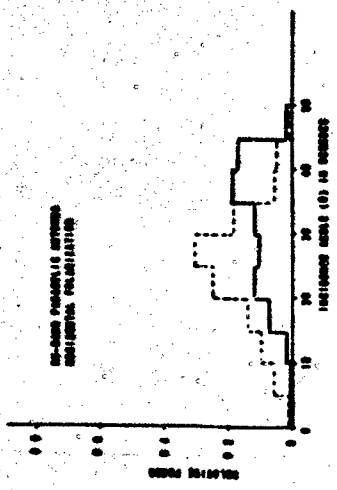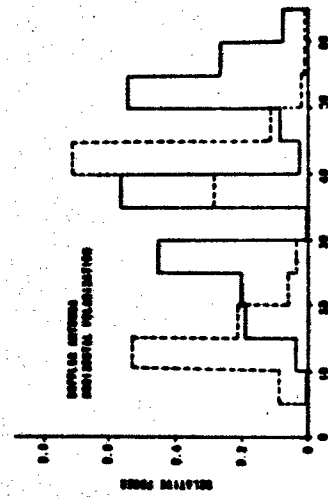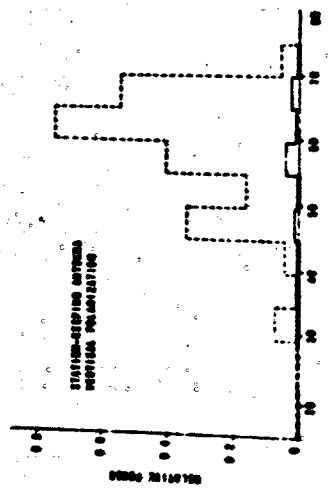
FIGURE 3. RELATIVE PHASE HISTOGRAMS OF INCIDENCE ANGLES

5° for the incidence angle increment, $\Delta\theta$. From the antenna ray analysis studies, it was noted that generally the incidence angle magnitudes and range for a given antenna (multimode system) were closely similar at the various elevation and azimuth offsets examined, excepting the 0° azimuth scan area where the magnitudes and range were somewhat higher. Consequently, plots for the multimode antennas were also developed for $(W_i \sin^4 \xi_i)$ and $(W_i \cos^4 \xi_i)$ summations of the 0° azimuth scan area. These plots then graphically describe not only the incidence and polarizing angle range, but the relative importance of each incidence angle increment and polarization.

CONSTRUCTION AND MATERIAL SELECTION

The multiple frequencies and severe incidence-polarizing angle ranges coupled with the structural, environmental, and weight criteria virtually dictated a sandwich construction consisting of alternating layers of high dielectric skin material ($\epsilon' \cong 4$) and low dielectric core material ($\epsilon' \cong 1$) in numbers and thicknesses determined by the design itself. Candidate skin materials (limited to pre-impregnated glass fabric for electrical uniformity) were all evaluated for their dielectric, loss, homogeneous, and isotropic properties, however the primary requirements were for a high flexural modulus, good storage stability, ease of cure at moderate temperatures and pressures, and favorable tack and drape properties. From a literature survey, eight materials were selected for empirical screening and of these, three were selected for an optimization study. The final skin material selection was based on numerous sample panels which were tested and examined for such properties as flexural strength and modulus, flatwise tensile strength, climbing drum peel strength, degree of fillet (into honeycomb core) density, resin content, void volume, volatile content, cure temperatures and durations, and interlaminar shear. The most critical structural property was judged to be flexural modulus (radome buckling) and the final selection of E-293 (an epoxy prepreg by the Cordo Division of Ferro Corporation) was based mainly on modulus values seven (7) to ten (10) percent higher than the other candidates. Concurrent studies on core materials resulted in the selection of bandsaw cut (as opposed to microsanded) nylon phenolic honeycomb of a four (4) pound density and 3/16" cell size with an established dielectric of 1.09 and loss tangent of .002. It is noted that although the E-293 material was not selected primarily on an electrical basis its dielectric constant was the lowest at both X and Ku-band (4.20 and 4.06 respectively) while the loss was average at X-band and a minimum at Ku-band (.018 and .021 respectively).

THEORETICAL AND EMPIRICAL FLAT PANEL STUDIES

The next segment of the design program was to determine the most optimum wall configurations using computer programmed flat panel calculations of transmission efficiency, reflection, phase delay, and absorption based on the ray analysis data, material characteristics and expressions (5) through (14). Maximizing the minimum transmission values and optimizing the average across the frequency, incidence angle, and polarization ranges was the principle objective. This design criteria also insured minimal reflection, particularly important since the primary error contribution in the phase interferometers is apparently not from phase delay

or attenuation changes in the wall, but rather from random reflections which cause pronounced changes due to the small effective aperture and phase center separation. Beam deflection values for the parabolic antennas should be insignificant due to the large effective apertures and somewhat lower incidence angle range. The most effective controls here are: minimization of physical variances and discontinuities in the radome fabrication. These parameters also affect antenna patterns, however this distortion appears to be principally a function of the radome geometry and metallic and dielectric anomalies in the window area.

The incidence angle weighting plots provide an excellent basis for the flat panel computer study. Normally in this design phase, the ray analysis results would be used to develop a "design angle" which would be used in evaluating the flat panel transmission data. Now the power weighting summations may be utilized in obtaining an accurate transmission figure of merit for each antenna with each panel configuration considered. For instance, the X-band phase interferometer polarization is almost exclusively perpendicular (Figure 3), hence the first term in the transmission expression dominates and yields very nearly

$$W_i \, T_{e_i}^2 \cong T_{1i}^2 \, (W_i \, \sin^4 \xi_i) \quad \text{for the } i^{th} \text{ ray,}$$

$$\sum_{(j)} W_i \, T_{e_i}^2 = T_{1j}^2 \cdot \sum_{(j)} (W_i \, \sin^4 \xi_i) \quad \text{for all rays at all scan positions in the } j^{th} \text{ incidence angle increment,}$$

and finally

$$T^2 \text{ (Figure of merit)} = \sum_{j=1}^{n} \sum_{(j)} W_i \, T_{e_i}^2 = \sum_{j=1}^{n} T_{1j}^2 [\sum_{(j)} (W_i \, \sin^4 \xi_i)].$$

The quantities $[\sum_{(j)} (W_i \, \sin^4 \xi_i)]$ for each incidence angle increment are obtained directly from Figure 3 while the T_{1j}^2 terms are determined in the flat panel calculations for the panel wall configuration being considered. For convenience the T^2 (Figure of Merit) was normalized and the operations performed on the G.E. 265 Computer in time-sharing FORTRAN. Varying the wall configuration to maximize the figure of merit while monitoring the general transmission levels as a function of incidence angle then provides an accurate method of approaching the optimum configuration. The task of course is a large and difficult one since the scan positions corresponding to minimum transmission efficiency, all antennas and operational modes, and all frequencies must be considered with each wall thickness configuration alteration to insure against unacceptable degradation of a particular mode, frequency, scan position, etc.

Three, five, seven, nine, and eleven layer wall configurations were all considered within reasonable structural bounds. Obviously a sufficient number of layers was needed for good matched Ku, X and C band response over a large incidence angle range; on the other hand, an excessive

number of layers would create overly critical fabrication tolerances and overall reduced performance in achieving unneeded broadbandedness. A number of constructions covering the reasonable range of thicknesses and combinations was then selected and each refined utilizing variations on individual layers and a process of successive approximation guided by the computed transmission values, the transmission figures or merit, and phase delay variations. This was necessary since it was not sufficient to assume that given an arbitrary initial construction, such a process of individual thickness variation of the layers would yield the electrically desired construction, simply because several maxima of varying performance levels may well exist with minimum levels intervening; nor could it safely be assumed that the "effective" thicknesses must necessarily follow a Gaussian or similar distribution, or a quadrant of the same.

Ultimately, the construction selected was a seven layer configuration with skin thicknesses of .025", .025", .020", and .015" and core thicknesses of .125", .190", and .125", progressing in each case from the outer to the inner radome surface. The transmission and phase delay response of this configuration with the inclusion of a standard Class II elastomeric rain erosion resistant and anti-static coating is shown in Figure 4 as a function of incidence angle.

To obtain empirical correlation, the wall configuration developed theoretically was fabricated as a 48" x 48" flat panel using the materials and processes to be employed in the actual radome construction. In building preliminary panels, it was noted that the total thickness was generally somewhat less than the sum of the individual sandwich layers. Microwave and physical measurements indicated that the nominal thickness values of .010" for 181 type fabric and .005" for the 120 style weave were closely approached and the theoretically desired values could be achieved using combinations of these two glass cloths. It was therefore felt that the overall thickness decrease was attributable to effectively thinner cores due to honeycomb compression during processing and/or seating of the honeycomb well into the skin fabric weave. Honeycomb sandwiched between aluminum sheets and subject to the same processing demonstrated no thickness changes, consequently the latter explanation was assumed. This seating effect was then of course appropriately compensated for in the fabrication procedure.

Three additional panels were also fabricated with incremented thicknesses about the design panel values. Empirical transmission data was obtained as a function of incidence angle at Ku, X, and C-bands for both perpendicular and parallel polarizations in the Brunswick anechoic chamber for each of the four panels to insure correlation with the theoretical calculations and yield an insight into the effect of layer thickness variances or tolerances. Comparison of the design panel results (Figure 5) with the theoretical data (Figure 4) showed reasonable agreement, however the actual experimental data was in general better by one to four percent, this difference being attributed to overly severe dielectric and loss values assigned to the rain erosion resistant and anti-static coatings. Transmission remains above 90% from 0° to 34° incidence at Ku-band, 0° to 60° at X-band, and 0° to 37° at C-band for perpendicular polarization. The configuration provides a good match over the incidence angles and polarizations required, but it is obviously not a broadbanded
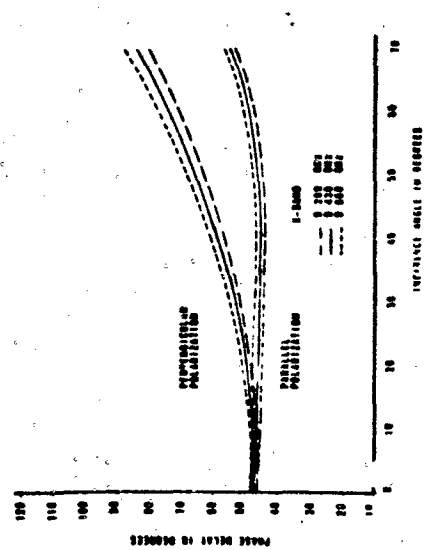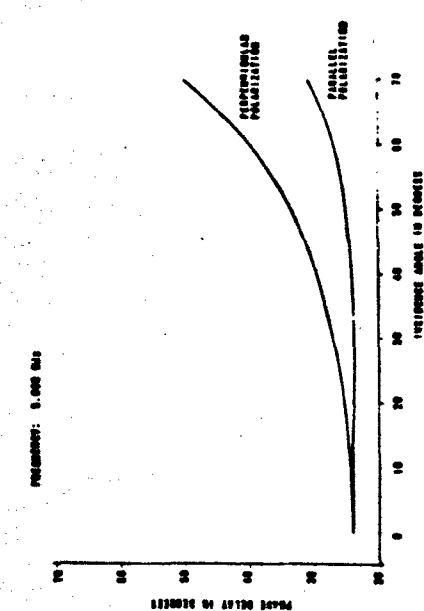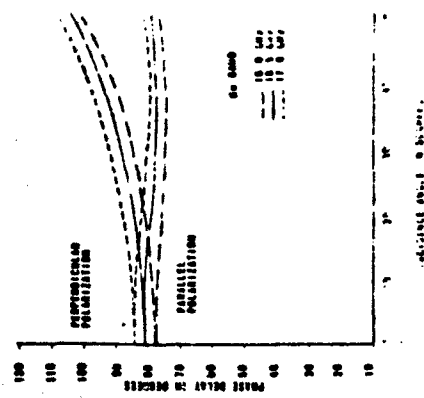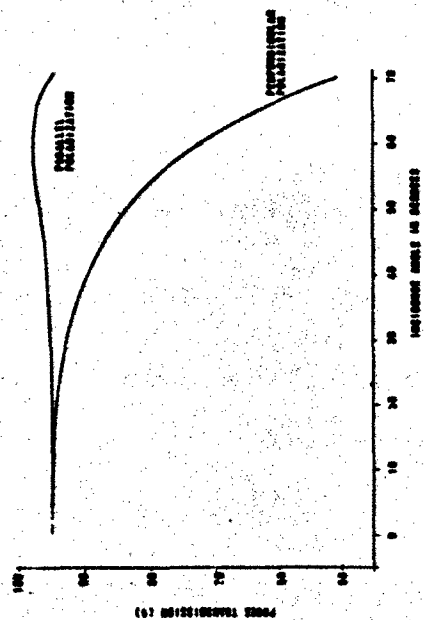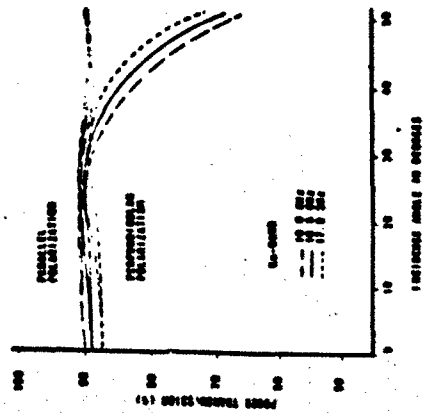
FIGURE 3. THEORETICAL FLAT PANEL TRANSMISSION AND PHASE DELAY PERFORMANCE - OPTIMUM WALL CONFIGURATION WITH EXTERIOR COATING

structure as evidenced by the perpendicular polarization degradation at
the intermediate and higher incidence angles for Ku- and C-band. This
was also apparent when, as a matter of interest, calculations were per-
formed at the doppler frequency of 13.325 GHz with a resulting 86%
transmission at 0° incidence decreasing to 63% at 50°. The doppler door
wall computations were accomplished in a manner similar to those of the
nose window area and also resulted in a 7-layer configuration. However
this was not most optimum electrically and with a relaxation of the
structural requirements following some test work, additional computations
were performed, ultimately yielding a 5-layer or C-sandwich construction
with skins of .025", .040", and .015" while the core thicknesses were
.165" and .195" progressing in each case from the outer to inner radome
wall surface. Figure 6 illustrates the transmission and phase delay
characteristics of this wall configuration with the exterior rain erosion
resistant and anti-static coating included, transmission remaining above
90% from 0° to 60° for the worst case polarization (perpendicular).

RESOLUTION OF CONFLICTING STRUCTURAL/ELECTRICAL CRITERIA

The optimum electrical wall was not at all acceptable structurally
due to the low total thickness (.525") and the unsymmetrical cross-
section of skin thicknesses, both of which considerably reduced the moment
of inertia. Efforts to achieve a comparable electrical wall involving
a greater total thickness were unsuccessful and it was imperative that
the skins be as thin as possible, the .025" outer skin being a minimum
for impact and abrasion resistance, the normal flight environment, etc.
Additional electrical degradation was not acceptable, consequently a
solution to the structural dilemma was sought. Since the critical mode
of failure was in overall shell buckling, the obvious recourse was to
somehow reduce the net pressures tending to cause buckling, the ultimate
solution being a flush mounted air scoop mounted beneath the station
keeping array in a non-window area (Figure 2). With the scoop ram
efficiency properly selected, the electrical wall configuration could
then be used without danger of radome buckling or "blow off" (due to high
tensile loads in the attachment latches). Additional difficulties were
encountered in the doppler door wall design where mechanical thickness
requirements dictated the use of a 7-layer configuration which appeared
marginal electrically, however empirical tests later indicated a greater
margin of safety than anticipated and the minimum total thickness was
relaxed sufficiently to permit use of the more desirable five-layer C-
sandwich construction (.440").

PERFORMANCE EVALUATION

The performance evaluation phase of the electrical design examined
the wall configuration developed in the preceding design phases. Calcula-
tions were performed to determine the theoretical transmission performance
levels for each antenna and operational mode over the applicable scan
areas and frequencies. Calculations were also conducted on the incremental
thickness configurations, the results being used to effect any necessary
configuration refinements and assure the optimum final wall construction.
The antenna-radome geometry and nature of the wall construction for the
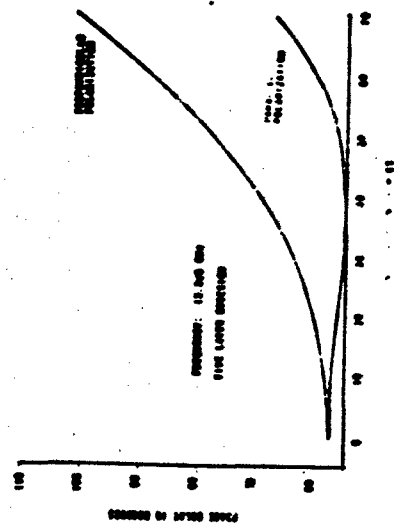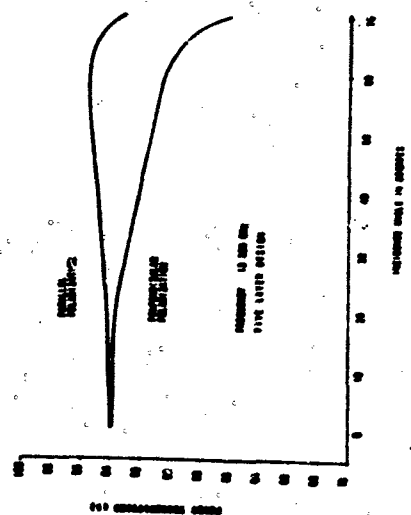
C5A system was such that the dominating and controlling characteristic was power transmission efficiency. Antenna pattern distortion is primarily a function of the radome shape and dielectric and metallic anomalies in the window area rather than any precise wall configuration. Small variances in the transmission and phase delay associated with the wall are not generally significant. One noteable distortion which sometimes occurs is the inducement of a reflection lobe in the pattern at a specific antenna scan position and pattern angular offset. These are most effectively reduced by minimizing the reflection coefficient over the incidence angle and frequency range involved. Since the transmission, reflection, and absorption characteristics are directly related, it is apparent that maximizing the power transmission will tend to minimize the reflection magnitudes for materials having specified absorption or loss characteristics. Power reflection and resultant coupling back into the system antenna due to the radome presence is another characteristic of importance, but again this parameter is minimized in the transmission efficiency optimization process. Beam deflection, which is of importance for the X and Ku-band parabolic antennas, is primarily a function of the attenuation and phase delay variance across the illuminated window area of the radome wall. The former is of course controlled by transmission optimization and selection of configurations providing minimum change with incidence angle and polarization. During the flat panel studies, phase delay plots as a function of incidence angle were monitored for various configurations. Although some magnitude changes were noted, the curve shapes remained closely similar, hence the phase delay variations with incidence angle were essentially constant despite wall construction changes. Effective phase delay variance could be achieved (thus altering beam deflection values) by tapered or stepped wall layer thicknessess, but this was unfeasible due to fabrication difficulties, extreme overlapping of the window areas for the various antenna operational modes, and the likelihood of additional electrical discontinuities in the wall. The larger apertures of these antennas also tend to integrate and thus minimize the effects of small wall construction variances, while the random reflection contribution to beam deflection should be insignificant due to the extremely narrow beamwidth.

Boresight error, applicable to the Ku and X band phase interferometers, the station keeping antenna, and the doppler antenna, is determined in part by the same criteria as beam deflection however the small aperture dimension in the error sensing plane (least pronounced in the doppler antenna) creates some increase in the effects of small wall construction variances while random reflections contribute perhaps the major error component due to the wide beamwidth and, in the case of the interferometers, the small phase center separation. These radome reflections are minimized by maximizing the transmission, but it is important that they be considered over the entire incidence angle range, particularly for near normal incidence.

Hence it is seen that the problem of achieving maximum electrical performance reduces to one of essentially optimizing the wall construction for transmission efficiency over the specified range of incidence angles and frequencies.

Calculation of the radome transmission efficiency was based on equations (15) and (16). Specifically the desired antenna scan position

is selected; then equation (15) is used to express the transmission value for each representative ray of the antenna. ξ is obtained from the ray analysis data, $T_\perp$ and $T_\parallel$ are taken directly from the empirical results (on the selected panel configuration) at the incidence angle determined from the ray study, and $\Delta_\perp$ and $\Delta_\parallel$ are from the theoretical flat panel computations. Equation (16) is a simple summation coupled with the antenna power weighting factors to obtain the approximate transmission through the radome for the initially selected antenna look position. A method of voltage summing over the representative rays was also performed to check the described technique with a resulting maximum difference of .3%. Transmission calculations were accomplished for each antenna and scan position evaluated in the ray analysis. Some resulting performance values derived in this evaluation are shown plotted in Figure 7 as a function of antenna azimuth scan position and are of course based on the pure dielectric window construction.

Calculations on the incremented thickness panel constructions indicated that the initially selected configuration was indeed the most favorable. The Figure 7 plots are self-explanatory however it is noted that generally transmission levels were relatively high, the most critical modes being the X-band phase interferometer (76% minimum) and the Ku-band parabolic antenna (84% minimum). For the station keeping antenna, the high values around 0° azimuth tapering off to about 86% at +90° azimuth are a direct consequence of the polarization changes from virtually all parallel at 0° to a significant perpendicular component at +90°. These performance levels will be degraded by the lightning protection system metallic hardware which creates radar blockage with accompanying reflective and diffractive effects. Lightning protection was deemed necessary due to the large radome size and the vulnerability of the enclosed antenna systems. The lightning protection developed is unique in that internal conductors are used with diverter probes through the wall to the exterior surface which also act as conductor attachments. Numerous advantages accrue from this approach such as reduction of thermal problems, minimization of maintenance due to flight environment deterioration, etc., however most important is the elimination of aerodynamic drag created by an external system and the capability of designing the hardware to achieve minimal blockage of the radiated energy without regard to the normal aerodynamic constraints of an external system.

The pattern configuration of the diverters on the radome is illustrated in Figure 8.

The energy blockage, reflection, and diffraction caused by this metallic hardware obviously introduce phase and amplitude variances which affect all radiation characteristics - antenna patterns, reflection, beam deflection or boresight error, and transmission efficiency, the latter two generally being the more critical. Transmission losses have sometimes been calculated simply by considering the effective blocked area of the aperture, however empirical results show wide deviations as a function of the relative anomaly size and shape, proximity to the aperture, and orientation of the electric field vector. At least qualitatively,
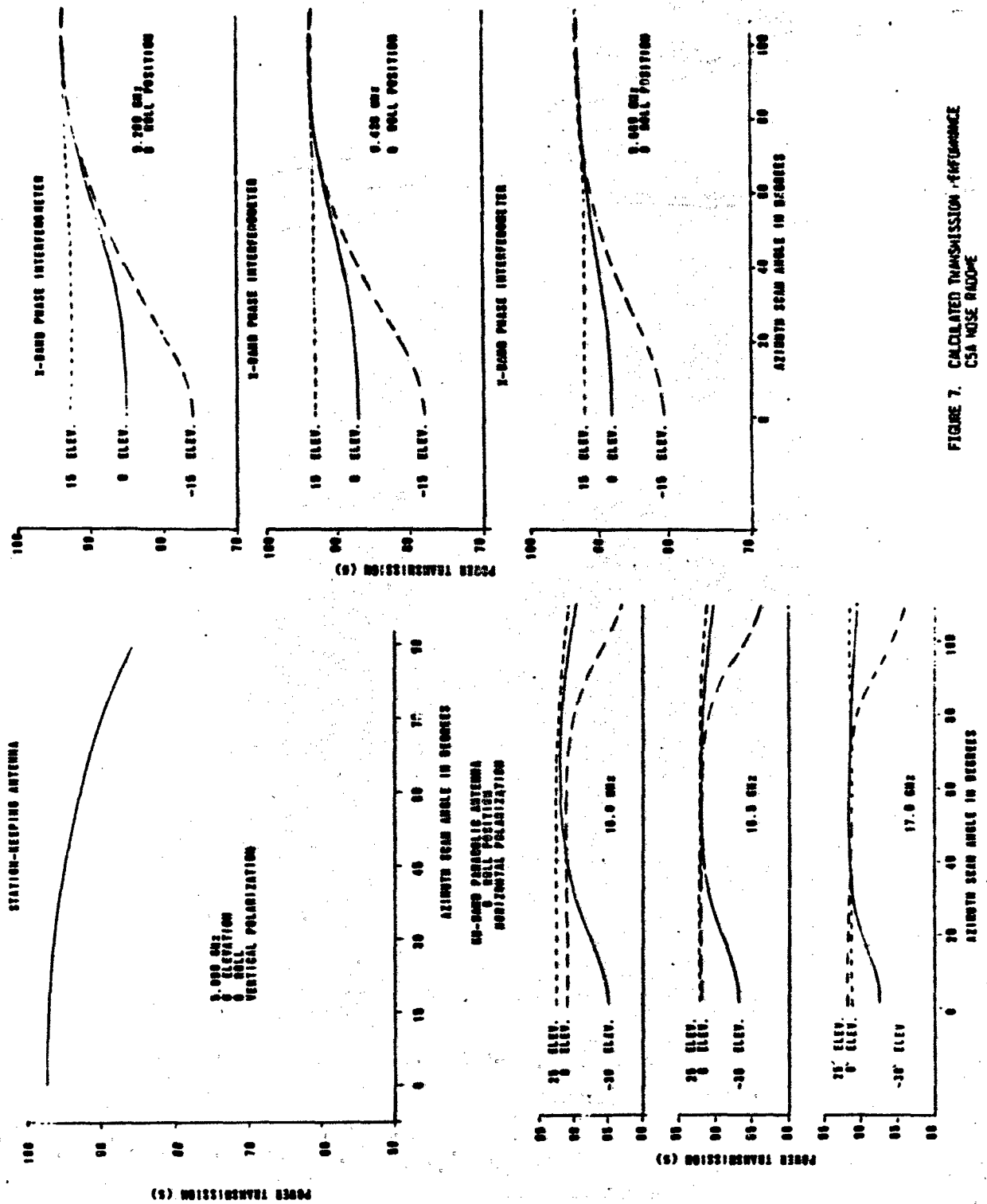
FIGURE 7. CALCULATED TRANSMISSION PERFORMANCE C5A NOSE RADOME

effects should be diminished by minimizing the object or anomaly size.

Loss estimates in this case were based primarily on previous experience obtained on other diverter systems and interference problems encountered with pitot-static tubes, wires, etc. The parabolic antennas should be virtually unaffected, however the interferometers, may suffer attenuations up to 10% as shown in Figure 9 where the loss is plotted as a function of the angle formed by the electric field vector and the plane of the diverter. Fortunately the diverter orientations provide for minimal loss around the critical 0° azimuth region while the maximum effects should occur only at the greater azimuth offsets. The small effective aperture of the station keeping array coupled with its vertical polarization dictated termination of the buttline 0 diverter in the primary window region (+15° elevation angle of arrival) however the radome unprotected surface distance was less than 30" and no wall punctures were encountered in the lightning tests.

The stringent doppler electrical requirements precluded use of any metallic items in the window area, consequently this region was protected solely by the peripheral strip shown in Figure 8.

Another possible source of electrical degradation is obviously divergence of the fabricated wall from the theoretical wall and flat panel samples. Every effort was made to minimize these effects by carefully selected lay-up patterns, minimum overlapping, closely controlled honeycomb thicknesses, use of pre-impregnated cloth, high quality vacuum cures, etc., nevertheless some deviations were expected due to the extreme size and the number of layers in the radome wall.

Evaluation of limited electrical test data to date indicates that the C-sandwich doppler door has exhibited transmission, boresight error, and reflection characteristics well satisfying the specification requirements. On the nose radome, transmission appeared good at X-band while some minimums fell below the 80% value at Ku-band. Beam deflection on both parabolas was well below the 3 milliradian maximum and 1 milliradian RMS requirements, however interferometer boresight errors appeared to be running higher than expected, indicative of the importance of aperture size and the phase center separation. Relative to testing, the complexity and number of antennas coupled with the radome's size dictated a special test range consisting of actually two ranges (1000' and 300') to provide the necessary far field illumination and power levels for the various antennas and tests. The radome holding fixture becomes a large multi-axis device capable of simulating aircraft roll, pitch, and drift movements about a number of gimbal points (Figure 1). Beam or null seeker movement for detection of error magnitudes becomes excessive at the 1000' range distance, consequently an electronically calibrated system was selected to avoid mechanical movement and the error resulting from such systems. Also, the extreme azimuth scan limits necessitated the development of a precision counter-rotating antenna movement and mount.
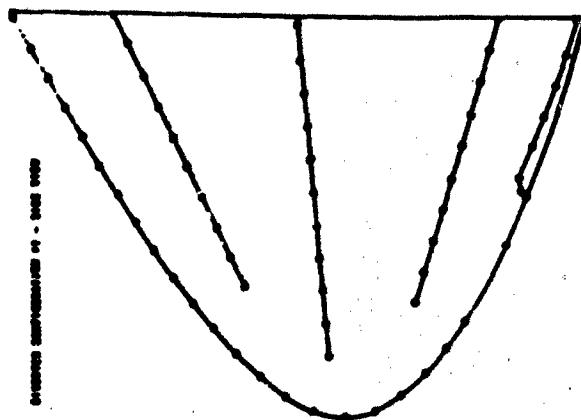
91
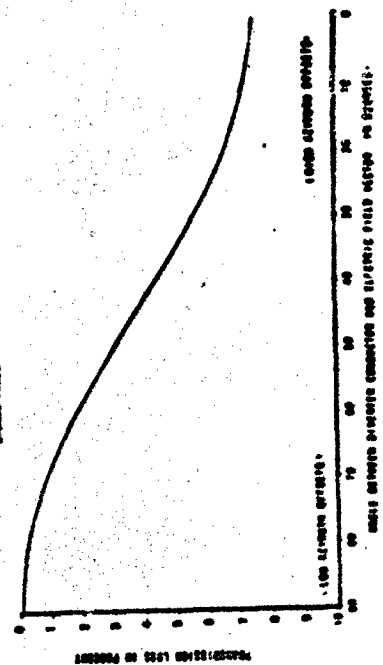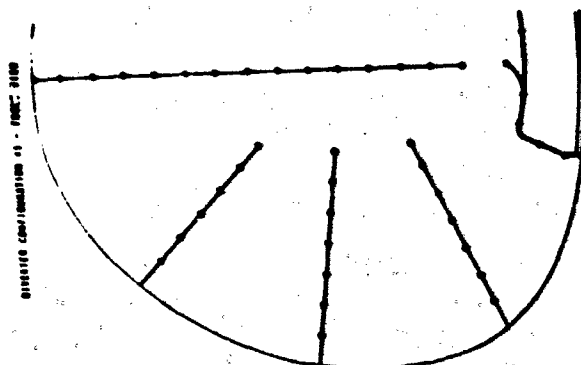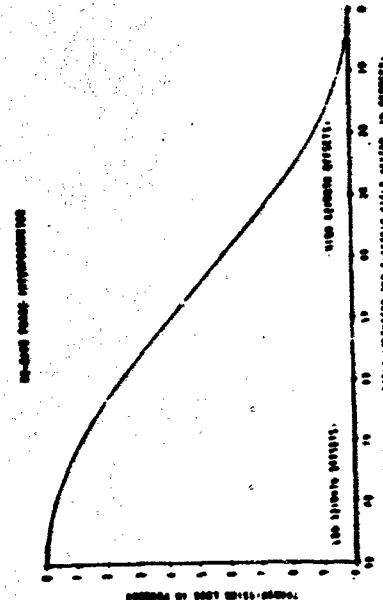
The C5A radome electrical program has then indeed been a unique challenge - from the design study discussed herein and resulting stringent physical tolerances necessary to achieve adequate electrical performance for the multiple antenna apertures and characteristics through the development of a special lightning protection system to the solution of the range testing problems occasioned by the large radome and antenna aperture sizes, the antenna gimbaling locations and the azimuth scan requirements.

EQUATIONS AND DEFINITIONS

The primary mathematical expressions and associated symbols and definitions utilized in the C5A Nose Radome electrical design are as listed below. The various equations were manipulated, combined, etc. as noted in the text to provide the most convenient form for computer programming or the specific operation to be performed. These expressions may also be found in the appropriate references of this report.

$$\tan^2 \theta_\perp + \tan^2 \theta_\parallel = \tan^2 \theta \tag{1}$$

$$\tan \theta_\perp = \tan \theta_\parallel \sin \xi \tag{2}$$

$$\tan \theta_\parallel = \tan \theta \cos \xi \tag{3}$$

$$\theta_o = \frac{\sum_{i=1}^{n} \theta_i A_i S_i}{\sum_{i=1}^{n} A_i S_i} \tag{4}$$

$$a_\perp^* = \frac{\epsilon'_i - \sin^2 \theta}{1 - \sin^2 \theta} \tag{5}$$

$$a_\parallel^* = \frac{\epsilon'^2_i (1 - \sin^2 \theta)}{\epsilon'_i - \sin^2 \theta} \tag{6}$$

$$r_i = \frac{\sqrt{a^*} - 1}{\sqrt{a^*} + 1} \tag{7}$$

$$L_i = \frac{\varepsilon'_i \; \text{Tan} \; \delta_i}{2 \; (\varepsilon'_i - \text{Sin}^2 \; \theta)} \tag{8}$$

$$\psi_i = \frac{2 \; \pi \; d_i}{\lambda_o} \; [\varepsilon'_i - \text{Sin}^2 \; \theta]^{1/2} \tag{9}$$

$$T = \frac{(1 - r_i^2) \; e^{-\psi_i \; L_i} \; e^{j\psi_i}}{1 - r_i^2 \; e^{-2\psi_i \; L_i} \; e^{2j\psi_i}} \tag{10}$$

$$R = \frac{-r_i \; (1 - e^{-2\psi_i \; L_i} \; e^{2j\psi_i})}{1 - r_i^2 \; e^{-2\psi_i \; L_i} \; e^{2j\psi_i}} \tag{11}$$

$$\Delta = \frac{2 \; \pi \; \Sigma \; d_i}{\lambda_o} \; \text{Cos} \; \theta - \text{ARG} \; T \tag{12}$$

$$T_{AB} = \frac{T_A \; T_B}{1 - R_A \; R_B} \tag{13}$$

$$R_{AB} = R_B + \frac{T_B^2 \; R_A}{1 - R_A \; R_B} \tag{14}$$

$$T_{e_i}^2 = (T_{\perp i} \; \text{Sin}^2 \xi_i)^2 + (T_{\parallel i} \; \text{Cos}^2 \xi_i)^2 + 2 \; T_{\perp i} \; T_{\parallel i}$$
$$\text{Sin}^2 \xi_i \; \text{Cos}^2 \xi_i \; \text{Cos} \; (\Delta_{\perp i} - \Delta_{\parallel i}) \tag{15}$$

$$T_{AV}^2 = \frac{\sum\limits_{i=1}^{n} T_{ei}^2 \; A_i \; S_i}{\sum\limits_{i=1}^{n} A_i \; S_i} \tag{16}$$

$\theta_\perp$ = Perpendicular component of incidence angle; the angle measured between a ray and the component of the normal to the radome surface (at the ray-surface intersection) which constitutes a plane perpendicular to the electric field vector.

$\theta_\parallel$ = Parallel component of incidence angle; the angle measured between a ray and the component of the normal to the radome surface (at the ray-surface intersection) which constitutes a plane including the electric field vector and the ray itself.

θ = True incidence angle - angle between the incident ray and the normal to the radome surface at the point of intersection of the ray and the radome wall.

θ_o = Design angle of incidence; weighted average incidence angle; defined by equation (4).

ξ = Polarizing angle; the angle between the plane of incidenc and the electric field vector.

A_i = A normalized numerical coefficient denoting the relative size of the antenna aperture area represented by the ith ray.

S_i = Weight factor describing relative power of the ith ray; the fraction of maximum power emergent from the area element, A_i.

ϵ'_i = Relative dielectric constant of the ith layer.

$\mathrm{Tan}\ \delta_i$ = Loss tangent of the ith layer; a measure of the ohmic (heat) loss or energy absorption of microwave radiation by the material.

λ_o = Free space wavelength in inches for a prescribed microwave frequency, f.

d_i = Physical thickness of the ith layer of material.

T = Amplitude transmission coefficient.

T_A = Amplitude transmission coefficient through layer A.

T_B = Amplitude transmission coefficient through layer B.

T_{AB} = Amplitude transmission coefficient through layers A and B.

T^2 = Power transmission coefficient.

R = Amplitude reflection coefficient.

R_A = Amplitude reflection coefficient through layer A.

R_B = Amplitude reflection coefficient through layer B.

R_{AB} = Amplitude reflection coefficient through layers A and B.

R^2 = Power reflection coefficient.

$T_{e_i}^2$ = Effective power transmission coefficient for the ith ray.

T_{AV}^2 = Average power transmission coefficient for the antenna in a given scan position.

Δ = Insertion phase delay; the phase difference which occurs when an air path is replaced by a physically equal dielectric path.

$\Delta_\perp$ = Perpendicular component of the insertion phase delay.

$\Delta_\parallel$ = Parallel component of the insertion phase delay.

θ_i = Incidence angle of the ith ray emergent from the antenna aperture in a given offset angle.

$T_{\perp AV}^2$ = Average power transmission coefficient, perpendicular polarization, for the antenna in a given scan position.

$T_{\parallel AV}^2$ = Average power transmission coefficient, parallel polarization, for the antenna in a given scan position.

$a_\perp{}^*$ = or is defined by equation (5).

$a_\parallel{}^*$ = or is defined by equation (6).

L_i = or is defined by equation (8).

ψ_i = or is defined by equation (9).

r_i = The interface reflection coefficient; it is a measure of the reflected energy relative to the incident energy at the ith dielectric interface.

$T_\perp$ = The perpendicular component of the amplitude transmission coefficient.

$T_\parallel$ = The parallel component of the amplitude transmission coefficient.

$\perp$ = Perpendicular polarization; a condition occurring when the electric field vector of radiation impinging on a surface is orthogonal to the plane which includes the incident ray and normal to the surface at the point of intersection (plane of incidence).

95

$\parallel$ = Parallel polarization; a condition occurring when the electric field vector of radiation impinging on a surface lies in the plane which includes the incident ray and normal to the surface at the point of intersection (plane of incidence).

i,n = i is one of a total number, n, of similar parameters or quantities.

$\sum\limits_{i=1}^{n}$ = a summation of the ith quantity as i varies from 1 to n.

j = one of the two imaginary square roots of -1.

π = a notation for a segment of a period, cycle, etc; the ratio of the circumference of a circle to its diameter; the value is 180° or 3.14159....radians.

e = the "exponential", the base of Naperian Logarithms; its value to the nearest thousandth: 2.718.

REFERENCES

(1) Radar Scanners and Radomes, Volume 26, Radiation Laboratory Series, Massachusetts Institute of Technology.

(2) Electrical Design of Lossy High Incidence Radomes, Report No. ADC EL-123-50, AEEL, USNADC; 11 July 1950.

(3) Techniques for Airborne Radome Design, WADC Technical Report 57-67, ASTIA Document No. AD 142001, September 1957.

(4) Military Specification MIL-R-7705A (ASG), Radomes General Specification for, 12 January 1955.

(5) Antenna Engineering Handbook, Henry Jasik, Editor, McGraw-Hill Book Company, 1961.

(6) An Introduction to Radome Electrical Design, Report Number BR-124-001, Revision A, dated March 9, 1964; Brunswick Corporation, Defense Products Division.

(7) ATC Report Number ARTC-4, "Electrical Test Procedures for Radomes and Radome Materials"; revised 30 July 1960.

MISSILE RADOME PROTECTIVE COVERS

D. R. Beeler
R. A. Eastridge
R. L. Copeland
V. A. Chase

Brunswick Corporation
Technical Products Division
Marion, Virginia

ACKNOWLEDGMENTS

ABSTRACT

Results are presented on the design, development and test of an in-flight (captive) removable, protective cover for missile nose cones. Areas investigated include selection of skin, backing, and junction block materials in addition to selection of a suitable pyrotechnic system capable of fragmenting the nose cover. Model caps were fabricated and tested and the results are presented. Rocket sled test runs were conducted at velocities up to Mach 1.5 with the velocity sustained during nose cover ejection. Results of these tests are presented.

INTRODUCTION

A problem exists where missiles are not carried in the bomb bay but are mounted externally to the aircraft and are continually exposed to the elements and repeated flights until fired. The nose cones of these missiles are not only subjected to rain erosion, but to the more drastic conditions of impact and abrasion from stones, sand, dust, mud and other debris thrown up by the landing gear from preceding aircraft during each take-off and landing, particularly on unimproved airfields. The object of the work reported here was to develop techniques to provide a removable cover for protecting these missile radomes against damage of this

type until just prior to launch. The design techniques developed are intended to be applicable to not only radomes but infrared domes and glass domes used in optical guided missiles.

Three operating environments are to be considered in the overall scope of the program. These are for missile radomes which, during captive flight, will see temperatures up to 250°F, 400°F, and 600°F. This paper deals with the first temperature range only, namely, -40°F to +250°F. Candidate materials for the 400°F requirement cover include a cross-linked polyethylene skin and a silicone foam.

DISCUSSION

Certain design goals were established at the beginning of the program pertaining to the capabilities and requirements which the protective cap must meet. These goals are as follows:

1. The covering shall protect the missile nose cone from erosion caused by dirt, sand, mud, stones, rain, hail, and other debris.

2. The covering shall protect the nose cone in such a way as to insure reliable operation upon its removal.

3. The covering shall be removable in flight prior to arming and firing of the missile.

4. The covering shall add a minimum of aerodynamic drag and weight.

5. The coverings shall withstand temperatures of from -40°F to +600°F.

6. The coverings shall have a minimum operational life of 1000 hours.

The basic design selected for the protective covers is shown in Figure 1. The diagram shows a thermoplastic outer skin, a foam backing with linear shaped charges, and a pyrotechnic detonator to fragment the protective cap at the time of removal.

Materials Evaluation

Thermoplastics were selected over reinforced plastics, metals or ceramics as potential cap materials. The major disadvantage of metals in this application is the potential hazard to control surfaces of the tail section of the aircraft, fins of missiles, and jet engines of the plane when such a metal cap was jettisoned. Ceramic coatings would tend to

Detonator

Junction
Block

Thermoplastic
Cap Skin

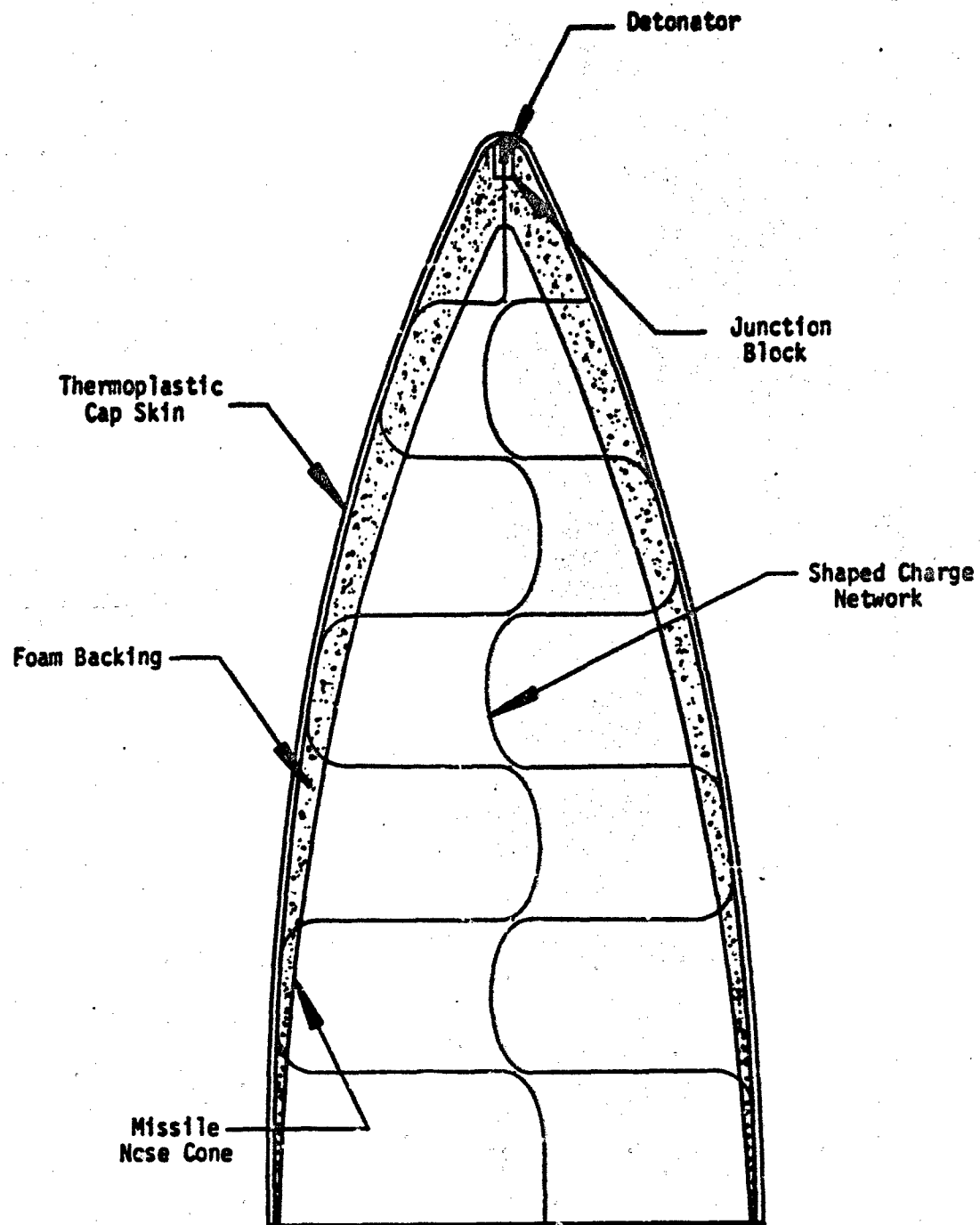Shaped Charge
Network

Foam Backing

Missile
Nose Cone

FIGURE 1

SCHEMATIC OF PROTECTIVE CAP
DESIGN

chip and delaminate upon impact in addition to causing severe damage and abrasion to jet engines if drawn into the intakes after ejection.

Several thermoplastic materials were evaluated as candidates for the protective cap skin for the -40°F to +250°F temperature class. The candidates, selected on the basis of the manufacturers recommended continuous service temperature, were polyphenylene oxide, polysulfone, polycarbonate, polypropylene, cross-linked polyethylene, and CTFE fluorocarbon. Fabrication processes, such as vacuum forming and laminating, were studied and established for the materials which were found promising.

Tests conducted on these materials included impact resistance, abrasion flammability, solvent resistance, and rain erosion resistance. The results of these tests are shown in Table 1.

Charpy impact strengths (unnotched) were determined in accordance with ASTM procedure D 256-56. This test was used to determine the susceptib ity of the candidate materials to fracture by shock. The amount of ene expended in breaking the specimens was recorded. Two materials, cross-linked polyethylene and polycarbonate, stand out in impact strength ove the other materials.

Abrasion resistance involves impacting the specimen with an abrasive under high air pressure. In these particular tests, the specimens were exposed to a silicon carbide grit of 30 grams/second in an air stream under 20 psi with perpendicular impingement and a nozzle distance of 3 inches from the specimen. All of the abrasion indices are acceptable. The polycarbonate and CTFE indices are very good while the cross-linked polyethylene value is quite exceptional.

Table 1 also shows the flammability characteristics of the various candidates. All are either self-extinguishing or non-flammable except for polypropylene which was slow burning. Based on this result and the low impact strength, polypropylene was dropped as a candidate material.

Rain erosion resistance was one of the principal criteria for selecting the skin material. Leading edge specimens were prepared and tested in a whirling arm fixture at 500 miles per hour in a simulated rainfall of 2 inches per hour. The results show cross-linked polyethylene as clearl outstanding in comparison with the other candidates.

In addition to these tests, the candidate materials were also tested for solvent resistance. The solvents used were:

    Hydraulic Fluid
    Anti-Icing Fluid (98+% Isopropyl Alcohol)
    JP-5 Fuel
    JP-4 Fuel
    Lubricating Grease

100

TABLE 1

PROTECTIVE SKIN CANDIDATE MATERIALS

	Impact Resistance, ft-lbs	Abrasion Index, sec/mil	Flammability[1]	Rain Erosion Resistance, min.
Cross-Linked Polyethylene	14.5	620	Self-Ext.	12.0
Polypropylene	1.5	--	Slow Burning	--
Polyphenylene Oxide	2.6	40	Self-Ext.	4.5
CTFE-Fluorocarbon	3.1	200	Non-Flammable	2.5
Polysulfone	1.2	90	Self-Ext.	2.9
Polycarbonate	16.0	150	Self-Ext.	5.0

[1] Data obtained from literature

The results of these tests showed all of the materials to be largely unaffected by the solvents.

Based on the data shown in Table 1 and also commercial availability, low cost, and ease of fabrication, cross-linked polyethylene was selected as the protective skin material for the 250°F temperature class.

Backing Evaluation

The principal candidates for the 250°F design were semi-rigid polyurethane foams. The purpose of the foam backing is to protect the missile nose cone from the shock caused by detonation of the pyrotechnic system and to absorb the impact caused by stones, sand, etc.

The criteria for selecting candidate materials were:

1. Temperature resistance
2. Solvent resistance
3. Compressive set
4. Flame retardant

Polyurethane foam formulations from several manufacturers were evaluated.

The same solvents were used on the foams as on the skin materials. Each solvent was brushed onto a foam sample and exposed to 250°F for 8 hours. None of the solvents showed any noticeable affect on the foams.

Compression set was used as the principal criteria for selecting the backing material. Compression set is the measure of a material to return to its original dimensions after exposure to environmental conditions. Specific conditions employed in these studies were placing the foam samples under a sustained load of 20 psi for 8 hours at 250°F. This loading duplicates the most severe loading in application due to aerodynamic pressure at the cap nose. A low compression set value was desirable so that if the protective cap were to receive impact from stones, sand, etc., the foam would absorb the impact and return to its original configuration; not leaving a deformed protective cap. From the results of this test, a urethane foam formulation was obtained which produced a compression set value of 10% under the above stated conditions. This was considered an exceptionally good foam.

Pyrotechnic Evaluation

The third component of the protective cap is the pyrotechnics, which consists of a detonator and linear shaped charges (LSC). The function of the detonator is to initiate the LSC and open up the nose of the cap. All of the cutting action comes from the LSC. The charge in both the detonator and LSC is cyclotrimethylenetrinitramine, or commonly known as RDX.

Linear shaped charges having 3 grains charge per foot and detonators containing 1.9 grains of charge were evaluated. Figure 2 shows the pyrotechnic system. The detonator will not fire under 0.5 amperes for 5 minutes, but 2 amperes will fire it instantaneously.

The detonators and LSC were tested for thermal and environmental pressure stability and cutting efficiency. Specimens were fabricated from skin and backing materials and from LSC as shown in Figure 3. The specimens were cycled from -40°F to +250°F to -40°F. Environmental pressure was maintained at approximately 1 lb/in^2 at temperatures between R.T. and 250°F. This pressure corresponds roughly to 60,000 feet of altitude. The pressure was allowed to return to normal (approximately 15 lbs/in^2) at temperatures between -40°F and R.T. Each complete cycle took approximately one hour. Specimens were fired at 250°F and -40°F after 1, 3, and 10 cycles. All of the detonators and LSC were successfully fired. The LSC cut all skin specimens cleanly. These tests showed that the 3 grain/ft. LSC has a sufficiently strong detonation wave to cut through 0.100 inch skin material and also maintains its stability at 250°F. As a result, the pyrotechnics used in these tests were selected for use in 250°F temperature protective cap.

Junction Block Evaluation

The junction block is the final component of the protective cap. It is located at the nose of the cap and its function is to securely hold the detonator and LSC in place and to assist in opening the skin at the nose to create aerodynamic turbulence.

Materials tested as junction block candidates were epoxy, phenolic, and Polymer 360 castings and rigid polyurethane foam. The candidates were formed into blocks and assembled so that the four of them made a square. A high powered detonator was inserted in the center so that each candidate was in contact with the side of the detonator. A polycarbonate sheet was secured over the assembly. The detonator was fired and the blocks examined for type and severity of fracture.

The rigid foam was destroyed completely but did nothing in the way of damaging the polycarbonate skin. The epoxy casting and Polymer 360 casting were successful in their own degree of fragmentation and in the destruction of the skin. As a result, the epoxy casting was arbitrarily chosen for this design.

Model Testing

Models of the protective cap were constructed and tested. The purpose of these tests was to determine the dispersion trajectory of the skins and foam. It was learned from these tests that the foam has to be pre-cut if it is to be blown free of the nose cone.
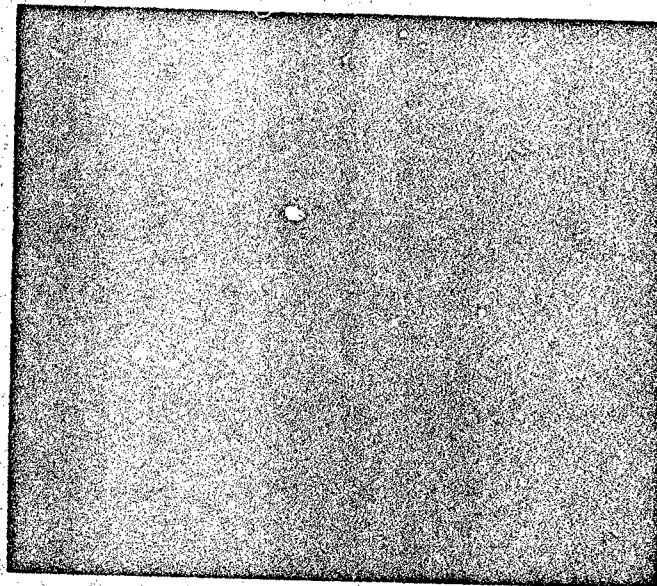
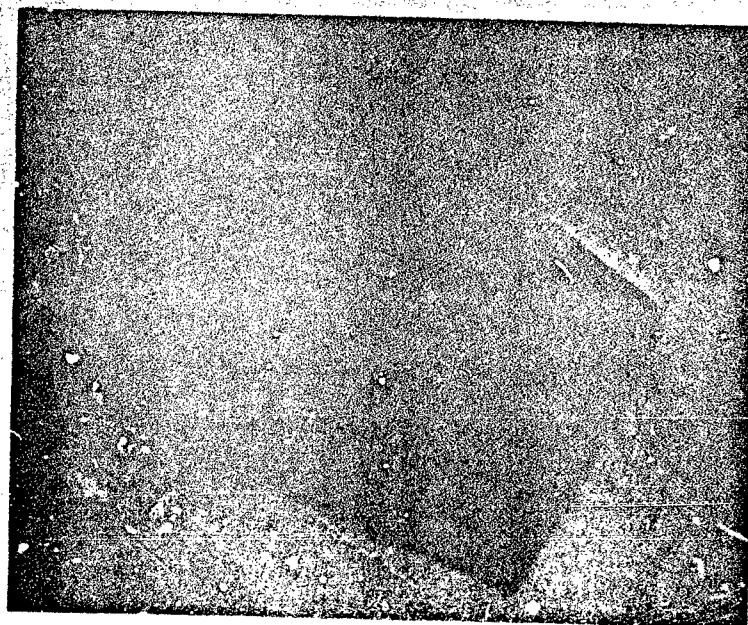Figure 2. Pyrotechnic System.

Figure 3. Pyrotechnic Test Specimen.

A preliminary radome and protective cap were selected and parts were fabricated. The overall length of the cap and radome was approximately 15 inches. This consists of a 3 inch cylindrical section and a 12 inch ogive section.

Two fiberglass reinforced epoxy radomes were fabricated along with polyurethane foam backings and cross-linked polyethylene skins. The skins, approximately 0.100 inches thick, were made by laminating in a female mold. A vacuum bag was applied to the lay-up and the assembly placed in an oven at 275°F for 24 hours. This fused the plies together and promoted cross-linking of the polymer.

Semi-rigid polyurethane foams were made using the polyethylene skin and glass reinforced radome as female and male molds, respectively. This provided a perfect fit between the radome, foam, and skin.

Figure 4 shows the protective cap and radome. At the left is the cross-linked polyethylene skin. The foam is in the center with the pyrotechnic system in place. The lead wires can also be seen running from the initiator down the side of the cap. The radome is shown on the right mounted on the attach ring. Figure 5 shows the assembled system.

The two radomes and protective caps were delivered to Holloman Air Force Base for rocket sled testing. Test runs were conducted at Mach 0.6 and Mach 1.5. The test velocity was sustained during nose cover ejection. High speed photography was used to study the break-up pattern of the covering and the size of the fragmented particles. Figure 6 shows the protective cap and the radome mounted on the rocket sled prior to testing.

Both tests were successful in that the protective covers were blown free of the nose cone with no damage occurring to the cones. The covers were fragmented into numerous pieces, all quite small in size. The LSC network cut through the CLPE skin and separated it from the rest of the system. The pre-cut foams were blown away by the aerodynamic turbulence.

Additional tests are being planned through a 6000 foot rain field prior to firing the cover at velocities of Mach 1.5.

CONCLUSIONS

A successful protective cap has been developed which will offer protection to missile nose cones against the various types of impact which may be encountered, but most important is the protection offered to the missile radomes during captive flight from rain erosion. The broadband performance required for ECM type missiles today indicate that low dielectric constant materials, which are susceptible to rain erosion, will be required for the best electrical performance. The protective cap can now eliminate the rain erosion problems during captive flight. Concepts such as the aerodynamics spike and/or thin ceramic rain erosion coatings can provide rain erosion protection to the radome for the short periods of time involved while it is performing its mission.
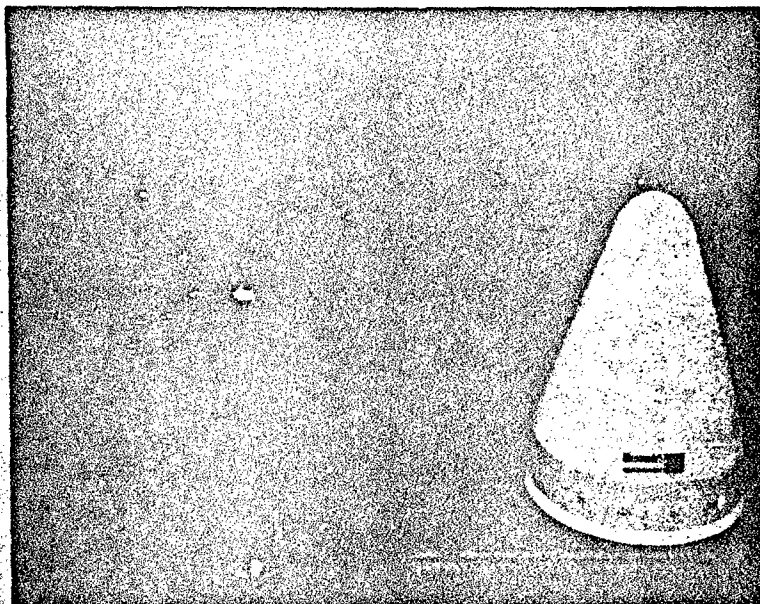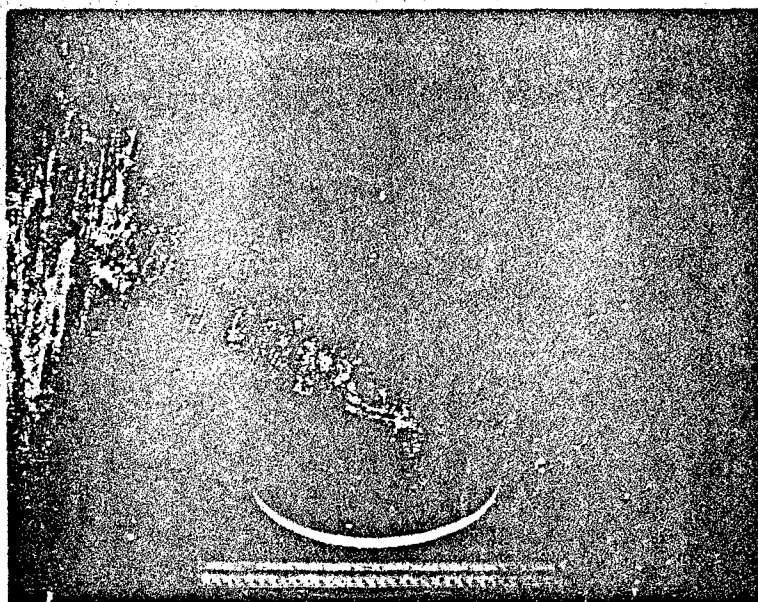
Figure 4. Disassembled Cap with Radome.
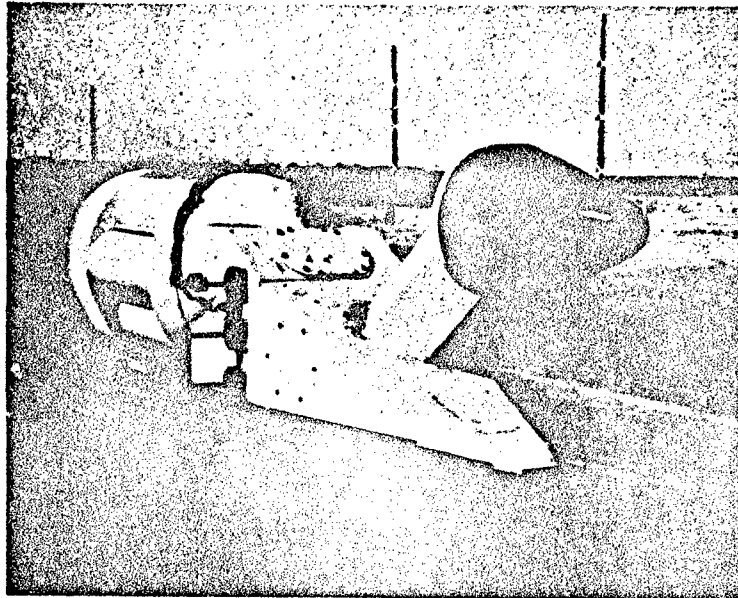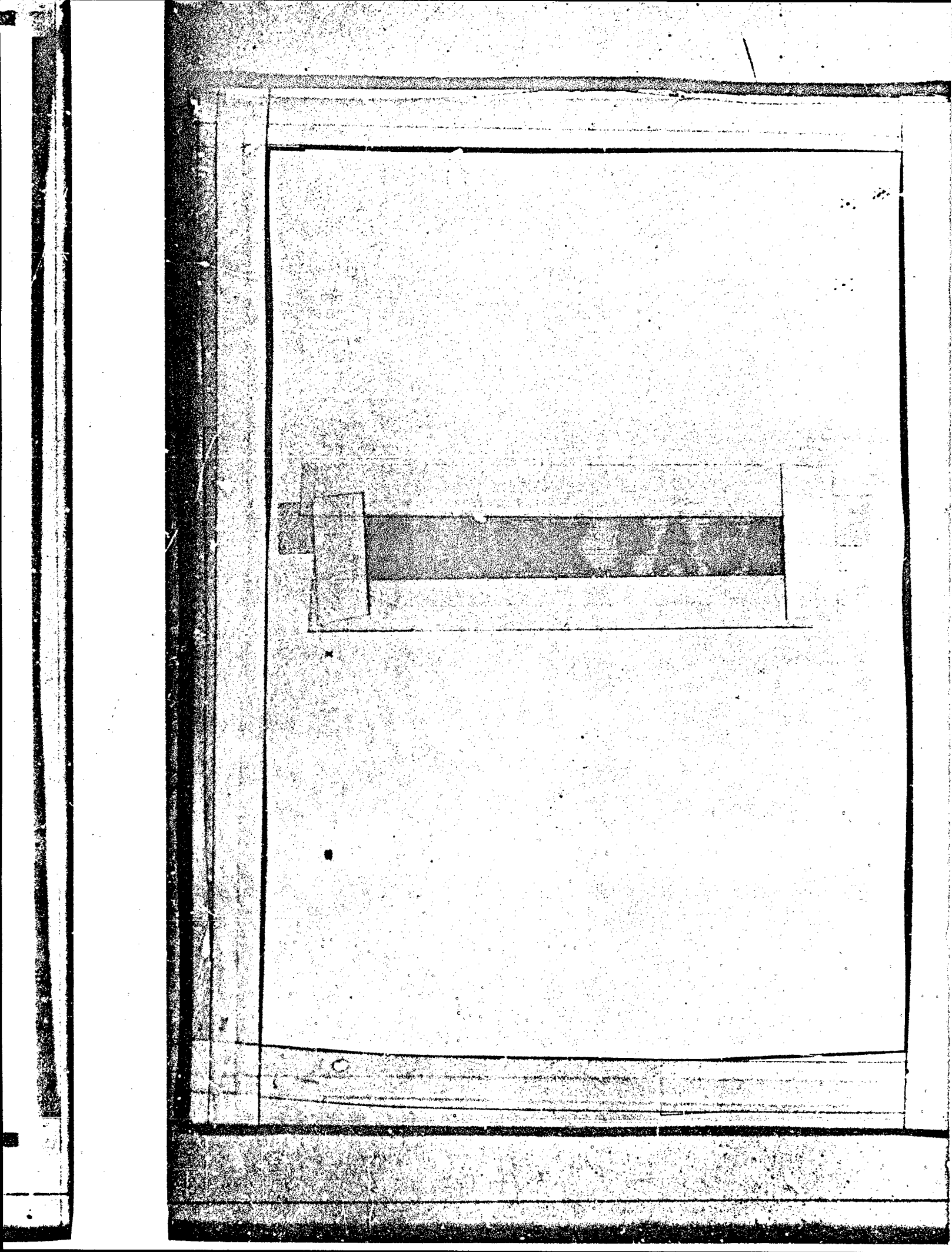

Figure 5. Assembled Cap on Radome.

Figure 6. Protective Cap on Rocket Sled.

DUAL MODE RADOME MATERIALS RESEARCH

S. C. Colburn
R. A. Miller

Pomona Division of General Dynamics
P. O. Box 2507
Pomona, Calif. 91766

ABSTRACT

This program was initiated to develop a radome/irdome material capable of operation in both radar (x-band) and infrared frequencies (1 - 5.5 microns).

Three types of materials -- single crystals, polycrystalline bodies, and glasses -- are discussed with regard to dual mode capabilities. Properties of specific materials within each classification are presented showing their limitations.

Criteria for the development of a glass for dual mode operation are presented. The most promising glass families are those containing germanium oxide as the glass forming constituent. This is based on the fact that the practical infrared cutoff of GeO_2 occurs in the range of 6 microns. Also, germania glasses can be formulated with relatively low thermal expansion.

Based on the criteria presented for developing low thermal expansion glasses with infrared transmittance to 5.5 microns, several glass compositions were melted. Compositional variations and the resulting effects on infrared transmittance and thermal expansion are presented. Compositional variations investigated include substituting MgO for BaO, varying the total alkali metal oxide content, and varying other constituent oxides such as TiO_2, ZrO_2 and Al_2O_3. Other properties of the glasses developed such as dielectric constant, loss tangent, and index of refraction are listed.

Silica and B_2O_3 were added to germania glasses in small quantities to show the detrimental effect on infrared transmittance and the helpful effects of lowering thermal expansion.

1. INTRODUCTION

The dual mode concept of a missile system capable of operating in both radar and infrared frequencies would make countermeasures very difficult. The radar would bring the missile close to the target and the infrared would do the final homing. This type of system would give greater target resolution and thus greater "kill potential". If the antennas and detectors are to be located together in the nose for this type of missile system, the use of material transparent to both R.F. and I.R. energy becomes necessary. The development of a

satisfactory radome/irdome material capable of fulfilling this need would provide a new impetus for designing new missile concepts. Most materials do not exhibit the properties required for both systems; thus there must be a compromise. The technology of radome materials is much more advanced than the technology of infrared domes. Unfortunately, materials now being used for radar will not transmit infrared energy so the concentration should be on locating infrared transmitting materials that will work for radar frequencies. It was decided to place the emphasis on developing glass compositions for dual mode purposes.

In formulating a glass for dual mode use, several factors must be considered simultaneously. These are the requirements for glass formation, the necessity of infrared transmittance from 1 to 6 microns, a low loss tangent at microwave frequencies and a low thermal expansion coefficient to impart good thermal shock resistance. When these desired features are considered independently, no difficulty is encountered. For example, a 100 percent silica glass has one of the lowest loss tangents and one of the lowest thermal expansion coefficients of glasses, and is a common material used for glass formation. However, the maximum infrared transmittance that can be expected of a silicate network is 4.5 microns. This is due to the absorption caused by the Si-O bond. Thus physical property trade-offs become necessary when selecting glass compositions. The water absorption band between 2.75 and 3 microns is an additional problem in developing a good infrared transparent glass.

2. MATERIALS CURRENTLY AVAILABLE FOR DUAL MODE USE

A literature search for materials for use in a dual mode capacity for both infrared and radar frequencies revealed that very little work has been done. Thus the majority of the search was concentrated on materials for infrared use.

Materials for infrared operation can be classified by useful wavelength regions, or by type of material. Three general wavelength regions are usually quoted for the military infrared. The terms that have been generally accepted are near, intermediate, and far. The near infrared region extends from a wavelength of 0.75 to about 2.7 microns, the intermediate region from 3 to 6 microns, and the far infrared region from 8 to 13 microns.

The three general types of materials that will be discussed are single crystal, polycrystalline bodies and glasses. There are many single crystal materials, both synthetic and natural, that are used for infrared instrumentation. Requirements that must be met for dual mode dome materials are high melting points, weather resistance, i.e., low degree of solubility in water, and desirable thermal, mechanical and electrical properties. Using these criteria, the search for single crystal materials was narrowed to sapphire, spinel, magnesium oxide and magnesium fluoride. Table 1 and Figure 1 present the dielectric constant, IR transmittance and size limitation of these materials.

110
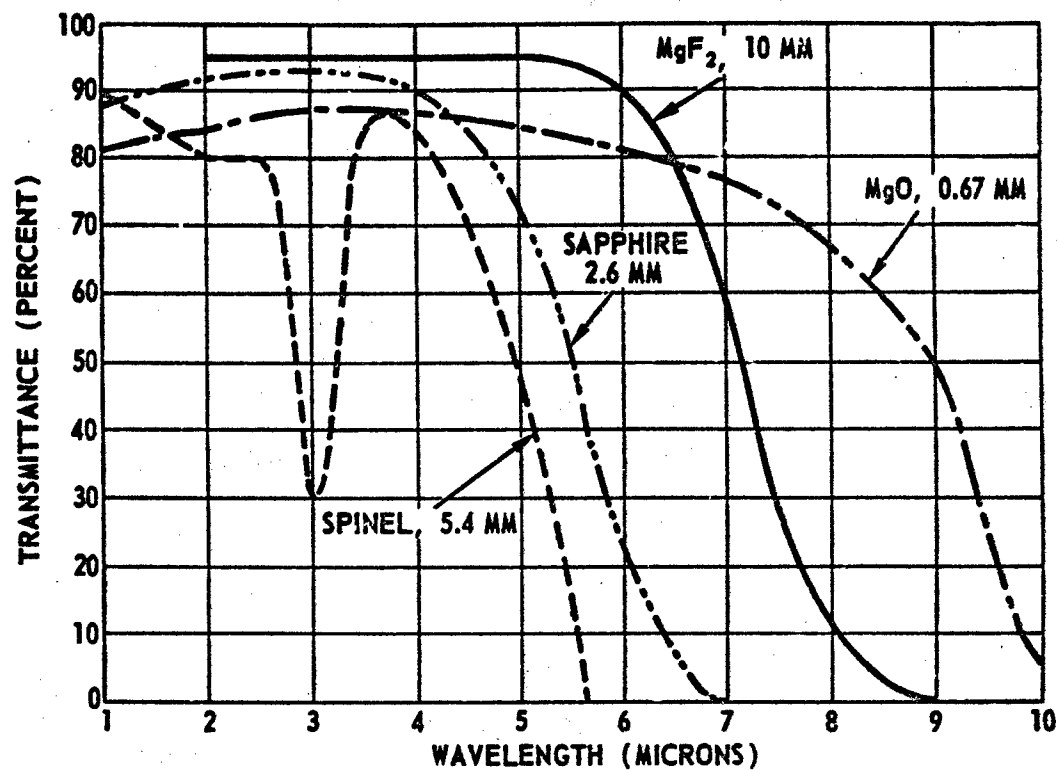
Figure 1. Transmittance of Single Crystals

111

MATERIAL	DIELECTRIC CONSTANT	FREQUENCY (CPS)	TRANSMISSION (μ)	SIZE LIMIT DOMES (DIA.)
SAPPHIRE (Al_2O_3)	10.55^P 8.6^A	$10^2 - 10^8$ $10^2 - 10^{10}$	$0.17 - 6.5$	3 INCHES
SPINEL ($MgO.3.5Al_2O_3$)	8 TO 9		$0.9 - 6.0$	
MAGNESIUM OXIDE (MgO)	9.5	10^{10}	$0.25 - 8.5$	1 INCH
MAGNESIUM FLUORIDE (MgF_2)	4.87^P 5.45^A	$10^5 - 10^7$	$0.11 - 7.5$	1 INCH

P — MEASURED PARALLEL TO C-AXIS
A — MEASURED PERPENDICULAR TO C-AXIS

Table 1. Single Crystal Materials for Dual Mode Operation

112

The two main limitations of the single crystal materials are size and cost. Laboratories throughout the country have been attempting to grow large single crystals of most of these materials. The Harshaw Chemical Company indicates that they are currently working on producing single crystals of magnesium fluoride 3 inches in diameter, approximately 1-3/4 inches tall.[1] The Linde Air Products Company manufacturers sapphire blanks that are large enough for 3 inch diameter domes and hemispheres. Their aim is to be able to make 6 inch diameter hemispheres. Price lists available for these materials show their cost to be extremely high, even for the small sizes presently available. Even if the state-of-the-art of crystal growing were to be improved so that larger crystals became available, it is highly unlikely that the cost could ever be justified. Improvements of both polycrystalline materials and glasses have been made recently which provides materials as good as the single crystals but at much lower cost.

The development of hot pressing and pressing and sintering polycrystalline materials to dense compacts has expanded the range of materials available. Of the materials reported, aluminum oxide, magnesium oxide, zinc sulfide, and zinc selenide can be considered candidates for dual mode operation.

Hot pressed polycrystalline magnesium fluoride is available commercially from Eastman Kodak Company (Irtran I) and Bausch and Lomb, Inc. (IR-51). Magnesium fluoride has a useful IR transmittance range from 0.45 to 9.2 microns and a relatively low dielectric constant of 5.1. Eastman Kodak Irtran II, a pressed and sintered zinc sulfide, has a long wavelength limit of 14.5 microns with a dielectric constant of 8.0. Another development of Eastman Kodak Company is hot pressed zinc selenide. This material was developed under Air Force contract and extends the useful IR transmittance range to 20 microns. No data is available on dielectric constant of this material.

General Electric Company has developed and patented transparent aluminum oxide that looks very good for the near and intermediate IR ranges, having good transmittance to 6 microns. Coors also has a transparent aluminum oxide. Transmittance curves for the polycrystalline materials appear in Figure 2 and properties are tabulated in Table 2.

Glasses can be classified as either oxide or non-oxide glasses. Extensive work has been carried out in the past few years in extending the useful infrared range to 15 or more microns. These studies have concentrated on the non-oxide forming glasses with one or more components from the chalcogen group (S, Se or Te).

There are several reasons why the non-oxide glasses are not useable for dual mode domes. In general, the softening points of these glasses range from 90 to 450°C. For most of today's high speed missile systems, these temperature limits are exceeded. One of the required features of a material for dual mode operation is

113
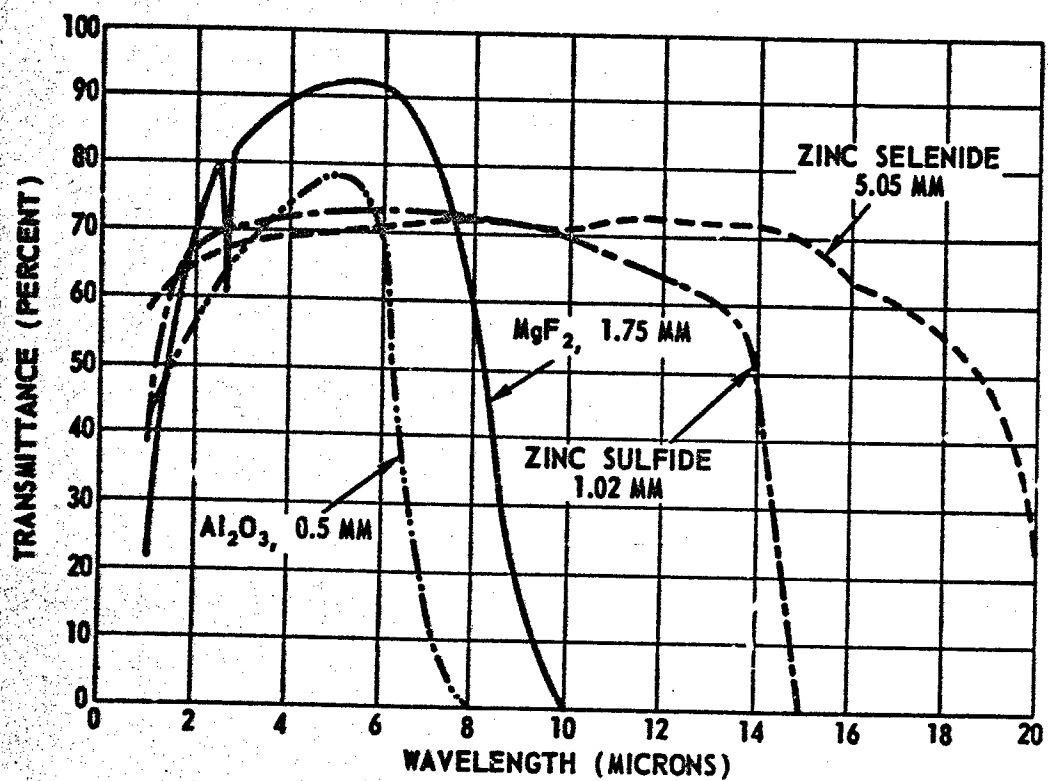
Figure 2. Transmittance of Polycrystalline Materials

PROPERTIES	MAGNESIUM FLUORIDE	ZINC SULFIDE	ZINC SELENIDE
DENSITY GM/CC	3.18	4.088	5.267
KNOOP HARDNESS (100 G)	576	354	150
MODULUS OF RUPTURE (PSI)	21,800	14,100	6,700
MODULUS OF ELASTICITY (X 10^6 PSI)	16.6	14	11.5
POISSON'S RATIO	0.30		
EXPANSION COEFFICIENT IN/IN/°F X 10^{-6}, RT TO 600°F	6.4	4.2	4.3
DIELECTRIC CONSTANT			
1 MC			
900 MC	5.1		
1100 MC	5.1		
8600 MC		8.0	
LOSS TANGENT			
1 MC			
900 MC	0.0010		
1100 MC	0.0010		
8600 MC			
REFRACTIVE INDEX			
0.486μ			2.786
0.656μ			2.578
1.014μ	1.378	2.290	2.491
1.590μ		2.269	
2.153μ	1.371	2.262	2.446
6.238μ	1.312	2.236	2.426

Table 2. Properties of Polycrystalline Materials for Dual Mode Operation

low thermal expansion to provide good thermal shock resistance.
The non-oxide glasses have expansion coefficients ranging from
90 to 360 X 10^{-7} in/in/°C. Because of their poor thermal properties
for dual mode purposes, infrared transmittance curves for non-oxide
glasses are not presented in this paper.

Figure 3 compares the transmittance of a number of commercial
infrared glasses and Table 3 compares the properties. Fused silica
as prepared by General Electric[4] has a wavelength limit of 4 microns.
This is to be considered one of the best choices for dual mode use
in the near infrared region. It has the best thermal shock character-
istics of any material, due primarily to its extremely low thermal
expansion. The dielectric constant and loss tangent changes very
little up to 2000°F. The main limitation is the infrared wavelength
cutoff. Corning Code 9753 silicate glass extends the transmittance
range to 4.5 microns. This is about the best that can be achieved
with a silicate system. Improvements can be made by replacing silicon
with a larger network forming cation or one of lower field strength.
Also shown in Figure 3 and Table 3 are the properties of non-silicate
glasses. Corning Code 9754 is a new germanate glass. It has some
outstanding advantages over other silica-free glasses. As can be
seen from the transmittance curve, it is free of the typical water
absorption between 2.7 and 3.0 microns, and can be made without
the use of expensive vacuum procedures. It has the lowest expansion
of the non-silicate glasses. One other non-silicate glass of interest
for dual mode purposes is the calcium aluminate glass. It has a
larger transmittance range than does the germanate glasses, but shows
the typical water absorption at 2.7 microns. The thermal expansion
is a little higher, and it is less weather resistant. The limiting
factor in improving the properties of the calcium aluminate glasses
is the fact that they have a narrow composition range in the vicinity
of $12CaO \cdot 7Al_2O_3$ and they tend to be unstable.

The cost and size limitation of single crystal materials as
noted above eliminate their consideration for dual mode operation.
Even though the hot pressed polycrystalline materials exhibit pro-
perties that are amenable to dual mode purposes, it was decided to
investigate the low expansion germanate glasses. It is believed that
the most promise for the best possible material lies in this area.

3.   CONSIDERATION FOR DEVELOPING DUAL MODE GLASS COMPOSITIONS

One of the primary goals is to achieve at least 80 percent
infrared transmittance from 1 to 5.5 microns. Since the majority of
targets for missiles with dual mode capabilities will be hot, a large
portion of the emitted energy from the target will be in that range.
The refractive index of glasses generally range from 1.3 to about 1.8.
One disadvantage of a high index of refraction is that infrared
reflection losses are increased. This problem can be alleviated
somewhat by coating the dome with an anti-reflection coating having
an index of refraction equal to the square root of the substrate index.
Also desirable is a small change in index of refraction with wavelength
(dispersion). The dielectric constant and loss tangent should be as
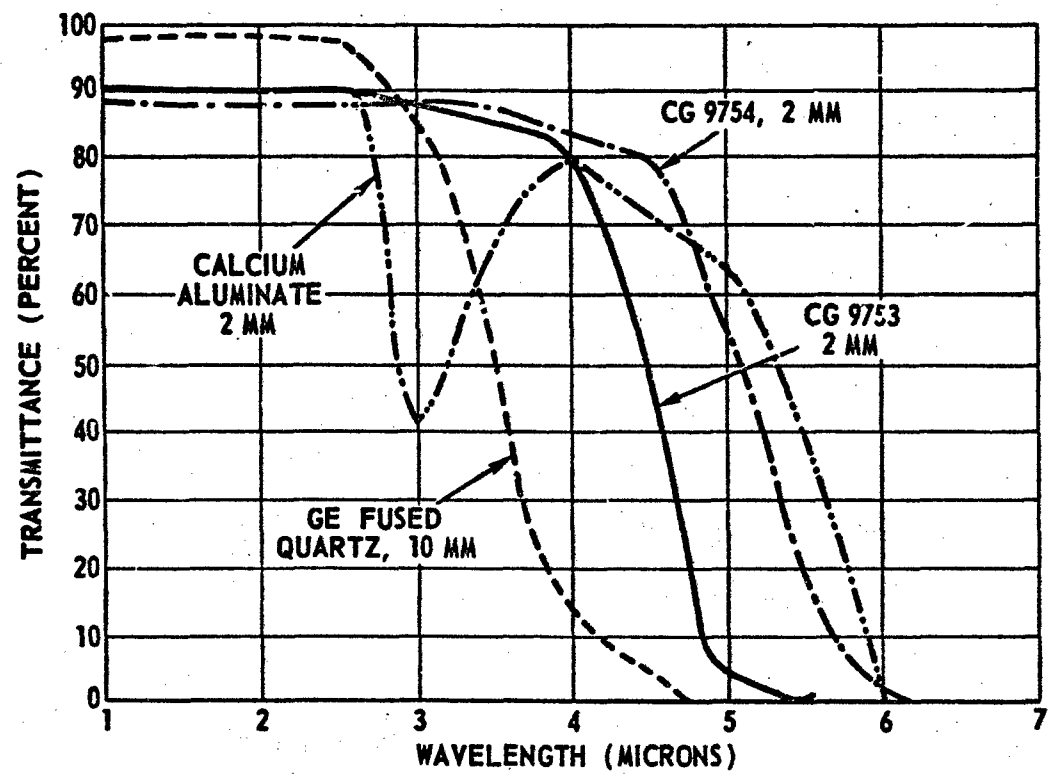
Figure 3. Transmittance of Selected Glasses

PROPERTIES	FUSED SILICA	CORNING CODE 9753	CORNING CODE 9754	CALCIUM ALUMINATE
DENSITY GM/CC	2.2	2.8	3.35	2.9
KNOOP HARDNESS (100 G)	640	658	560	600
MODULUS OF RUPTURE (PSI)	8,000	8,000	7,240	
MODULUS OF ELASTICITY (X 10^6 PSI)	10.4	14.3	13.6	15.2
POISSON'S RATIO	0.16	0.28	0.29	0.287
EXPANSION COEFFICIENT IN/IN/°C X 10^{-6} RT – 300°C	0.54	5.95	6.36	8.3
DIELECTRIC CONSTANT				
1 MC	3.8	8.87	10	
900 MC	3.8			
1100 MC	3.8			
8600 MC	3.8	8.27		9.6
LOSS TANGENT				
1 MC	0.0004	0.0025	0.0014	
900 MC				
1100 MC				
8600 MC	0.0002	0.0110		
REFRACTIVE INDEX				
0.486μ		1.613	1.670	
0.656μ		1.602	1.656	
1.014μ				
1.590μ	1.458	1.605		1.669
2.153μ			1.628	
3.500μ			1.615	

Table 3. Properties of Glasses for Dual Mode Operation

low as possible. A low dielectric constant will reduce RF reflection losses and enable a thicker mechanical wall to withstand higher mechanical and thermal stresses. Another goal is to have as low a thermal expansion as possible to resist thermal stresses due to aerodynamic heating. To achieve these goals or to approach them, several tradeoffs have to be made.

One of the most important considerations in the development of a dual mode material is the IR transmittance. For the purpose intended, a transmittance of 80 percent from 1 to 5.5 microns is desired.

The absorption of infrared energy in glasses depends on atomic vibrations[5] and is expressed by the formula:

$$\nu \propto \sqrt{\frac{f}{\mu}}$$

where

ν = frequency   (1)

f = force constant between ions

μ = reduced mass

For absorption to occur at lower frequency or longer wavelength, the mass of the ions should be high, and attractive forces between the ions should be low. Although this is an oversimplification, mass and bond strength can be used to allow a rough prediction of certain elements on infrared absorption.

Table 4 shows the fundamental absorption wavelengths for several oxides. The actual transmittance limit for oxide glasses in ordinary thicknesses is determined by absorption in the first overtone region which places the practical limit at 3.4 to 7.5 microns.

Silica and B_2O_3 are the most common glass forming oxides used in glass formulations. However, the Si-O bond causes a large cutoff absorption centering around 5 microns. For this reason most silicate glasses have a useful IR transmittance of only 4.5 microns. The practical limit for B_2O_3 glasses is somewhat lower, hence it is not considered for IR glass formulations. Tellurium oxide and antimony oxide networks would give the best transmittance of the glass formers when considering only the fundamental absorption wavelength. However, the glass forming ability of antimony oxide is rather limited, and the glasses are not very stable. Both tellurium oxide and antimony oxide glasses have poor thermal shock characteristics and poor chemical durability. Germanium oxide has better infrared transmittance properties than SiO_2 and B_2O_3, but not as good as TeO_2 and Sb_2O_3. The thermal and chemical properties of GeO_2 glasses are superior to TeO_2 and Sb_2O_3. Germanium oxide glass, thus, was chosen for extensive investigation to meet the requirements of a dual mode material.

	OXIDE	WAVELENGTH (MICRONS)
GLASS FORMERS	B_2O_3	7 – 8
	SiO_2	9
	V_2O_3	10.5
	GeO_2	11.2
	SeO_2	11.5
	WO_3	11.5
	As_2O_3	12.5
	Sb_2O_3	13.5
	TeO_2	13.5
INTERMEDIATES	BeO	11 – 14
	Al_2O_3	13.5
	ZnO	22
MODIFIERS	Li_2O	7
	Na_2O	8
	MgO	14.5
	CaO	22
	PbO	31
IMPURITIES	FeO	1 – 1.1
	H_2O	2.7 – 3.0

Table 4. Fundamental Absorption Wavelengths of Oxides

One disadvantage of most glasses for high speed missile applications has been poor thermal shock resistance. Several authors have developed expressions rating the relative thermal shock resistance of ceramic materials. Most of these equations use only material properties without regard to environment. Manson (Ref. 6) developed an expression relating the temperature differential through which a material can be quenched with the environment. The expression is:

$$T_O, \max = \left[\frac{\sigma (1 - \mu)}{E \alpha} \right] \left[(1.5 + 3.25 \frac{1}{\beta} - 0.5 e^{-16/\beta} \right] \quad (2)$$

where:

$T_O, \max$ = Initial temperature less temperature of the medium in which it is immersed (assumed to be zero)

σ = strength
μ = Poisson's ratio
E = Modulus of elasticity
α = Thermal expansion coefficient
β = Biot's modulus

and: $\beta = \frac{ah}{k}$

where:
a = One-half the thickness of material
h = Heat transfer coefficient
k = Thermal conductivity.

The most effective means of increasing $T_O, \max$, i.e., improving thermal shock resistance, is lowering the thermal expansion coefficient. Several investigators have correlated the relationship that exists between thermal expansion and chemical composition of glasses. The earliest efforts were those of Winkelmann and Schott in the 1890's, who developed a set of expansion factors to calculate thermal expansion from the glass formula weight.

The expression $3\alpha = a_1 p_1 + a_2 p_2 + - - - a_n p_n$ (3)

where:
3α = Cubical thermal expansion coefficient
a = Expansion Factor which is constant for each component
p = Weight percent of component.

as developed assumes a linear relationship. Several investigators have developed their own expansion factors, most of which are for special compositions[7][8][9][10]. Table 5 lists expansion factors proposed by different investigators. The work by English and Turner was accomplished with silicate glasses, but was found to be the most appropriate for the

121

COMPOSITION	M & H IN/IN/°C X 10⁻⁷	W & S IN/IN/°C X 10⁻⁷	E & T IN/IN/°C X 10⁻⁷	S IN/IN/°C X 10⁻⁷
SiO_2	0.8	0.8	0.15	0.84
Al_2O_3	5.0	5.0	0.42	0.72
B_2O_3	0.1	0.1	−1.98	−1.80
Na_2O	10.0	10.0	12.96	11.58
K_2O	8.5	8.5	11.7	9.6
PbO	4.2	3.0	3.18	
ZnO	2.1	1.8	2.1	
CaO	5.0	5.0	4.89	4.08
MgO	0.1	0.1	1.35	2.19
BaO	3.0	3.0	4.2	3.24
As_2O_5	2.0	2.0		
P_2O_5	2.0	2.0		
TiO_2	4.1			
ZrO_2	2.1	2.1		
Li_2O				19.68

Table 5. Factors for Calculating Cubical Thermal Expansion of Glasses

germanate glasses in this program. From the factors presented in Table 5, it can be seen that the alkali content, i.e., K_2O and Na_2O, should be as low as feasible to achieve a low thermal expansion. Silica and B_2O_3, previously mentioned as producing a negative effect on infrared transmission, would impart the lowest expansion.

Alkali ions in glasses give rise to high dielectric losses, which increase as the number of ions present increases. This has been explained by Navias and Green[11] to be the result of modifications of the continuous atomic networks of the glass formers by the additional oxides. Alkali ions produce gaps in the continuous random network. The Na——O bond is relatively weak, and the oxygen atoms adjacent to each alkali ion are essentially single bonded. The net effect is that the alkali ions are weakly held in the interstices of the glassy network. In a high frequency field these ions are easily set into motion and consequently absorb energy giving rise to dielectric losses.

Barium oxide and the other alkaline earth oxides, like the alkali oxides, result in breaks in the previously continuous network. The divalent charges and their large ionic diameters secure them more firmly than the alkali ions to the adjacent atoms, causing them to be less mobile. Ionic radii are listed in Table 6 for reference. Rinehart and Bonino[12] pointed out that some oxides such as Al_2O_3 when added in small amounts to simple glass compositions reduced losses, but in larger quantities increases losses. These investigators and others have concluded that as a general rule, increasing the number of elements in the R_2O and RO groups tends to decrease the dielectric losses.

4. EXPERIMENTAL GLASS FORMULATIONS

Florence[13], Kreidl[14] and Nielsen[15] have investigated various glass compositions containing germanium oxide. Based on the criteria presented for selecting a glass composition to meet dual mode purposes, it was decided to use Kreidl's composition 1A6235 as a starting point. Kreidl's Composition 1A6235 was slightly modified and re-designated GD 3471. Compositions investigated are listed in Table 7. All glasses were melted in platinum crucibles in an electric furnace at 2200°F to 2800°F. The melted glasses were fined for 3 hours and poured into desired shapes for property measurements and cooled slowly for annealing.

A summary of the measured properties appears in Table 8. The calculated thermal expansion coefficients listed were calculated using E & T factors. The measured thermal expansion coefficients were run on an Orton Automatic Recording Dilatometer. The index of refraction measurements were made by two methods, per ASTM D542-50. The dielectric constant and loss tangents were measured by Delsen Testing Laboratory, Glendale, California. The composition variables are listed on the same table to facilitate comparison of property changes.

123

Å	Å	Å	Å
Li^+ 0.60	Be^{+2} 0.31	Al^{+3} 0.50	B^{+3} 0.20
Na^+ 0.95	Mg^{+2} 0.65	Cr^{+3} 0.69	Si^{+4} 0.41
K^+ 1.33	Ca^{+2} 0.99	Ti^{+4} 0.68	Ge^{+4} 0.53
	Sr^{+2} 1.13	Zr^{+4} 0.80	O^{-2} 1.40
	Ba^{+2} 1.35	Ta^{+5} 0.73	
	Zn^{+2} 0.74		
	Pb^{+2} 1.20		

Table 6. Ionic Radii

SAMPLE NO.	GeO$_2$	SiO$_2$	B$_2$O$_3$	K$_2$O	Na$_2$O	CaO	PbO	BaO	ZrO	Al$_2$O$_3$	TiO$_2$	ZrO$_2$	MgO
GD 3471	54.0	0	0	12.0	4.0	3.0	0	11.0	10.0	0	4.0	2.0	0
GD 3472	64.2	0	0	0	0	3.6	0	13.1	11.9	0	4.3	2.4	0
GD 3473	58.6	0	0	6.5	2.2	3.3	0	12.0	10.9	0	4.3	2.2	0
GD 3474	58.6	0	0	6.5	2.2	3.3	0	10.9	10.9	0	4.3	2.2	1.1
GD 3475	58.6	0	0	6.5	2.2	3.3	0	9.8	10.9	0	4.3	2.2	2.2
GD 3476	58.6	0	0	6.5	2.2	3.3	0	8.7	10.9	0	4.5	2.2	3.3
GD 3477	58.6	0	0	6.5	2.2	3.3	0	7.6	10.9	0	4.3	2.2	4.4
GD 3478	58.6	0	0	6.5	2.2	3.3	0	6.5	10.9	0	4.3	2.2	5.5
GD 3479	58.6	0	0	6.5	2.2	3.3	0	5.5	10.9	0	4.3	2.2	6.5
GD 3480	58.6	0	0	6.5	2.2	3.3	0	4.4	10.9	0	4.3	2.2	7.6
GD 3481	58.6	0	0	6.5	2.2	3.3	0	3.3	10.9	0	4.3	2.2	8.7
GD 3482	58.6	0	0	6.5	2.2	3.3	0	2.2	10.9	0	4.7	2.2	9.8
GD 3483	58.6	0	0	6.5	2.2	3.3	0	1.1	10.9	0	4.3	2.2	10.9
GD 3484	58.6	0	0	6.5	2.2	3.3	0	0	10.9	0	4.3	2.2	12.0
GD 3485	59.0	0	0	2.0	2.0	8.0	0	0	11.0	0	4.0	2.0	12.0
GD 3486	59.0	0	0	1.0	1.0	10.0	0	0	11.0	0	4.0	2.0	12.0
GD 3487	59.0	0	0	0.5	0.5	11.0	0	0	11.0	0	4.0	2.0	12.0
GD 3488	61.0	0	0	1.0	1.0	6.0	0	2.0	11.0	0	4.0	2.0	12.0

Table 7. Compositions of Germanate Glasses, Mole Percent. (Sheet 1 of 2)

125a

Table 7. Compositions of Germanate Glasses, Mole Percent. (Sheet 2 of 2)

SAMPLE NO.	GeO₂	SiO₂	B₂O₃	K₂O	Na₂O	CaO	PbO	BaO	ZnO	Al₂O₃	TiO₂	ZrO₂	MgO
GD 3489	59	0	0	1.0	1.0	6.0	2.0	2.0	11.0	0	4.0	2.0	12.0
GD 3490	57	0	0	1.0	1.0	6.0	4.0	2.0	11.0	0	4.0	2.0	12.0
GD 3491	55	0	0	1.0	1.0	6.0	6.0	2.0	11.0	0	4.0	2.0	12.0
GD 3492	59	0	2.0	1.0	1.0	6.0	0	2.0	11.0	0	4.0	2.0	12.0
GD 3493	57	0	4.0	1.0	1.0	6.0	0	2.0	11.0	0	4.0	2.0	12.0
GD 3494	55	0	6.0	1.0	1.0	6.0	0	2.0	11.0	0	4.0	2.0	12.0
GD 3495	59	0	0	1.0	1.0	6.0	2.0	2.0	11.0	6.0	0	0	12.0
GD 3496	59	0	0	1.0	1.0	6.0	2.0	2.0	11.0	3.0	3.0	0	12.0
GD 3497	59	0	0	1.0	1.0	6.0	2.0	2.0	11.0	0	6.0	0	12.0
GD 3498	59	0	0	1.0	1.0	2.0	2.0	2.0	11.0	10.0	0	0	12.0
GD 3499	59	0	0	1.0	1.0	2.0	2.0	2.0	11.0	5.0	0	5.0	12.0
GD 3500	59	0	0	1.0	1.0	2.0	2.0	2.0	11.0	0	0	10.0	12.0
GD 3501	72	0	0	1.0	1.0	6.0	0	2.0	0	0	4.0	2.0	12.0
GD 3502	70	0	0	1.0	1.0	6.0	0	2.0	2.0	0	4.0	2.0	12.0
GD 3503	66	0	0	1.0	1.0	6.0	0	2.0	6.0	0	4.0	2.0	12.0
GD 3504	59	2.0	0	1.0	1.0	6.0	0	2.0	11.0	0	4.0	2.0	12.0
GD 3505	57	4.0	0	1.0	1.0	6.0	0	2.0	11.0	0	4.0	2.0	12.0
GD 3506	55	6.0	0	1.0	1.0	6.0	0	2.0	11.0	0	4.0	2.0	12.0

COMPOSITION NUMBER	CALCULATED THERMAL EXPANSION COEFFICIENT $\times 10^{-7}$ IN/IN/°C RT–300°C	MEASURED THERMAL EXPANSION COEFFICIENT $\times 10^{-7}$ IN/IN/°C RT–300°C	INDEX OF REFRACTION	DIELECTRIC CONSTANT 9 375 MC	LOSS TANGENT 9 375 MC	COMPOSITION VARIABLE MOLE PERCENT
GD 3471	114.3	–	1.6612	–	–	12.0 K_2O; 4.0 Na_2O
GD 3472	70.5	–	1.6730	–	–	0 K_2O; 0 Na_2O
GD 3473	94.0	92.4	1.6620	9.4	0.0064	6.5 K_2O; 2.2 Na_2O
GD 3474	93.0	89.1	1.6658	–	–	10.9 BaO; 1.1 MgO
GD 3475	92.1		–	–	–	9.8 BaO; 2.2 MgO
GD 3476	91.1		1.71+	–	–	8.7 BaO; 3.3 MgO
GD 3477	90.0		1.71+	–	–	7.6 BaO; 4.4 MgO
GD 3478	89.0		1.71+	–	–	6.5 BaO; 5.5 MgO
GD 3479	87.9		1.71+	–	–	5.5 BaO; 6.5 MgO
GD 3480	86.7		1.7090	–	–	4.4 BaO; 7.6 MgO
GD 3481	85.7	85.9	1.7084	–	–	3.3 BaO; 8.7 MgO
GD 3482	84.4		–	–	–	2.2 BaO; 9.8 MgO
GD 3483	83.3		–	–	–	1.1 BaO;10.9 MgO
GD 3484	82.0	83.3	1.7020	–	–	0 BaO;12.0 MgO

SAMPLES THROUGH GD 3484 RUN BY
ASTM D542-50; REFRACTOMETRIC METHOD, BEYOND GD 3484 BY
ASTM D542-50; MICROSCOPIC METHOD

COMPOSITION NUMBER	CALCULATED THERMAL EXPANSION COEFFICIENT $\times 10^{-7}$ IN/IN/°C RT-300°C	MEASURED THERMAL EXPANSION COEFFICIENT $\times 10^{-7}$ IN/IN/°C RT-300°C	INDEX OF REFRACTION	DIELECTRIC CONSTANT 9375 MC	LOSS TANGENT 9375 MC	COMPOSITION VARIABLE MOLE PERCENT
GD 3485	69.2	68.2	1.762	8.79	0.008	2.0 K_2O; 2.0 Na_2O; 8.0 CaO
GD 3486	64.4	68.4	1.732	8.72	0.008	1.0 K_2O; 1.0 Na_2O;10.0 CaO
GD 3487	62.0	56.2	1.779	9.47	0.008	0.5 K_2O; 0.5 Na_2O;11.0 CaO
GD 3488	64.1	64.8	1.744	9.06	0.008	0 PbO; 61 GeO_2
GD 3489	66.5	70.5	1.744	9.48	0.007	2 PbO; 59 GeO_2
GD 3490	68.8	72.7	1.763	10.17	0.008	4 PbO; 57 GeO_2
GD 3491	70.9	74.5	1.730	10.55	0.008	6 PbO; 55 GeO_2
GD 3488	64.1	64.8	1.744	-	-	0 B_2O_3; 61 GeO_2
GD 3492	62.5	63.8	1.747	-	-	2 B_2O_3; 59 GeO_2
GD 3493	60.9	65.8	1.745	-	-	4 B_2O_3; 57 GeO_2
GD 3494	59.2	61.1	1.736	-	-	6 B_2O_3; 55 GeO_2

SAMPLES THROUGH GD 3484 RUN B''
ASTM D542-50; REFRACTOMETRIC METHOD, BEYOND GD 3484 BY
ASTM D542-50; MICROSCOPIC METHOD

COMPOSITION NUMBER	CALCULATED THERMAL EXPANSION COEFFICIENT x10^{-7} IN/IN/°C RT-300°C	MEASURED THERMAL EXPANSION COEFFICIENT x10^{-7} IN/IN/°C RT-300°C	INDEX OF REFRACTION	DIELECTRIC CONSTANT 9 375 MC	LOSS TANGENT 9 375 MC	COMPOSITION VARIABLE MOLE PERCENT
GD 3495	62.9	66.1	1.669	8.38	0.008	6 Al$_2$O$_3$; 0 TiO$_2$
GD 3496	65.6	66.7	1.717	8.91	0.008	3 Al$_2$O$_3$; 3 TiO$_2$
GD 3497	68.4	75.6	1.796	9.95	0.008	0 Al$_2$O$_3$; 6 TiO$_2$
GD 3498	58.5	64.2	1.669	8.08	0.009	10 Al$_2$O$_3$; 0 ZrO$_2$
GD 3499	58.6	61.2	1.682	8.82	0.009	5 Al$_2$O$_3$; 5 ZrO$_2$
GD 3500	58.6	-				0 Al$_2$O$_3$; 10 ZrO$_2$
GD 3501	61.5	60.7	1.704	8.36	0.007	0 ZnO; 72 GeO$_2$
GD 3502	61.9	68.4	1.724	-	-	2 ZnO; 70 GeO$_2$
GD 3503	62.9	69.4	1.740	8.84	0.008	6 ZnO; 66 GeO$_2$
GD 3488	64.1	64.8	1.744	9.06	0.008	11 ZnO; 61 GeO$_2$
GD 3488	64.1	64.8	1.744	-	-	0 SiO$_2$; 61 GeO$_2$
GD 3504	63.8	62.2	1.737	-	-	2 SiO$_2$; 59 GeO$_2$
GD 3505	63.4	69.8	1.733	-	-	4 SiO$_2$; 57 GeO$_2$
GD 3506	62.9	64.6	1.729	-	-	6 SiO$_2$; 55 GeO$_2$

SAMPLES THROUGH GD 3484 RUN BY
ASTM D542-50; REFRACTOMETRIC METHOD, BEYOND GD 3484 BY
ASTM D542-50; MICROSCOPIC METHOD

BLANK PAGE

The first three glasses show the effect of lowering the alkali content. GD3471 has a total of 16 mole percent, GD 3473 has 8.7 percent and GD 3472 has no alkali. The calculated thermal expansion coefficient was reduced from 114.3 X 10⁻⁷ in/in/°C to 70.5 X 10-7 in/in/°C. The one measured value for this series, GD 3473, was 92.4 X 10-7 in/in/°C versus 94.0 for the calculated value. Figure 4 shows the infrared transmittance of glasses GD 3471 to GD 3473. The large absorption at three microns is due to the oxygen-hydrogen bond vibrations from water in the glass. As the alkali content is increased the low point of the absorption band is shifted to a longer wavelength. This shift has been noted by other investigators and has been attributed to an increased amount of modifier. The apparent longer wavelength cutoff beyond 5 microns for the samples with the largest alkali content is thought to be caused by the sample thickness only, and not the alkali variation.

Samples GD 3474 through GD 3484 have increasing amounts of MgO substituted for BaO. The measured thermal expansion coefficient is reduced from 89.2 X 10⁻⁷ in/in/°C to 83.3 X 10-7 in/in/°C. This corresponds very well with the predicted expansion coefficients. The index of refraction increases to a maximum of 1.71⁺ (limit of Abbe refractometer used for these measurements) at an equal mole percentage of BaO and MgO and decreases as more MgO is added. No dielectric constant measurements were made for this series of glasses. The effect of substituting MgO for BaO on the infrared transmittance is shown in Figure 5. Little differences in IR transmittance were noted. The intensity of the transmittance increases slightly with increasing MgO until an equal mole ratio of MgO and BaO is reached. Additional MgO substitution for BaO shows a slight decrease in the intensity of the IR transmittance. These slight changes in transmittance are significant only to the extent of backing up previous investigators who have noted that IR transmittance is improved by complicating the glass structure by including more than one member of the RO and R₂O groups.

Figure 6 shows several infrared transmittance curves of GD 3485 demonstrating the effect of heat treatment and sample thickness. The curves marked a. are samples melted in air and the samples marked b. are samples melted with dry argon flowing over the surface. The argon melting definitely removes water from the glass melt. The water absorption band increased from 55 percent (air) to 71 percent (argon). Similar increases are noted throughout the transmitting range. Both thin samples show an increase in transmittance throughout the range and have a longer wavelength cutoff. The two samples melted in argon shown on Figure 6 are the only samples so treated. The balance of samples were melted in air.

GD 3485 is based on GD 3484 except the alkali content is reduced from 8.7 percent to 4 percent and the CaO content is increased from 3.3 percent to 8 percent. The alkali content is further reduced in samples GD 3486 and GD 3487 to two percent and one percent respectively. The data is not entirely consistent, but it can be stated generally that the expansion is lowered with a reduction in alkali content and the index of refraction and the dielectric constant increased. The infrared transmittance curves shown in Figure 7 indicate essentially
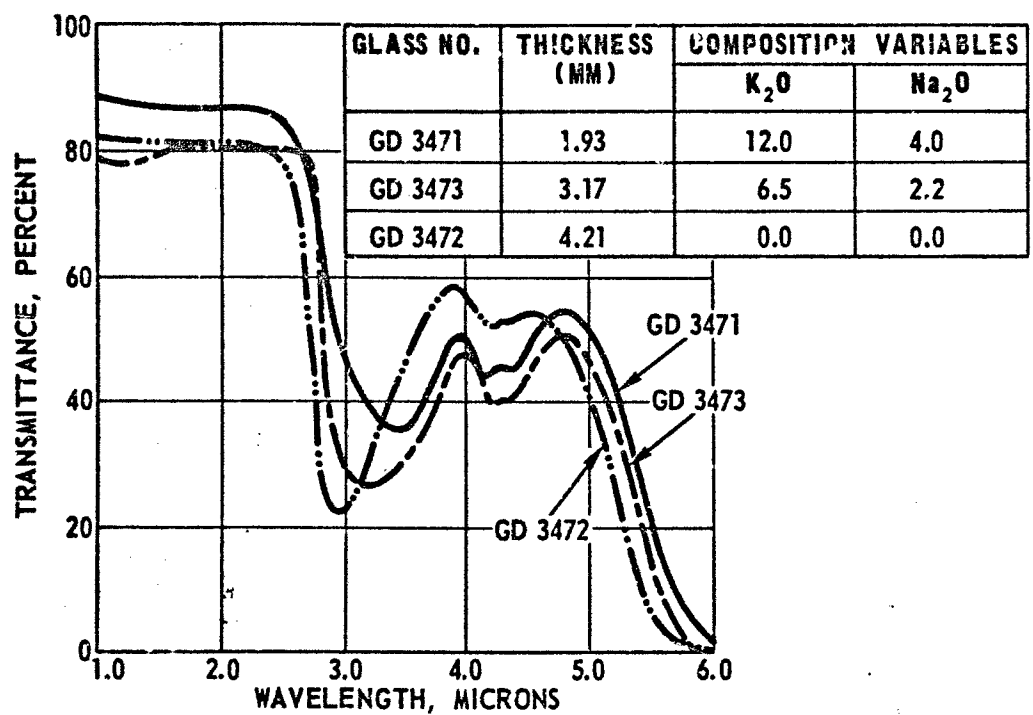
127

GLASS NO.	THICKNESS (MM)	COMPOSITION VARIABLES	
		K$_2$O	Na$_2$O
GD 3471	1.93	12.0	4.0
GD 3473	3.17	6.5	2.2
GD 3472	4.21	0.0	0.0

Figure 4. Effect of Lowering Alkali Oxide Content

GLASS NO.	THICKNESS (MM)	COMPOSITION VARIABLES	
		BaO	MgO
GD 3474	4.47	10.9	1.1
GD 3478	4.47	6.5	5.5
GD 3484	4.55	0.0	12.0
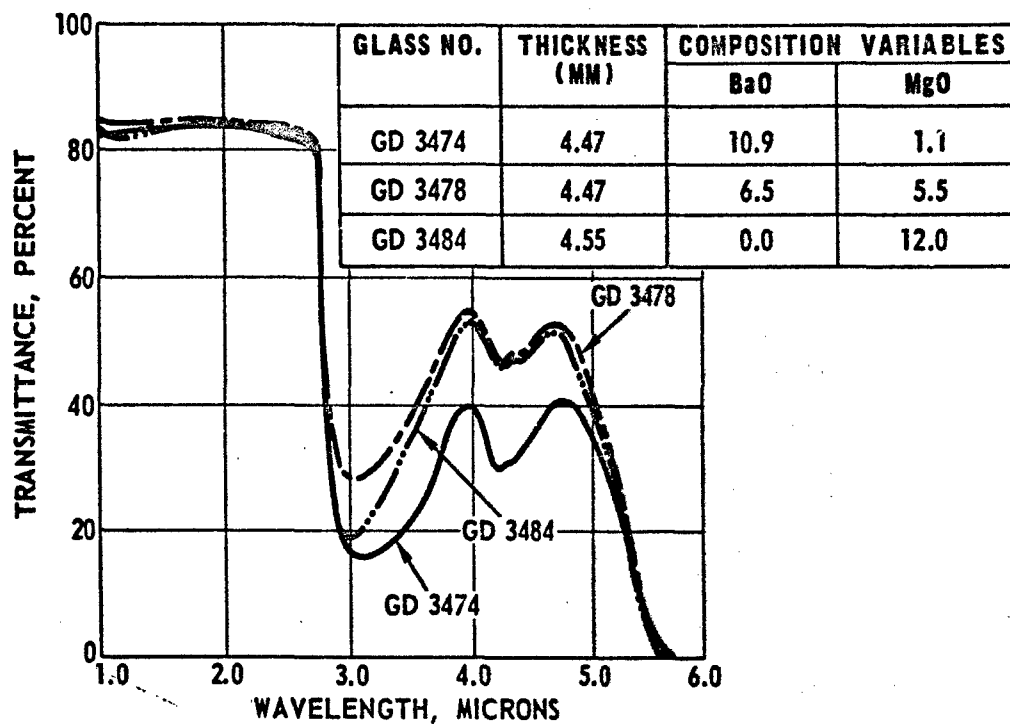
Figure 5. Effect of Substituting MgO for BaO.

129

NO. GD 3485
a. MELTED IN AIR
b. MELTED WITH ARGON
   FLOWING OVER SURFACE
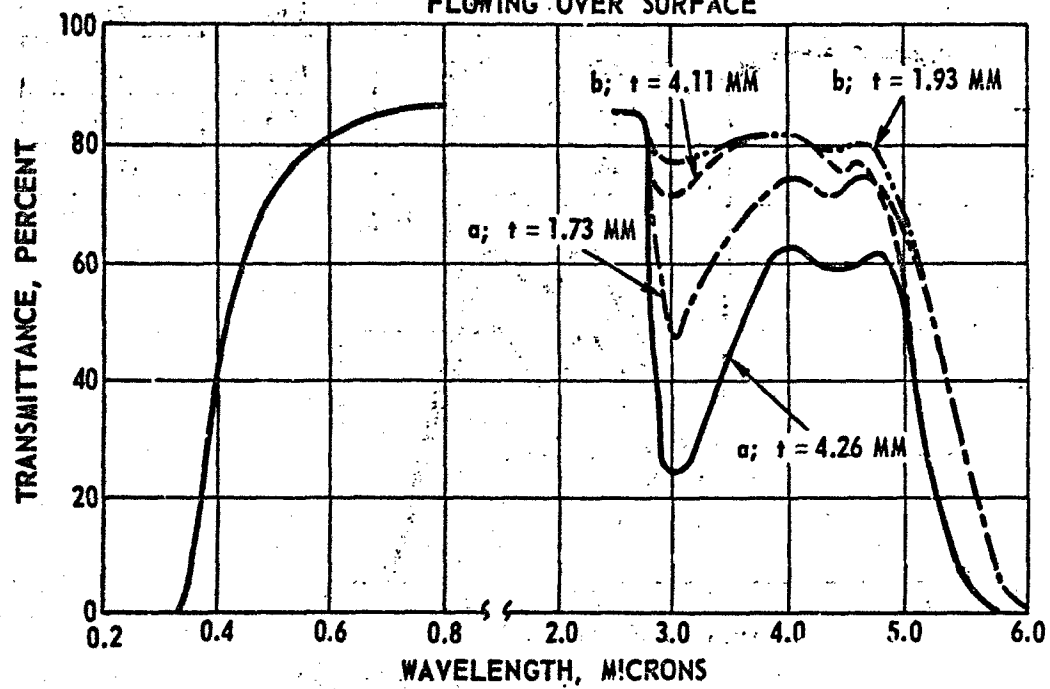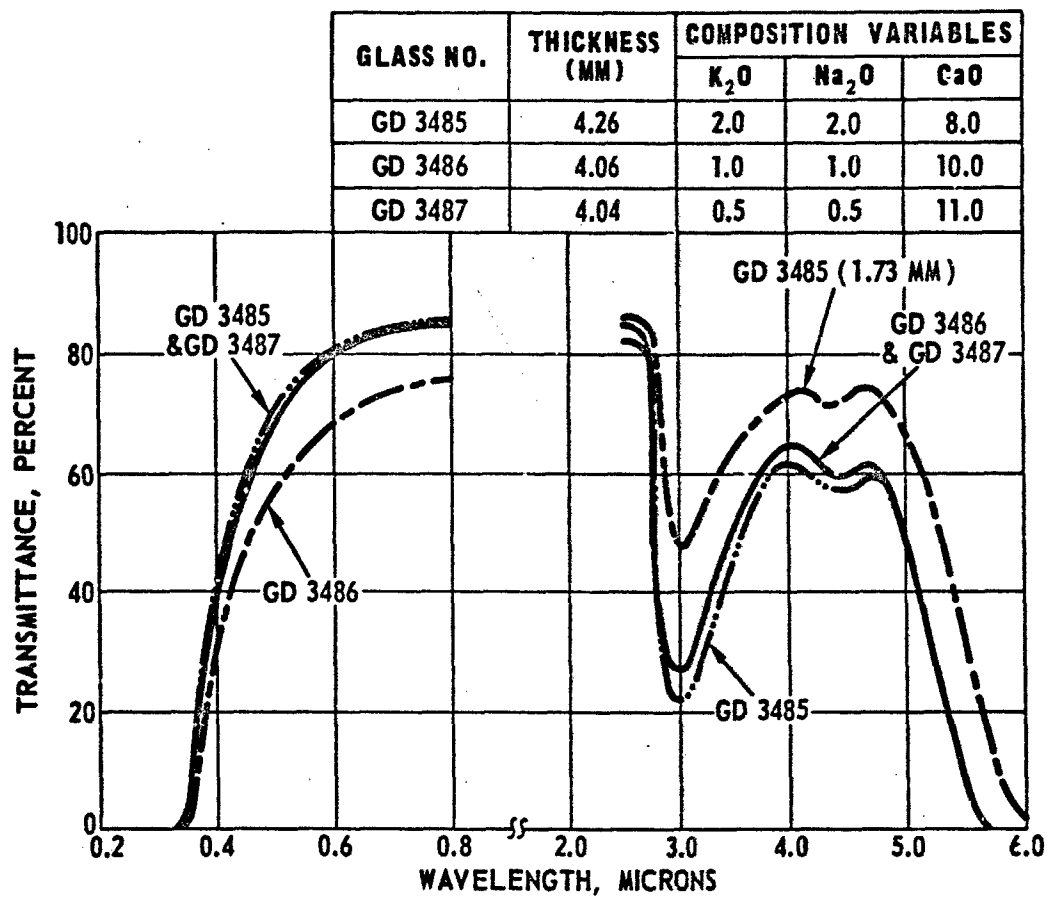
Figure 6. Transmittance of Glass.

130

GLASS NO.	THICKNESS (MM)	COMPOSITION VARIABLES		
		K_2O	Na_2O	CaO
GD 3485	4.26	2.0	2.0	8.0
GD 3486	4.06	1.0	1.0	10.0
GD 3487	4.04	0.5	0.5	11.0

Figure 7. Effect of Substituting CaO for Alkali Oxides

no changes occurred with reduction of alkali content.

The next series of glasses, GD 3488 - GD 3491, show the result of substituting PbO for GeO_2. The thermal expansion increases as does the index of refraction and the dielectric constant with increasing PbO content. Lead oxide added at the expense of GeO_2 depresses the IR transmittance slightly as shown in Figure 8. The ultraviolet transmittance, however, is radically changed. As the PbO content increases, the UV cutoff occurs at longer wavelengths.

Theory presented indicated that B_2O_3 would decrease the thermal expansion. In general this was found to be true. The expansion of GD 3488, having no B_2O_3, was lowered from 64.8×10^{-7} in/in/$^{\circ}$C to 61.1×10^{-7} in/in/$^{\circ}$C for 6 percent B_2O_3 (sample GD 3494). Very little effect on index of refraction was noted with B_2O_3 content. Since B_2O_3 containing glasses would not be considered for dual mode purposes because of infrared transmittance characteristics, dielectric constant measurements were not made. The effect of B_2O_3 on the IR transmittance is shown graphically in Figure 9. GD 3488 has no B_2O_3 and has transmittance properties similar to the previous samples. As little as 2 mole percent B_2O_3 (GD 3492) effectively makes the glass useless for IR purposes.

The substitution of TiO_2 for Al_2O_3 (samples GD 3495 through GD 3497) shows that the thermal expansion is increased. Quite large increases occur in both the index of refraction and the dielectric constant. Samples GD 3498 and GD 3499 show the effect of adding ZrO_2 in place of Al_2O_3. The thermal expansion is decreased while the index of refraction and dielectric constant increased with added ZrO_2. Variations of mole percentages of CaO, Al_2O_3, TiO_2 and ZrO_2 have little effect on IR transmittance as shown in Figure 10. The transmittance of samples GD 3495 through GD 3499 were all in the shaded area. No conclusions can be made except that mutual substitution of the above mentioned oxides did not radically improve or harm the IR transmittance. It appears that TiO_2 and ZrO_2 may cause the UV transmittance cutoff to occur at longer wavelengths.

Zinc oxide increases the thermal expansion when substituted for GeO_2. The index of refraction and the dielectric constant increase with added ZnO. Figure 11 depicts the effect of zinc oxide substitution for GeO_2 on the infrared transmittance. As the zinc oxide increases, the IR transmittance is reduced slightly through most of the range, but the long wavelength cutoff occurs at slightly longer wavelengths.

Samples GD 3488 and GD 3504 through GD 3506 show the effects of increasing the SiO_2 content from 0 to 6 mole percent. The expansion data did not correlate with theory but the magnitude of the measured expansions were similar to the calculated values. The index of refraction was lowered by the SiO_2 additions. The effect of silica additions on IR transmittance is shown in Figure 12. As the silica content increases the IR transmittance cutoff occurs at shorter wavelengths, thus again verifying theory. Silica additions raise the transmittance below 4.5 microns.
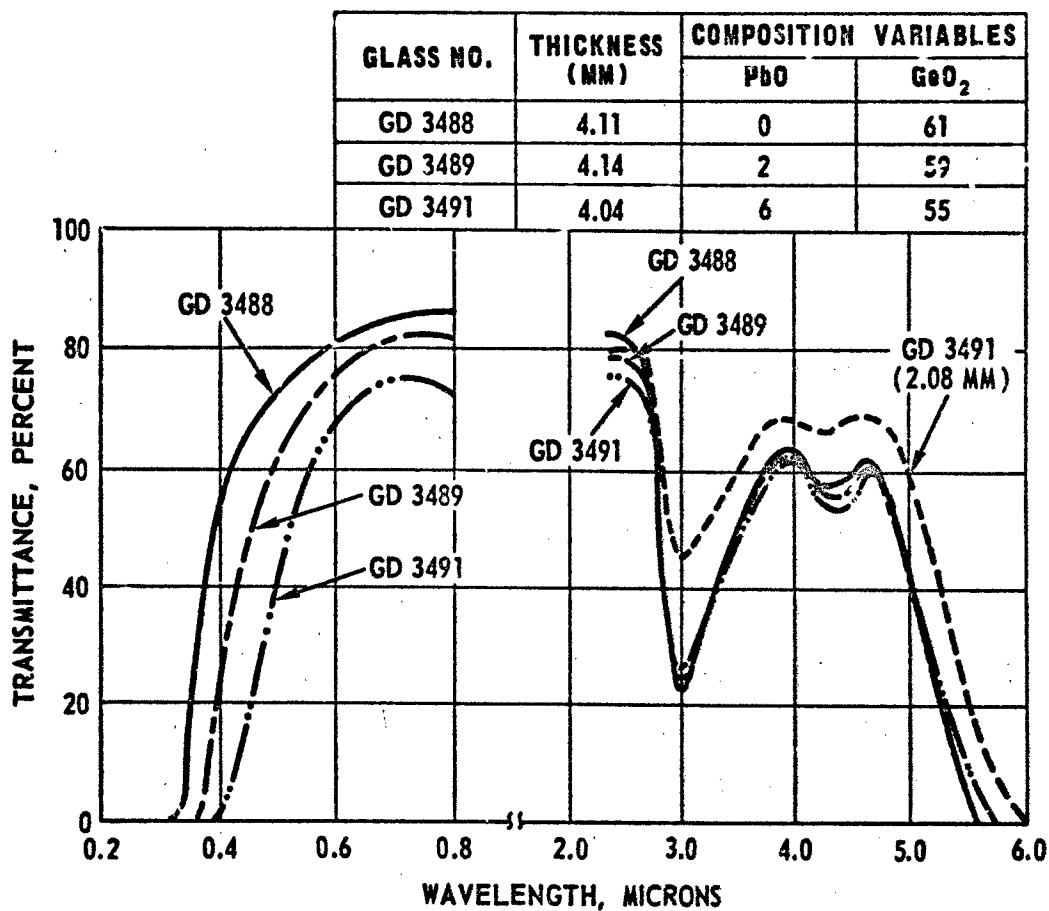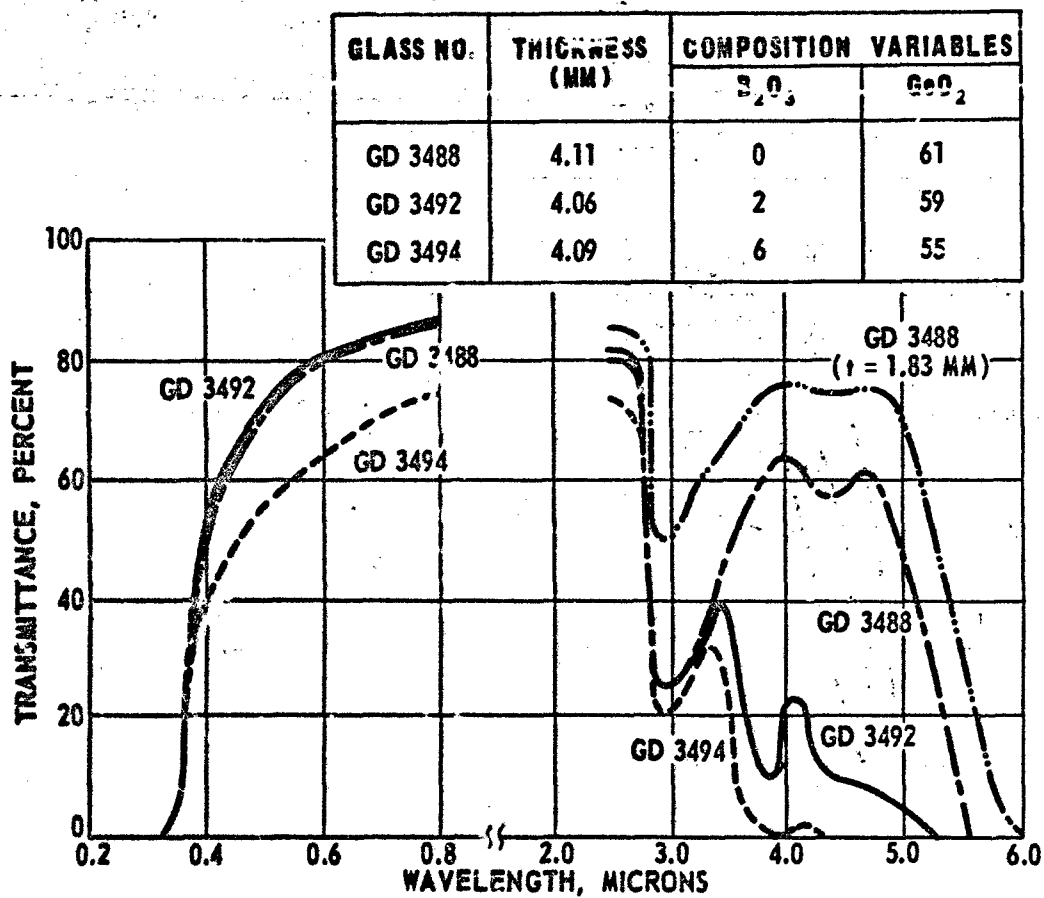
GLASS NO.	THICKNESS (MM)	COMPOSITION VARIABLES	
		PbO	GeO$_2$
GD 3488	4.11	0	61
GD 3489	4.14	2	59
GD 3491	4.04	6	55

Figure 8. Effect of Increasing PbO

133

GLASS NO.	THICKNESS (MM)	COMPOSITION VARIABLES	
		B_2O_3	GeO_2
GD 3488	4.11	0	61
GD 3492	4.06	2	59
GD 3494	4.09	6	55

Figure 9. Effect of Adding B_2O_3

GLASS NO.	COMPOSITION VARIABLE			
	CaO	Al_2O_3	TiO_2	ZrO_2
GD 3495	6.0	6.0	0.0	0.0
GD 3496	6.0	3.0	3.0	0.0
GD 3497	6.0	0.0	6.0	0.0
GD 3498	2.0	10.0	0.0	0.0
GD 3499	2.0	5.0	0.0	5.0
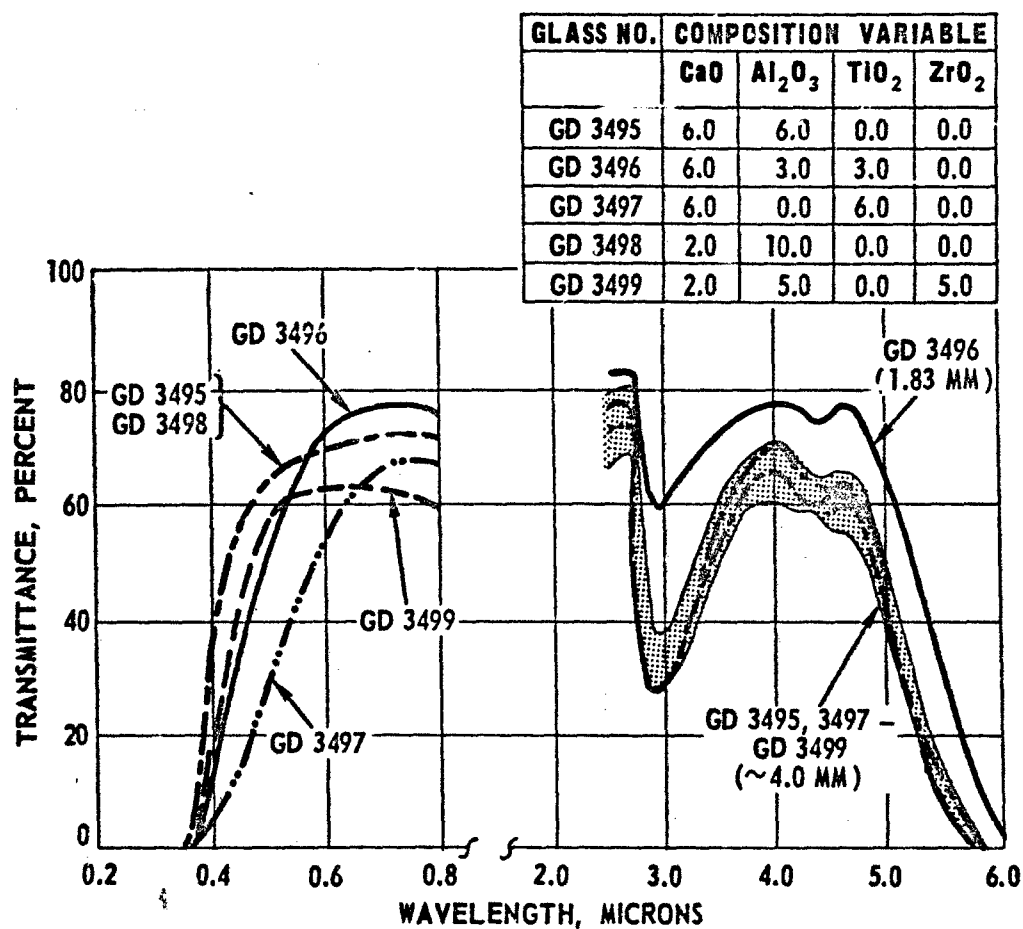
Figure 10. Transmittance of Glasses GD 3495 through GD 3499

GLASS NO.	THICKNESS (MM)	COMPOSITION VARIABLES	
		ZnO	GeO$_2$
GD 3501	4.11	0	72
GD 3503	4.09	6	66
GD 3488	4.11	11	61
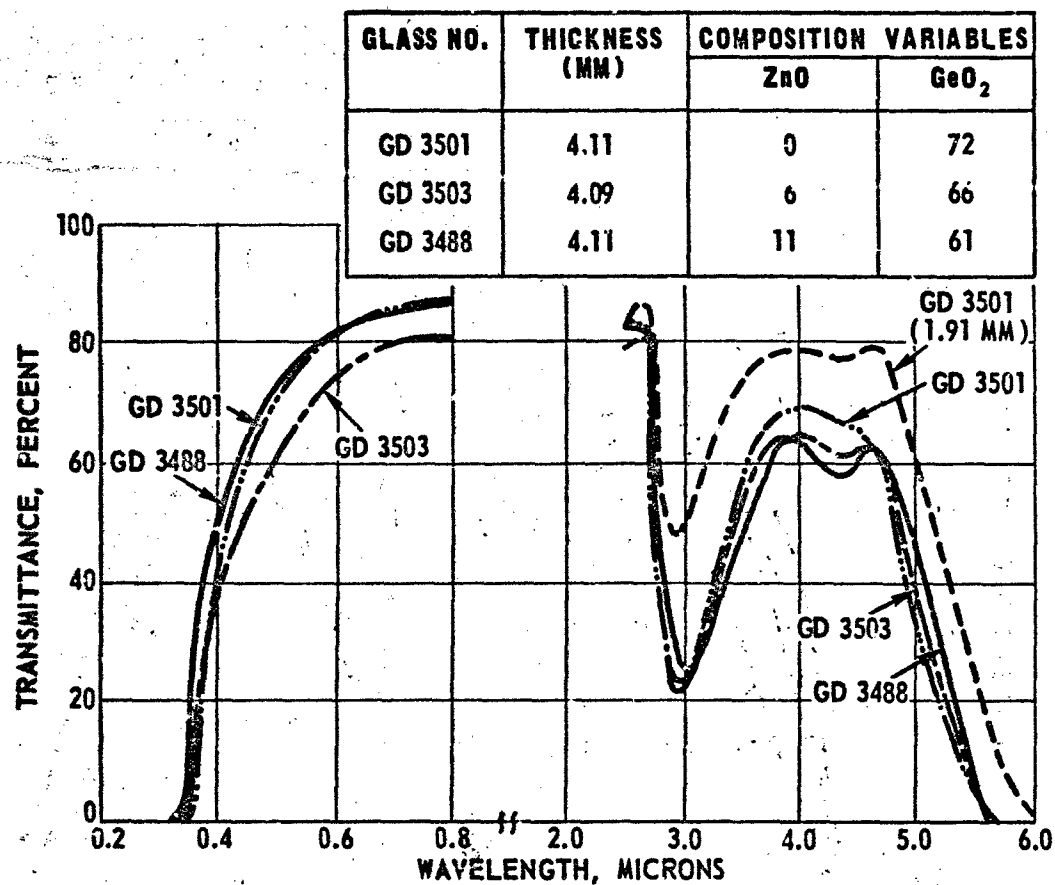
Figure 11. Effect of Increasing ZnO Content

GLASS NO.	THICKNESS (MM)	COMPOSITION VARIABLES	
		SiO$_2$	GeO$_2$
GD 3488	4.11	0	61
GD 3504	4.09	2	59
GD 3506	4.01	6	55
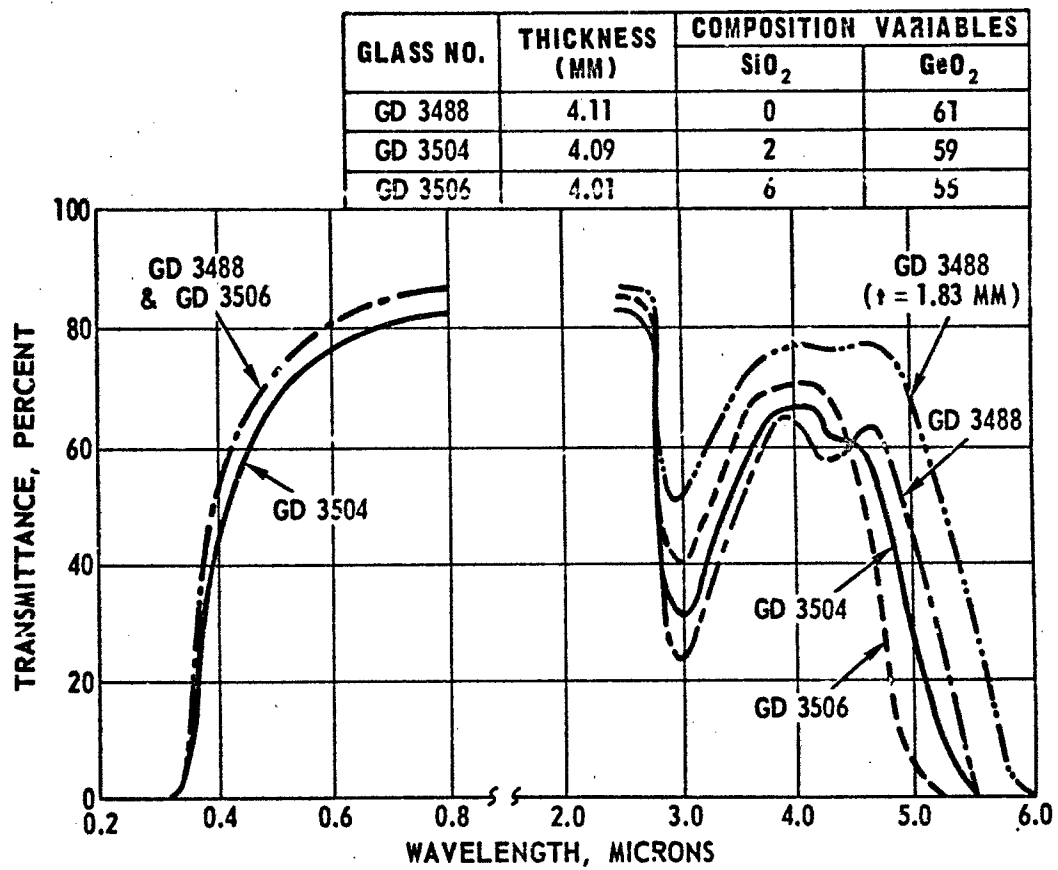
Figure 12. Silica Additions to Germanate Glasses.

137

5. CONCLUSIONS AND RECOMMENDATIONS

Several materials are commercially available for use in a dual mode capacity. For the near infrared, fused silica is the best candidate because of its excellent electrical and thermal properties. Corning Code 9754 glass, calcium aluminate glass, Irtran I and Irtran II are the best choices if the intermediate infrared range is of prime importance. The limitation of materials for dual mode use in the intermediate infrared range then, is their relatively poor thermal shock resistance.

The germanate glasses investigated, although preliminary in nature, show that some improvements over commercially available glasses can be achieved. The lowest expansion glass developed was GD 3501, with an expansion coefficient of 60.7×10^{-7} in/in/°C. This is slightly lower than the expansion coefficient of Corning Code 9754 Glass (63.6×10^{-7} in/in/°C).

The theory used to formulate the glass compositions did not correspond to actual measured properties but in all cases trends that were predicted from the theory were reflected in the measured values.

It is recommended that the information developed on germanate glasses be used to formulate new compositions to further improve currently available glasses for dual mode use.

6. REFERENCES

1. Letter, from R. W. Johnson, Sales Manager, Optical Crystals/Crystal-Solid State Division of the Harshaw Chemical Company, Cleveland, Ohio

2. "Long Wavelength Infrared Domes", Report No. AL-TDR-64-9, March, 1964, Eastman Kodak Company, Apparatus Optical Division.

3. "Transparent Alumina and Method of Preparation", U. S. Patent No. 3,026,210; Cable, R. L., Assignor to General Electric Company.

4. Fused Quartz Catalog, from Lamp Glass Division of General Electric Co.

5. Dumbaugh, W. H., "Infrared Transmitting Glasses", Corning Glass Works, Presented at the Air Force/Georgia Tech Symposium on Electromagnetic Windows, 1965

6. Manson, S. S., "Thermal Stresses", Machine Design 30, 114-120 (June 1958) and "Theraml Stresses in Design", Machine Design 30, 99-103, (June 26, 1958)

7. Mayer and Havas, Sprech Saal, Vol. 42, page 497 (1909); Vol. 44, pages 188, 207, 220 (1911)

8. Winkelmann and Schott, Wiedmann's Annalen Bd., Vol. 51, page 731 (1894)

9. English, S., and Turner, W. E. S., "Relationship Between Chemical Composition and the Thermal Expansion of Glasses", J.A.C.S., Vol. 10 #8, pages 551-560, 1927

10. Silverman, W. B., "The Effect of Alumina on the Expansion and Deformation Temperatures of Soda-Lime-Silica Glasses", J. Soc. Glass Technol, Vol. 24, pages 59-71, 1940

11. Navias, L., & Green, R. L., "Dielectric Properties of Glasses at Ultra-High Frequencies and Their Relation to Composition", J. Am. Ceram. Soc., Vol 29, #10, pages 267-276, 1946

12. Rinehart, D. W. & Bonino, J. J., "Dielectric Losses of Some Simple Ternary Silicate Glasses", J. Am. Ceram. Soc., Vol. 42, #3, pages 107-112, 1959

13. Florence, J. M. Glaze, F. W., & Black, M. H., "Infrared Transmittance of Some Calcium Aluminate and Germanate Glasses", J. Research NBS, Vol. 55, page 231, 1955.

14. Kreidl, N. J., Hofner, H. C., Hensler, J. R., Weidel, R. A., & Letter, E. C., "An Investigation of Infrared Transmitting Materials", WADC-TR-55-550, Part I & III, October 1958

15. Nielsen, S., Lawson, W. D., & Fray, A. F., "Some Infrared Transmitting Glasses Containing Germanium Dioxide", Infrared Physics, Vol. 1 #21, 1961

BLANK PAGE
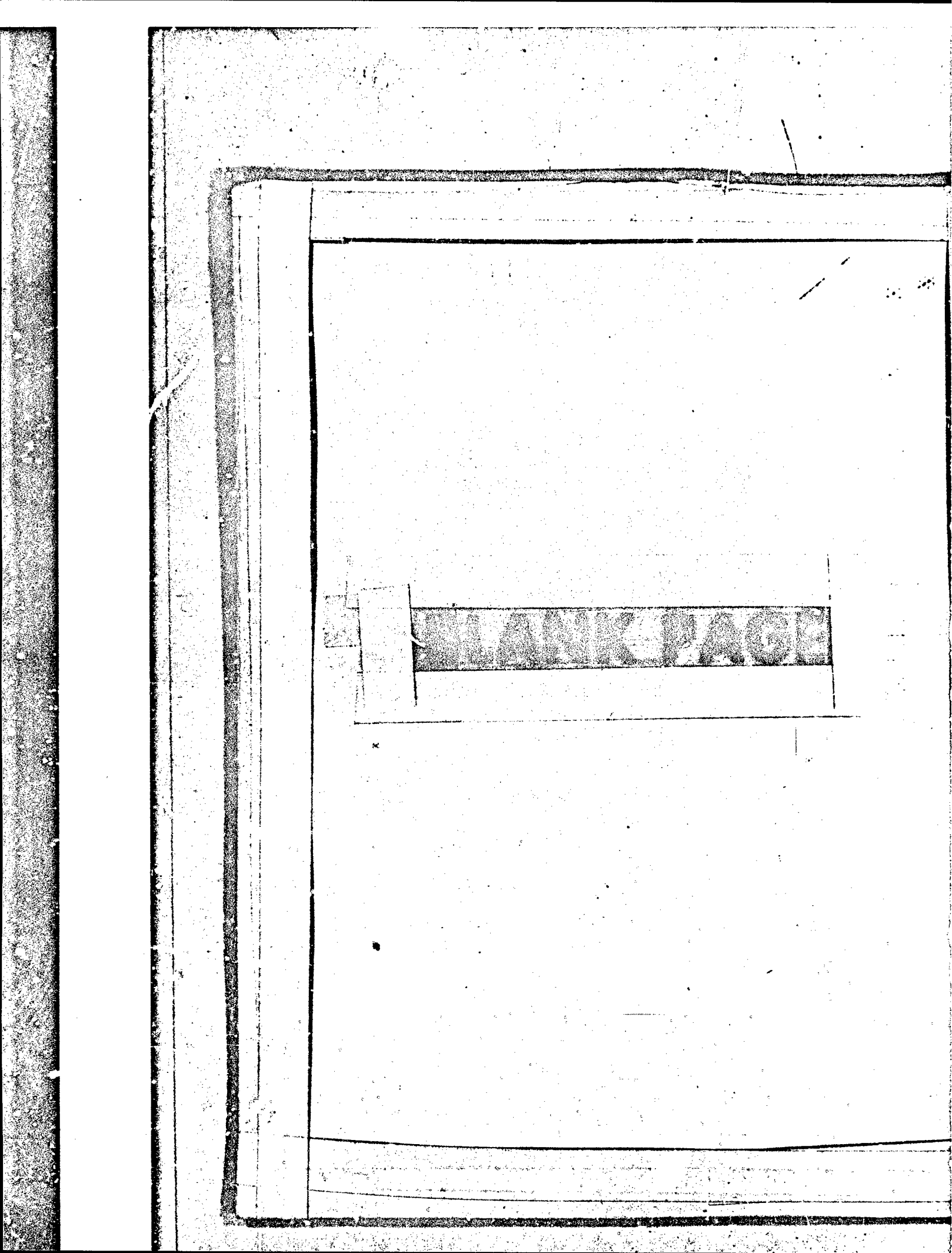
FIBER REINFORCED CERAMIC ELECTROMAGNETIC WINDOWS

J. J. Krochmal
Air Force Materials Laboratory
Wright-Patterson Air Force Base, Ohio 45433

ABSTRACT

Fiber reinforced ceramic activities and findings of the past 8-10 years are very briefly reviewed and it is noted that fiber reinforcements were shown to improve both the strength and thermal shock resistance of ceramics. Additionally, reinforced ceramics are noted to have always failed in predictable locations in three point bend tests, viz. at the point of maximum outer "fiber" tensile stress, and failures were not catastrophic but, rather, gradual and accompanied by substantial inelastic deformation. The model material systems that were resorted to in reaching these findings are indicated as having circumvented such problems as expansion coefficient mismatches, matrix-fiber interactions during processing or at use temperatures, and reinforcement oxidation.

Of concern now is the extent to which past achievements, when coupled with newly developed materials and processing techniques, offer promise of providing improved window capabilities. Opportunities afforded by low temperature processing are reviewed in that they now permit consideration of ceramic fiber or metal fiber-reinforced dielectrics. Questions as to the extent to which the mechanical benefits of metal fiber additions can be tolerated electrically are presently unanswered and should be resolved since mechanical benefits not only include improved thermal shock resistance but also improved mechanical reliability. Potentially useful materials combinations are discussed and investigations with such systems are encouraged.

INTRODUCTION

Of concern is whether fiber reinforced ceramics can provide improved electromagnetic window capabilities. The discussions to follow will not answer this unequivocally. Rather, approaches will be suggested which might well prove beneficial.

The area of fiber reinforced ceramics is one that has been periodically referred to as a potential panacea for many of the problems that arise when attempts are made to employ brittle ceramic materials as components where loads

are induced by mechanical or thermal means. Perhaps follow-ing a review of the research that has been conducted in this area, potential opportunities for windows will be apparent.

PREVIOUS WORK

The most extensive as well as comprehensive research effort in the area of fiber reinforced ceramics was one concerned with metal fibers which was conducted at the State University of New York, College of Ceramics at Alfred Univer-sity, during the period of 1 July 1957 to 31 August 1960 (Reference 1). This three-year effort will be referred to rather extensively in the following review since the find-ings or relationships developed or identified under that effort have persisted to date. Lest one question any radome oriented concern with such research involving metal fibers, it should be noted that recent research has indicated that the behavior of a composite of sapphire whiskers in an Al_2O_3 matrix closely resembled that of a metal fiber reinforced ceramic (Reference 2).

1. Mechanical Properties and Behavior

Figure 1 shows the microstructure of an aluminum oxide body containing 5 weight % of molybdenum fiber. Due to the fact that the expansion coefficient of molybdenum is sub-stantially less than that of the alumina, one would expect microcracks throughout the microstructure. At such low levels of fiber additions, microcracks sometimes did not appear. Figure 2 depicts an aluminum oxide body containing 10 weight % of molybdenum fiber and here the occurrence of cracks is clearly evident. Figure 3 indicates a behavior typical of a cracked system. It is noted that prior to thermal shocking the strength of the unreinforced matrix material is higher than any of the reinforced specimens. Subsequent to thermal cycling, however, when the unreinforced matrix has deteriorated to essentially no strength, the strength levels of the reinforced specimens are maintained. This figure also shows that the greater the amount of rein-forcement present, the higher the strength of the reinforced specimen. It should be noted that the thermal shock cycles referred to in this figure, as well as those which will be referred to in later figures, are produced as follows: The specimens are placed in a furnace at 2200°F and permitted to remain there for a period of ten minutes. The specimens are then removed, placed on a thick steel plate, and allowed to cool to room temperature.

Figure 4 depicts the microstructure of the typical non-microcracked fiber reinforced specimen. In this case a matrix consisting of a precise mixture of mullite and aluminum oxide, designated "Body 712," was selected in order to match the coefficient of thermal expansion of molybdenum. Table I
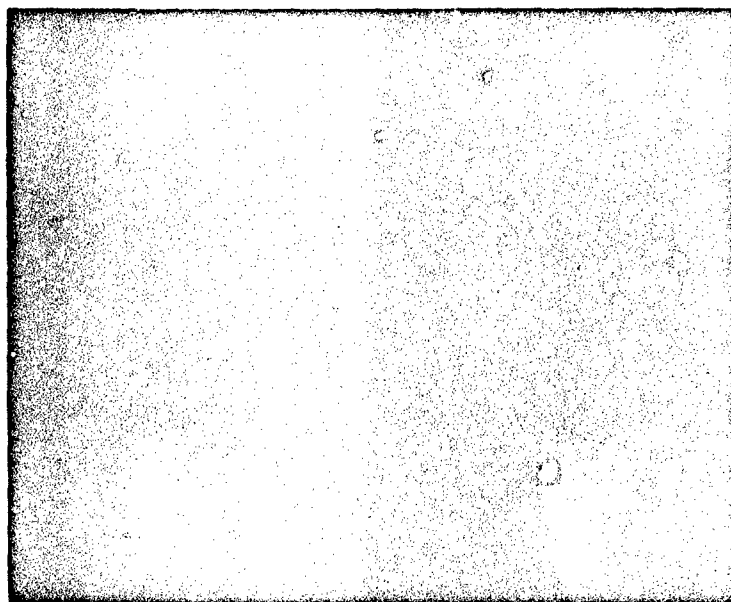
Figure 1. Alumina Containing 5 Wt. % Molybdenum Fiber (30X) (Reference 1.a.).
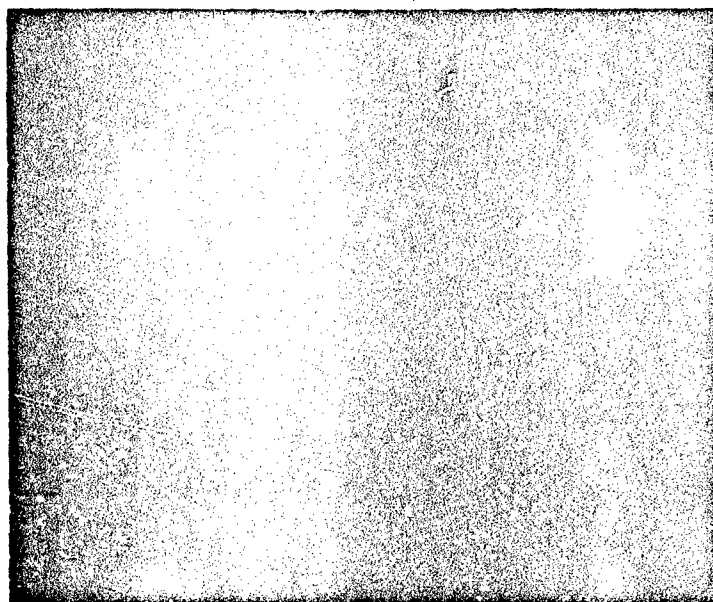
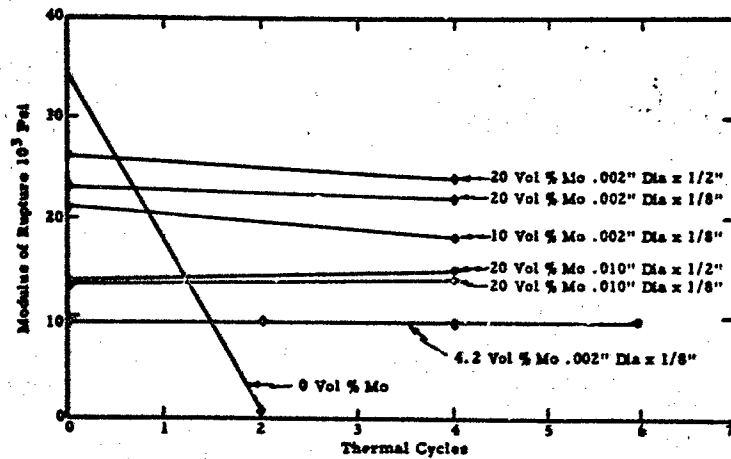Figure 2. Alumina Containing 10 Wt. % Molybdenum Fiber (30X) (Reference 1.a.).

Figure 3. Modulus of Rupture as a Function of
Thermal Cycling for the Alumina-
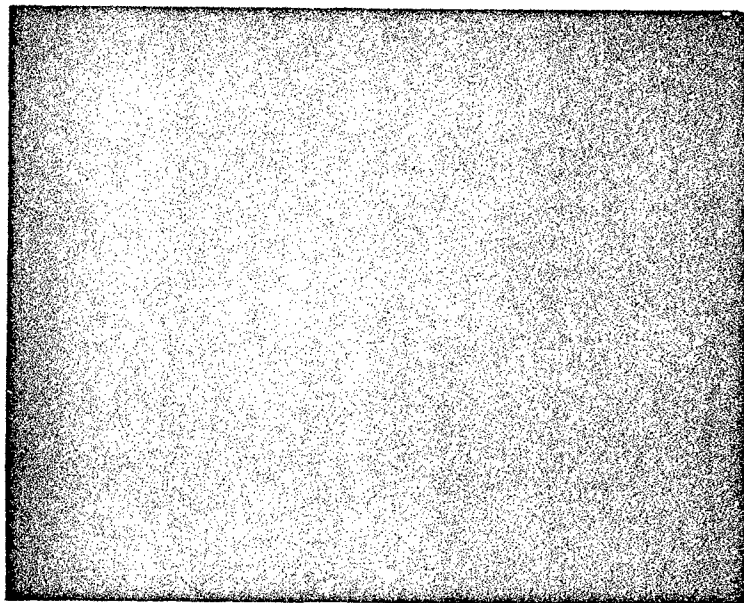Molybdenum Fiber System (Reference 1.b.).

Figure 4. Non-microcracked Fiber Reinforced
Specimen (80X) (Reference 1.c.).

depicts the calculated as well as measured properties of
Body 712 containing various amounts of molybdenum fibers.

TABLE I

EXPLORATORY EXPERIMENTS WITH MOLYBDENUM FIBER-BODY 712 (Reference 1.c)

Dimensions of Moly Fiber	% Vol. Fiber	E at R.T. (10⁶ PSI)	Calc. E (10⁶ PSI)	Modulus of Rupture After 4 cycles	Calc. % Total Stress Assumed by Fiber	Calc. Stress Assumed by 712
0.006 x 1/4 in.	30	40.5	36	27,900 PSI	35.0	18,150 PSI
0.002 x 1/3 in.	30	35.7	36	30,700 PSI	35.0	20,000 PSI
0.006 x 1/4 in.	43	36.5	37.5	35,800 PSI	48.8	18,000 PSI
0.006 x 3 in.	25	35.4	35.9	32,000 PSI	29.0	22,735 PSI
0.002 x 1/3 in.	4.2	32.2	34.2	1,400 PSI	5.24	——*
None	0	33.8		0		——
					Average:	19,946 PSI

*This value has no meaning due to the extremely low value of modulus of rupture after four thermal cycles.

It is interesting to note the excellent agreement between
the calculated and measured elastic moduli. Since the
elastic modulus of the molybdenum filaments exceeded that
of Body 712, the reinforcements assumed slightly more stress
than would be normally expected by simply viewing the volume
percent present. Also of interest is the average of the
calculated stresses assumed by Body 712, viz. 19,946 PSI,
which fell rather close to the 21,640 PSI modulus of rupture
value that represented the average strength of Body 712
without reinforcements and before thermal shocking. Figure
5 depicts the behavior of Body 712 containing various per-
centages of 2-mil molybdenum fiber. Here we note features
which differ from those of Figure 3 in that the strengths,
prior to thermal cycling, of reinforced specimens are higher
or at least equivalent to the unreinforced Body 712. Figure
6 is somewhat similar except that in this case 10-mil fiber
was employed. In Reference 1-b the relationships in Figure
5 and 6 are clarified further and compared by plots of the
effects on modulus of rupture, after four thermal cycles,
of volume percent molybdenum for the two fiber diameters
and lengths, and of fiber length for the two diameters and
percentage additions.

At this point an explanation is in order as to the
characterization of the specimens considered in this work.
First, it should be noted that all test specimens were hot-
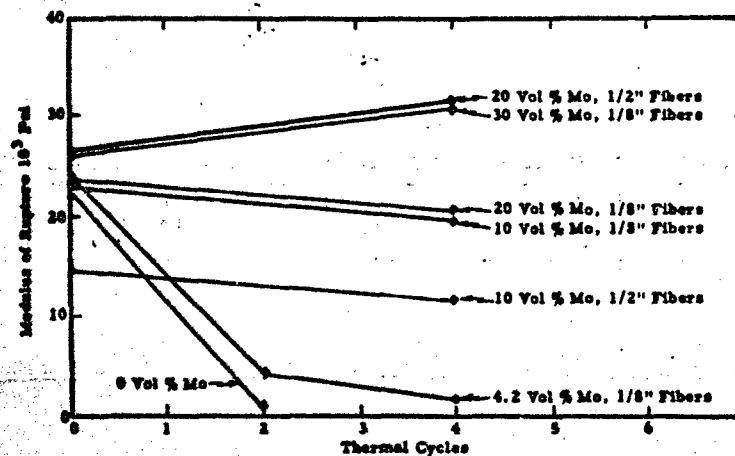pressed. Also, it should be mentioned that these materials,

145

Figure 5. Modulus of Rupture as a Function of Thermal Cycling for the Body 712-.002-Inch Diameter Molybdenum Fiber System (Reference 1.b.).
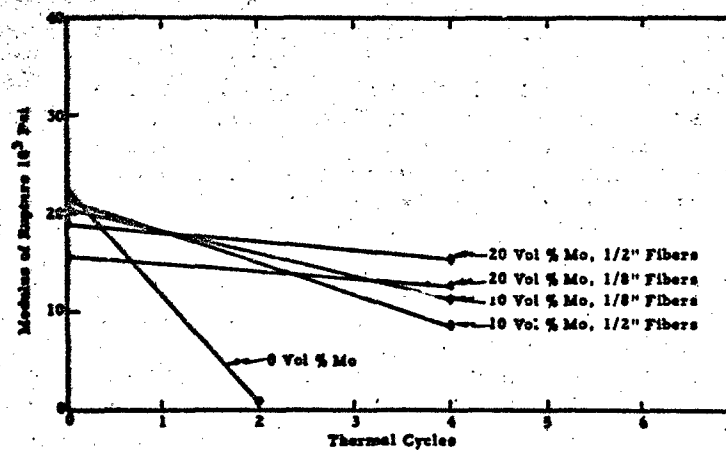

Figure 6. Modulus of Rupture as a Function of Thermal Cycling for the Body 712-.010-Inch Diameter Molybdenum Fiber System (Reference 1.b.).

146

as fabricated, are not isotropic. Figure 7 presents a section of a fiber reinforced specimen which has been sectioned parallel to the specimen's length and direction of pressing. This is in contrast to the following figure (Figure 8) which shows a specimen which has been sectioned also parallel to the specimen's length but normal to the direction of pressing. All of the investigations under this program were concerned with the strong fiber orientation. No strengths were determined for what would be expected to be the weaker direction.

Figure 9 depicts a transverse section of what was designated Body 715, in this instance reinforced with 10 volume % of tungsten fibers. Body 715 consisted of calcined Kaolin, flint, and feldspar and represented a composition which was developed first, to achieve a compatible relationship from an expansion coefficient standpoint with the tungsten reinforcement and second, to achieve an elastic modulus relationship whereby that of the matrix was approximately 1/5 that of the reinforcing filaments. Figure 10 depicts a transverse section of the same body, in this case reinforced with 50 volume % tungsten fibers. This figure depicts the problem associated with higher filamentary additions, viz. fiber agglomerations appear and each of the fibers within these groupings does not enjoy a complete matrix environment. Figure 11 shows this same specimen sectioned longitudinally and normal to the direction of pressing. Attempts to surface grind and polish such specimens resulted for the most part in the ceramic matrix pulling out from the surface and exposing an array of fibers beneath it. At this fiber level, agglomerates of fiber actually act as matrix and contain pockets of low density ceramic within them. This is also presented in Figure 12 which attests to the inability to achieve at least 90% calculated density bodies when fiber additions exceed 20 volume %. A discontinuity in behavior would therefore be expected for all bodies containing more than 20% fiber and this is borne out by Figure 13 which shows the modulus of rupture values as a function of volume % fiber reinforcement. Figure 14 presents typical stress-strain diagrams for Body 715 with various volume % fiber additions while Figure 15 presents a stress-strain diagram of successive tests of a single specimen. Studies of the behaviors depicted in Figures 14 and 15 coupled with microscopic studies of the surfaces of the ceramic specimens as they were being stressed led Tinklepaugh, et al to the following conclusions:

"From a study of the various stress-strain diagrams, a general concept evolved as a possible explanation for observations made as the specimens were loaded. Within the proportional limit the composite behaved as any other elastic material behaves. For specimens with no fiber reinforcement the proportional limit was also its point of failure -- a condition common

147
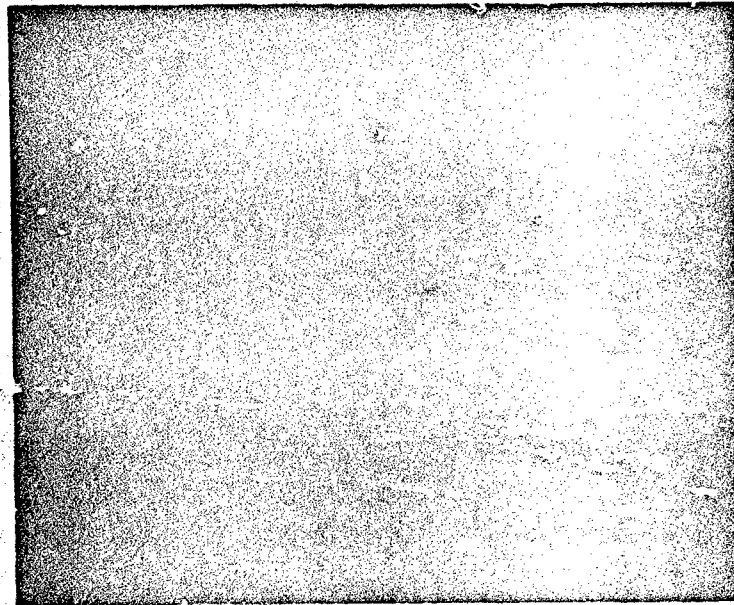
Figure 7. Fiber Reinforced Specimen Sectioned Parallel to the Specimen's Length and Direction of Pressing (15X) (Reference 1.c.).
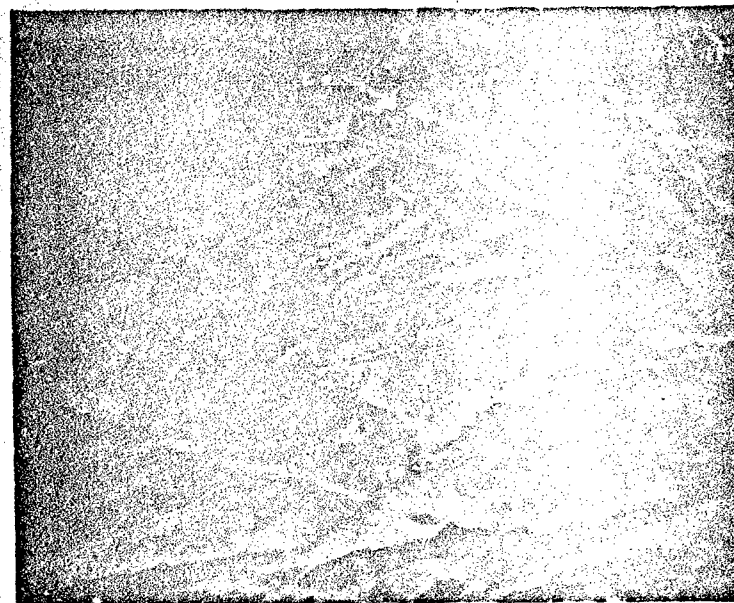
Figure 8. Fiber Reinforced Specimen Sectioned Parallel to the Specimen's Length and Normal to the Direction of Pressing (15X) (Reference 1.c.).

148

Figure 9. Transverse Section of Body 715
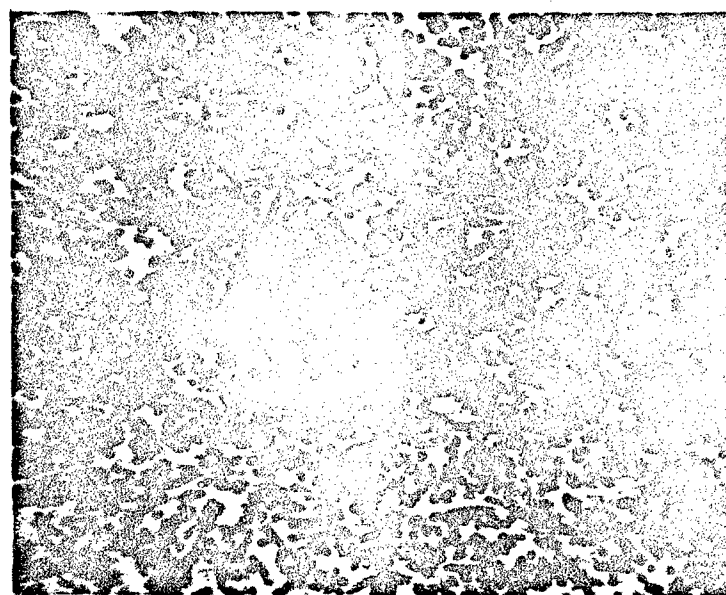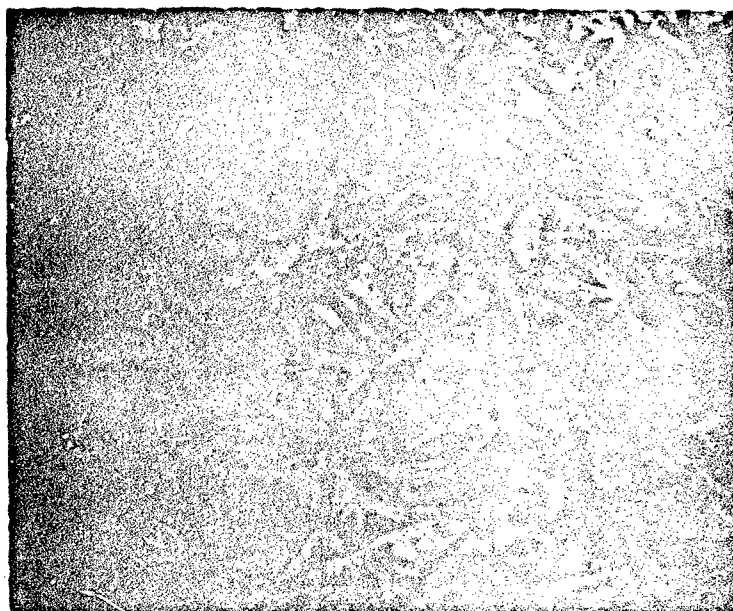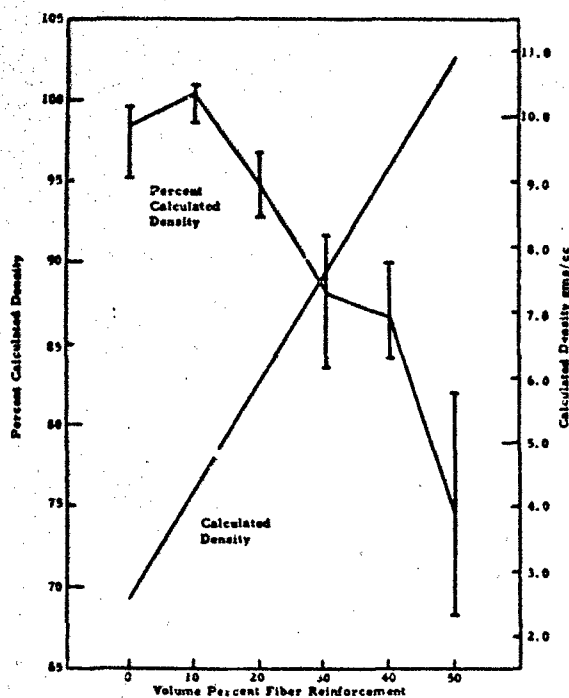Reinforced with 10 Volume %
Tungsten Fibers (15X) (Reference 1.c.).

Figure 10. Transverse Section of Body 715
Reinforced with 50 Volume %
Tungsten Fibers (15X) (Reference 1.c.).

Figure 11 A 50 Volume % Fiber Reinforced
Specimen Sectioned Longitudinally
and Normal to the Direction of
Pressing (15X) (Reference 1.c.).

Figure 12. Calculated Density and %
Calculated Density vs.
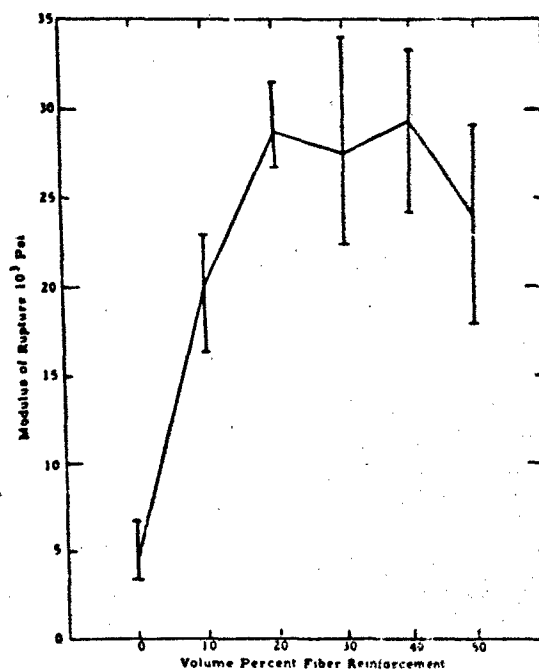Volume % Fiber Reinforcement
(Reference 1.c.).

150

Figure 13. Modulus of Rupture vs. Volume % Fiber
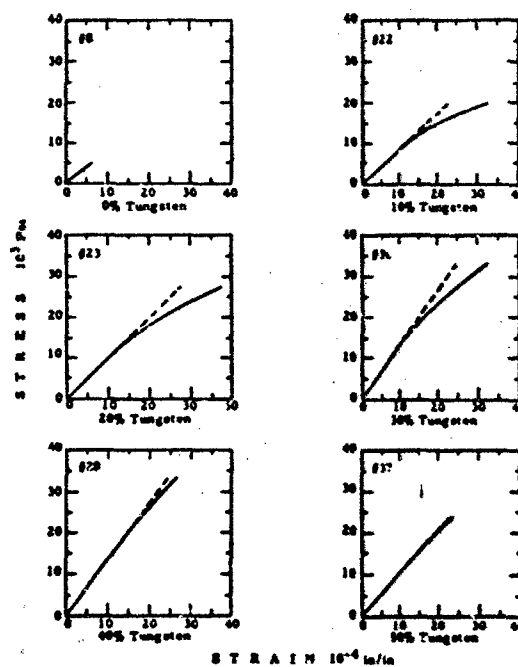Reinforcement (Reference 1.c.).

Figure 14. Typical Stress-Strain Diagrams
for Body 715 with Various Volume
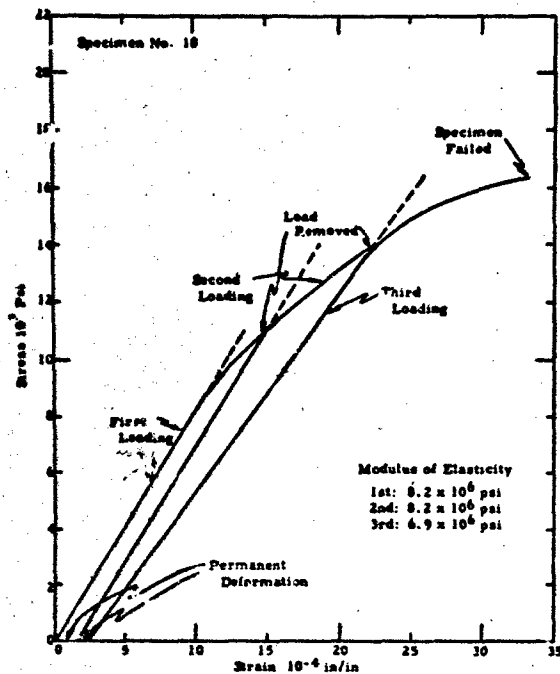% Fiber Additions (Reference 1.c.).

151

Figure 15 Stress-Strain Diagram for Successive Tests of a
10 Volume % Fiber Reinforced Specimen (Reference 1.c.)

to ceramic materials in general. However, when
reinforced with tungsten fibers, specimens failed
only after the outer fiber stress had been in-
creased several hundred percent over that of
specimens without reinforcement. Although the
reinforced specimens did not fail, the stress-
strain diagram did deviate from a straight line
at a point that appeared to be dependent upon
the amount of fiber present. This deviation
from a straight line -- or the proportional
limit -- became the key to the explanation.
When the load on the ceramic reached the level
of stress which caused the non-reinforced ceramic
specimen to fail, the ceramic in the reinforced
specimen also failed. The reinforcement, however,
held the composite together. As the load was in-
creased beyond this point, the outer fibers were
gradually pulled loose from the ceramic matrix.
This accounted for the deviation from the straight
line that was observed in all of the reinforced
specimens tested. Finally, when the load on the
outer fibers reached a stress that would com-
pletely separate them from the ceramic matrix,
the specimen failed completely. The modulus of

rupture then is that stress which caused the
fibers to be pulled out of the ceramic matrix.
The proportional limit increased with increasing
percentages of fiber present because the fibers
assumed an increasing proportion of the load, the
ceramic still failing at its original stress
level.

The amount of deformation a reinforced specimen
would withstand before failure appeared to be a
function of the amount of fiber reinforcement in
the specimen. In low volume percent reinforced
specimens the amount of deformation was great.
This meant that the stress required to cause the
reinforced specimen to deviate from a straight
line relationship was considerably less than the
stress required to cause complete failure of the
specimen. However, in high volume percent rein-
forced specimens the deformation was small. In
this case, the stress required to cause the rein-
forced specimen to deviate from a straight line
relationship was only slightly less than the stress
required to cause complete failure of the specimen.
It is conceivable that if it were possible to
produce dense specimens having a high volume
percentage of fiber reinforcement, then greater
deformation would be observed in such specimens
before failure occurred."

Figure 16 shows a fracture surface of a specimen where
it can be seen that fibers had actually been pulled out of
the ceramic matrix.

In a very recent study, DeBoskey and Hahn (Reference 2)
found that sapphire whiskers were amenable to incorporation,
still retaining their whisker morphology, in an Al_2O_3 body
by hot-pressing with a minor lithium fluoride addition.
They claimed that the presence of the whiskers in a nearly
dense body increased the strength of the body and changed
the mode of fracture to a more energy absorbing form. They
also noted that both higher density and greater strength-
ening occurred as the whisker size was decreased.

2. Oxidation of the Refractory Metal Fibers in Ceramic-
    Metal Composites

To better understand a small sampling of the experiments
conducted at Alfred University, an explanation of the method
of specimen preparation is necessary. The specimens were
hot-pressed in graphite molds where the inner surfaces of
each mold were treated with a wash of the matrix ceramic.
When the specimen was pressed, this coating became an inte-
gral part of the sample, and thus provided a surface essen-
tially free of fibers. The amount of such a coating on a
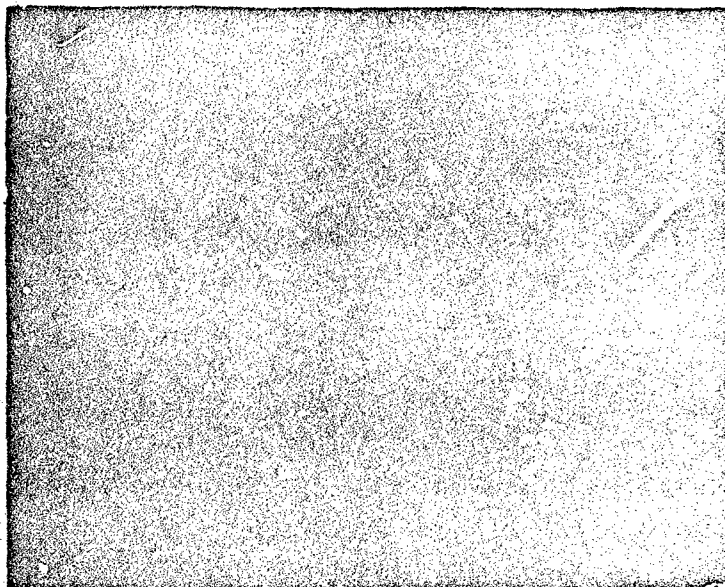specimen was determined by weighing the specimen after

Figure 16. Reinforced Specimen Fracture Showing
Fiber Protrusions (40X) (Reference 1.c.).

pressing and comparing this with the known weight of the
charged ingredients. The weight of the coating, in grams,
is shown by several of the figures referred to in the
discussion.

Figure 17 depicts an oxidation weight loss at 2700°F
(1490°C) for a composite which is typical of that of a
cracked system. In this case the porosities of the samples
were approximately the same but the weights of the coatings
varied. The oxidation rate was highest in the sample having
the lightest coating of fiber free ceramic. Figure 18
shows the oxidation results of a noncracked system, also at
2700°F(1490°C), and here the effect of the coating is again
evident. The porosities of these samples were uniformly
low. Sample Number 4 had no coating and the high oxidation
rate of the metal fibers is evident. Sample Number 5 was
recoated following hot-pressing in order to provide an even
thicker protective coat which resulted in a very low oxida-
tion rate.

Figure 19 presents a comparison of the oxidation behav-
iors of 2-mil versus 6-mil diameter molybdenum filament in
alumina (a cracked system) at 1032°F(1000°C). It is shown
clearly that the finer the filaments, the higher the oxi-
dation rates. This holds true, as is shown in Figure 20
for noncracked systems; although in this case, the oxidation
rates at 1832°F(1000°C) are substantially lower. Fiber-
free coatings were also employed on the specimens represented
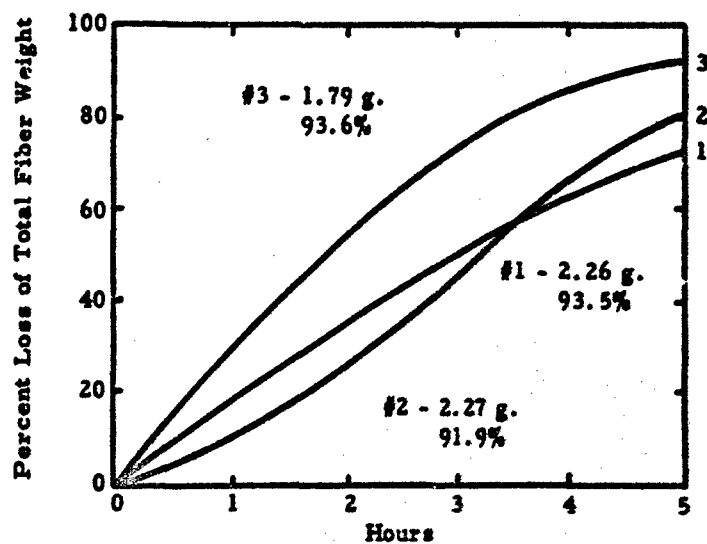by Figures 19 and 20.

Figure 17. Oxidation Weight Loss for Alumina + 15 Volume % Molybdenum Fiber (Cracked System) (Reference 1.c.).
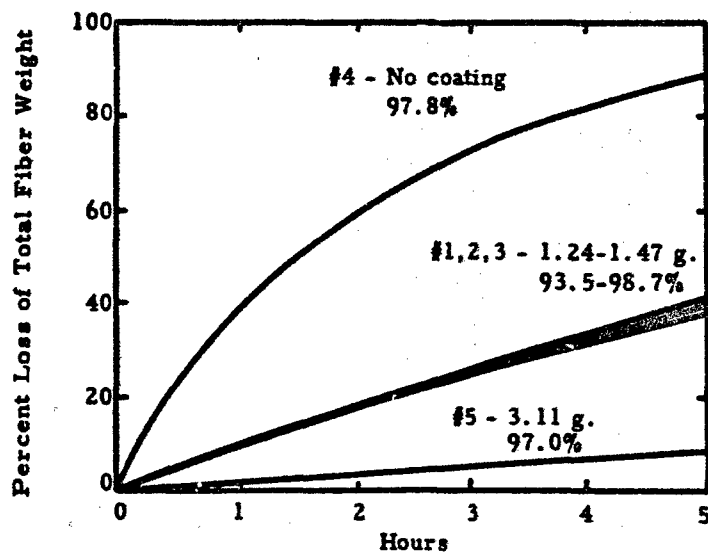

Figure 18. Oxidation Weight Loss for Composition 712 + 15 Volume % Molybdenum Fiber (Noncracked System) (Reference 1.c.).
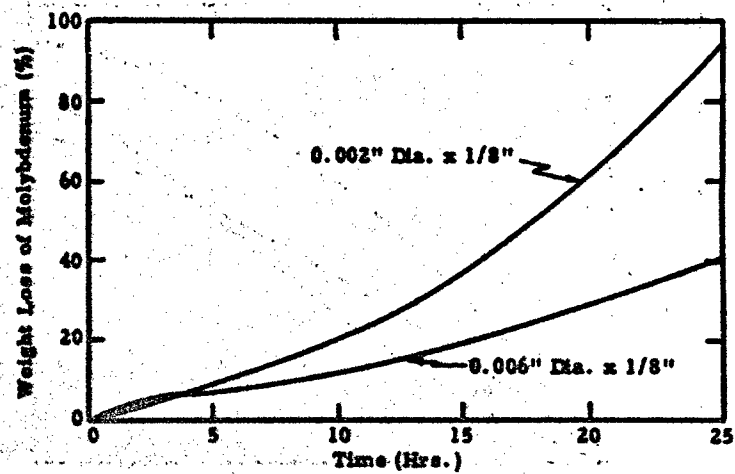
Figure 19. Percent Weight Loss by Oxidation for the Alumina-4.22 Volume % Molybdenum Fiber System (Cracked System) (Reference 1.b.).
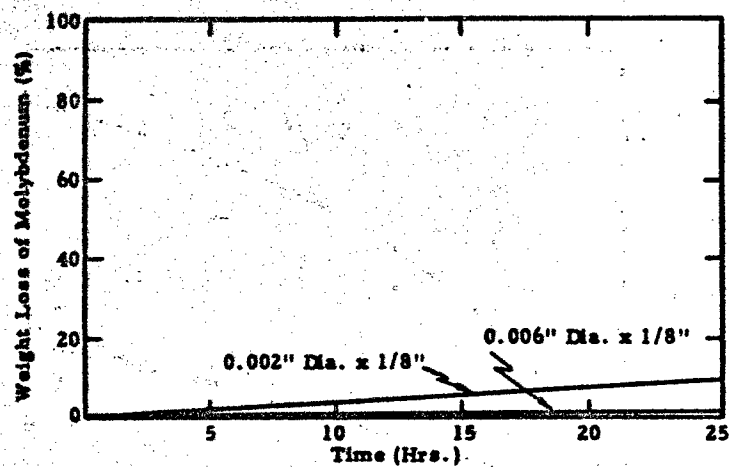

Figure 20. Percent Weight Loss by Oxidation for the Body 712-3.66 Volume % Molybdenum Fiber System (Noncracked System) (Reference 1.b.).

More examples of the oxidation behavior of metal fiber reinforced ceramics, though not particularly applicable to radome technology, may be found in Reference 3, 4 and 5.

3. Discussion

Metal-fiber reinforced ceramics were shown to improve both the strength and thermal shock resistance of noncracked combinations (References 1, 3, 6). Even in cracked combinations thermal shock resistance was improved, although at the expense of strength (References 1, 7). The thermal conductivities of metal-fiber reinforced ceramics were higher than unreinforced matrices, particularly at high temperatures (Reference 4). Strengths were attained that are considerably higher than those predicted by theoretical calculations, including the assumption of a prestressed matrix (Reference 3). Also, strength levels attained with random chopped fiber orientations (within a plane perpendicular to the pressing direction) were found to be equivalent to what was predicted (Reference 1) and experimentally found (Reference 6) for oriented fiber arrays. Finally, in addition to evidencing predictable failure locations in three point bend tests (viz. always at the point of maximum tensile stress), failures were not catastrophic but were instead gradual and accompanied by a substantial degree of inelastic deformation (Figure 21) (Reference 1).

In spite of the earlier imposing listing of the virtues of such composites, metal-fiber reinforced ceramics have enjoyed little attention since the completion of the work of Baskin, et al (References 4, 7) and that of the Alfred University group (Reference 1) in 1960. It appears that when attempts were made to extend such an approach from convenient model materials to materials that would serve some meaningful purpose, particularly at the high temperatures where ceramics are normally considered for use, expansion coefficient mismatches, matrix-fiber interactions during processing or at use temperatures, and reinforcement oxidation proved to be formidable obstacles.

However, the recent work of DeBoskey and Hahn (Reference 2), involving sapphire whiskers in an Al_2O_3 body, seemingly offers new possibilities for improving the mechanical and thermal shock/stress behavior of ceramic radomes/windows. Additionally, it is felt that some possibilities still exist for utilizing metal fiber reinforced ceramics to advantage in radomes, particularly with Al_2O_3 and BeO matrices where low to negligible oxygen diffusion rates, even at rather high temperatures, have been reported (Reference 8). Not only could consideration be given to the areas adjacent to attachment points but additionally, frontal protions subjected to high thermal stresses might tolerate some small percentage of metallic additions. Although it is understood that theoretical calculations have indicated the tolerable levels/sizes/arrangements of metallic inclusions or supports, researchers associated with radome technology have appeared
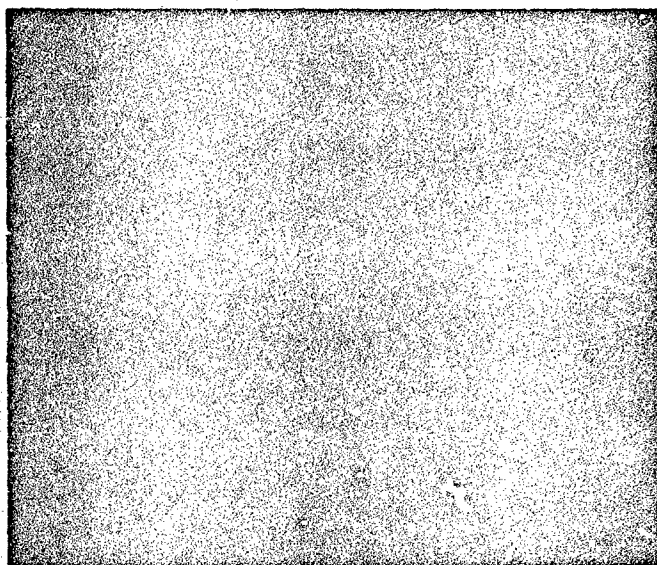
Figure 21. Reinforced Specimen Still Intact After Failure (Reference 1.c.).

dubious. No references of dielectric constant and loss tangent measurements of ceramics containing low percentage additions of metal fibers can be found and it would thus appear that some measurements in the near future would be desirable and instructive.

POSSIBLE MATRIX-FIBER COMBINATIONS

This section will consider the thermal expansion and thermochemical compatibilities of matrices of Al_2O_3, BeO, and $MgO \cdot Al_2O_3$ with reinforcements of filamentary W, Mo, Ta, B, C, SiC, B_4C, and Al_2O_3. Fused silica is not discussed for a number of reasons. Its exceptionally low coefficient of thermal expansion (CTE) usually obviates failures due to thermal shocks and stresses and such types of failures represent a major purpose for utilizing the composite approach. Should one be interested in the use of reinforcements in fused silica for strengthening purposes or to alter the mode of fracture, CTE compatibility would exist with any selected filament and attention then would be directed only to thermochemical compatability considerations, matrix-reinforcement bonds, and the amount of residual compressive stresses desired.

1. W and Mo Filaments

Gitzen indicates that alumina is not reduced by molybdenum even above the melting point of alumina (Reference 9). Grossman (Reference 10) reports a pseudobinary eutectic for $W-Al_2O_3$ as 1997 $\pm20°C$ (3627 $\pm36°F$). Ryshkewitch (Reference 11) notes National Beryllia's experience, viz. that BeO sintered in hydrogen does not react with W or Mo up to 2000°C (3632°F) for several hours although at higher temperatures under vacuum or argon atmosphere, reaction was observable. Brown (Reference 12) indicated that in a hydrogen atmosphere at temperatures up to 1800°C (3272°F), sintered BeO showed no interaction with Mo even after hundreds of hours.

Kieffer and Benesovsky (Reference 13) in describing the stability of high temperature heating element materials toward oxides, note that Al_2O_3 is compatible with both Mo and W "up to 1900°C," irrespective of environment. They also note, in "up to" terms, the following temperature limits for an environment of 10^{-4} torr and in each case about 100-200°C (180-360°F) less for a protective gas environment owing to the "usual residual impurities": BeO-Mo, 1900°C (3452°F) and BeO-W, 2000°C (3632°F).

An earlier investigation by Johnson (Reference 14) employed documented and relatively pure oxides. Powder mixtures were dry-pressed and then subjected to a degassing treatment followed by a series of time-temperature treatments in a vacuum of 0.1-0.5μ. Temperatures at which surface

stability no longer existed in surface-to-surface contact after the indicated number of minutes are indicated as follows: BeO-Mo, 1900°C(3452°F), 4 minutes and BeO-W, 2000°C(3632°F), 2 minutes. The validity of Johnson's data is certainly enhanced by the excellent agreement achieved, however qualitative, by Kieffer and Benesovsky.

Results by White (Reference 15) generally support the preceding. Recent research by Grossman and Kaznoff (Reference 16) also supports the above findings relative to Al_2O_3-W and BeO-W, but they differ significantly relative to these oxides with Mo.

Based upon the previous information and the composite studies described earlier, thermochemical compatibility, at least to processing temperatures, may be expected for these metals in combination with $MgO \cdot Al_2O_3$, the only oxide for which no compatibility data may be found.

Combinations of the three oxides with W and Mo are incompatible from a CTE standpoint and microcracked systems are expected (Reference 17, 18). Recalling the earlier discussion of the oxidation behavior of metal reinforced ceramics, it would appear that even for temperatures greater than 1200-1500°C(2192-2732°F) and for periods of time greater than 5 to 10 hours, Al_2O_3 and BeO can be considered with either Mo or W filaments due to the very low permeability of these oxides to oxygen (Reference 8). Fiber additions should be kept low, preferably less than 5 volume %, to preclude or minimize cracking and fiber free "skins" or surface layers should be as thick as can be tolerated. Such composites should provide an "all environment" capability which is particularly important since the combination of high temperature and vacuum is often encountered in aerospace applications.

2. Ta Filaments

Grossman and Kaznoff (Reference 16) as a result of compatibility experiments in a nuclear thermionic fuel element environment have estimated the following temperatures as upper limits to long term compatibility, under reducing conditions, between Ta and the indicated oxides: Al_2O_3-1000°C (1832°F) and BeO-1500°C(2732°F). Brewer and Searcy (Reference 19) found the volatilization of Al_2O_3 much greater when Al_2O_3 was heated in Ta than when heated in W. Later work by Drowart, et al (Reference 20) and Chupka, et al (Reference 21) also indicated, during mass spectrometer studies, that W does not have the reducing power of Ta or Nb. Navias (Reference 22) conducted experiments involving the heating of sapphire by W and Ta, neither of which were in contact with the sapphire. His experiments with Ta at a vacuum of 3 µ resulted in deposits of Al on the surrounding glass bulb at 1600°C (2192°F) while with W and a vacuum of 10^{-2}-10^{-4}µ, no deposit of Al was noted even at temperatures of 1900°C(3452°F). Kieffer and Benesovsky (Reference 13), under conditions noted

160

earlier, described Al_2O_3 and BeO as being stable in the presence of Ta up to temperatures of 1900°C(3452°F) and 1600°C(2912°F) respectively. It would appear that the environment as well as the degree of surface to surface contact may be more critical in the case of Ta than with W or Mo. Certainly, for use in high temperature air environments and the problem of permeability to oxygen, Al_2O_3 and BeO are considered reasonable condidates for reinforcement by Ta. Processing will present a problem and the reaction thresholds of nominally 1000°C(1832°F) and 1500°C (2732°F) between Ta and Al_2O_3 and BeO respectively are to be avoided. "Pressure calcintering", a relatively new low temperature processing technique (Reference 23), might certainly be utilized advantageously to minimize the relative magnitudes of differential thermal contractions following high temperature consolidation. Though the CTE of Ta exceeds that of W and Mo, it is still low enough below the oxides such that all of the above indicated systems are expected to be microcracked.

3. B Filaments

The mechanical properties of present day B filaments degrade severely and permanently, as a result of any extended exposure (~several hours) at temperatures of nominally 800°C(1472°F) and higher (Reference 24) and neither Al_2O_3, BeO, nor spinel offer the potential, thus far, of consolidation to near theoretical density by any means at such low temperatures. With respect to the severe debilitating effects of even minor additions of B_2O_3 (which might well form during processing) on such oxides, Reference 25 will be found to be most descriptive. Chemical vapor deposition of thin films of oxides on B filament is being considered to improve compatibility with nonceramic matrices (Reference 26) and this approach might well prove interesting in terms of thick oxide bodies. Maximum use temperature capabilities of such systems naturally are limited to 800°C(1472°F).

4. C Filaments

Johnson (Reference 27) studied BeO-C by means of changes in bulk density, shrinkage, and weight of dry pressed specimens which were fired for 2, 4, and 8 minutes in vacuum and the lowest temperature of reaction was 2300°C(4172°F). Kroll and Schlechten (Reference 28) briquetted their powdered reactants and obtained the following rather low temperatures at which a noticeable breakdown of the reactant occurred, in vacuum: BeO-1315°C(2399°F) and Al_2O_3-1350°C(2462°F). Nadler and Kempter (Reference 29), employing thermodynamic considerations with respect to five oxides, obtained the following decreasing order of stability towards carbon: BeO, ThO_2, Al_2O_3, MgO, and ZrO_2. Klinger, Coucoulas, and Komarek (Reference 30) studied reactions between Al_2O_3, and spinel (MgO·3.3 Al_2O_3) and graphite in vacuum by measuring the amount of carbon monoxide formed. They found diffusion controlled reactions between Al_2O_3 and BeO with C and phase

161

boundary controlled reactions between BeO and spinel with C. They found the relative stabilities of the oxides in contact with graphite, in order of decreasing stability, to be: BeO, spinel, and Al_2O_3. Table II cites the specific rates of reations between oxides and graphite, as determined by Klinger, et al while Table III cites their determined stabilities, with the applicable data, associated with a 0.1% reduction in 900 seconds.

Criscione, et al (Reference 31) reported a minimum reaction temperature, defined as the temperature where the CO pressure became noticeable, "i.e. a few torr," 1300°C (2372°F) for BeO.

As to CTE relationships, it is expected that all of the above oxides, when reinforced with C, would be microcracked. However, under one investigation involving C filaments and an oxide having one of the highest CTE's, viz. MgO, cracks were not observed for the only reinforcement level studied, 5 volume % (Reference 32), which was prepared by pressure calcintering at 1200°C(2192°F).

For air environments, oxygen permeability considerations place an additional constraint upon C-MeO systems. However, it would appear that Al_2O_3 and BeO could be utilized for extended times at temperatures not exceeding 1200°C(2192°F). Reinforcement levels should be minimized to preclude cracking and as indicated earlier, fiber-free "skins" should be as thick as can be tolerated.

5.   SiC Filaments

Patents awarded to Riddle (Reference 33) and Pieper (Reference 34) refer to strengths of Al_2O_3-SiC mixtures at 1405°C(2642°F) and firing or consolidation of same at 1650°C (3002°F), respectively. Alumina is recognized as one of the most stable refractory compounds and is said to be stable in oxidizing or reducing atmospheres to 3500°F for short periods of time (Reference 35). Accordingly, one would expect it to be stable in the presence of SiC to an equivalent temperature, thus reducing considerations primarily to mechanical compatibility.

While the combinations of Al_2O_3, BeO, or spinel with SiC are expected to form microcracked systems, microcracks have not been found in pressure calcintered MgO-SiC (although some unexplained interaction might have altered this system somewhat).

For air environments, oxygen permeability considerations again are applicable. The product of the oxidation of SiC, viz. SiO_2 wrecks havoc with the phase stability (and naturally the properties) of each of the oxides, as may be seen in the phase diagrams of Reference 25. Accordingly, Al_2O_3 and BeO again appear favorable where for extended times, temperature of up to 1500°C(2732°F) might be tolerated. Previously made comments relative to amounts of fiber additions and thickness of fiber-free "skins"

TABLE II

SPECIFIC RATES OF REACTIONS BETWEEN OXIDES AND GRAPHITE (Reference 30)

Oxide	Temperature Range °K	Specific Rate	
MgO	1625 - 1831	K_1	$6.34 \times 10^{-2} \exp(-59,800/RT)$
Spinel	1888 - 1938	K_1	$1.82 \times 10^{-2} \exp(-59,500/RT)$
BeO	2018 - 2186	K_1	$7.64 \times 10^{-3} \exp(-61,300/RT)$
Al_2O_3	1580 - 1723	k_p	$2.42 \times 10^{28} \exp(-316,000/RT)$
BeO	1788 - 2018	k_p	$1.01 \times 10^{-.0} \exp(-40,000/RT)$

TABLE III

STABILITIES OF OXIDES AND GRAPHITE
(Reference 30)

Oxide	Moles CO Evolved for 0.1% Reduction	Rate Constant for 0.1% Reduction in 900 Seconds	Temperature for 0.1% Reduction in 900 Sec.
Al_2C_3	119×10^{-8}	8.34×10^{-16} $(moles)^2-(sec)^{-1}$	1316°C
MgO	91×10^{-8}	1.01×10^{-9} $moles-(sec)^{-1}$	1404°C
$MgO \cdot 3.3Al_2O_3$	107×10^{-8}	1.19×10^{-9} $moles-(sec)^{-1}$	1532°C
BeO	118×10^{-8}	1.31×10^{-9} $moles-(sec)^{-1}$	1707°C

163

are also applicable hereto.

6. B_4C Filaments

The reactions of metal oxides with B_4C are well recognized and usually employed in the presence of carbon to form the borides. This borocarbide process (Reference 36) usually leads to better results when carried out under vacuum (Reference 37) and has resulted in the formation of TiB_2 from TiO_2 at temperatures as low as 1100-1150°C(2012-2102°F). However, temperatures of nominally 2000°C(3612°F) are usually employed.

Composites of the oxides and B_4C must necessarily be utilized at relatively low temperatures not only to avoid interaction but also to avoid oxidation of the reinforcement and the resulting formation of B_2O_3. Problems with such composites are compounded by the relatively low CTE of B_4C which should result in all systems being microcracked. Earlier comments relative to oxygen permeability, low levels of reinforcements, and thick fiber-free "skins" apply hereto. It would appear that only by means of pressure calcintering or chemical vapor deposition might one obtain composites of reasonable integrity.

Metal oxides--B_4C systems are thus fraught with such obstacles in both preparation and use that no detailed information has apparently ever been generated as to the temperature levels at which such materials might be employed.

7. Al_2O_3 Filaments

a. Al_2O_3 - Al_2O_3

DeBoskey and Hahn (Reference 2) have indicated that higher strengths have been obtained by means of an Al_2O_3 - Al_2O_3 approach, thus suggesting that even by means of ordinary processing techniques, some filaments or fragments of filaments retain their integrity and contribute to the system's overall effectiveness. It would appear that studies of powder particle size in relation to filament length and diameter might now be profitably pursued. Also, pressure calcintering might offer considerable promise in terms of decreasing the extent of filament damage during processing.

b. Al_2O_3 - BeO

Three intermediate equilibrium phases occur in this binary system, $3BeO \cdot Al_2O_3$, $BeO \cdot Al_2O_3$, and $BeO \cdot 3Al_2O_3$ (Reference 38). Since no studies of subsolidus kinetics have been documented, the extent of the reactions taking place below 1835°C(3335°F), the lowest eutectic temperature of the system, are unknown. CET's for these components are sufficiently close (that of BeO exceeds that of Al_2O_3) that should one satisfactorily prepare a composite without extensive reaction, in all probability it will not be cracked (Reference 17). Use temperatures, like processing temperatures, cannot be estimated.

164

c. Al_2O_3 - $MgO \cdot Al_2O_3$

The boundary of the spinel solid solution extends from the 50 MgO-50 Al_2O_3 composition to nominally 85 mole % Al_2O_3 at the spinel - Al_2O_3 eutectic, nominally 1910°C (3470°F), with the sharpest increases in the homogeniety range of the Al_2O_3 side occurring above 1400°C(2552°F) (Reference 39).[2] From normal temperatures to nominally 1315°C(2400°F) the CTE's are compatible and a non-cracked system would be expected. The major problem anticipated is that of achieving a nominally 99% dense spinel matrix at temperatures below about 1400°C(2550°F) and again, pressure calcintering might be utilized advantageously. This would involve the use of a mixed hydroxide or another suitable combination of salts.

DISCUSSION AND CONCLUSIONS

It has been shown that despite a number of virtues of fiber reinforced ceramics, as demonstrated with model materials, the present technology has not yet been able to capitalize on this approach to achieve more thermally shock resistant ceramics having predictable mechanical integrity. This inability to extrapolate model behavior to "real" or technologically interesting materials has been considered and found to stem from several factors. Thermochemical interaction has been shown to prevent the utilization of many combinations of reinforcements and matrices owing to reactions at intended use temperatures or at processing temperatures where these exceed the use temperatures. Approaches to overcome interaction problems, where processing temperatures exceed use temperatures, include lower temperature processing techniques such as pressure calcintering. Decomposition processes involving both salts and metal-organic compounds also warrant consideration. Chemical vapor deposition processes may well deserve some attention since the unusual "throwing" power of some of these processes offers the possibility of achieving high density matrices with high volume fractions of undamaged reinforcements at low temperatures. Microcracks, sometimes tolerable, caused by differential thermal contraction following densification at high temperatures when the CTE of the matrix exceeds that of the reinforcement, might be avoided by lower temperature processing as well as by a composite filament approach.

Early reinforcement oxidation studies indicated this aspect to represent a formidable problem, even at temperatures as low as 1000°C (~1800°F) for many reinforced oxides (Reference 3). However, this is not anticipated to be a significant consideration with dense, uncracked Al_2O_3 and BeO which are, for practical purposes, essentially[2] impermeable to oxygen. Oxidation of reinforcements has been

shown to either result in the mechanical disruption of the composite or degradation owing to reaction between the oxidation product and the matrix (Reference 4).

The need for studies of the "micromechanics" of reinforced ceramics has been indicated, as has the need for studies of subsolidus kinetics in some systems. Of particular interest is the matrix-reinforcement bond and one wonders how a good bond might affect properties and mechanical behavior. In the Alfred work described earlier, it was apparent that little, if any, matrix-reinforcement bond existed and Figure 16 is offered as evidence of this.

Chromium filaments were not considered in this review since none are available. However, because of its high CTE (Reference 40) and its compatibility with Al_2O_3 as shown by much cermet work during the early to mid 1950's, chromium should prove to be an ideal reinforcement for Al_2O_3 and perhaps also for BeO.

REFERENCES

1. a. R. S. Truesdale, J. J. Swica, and J. R. Tinklepaugh, "Metal Fiber Reinforced Ceramics." Prepared under Contract No. AF33(616)-5298, State University of New York, College of Ceramics at Alfred University, Alfred, New York, WADC TR 58-452, December 1958

    b. J. J. Swica, W. R. Hoskgus, B. R. Goss, J. H. Connor, and J. R. Tinklepaugh, "Metal Fiber Reinforced Ceramics." Prepared under Contract No. AF33(616)-5298, State University of New York, College of Ceramics at Alfred University, Alfred, New York, WADC TR 58-452, Part II, January 1960.

    c. J. R. Tinklepaugh, B. R. Goss, W. R. Hoskgus, J. H. Connor, and D. D. Button, "Metal Fiber Reinforced Ceramics." Prepared under Contract No. AF33(616)-5298, State University of New York, College of Ceramics at Alfred University, Alfred, New York, WADC TR 58-452, Part III, November 1960.

2. W. R. DeBoskey, and H. Hahn, "Opaque Lightweight Armor," Prepared under Contract No. N178-9003, Melpar, Inc., Falls Church, Virginia, Final Report, November 1967.

3. D. G. Miller, R. H. Singleton, and A. V. Wallace, "Metal Fiber Reinforced Ceramic Composites," Amer. Ceram. Soc. Bul., 45 (5) 513-17 (1966).

4. Y. Baskin, Y. Harada, and J. H. Handwerk, "Some Physical Properties of Thoria Reinforced by Metal Fibers," Journ. Amer. Ceram. Soc., 43 (9) 489-492 (1960).

5. M. R. Licciardello, B. Ohnysty, and A. R. Stetson, "Development of Frontal Section for Super-Orbital, Lifting, Re-entry Vehicle, Volume II, Materials and Composite Structure Development." Prepared under Contract No. AF33(616)-8497, Solar, a Division of International Harvester Company, San Diego, Calif., FDL-TDR-64-59, 29 May 1964.

6. S. Bortz, Private communication pertaining to an aluminum oxide-borosilicate glass containing stainless steel filaments.

7. Y. Baskin, C. A. Arenberg, and J. H. Handwerk, "Thoria Reinforced by Metal Fibers," Amer. Ceram. Soc. Bul., 38 (7) 345-48 (1959).

8. J. M. Criscione, S. Sarian, H. F. Volk, R. A. Mercuri, J. W. Nuss, and P. W. Meszaros, "High Temperature Protective Coatings for Graphite." Prepared under Contract Nr AF33(657)-11253, Carbon Products Division, Union Carbide Corp., Parma, Ohio ML-TDR-64-173, Part IV, November 1966.

9. W. H. Gitzen, "Alumina Ceramics," Prepared under Contract Nr AF 33(657)-8741, Ohio State University Research Foundation, Columbus, Ohio, AFML-TR-66-13, January 1966.

10. L. N. Grossman, "High Temperature Thermal Analysis of Ceramic Systems." Presented at the Annual Meeting, American Ceramic Society, Washington, D.C., April 1966.

11. E. Ryshkewitch, "Beryllium Oxide Ceramics-Processes, Properties and Applications." Prepared under Contract Nr AF33(615)-1621, National Beryllia Corporation, AFML-TR-65-378, May 1966.

12. R. J. Brown, in a report presented before the International Conference on Beryllium Oxide, Sydney, Australia, October 1963.

13. R. Kieffer and F. Benesovsky, "Metallic Heating Element Materials for High Temperature Furnaces," Metallurgia, 58 (September 1958).

14. P. D. Johnson, "Behavior of Refractory Oxides and Metals, Alone and in Combination in Vacuo at High Temperatures," Journ. Amer. Ceram. Soc. 33 (5), 168-171 (May 1950).

15. J. E. White, "Observations on the Effect of Vacuum Heat-Treatment (up to 4000°F) on Dispersions of Various Oxides, Nitrides, and Borides in Molybdenum," Powder Metallurgy, 8, 15, 1965.

16. L. N. Grossman and A. I. Kaznoff, "Insulators for Thermionic Energy Converter Application." In the Proceedings of the Conference on Nuclear Applications of Nonfissionable Ceramics, Washington, D.C., May 1966.

17. J. F. Lynch, G. G. Ruderer, and W. H. Duckworth, "Engineering Properties of Ceramics." Prepared under Contract No. AF33(615)-2316, Battelle Memorial Institute, Columbus, Ohio, AFML-TR-66-52, June 1966.

18. A. Goldsmith, T. E. Waterman, and H. J. Kirschhorn, "Thermophysical Properties of Solid Materials, Vol. I - Elements." Prepared under Contract No. AF33(616)-5212, Armor Research Foundation (now IIT Research Institute), Chicago, Illinois, WADC TR 58-476, Vol. I., August 1960.

19. L. Brewer and A. W. Searcy, "The Gaseous Species of the Al-Al$_2$O$_3$ System" J. Am. Chem. Soc. $\underline{73}$ (11) 5308-14, 1951.

20. J. Drowart, et al., J. Chem. Phys., $\underline{32}$, 1366-1373 (1960).

21. W. A. Chupka, J. Berkowitz, and C. F. Giese, J. Chem. Phys. $\underline{30}$, 827 (1959).

22. L. Navias, "Comparison Between Al$_2$O$_3$-Ta and Al$_2$O$_3$-W Reactions Above 1600°C in a Vacuum," Amer. Ceram. Soc. Bul., $\underline{38}$ (5) 256-59 (1959).

23 P. E. D. Morgan and N. C. Schaeffer, "Chemically Activated Pressure Sintering of Oxides." Prepared under Contract Nr AF33(615)-3065, Cornell University, Ithaca, N. Y., AFML-TR-66-356, November 1966.

24. J. A. Herzog, Private Communication.

25. E. M. Levin, C. R. Robbins, and H. F. McMurdie, Phase Diagrams for Ceramists, American Ceramic Soc., Inc., Columbus, Ohio, 1964.

26. C. T. Lynch, Private Communication.

27. P. Johnson, Journ. Amer. Ceram. Soc. $\underline{33}$ (1950) 168.

28. W. J. Kroll and A. W. Schlechten, Trans. Electrochem. Soc. $\underline{93}$ (1948) 247.

29. M. R. Nadler and C. P. Kempter, Rev. Sci. Inst. $\underline{32}$ (1961) 43-47.

30. N. Klinger, A. Coucoulas, and K. L. Komarek, "Study of the Reaction Rates Between Refractory Oxides and Graphite." Prepared under Contract Nr AF33(616)-6082, New York Univ., N. Y., N. Y., AFL 62-325, April 1962.

31. J. M. Criscione, H. F. Volk, J. W. Nuss, R. A. Mercuri, S. Sarian, and F. W. Meszaros, "High Temperature Protective Coatings for Graphite." Prepared under Contract No. AF33(657)-11253, Carbon Products Div., Union Carbide Corp., Parma, Ohio, ML-TDR-64-173, Part III, December 1965.

32. E. Scala, Private communication relative to work in process at Cornell University under Contract No. AF33 (615)-3065.

33. F. H. Riddle, "Alumina & Silicon Carbide Refractory. "U.S. 2,388,080,10/30/45.

34. A. D. Pieper, "Process of Making Refractory Material." U.S. 2,770,552, 11/13/56.

35. I. E. Campbell, High Temperature Technology, John Wiley and Sons, New York (1957).

36. R. Kieffer, F. Benesovsky, and E. Honak, Z. anorg. Chem., 268, 191-200, 1952.

37. G. A. Meerson, G. V. Samsonov, ZhPKh (Journ. Applied Chem), 27, 1954, 1115-1120.

38. As presented in Reference 25 with data from S. M. Long, C. L. Fillmore, and L. H. Maxwell, Journ. Res. Nat'l. Bur. Stds., 48 (4) 301, 1952; RP 2316 and Galakhov, F. Ya., Izvest. Akad. Nauk S.S.S.R., Otdel. Khim. Nauk, 1035 (1957).

39. D. M. Roy, R. Roy, and E. F. Osborn, Journ. Amer. Ceram. Soc., 36 (5) 149, 1953. (Diagram may be found in Reference 25)

40. Y. S. Touloukian, Thermophysical Properties of High Temperature Solid Materials, Vol. I, Macmillan, 1967.

A THERMAL ANALYSIS OF AN

ABLATING ELECTROMAGNETIC WINDOW

by

LT RICHARD C. BUGGELN

AIR FORCE WEAPONS LABORATORY

KIRTLAND AFB, NEW MEXICO   87117

ABSTRACT

A numerical technique has been developed to determine the recession
and temperature profiles for subliming electromagnetic windows on reentry
vehicles at any point in the vehicle trajectory. The technique utilizes
a new coordinate transformation to solve the time-dependent one-dimensional
heat conduction equation subject to the appropriate boundary conditions.
Use of the transformation results in a decrease of computation time by
almost an order of magnitude over previously used techniques. The numeri-
cal technique was programmed for use on the CDC 6600 computer and several
samples cases were run.

INTRODUCTION

A vehicle reentering the earth's atmosphere at hypersonic velocities is subjected to severe environmental conditions in the form of high heat-transfer rates, temperature and structural loads. Antennas for these vehicles generally take the form of a slot array or other slot closure located well aft of the stagnation point on the vehicle. In order to protect these antennas and the internal equipment from excessive heat, use is made of ablative dielectric materials which covers the apertures of the antennas. The high heating rates encountered during reentry produce changes in both the physical and electrical properties of these window materials. Therefore, the window design should be a compromise between the minimum acceptable thickness to protect the antenna, considering the expected heating rates and recession due to ablation, and the transmission loss of the window during the most critical phase of the mission. To aid in the thermal design of electromagnetic (EM) windows, a computer program has been developed to determine window recession and the temperature profiles in the window as a function of any point in the vehicle trajectory.

DESCRIPTION OF THE PROBLEM

Consider the model shown in Figure 1. When a heat flux, Q, is applied to the front face of an electromagnetic window, a temperature rise results throughout the window material. At a later time the front face reaches the ablation temperature, T_{AB}, and the surface starts to recede at a rate $\dot{s}(t)$. The mathematical treatment of the above phenomena consists of three parts: (1) The equation governing the heat flow in the window material, (2) the front face boundary condition, and (3) the back face boundary condition.

To simplify the mathematical analysis, several assumptions are made. First, heat conduction in the window is assumed to be one-dimensional and the ablation process occurs by sublimation only. Second, the thermophysical properties of the window material, specific heat, thermal conductivity, and emissivity are temperature dependent and, third, the ablation temperature is a function of the boundary layer edge pressure only. The gas surrounding the reentry vehicle is assumed to be ideal; however, the specific heat, enthalpy, and viscosity are functions of temperature. For the cases considered in this paper, the back face of the EM window is assumed to be thermally insulated. In a subliming ablator the internal heat flow is governed by the heat conduction equation

$$\rho c_p \frac{\partial T}{\partial t} = \frac{\partial}{\partial x}\left(k \frac{\partial T}{\partial x}\right)$$
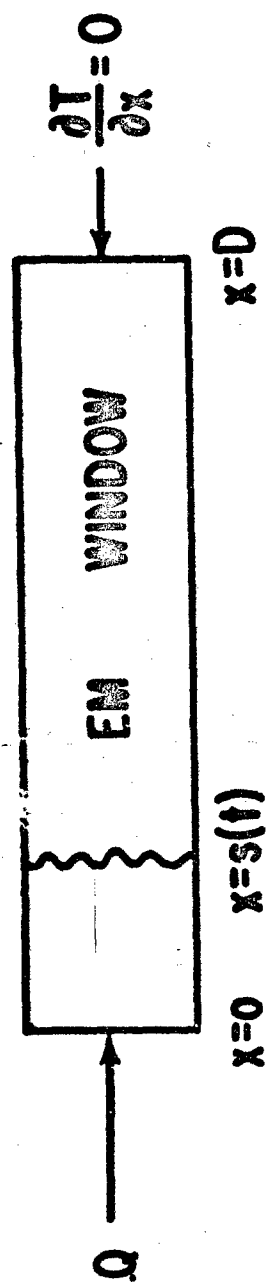
(1)

172

FIGURE 1. ONE DIMENSIONAL WINDOW

where

T is temperature

t is time

ρ is density

c_p is heat capacity

k is thermal conductivity

For a thermally insulated window the back face boundary condition is given by

$$\left.\frac{\partial T}{\partial x}\right|_{x = D} = 0 \tag{2}$$

The boundary condition at the front face of the EM window depends on whether the window is ablating. When the window is not ablating $\left(T_{wall} < T_{AB}\right)$ the energy balance gives

$$Q_{co} - Q_r = Q_{cond} = -k \left.\frac{\partial T}{\partial x}\right|_{x = s} \tag{3}$$

Where Q_{co} is the nonablating convective heat transfer rate to the surface, Q_r is the total radiative heat transfer away from the surface, and Q_{cond} is the heat conducted into the window material.

When the window ablates, the effective convective heat transfer rate to the surface decreases. For a subliming ablator, this decrease is caused by three mechanisms: (1) Energy, ΔE, is absorbed due to the change of phase of the ablation material, (2) the ablation material products react with the free stream gases, and if the reactions are endothermic, an amount of energy, ΔE_c, is absorbed, (3) ablation materials diffuse into the boundary layer and cause it to become thicker. This reduces the temperature gradient between the boundary layer edge and the ablating surface which in turn decreases the convective heat transfer rate.

Figure 2 depicts the surface reaction zone energy balance. The energy balance can be written

$$Q_{cond_{gas}} + \rho \dot{s} h \left(T_{AB}\right) + k \left.\frac{\partial T}{\partial x}\right|_{x = s} - Q_r - \rho \dot{s} \left(\Delta E + \Delta E_c\right) = 0 \tag{4}$$

where $h \left(T_{AB}\right)$ is the enthalpy of the ablator material evaluated at the ablation temperature, and $Q_{cond_{gas}}$ is the gaseous conduction term which is equal to the convective heat transfer rate with ablation, Q_c

$$Q_{cond_{gas}} = Q_c \tag{5}$$

174
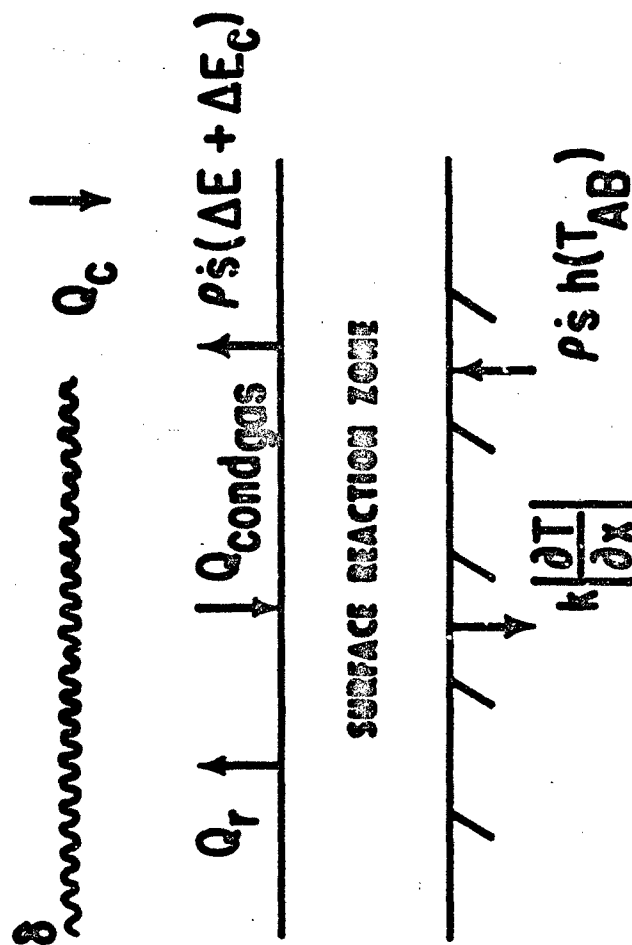
FIGURE 2. SURFACE REACTION ZONE ENERGY BALANCE

175

The relationship between the convective heat transfer rates with and without ablation is

$$Q_c = Q_{co} - L\rho\dot{s}\,\Delta h \tag{6}$$

where L is obtained from a correlation of experimental data (Ref 1) which is different for laminar and turbulent flow. Δh is the boundary layer enthalpy potential, i.e., the recovery enthalpy minus wall enthalpy.

Substitution of Equations (5) and (6) into Equations (4) yields the front face boundary condition for a subliming ablator.

$$\dot{s} = \frac{1}{\rho} \left[\frac{Q_{co} - Q_r + k\left.\frac{\partial T}{\partial x}\right|_{x=s}}{L\Delta h + \Delta E + \Delta E_c - h\left(T_{AB}\right)} \right] \tag{7}$$

To simplify Equation (7) the concept of an effective heat of ablation, $\overline{H}_{eff}$, is used. It is defined by

$$\overline{H}_{eff} = \frac{Q_{co} - Q_L}{\rho\dot{s}} \tag{8}$$

where

$$Q_L = -k\left.\frac{\partial T}{\partial x}\right|_{x=s} - \rho\dot{s}h\left(T_{AB}\right) + Q_r \tag{9}$$

Substitution of Equation (7) and (9) into Equation (8) yields:

$$\overline{H}_{eff} = L\Delta h + \Delta E + \Delta E_c \tag{10}$$

Hence, Equation (7) becomes

$$s = \frac{1}{\rho} \left[\frac{Q_{co} - Q_r + k\left.\frac{\partial T}{\partial x}\right|_{x=s}}{\overline{H}_{eff} - h\left(T_{AB}\right)} \right] \tag{11}$$

The terms ΔE and ΔE_c are determined from an equilibrium thermo-chemistry program for specified temperature, pressure, and element ratios. In general, $\overline{H}_{eff}$ is not a linear function of Δh since the term $\left(\Delta E + \Delta E_c\right)$ is dependent upon combustion reactions in the boundary layer. However, for most ablation materials, the linear dependence of $\overline{H}_{eff}$ on Δh is a good approximation.

NUMERICAL PROCEDURE

The heat conduction equation with appropriate boundary conditions is solved by using an explicit finite difference technique that employs a new coordinate transformation. The transformation allows the physical spacial step size to vary with both position in the window and time while the computational step size remains constant. Thus, the problems of a large temperature gradient at the front face of the windows and a receding boundary that make standard finite difference techniques unwieldy and time consuming are circumvented.

The transformation can be written as

$$T(x,t) \rightarrow T(\xi(\eta), t) \tag{12}$$

where

$$\eta = \frac{x-e}{D-s} \tag{13}$$

and $\xi(\eta)$ is called the stretching parameter. The range of η is 0 to 1 as x varies between s and D. The stretching parameter, $\xi(\eta)$, is arbitrary but for the present use it is desirable to define it such that the spacial step size, Δx, is very small (on the order of 5×10^{-3} cm) at the front face and gradually increases as the back face is approached.

Applying the transformation to the heat conduction equation yields

$$\frac{\partial T}{\partial t} = \frac{s}{D-s} \, B \, \frac{\partial T}{\partial \xi} + \frac{1}{\rho c_p} \, (D-s)^2 \left[CTXX + E \, k \, \frac{\partial T}{\partial \xi} \right] \tag{14}$$

where

$$B = (1-\eta) \, \frac{d\xi}{d\eta} \tag{15}$$

$$C = \left(\frac{d\xi}{d\eta} \right)^2 \tag{16}$$

$$E = \frac{d\xi}{d\eta} \, \frac{d}{d\xi} \left(\frac{d\xi}{d\eta} \right) \tag{17}$$

and

$$TXX = \frac{\partial}{\partial \xi} \left(k \, \frac{\partial T}{\partial \xi} \right) \tag{18}$$

177

A convenient relationship between η and ξ is given by:

$$\eta = \frac{\xi\left(\xi^n + c_1\right)}{1 + c_1} \qquad (19)$$

where n and c_1 are constants. The range of ξ is 0 to 1 as η varies between 0 and 1. (This is convenient but not necessary). Using Equation (19) the expressions for B, C, and E become

$$B = \frac{1 + c_1 - \xi\left(\xi^n + c_1\right)}{(n + 1)\,\xi^n + c_1} \qquad (20)$$

$$C = \left[\frac{1 + c_1}{(n + 1)\xi^n + c_1}\right]^2 \qquad (21)$$

$$E = \frac{\left(1 + c_1\right)^2 n\,(n + 1)\,\xi^{n-1}}{\left[(n + 1)\xi^n + c_1\right]^3} \qquad (22)$$

A finite-difference technique can now be used to solve Equation (14). The left hand side of Equation (14) is represented by a forward difference (in time) approximation as

$$\frac{\partial T}{\partial t} = \frac{T_n^{t+\Delta t} - T_n^t}{\Delta t} \qquad (23)$$

where the subscript refers to the spacial position or computational node and the superscript refers to the time position. The term $\partial T/\partial \xi$ is written in central difference form as

$$\frac{\partial T}{\partial \xi} = \frac{T_{n+1}^t - T_{n-1}^t}{2\Delta \xi} \qquad (24)$$

and the central difference of the term TXX is

$$TXX = \frac{1}{2\Delta \xi^2}\left[\left(k_{n+1}^t + k_n^t\right)\left(T_{n+1}^t - T_n^t\right) - \left(k_n^t + k_{n-1}^t\right)\left(T_n^t - T_{n-1}^t\right)\right] \qquad (25)$$

where the thermal conductivity is a function of temperature.

Substitution of Equations (23) and (25) into Equation (14) yields

$$T_n^{t + \Delta t} = T_n^t + \Delta t \left[\frac{s}{D-s} \, B_n \, \frac{T_{n+1}^t - T_{n-1}^t}{2\Delta \xi} \right.$$

$$\left. + \frac{1}{\rho c_p} \frac{1}{(D-s)^2} \left(C_n \, TXX + E_n \, K_n \, \frac{T_{n+1}^t - T_{n-1}^t}{2\Delta \xi} \right) \right] \quad (26)$$

Equation (26) is the conventional explicit form solution of Equation (14).

Explicit form solutions have an associated stability criterion. The stability criterion for the heat conduction equation in the x, t coordinate system is

$$\rho \frac{c_p}{k} \, \frac{\Delta x^2}{\Delta t} \geq 2 \quad (27)$$

In the ξ, t coordinate system this becomes

$$\frac{\rho c_p}{k} \left[\frac{D-s}{1+c_1} \left[(n+1) \, \xi^n + c_1 \right] \Delta \xi \right]^2 \Big/ \Delta t \geq 2 \quad (28)$$

The boundary condition at the exposed surface depends on whether the surface is ablating. This is determined as follows: It is assumed that the surface is not ablating and the corresponding surface temperature is calculated. For a nonablating surface the boundary condition is given by:

$$Q_{co} - Q_r = - k \left. \frac{\partial T}{\partial x} \right|_{x=s} \quad (3)$$

Equation (3) can be expressed in finite difference form; however, because the finite difference method is an approximation, the heat capacity of the element of the wall at the boundary cannot be neglected. Hence, Equation (3) becomes (in finite difference form)

$$T_1^{t + \Delta t} = T_1^t + \frac{2\Delta t}{c_p} \frac{\sqrt{c_1}}{(D-s)\Delta \xi} \left[Q_{co} - Q_r - k_1 \frac{\sqrt{c_1}}{(D-s)} \frac{T_2^t - T_1^t}{\Delta \xi} \right] \quad (29)$$

Equation (29) allows the calculation of the wall temperature at time $t+\Delta t$ using parameters known at time t. This new wall temperature, $T_1^{t+\Delta t}$ is compared with the ablation temperature $T_{AB}(P_B)$. If $T_1^{t+\Delta t}$ is greater (less) than $T_{AB}(P_B)$ the material is ablating (not ablating). If the wall is ablating, the wall temperature is set equal to the ablation temperature. To calculate the surface recession rate, Equation (7) is used

$$\dot{s}(t) = \frac{1}{\rho} \left[\frac{Q_{co} - Q_r - k \frac{\partial T}{\partial x}\Big|_{x=s}}{\bar{H}_{eff} - h(T_{AB})} \right] \qquad (7)$$

The total surface recession is given by

$$s(t+\Delta t) = s(t) + \dot{s}(t) \Delta t \qquad (30)$$

The boundary condition at the back face is expressed in finite difference form as

$$T_N^{t+\Delta t} = T_{N-1}^{t+\Delta t} \qquad (31)$$

where N refers to the total number of computational nodes.

A summary of the numerical procedure for calculating the temperature profile and window recession as a function of the point (time) in the trajectory is as follows:

(1) An initial (at time t=0) temperature profile is assumed.

(2) The boundary layer edge Reynolds number is checked to see if the flow is laminar or turbulent.

(3) The nonablating heat transfer rate is calculated by standard techniques, e.g., reference enthalpy method.

(4) Equation (29) is used to calculate the front face temperature at time $t+\Delta t$.

(5) This temperature is compared with the ablation temperature to determine if the window is ablating. If the window is ablating Equations (7) and (30) are used to calculate the window recession rate and the total window recession respectively.

180

(6) Equations (26) and (31) are used to solve for the temperature profile at time t + Δt.

An advance in time is achieved by taking the calculated temperature profile and using it as the initial profile in step 1 and proceeding through the remaining five steps. This process is repeated until the reentry vehicle impacts.

4. RESULTS

The numerical procedure was programmed for the CDC6600 computer (Ref 1) and several sample cases were run for typical trajectories. The resulting temperature profiles and window recessions at selected altitudes were determined. (Ref 1)

REFERENCE

1. Buggeln, R. C., A Thermal Analysis of an Ablating Electromagnetic
Window, AFWL-68-11, Air Force Weapons Laboratory, Kirtland AFB,
New Mexico, February 1968.

THE DEVELOPMENT OF PHOSPHATE-NUCLEATED GLASS-CERAMIC RADOMES

by

P. W. McMillan, G. Partridge, A. Bennett and J. R. Brown
Nelson Research Laboratories
The English Electric Co., Ltd.
Stafford, England

ABSTRACT

In the Nelson Research Laboratories it has been shown that fine-grained glass-ceramics can be made from a wide range of glass compositions using phosphorous pentoxide as a nucleation catalyst. These materials have high mechanical strength, good electrical insulating properties and their thermal expansion coefficients can be varied in a controlled manner. The valuable combination of properties of the glass-ceramics suggested that they would be suitable for the manufacture of missile radomes and this possibly has been investigated in a research program sponsored by the Ministry of Technology.

At the onset of the work it was decided to study the possibility of making the radomes by pressing from molten glass since this was considered to be a simpler and probably cheaper process than centrifugal casting. In addition, it was proposed to melt the glass in normal refractory-lined rather than platinum-lined furnaces since this would also result in reduced cost.

A glass-ceramic composition which was thought to have suitable characteristics for this method of manufacture was chosen and intensive trials were carried out which showed the properties were reproducible from melt to melt. It was also shown that experimental ogival radomes 14 inches long and 7-1/2-inches base diameter could be made by pressing and that these were dielectrically homogeneous from point to point. An investigation of the process of grinding the radomes to the final accurate shape was undertaken and it was shown that the high strength of the glass-ceramic could be retained after grinding. Full measurements of mechanical strength, dielectric properties, density and thermal expansion coefficient were carried out and these generally confirmed the suitability of the glass-ceramic as a radome material. Rain erosion tests both on small specimens and on radomes showed that the material behaved well in this respect. The work has demonstrated feasibility of this method of manufacturing missile radomes and current work is directed towards achieving improved dielectric properties.

INTRODUCTION

Glass-ceramics which are made by the controlled devitrification of special glass compositions and which have outstanding physical properties are now well known and are finding use in many applications. The preparation of a satisfactory glass-ceramic depends on devitrifying a suitable glass composition under strictly controlled conditions in order to provide a closely interlocking microcrystalline structure and a smooth, uncrazed surface. In order to do this it has generally been necessary to include in the glass a material which will provide nuclei for subsequent crystal growth or control the crystal

formation in such a manner that many crystals of the desired form grow simultaneously in the glass. The resultant material has improved mechanical properties and refractoriness as compared with the parent glass and has good electrical and thermal properties.

Work carried out in the Nelson Research Laboratories of the English Electric Co., Ltd., has demonstrated that phosphorous pentoxide can be used to catalyze the controlled crystallization of a wide range of silicate glass compositions. It has been shown that glass-ceramics of this general type can have very good mechanical, thermal and electrical properties. For example the mechanical strengths of the material are generally high (measured on a three-point loading cross-breaking strength test) and mean values up to 60,000 lb/in^2 are attainable. Generally speaking it has been found that the higher expansion materials are stronger than the lower expansion materials but this is not a rigid rule. Other mechanical properties such as impact strength compare favorably with those of high alumina ceramics. Young's moduli values in the range 10 to 21 x 10^6 lb/in^2 have been measured and it has been shown that glass-ceramics of this type can be prepared which have hardnesses comparable to those of high alumina ceramics.

It has been shown that phosphate nucleated glass-ceramics can have linear thermal expansion coefficients covering a wide range of values (-40 to + 180 x 10-7/°C) depending on composition, and this has lead to their use in the preparation of seals to a wide variety of metals. The glass-ceramics can withstand temperatures ranging from about 700° C to about 1200° C depending on composition. Generally speaking, the lower expansion materials withstand higher temperatures than the higher expansion materials. The thermal conductivities of the materials lie below that of alumina but above those of conventional glasses. A simple thermal shock test in which heated rods were quenched in cold water has shown that materials of this type can have better resistances to thermal shock than alumina ceramics.

The phosphate nucleated glass-ceramics have been shown to have good electrical properties. Dielectric breakdown strengths at power frequencies are much higher than those of conventional ceramics, including alumina, and their volume resistivities are similar to that of alumina at room temperature and are only slightly inferior at elevated temperatures. Materials have been made having values of dielectric constant in the range 4.5 to 7.0 and with loss angles which can be as low as 0.0003 depending on composition and the frequency of test within the range of 10^3 Hz to 10^{10} Hz.

It was considered that, in view of the possible properties of the phosphate nucleated glass-ceramics, materials of this type could be used in radome applications for aircraft and guided missiles, fulfilling the following requirements.

SPECIFICATION OF MATERIAL AND PROCESS

Typical requirements for the glass-ceramics for use in radome applications can be summarized as follows:

1. Dielectric Constant at X-band (10^{10} Hz) - the exact value is not important provided that the value achieved is reproducible and that the individual radomes are homogeneous. The tolerance on the dielectric constant value is ±0.05 (variation over the individual radome and from the nominal) and it should show no greater than a 0.1 change over the temperature range 20-400° C.

2. Loss Angle - this should be less than 0.01 up to a temperature of 400° C at X-band.

3. Thermal Shock Capacity - the material should be capable of withstanding a temperature rise of 400° C in one second on the outer surface without cracking.

4. Water Absorption - after soaking for a considerable period the absorption should be less than 0.06 per cent by weight (this implies a change in dielectric constant of less than 0.05).

5. Rain Erosion - the material should be capable of withstanding 2 mins at mach 4 in 3 in./hour rain without detectable damage.

6. Modulus of Rupture - this should be greater than 16,000 lb/in^2 and preferably should be comparable with those of high alumina ceramics (ca.40,000 lb/in^2).

The requirements for the process can be summarized as follows:

1. Melting. It was considered that melting should ideally be carried out in refractory containers rather than the expensive platinum lined containers which are used in the melting of other glass-ceramic materials which have been used in radome applications.

2. Forming. It was considered that the forming operation to give the desired radome shape should be a simple pressing operation since it was felt that this would take better advantage of techniques which had already been practised in the Nelson Research Laboratories and would be a more economic process than centrifugal casting.

3. Grinding. The pressed radome blanks would require grinding accurately to the desired shape and for this purpose conventional grinding techniques were proposed.

It was realized that in order to fulfill the melting and forming requirements the type of glass-ceramic used would be restricted to certain compositional ranges and so the material might not possess the best attainable dielectric properties but it was considered that materials could be made which had adequate properties for the required applications.

FABRICATION

For this work glass-ceramics of the lithium-alumino-silicate type were selected. These had been shown on small scale preparation to have suitable physical properties.

A. Melting

The raw materials required for the preparation of the various glass-ceramics were thoroughly mixed. The mixtures were melted in molochite refractories at temperatures in the region of 1450° C. The glasses were allowed to refine until free from bubbles and unincorporated raw materials and a homogeneous melt was formed. The molten glass was then worked as described below. It was found that the extent of the attack by the glasses on the refractories was only slight and chemical analysis showed that any individual material was reproducible to fairly close compositional limits.

B. Forming

In order to enable the desired ogival CTV5 radome shape to be pressed a mould and plunger were designed for use with a hydraulic press. The molten glass was introduced, in suitable quantities, into the mould and then pressed to the desired shape (14 inches long x 7 inches base dia.) using the plunger and press. The pressed shapes were allowed to cool in the mould and when sufficiently cool to retain their shape they were removed from the mould and transferred to a furnace where they were annealed for a period followed by slow cooling to room temperature. The blanks were thus obtained in the glass state which facilitated examination for voids, inclusions and other inhomogeneities.

C. Heat-treatment

Satisfactory glass blanks were subjected to a carefully controlled heat-treatment schedule to convert them to micro-crystalline glass-ceramics. This process was controlled so that no significant distortion of the radome shape occurred. A linear change of approximately one per cent in dimensions occurred on heat-treatment but this was controllable and reproducible.

D. Grinding

The glass-ceramic blanks were ground on the internal and external surfaces using a converted Springfield Lathe as shown in Figure 1. Radome blanks 14 inches long were ground on both interior and exterior surfaces and blanks 8 inches long were ground on the external surface only. Two sizes of ground radomes are shown in Figure 2.

TESTING THE MATERIALS AND PRESSED RADOME SHAPES

Tests have been carried out on samples taken from pressed radome shapes, on the radome shapes themselves and on rod and block samples prepared from the glass-ceramic materials and subjected to similar heat-treatments to the radomes. The tests carried out were as follows:

1. Modulus of Rupture. Glass-ceramics which could be shaped as above have been shown to have moduli of rupture in the region of 40,000 lb/in^2 at room temperature on a three-point bending test on rod samples. The strength figures obtained were reasonably consistent
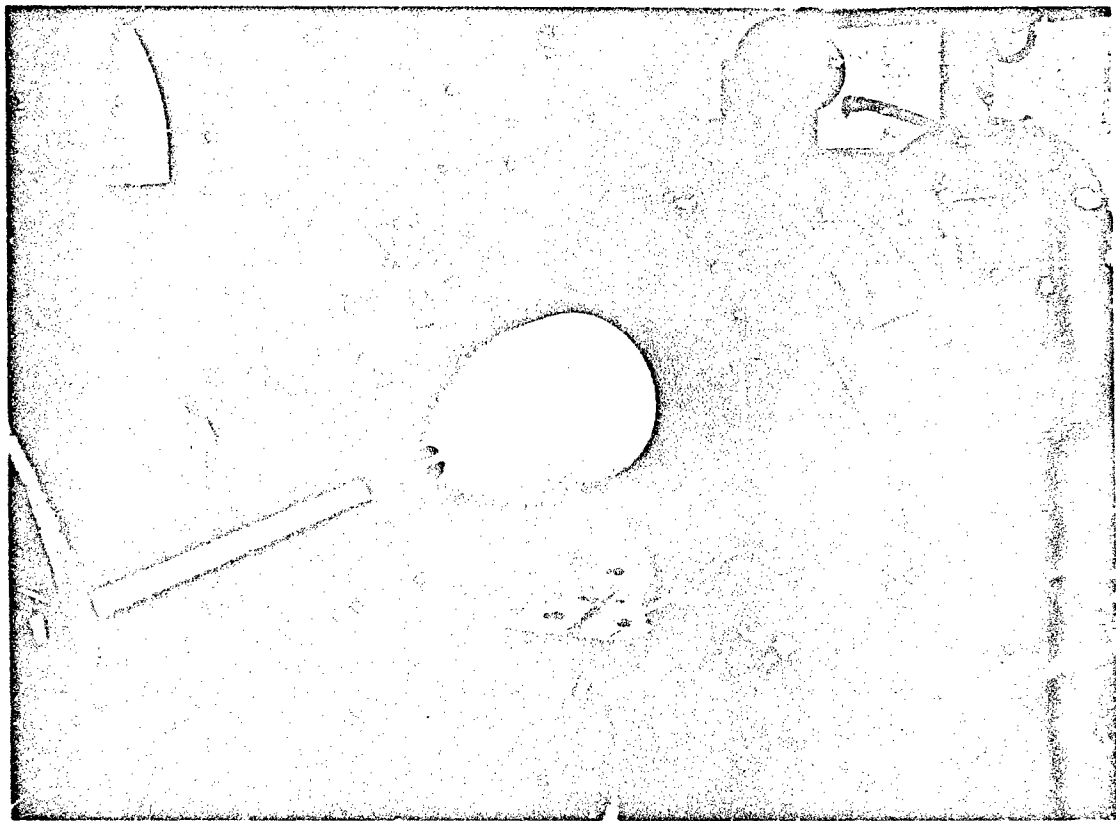
186

Figure 1. Glass-Ceramic Radome Cone Mounted on the Converted Springfield
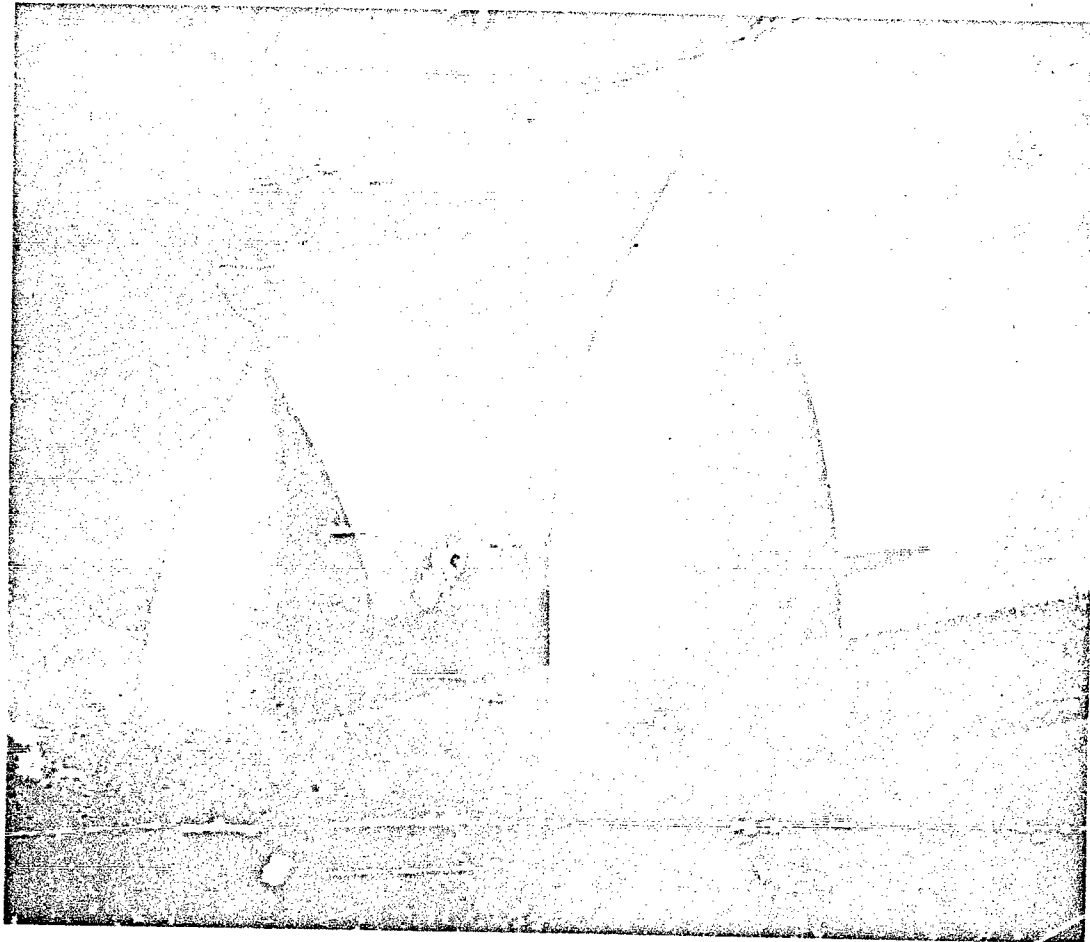Lathe for External Grinding.

Figure 2. Cones for Dielectric and Rain Erosion Testing.

from melt to melt and throughout each melt. The influence of temperature on modulus of rupture has also been examined and it has been shown that the modulus of rupture of a typical material remained significantly unchanged up to a temperature of 500° C and was greater than 85 per cent of its room temperature value at a temperature of 700° C. See Figure 3 in which data for a high alumina content ceramic are also given.

2. Impact Strength. The impact strength has been measured on rod samples using a Charpy test technique. The impact strengths obtained were about 0.32 ft. lb at room temperature (compared with 0.16 ft.lb for an alumina ceramic tested under similar conditions). The impact strengths fell to between 60 and 80 per cent of the room temperature value at a temperature of 700° C but this decrease was much less than occurred with an alumina ceramic the impact strength of which had fallen to 50 per cent of its room temperature value at 300° C and was too low to measure with the test equipment at higher temperatures.

3. Linear Thermal Expansion Characteristics. The initial materials prepared in this work had linear thermal expansion coefficients in the range 55 - 60 x 10^{-7}/°C but later materials had expansion coefficients of 45 - 50 x 10^{-7}/°C or even] (compared with the figure for alumina of about 75 x 10^{-7}/°C) for the temperature range 20-500° C. The values obtained were reproducible from melt to melt and throughout each melt. The glass-ceramics prepared would all withstand temperatures up to 700° C for prolonged periods and up to 800° C for short periods.

4. Density. The densities of glass-ceramic samples were determined to ±0.002 g/cc at 20° C and were generally in the range 2.400 to 2.600 g/cc for the series of materials examined. Density measurements have long been used in the glass industry as a quick and accurate check on the reproducibility of a glass and the density figures obtained on the glass ceramics showed that individual materials were homogeneous within each melt and that only very slight changes occurred from melt to melt.

5. Microstructure. Electron microscopical examination revealed that the glass-ceramics under test were fine grained materials with closely interlocking crystals about one micron in size. A typical electron micrograph is shown in Figure 4.

5. Rain Erosion Resistance. Rain erosion tests have been carried out on a material of the type under investigation on test samples one inch square by 1/4-inch thick using a whirling arm test at 500 mile/hour in one inch/hour of rain and on ground ogival radome shapes using a rocket sledge technique at a speed of 1624 ft/second through 5 inch/hour of rain. While the conditions of test were less severe than those specified earlier, the general conclusion from these tests was that the rain erosion of the material was sufficiently high for immediate requirements. It is the aim of current work to improve this quality.
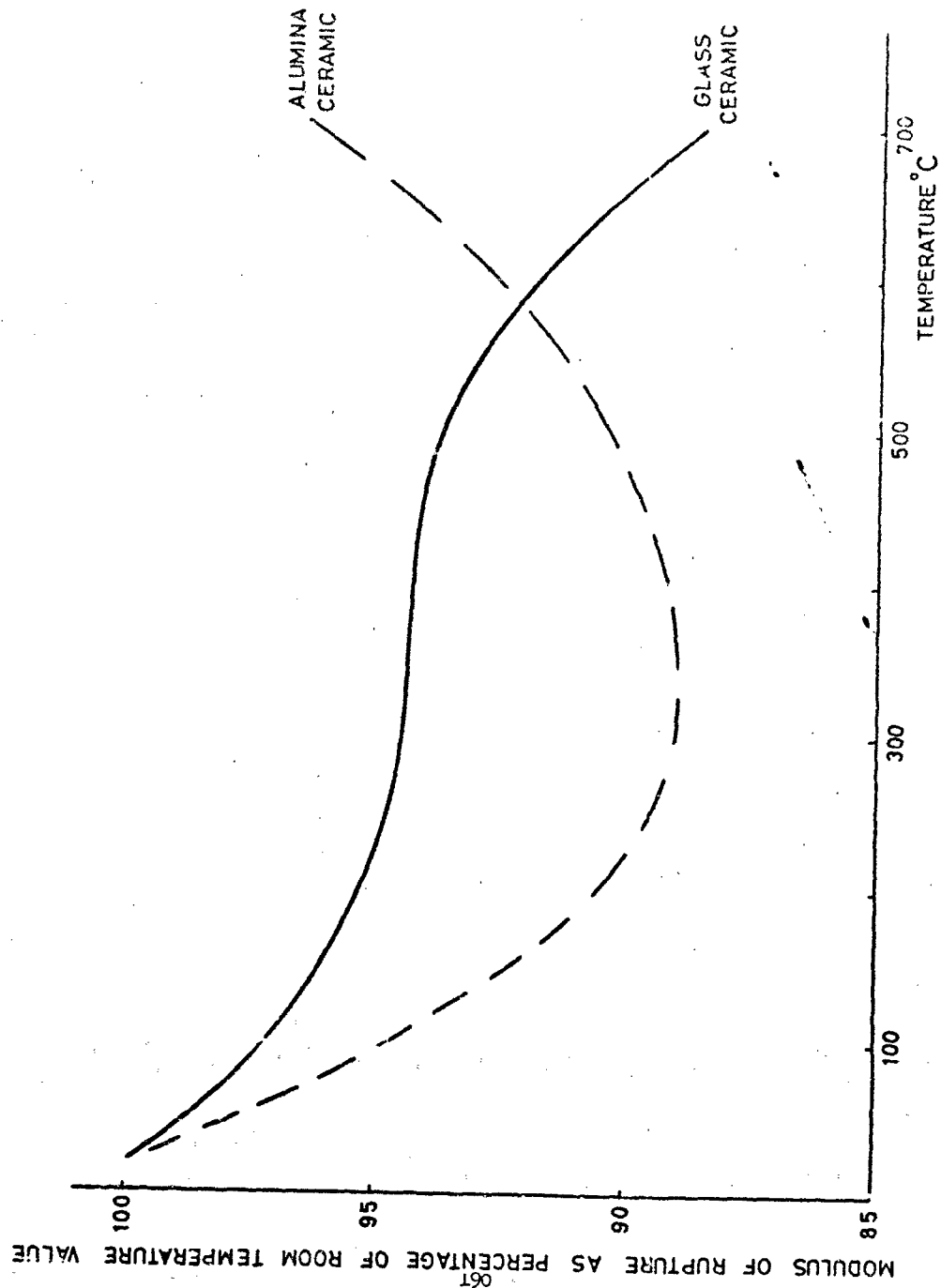
Figure 3. Influence of Temperature on the Moduli of Rupture of an Alumina Ceramic and a Typical Phosphate Nucleated $Li_2O-Al_2O_3-SiO_2$ Glass-Ceramic Tested for Suitability in Radome Applications.
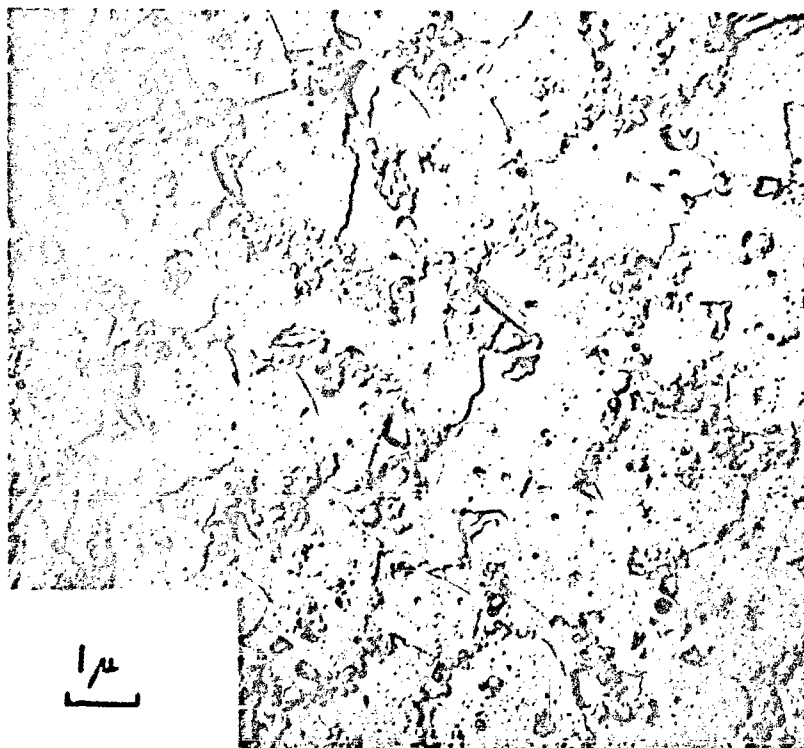
Figure 4.   Electron Micrograph of $Li_2O-Al_2O_3-SiO_2$ Glass-Ceramic.

7. <u>Dielectric Properties at X-band.</u> Dielectric property measurements have been carried out on test samples made directly from the melts of the various materials and on samples cut from various positions in pressed radome blanks. The tests were carried out generally at a frequency of 9.6 GHz on rectangular samples (measuring 0.9 x 0.4 in. waveguide fit) using a shorted waveguide technique and at temperatures up to 400° C.

The dielectric constant figures for the various materials tested in the work described fell in the range 5.5 to 6.5 at room temperature, and were reasonably consistent throughout a particular melt but showed slight variations from melt to melt of a particular material. Measurements have also been carried out on samples cut from pressed radome shapes and the results obtained have shown that each material is homogeneous from a dielectric point of view throughout individual pressed shapes and generally from shape to shape. Measurements carried out by Elliott Brothers Ltd. on ground radome shapes pressed in one of the materials showed that the material had an acceptable tolerance on dielectric constant (± 0.05) throughout an individual pressed shape and amongst the various shapes tested.

The variation in dielectric constant with temperature up to 400° C is shown in Figure 5. In the initial material tested in this work (designated Glass-ceramic A) the change in dielectric constant (0.6 : 20-400° C) was slightly greater than that for a high alumina ceramic (0.5 : 20-400° C) but this was reduced considerably for later materials (designated Glass-ceramics B and C) which had changes in dielectric constant of 0.4 and 0.3 respectively, 20-400° C.

The loss angle of the initial materials was slightly above the deisred limit of 0.01 at room temperature and increased at temperatures approaching 400° C. Later materials, however, have been shown to have loss angles in the region of 0.007.

CONCLUSIONS

It has been demonstrated that phosphate nucleated glass-ceramics, basically of the lithium-alumino-silicate type can have suitable properties for use as radome materials and that these can be melted in refractory crucibles and shaped by conventional pressing techniques.
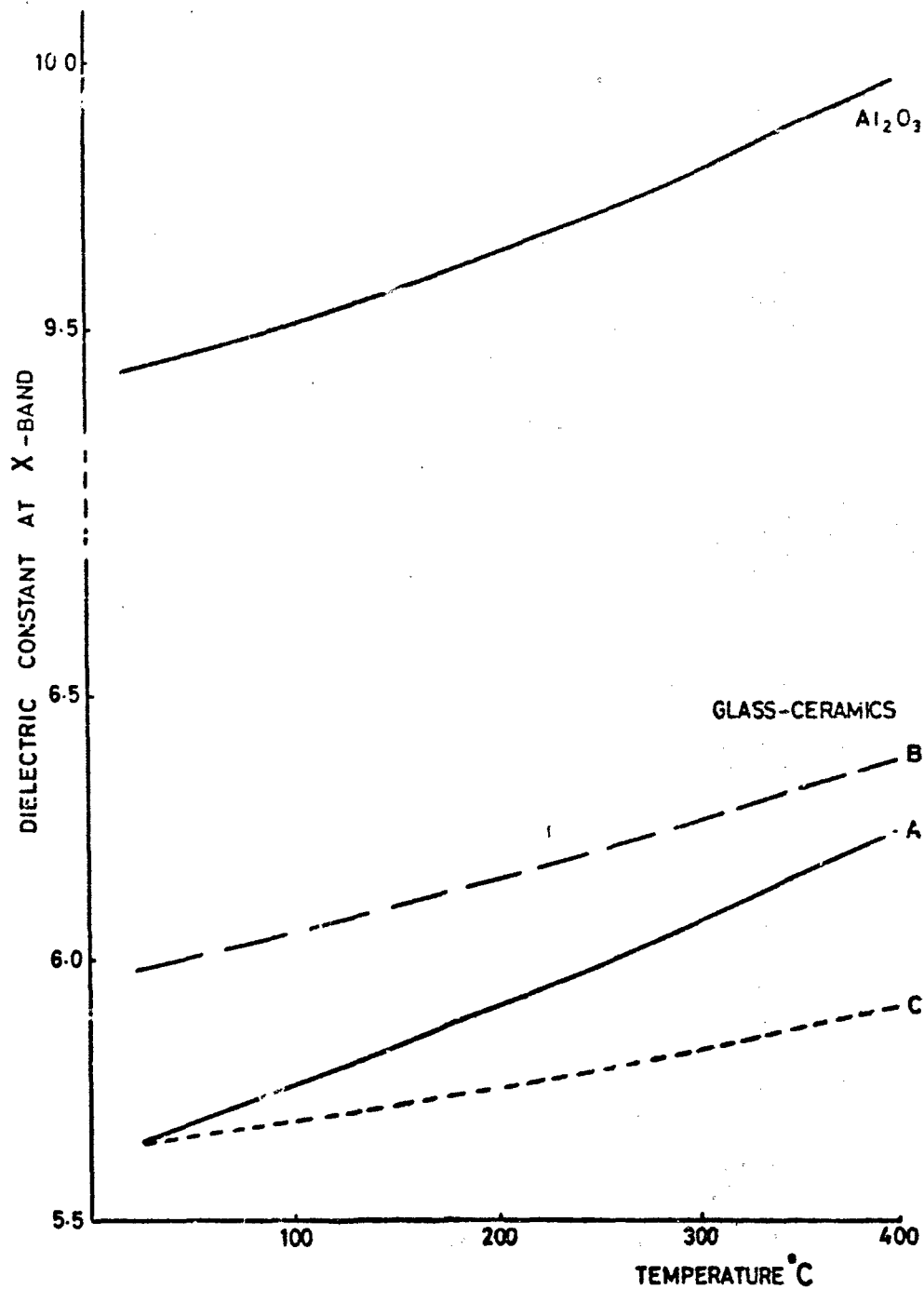
Figure 5. Variation of Dielectric Constant over the Temperature Range
20-400°C for a High Purity Alumina and Glass-Ceramics A, B and C.

BLANK PAGE

MECHANICAL BEHAVIOR OF CERAMICS

BY

J. D. Walton, Jr.
Engineering Experiment Station
Georgia Institute of Technology
Atlanta, Georgia

ABSTRACT

The spread in values for much of the mechanical property data reported
for ceramics has given rise to the charge that these materials lack unifor-
mity, reproducibility, and reliability. This paper reviews the state of the
art of relating the mechanical properties of ceramics to such character fea-
tures as microstructure, porosity, surface finish, strain rate, etc. Special
attention is given to methods and techniques used for evaluating ceramics in
an effort to determine: (1) their ability to identify the sources of vari-
ability, and (2) the degree to which the test techniques themselves introduce
variability.

INTRODUCTION

During recent years a multitude of electrical and mechanical property
data have been reported for various ceramic radome materials. These data have
suggested a rather wide range of property values for apparently equivalent
materials. This situation has focused attention on the problem of determining
the mechanical behavior of ceramic radome materials.

With respect to electrical property data, there is a growing awareness
that the purity of the material is an important variable, particularly at high
temperatures. K. H. Breeden's paper mentioned the importance of specimen shape
and dimension tolerance in obtaining meaningful dielectric properties at milli-
meter wave lengths. However, in the radome field in general, there has been
little attention given to considering variability in mechanical property data
other than to assume that the same generalizations apply as in the case for
electrical properties. Since mechanical property data are a result of many
interdependent factors that are not generally recognized it was felt that the
radome engineer should be given some background into the mechanical behavior
of ceramics. This subject was therefore discussed in an informal talk during
the Symposium. This talk was based on the author's activities on the Materials
Advisory Board's Ac Hoc Committee on Ceramic Processing.

BACKGROUND

The past few years have witnessed increasing efforts by many investigators
to develop a better understanding of the behavior of ceramics based on the
microstructural nature of these materials.

Recently several excellent reviews have been published on the subject.
Examples of these are reviews by Stokes 1/, Wachtman 2/, Spriggs 3/,
Carniglia 4/, and Kingery and Cable 5/. Based on these reviews, attempts

have been made to identify those microstructural features which were most significant with respect to mechanical behavior. However, the results of these reviews have illustrated the complexity of such a relationship and have focused attention on the fact that numerous interdependent variables influence the mechanical behavior of ceramics. In fact, such reviews serve to caution us against drawing sweeping conclusions from data which are reported in the literature. This is particularly true where little attention was given to characterization and/or test techniques. They also suggest that much more attention will have to be given to planning and designing future programs involving material characterization and property measurements if the data obtained are to have the desired significance.

CHARACTER-PROPERTY RELATIONSHIPS

The limited use of ceramics and other brittle materials for critical mechanical applications is often associated with their apparent lack of uniformity, reproducibility, and reliability. Uniformity refers to consistency of character throughout a specimen or part. Reproducibility indicates consistency of character from part to part. Reliability means consistency of the character of a product from day to day.

If adequate characterization techniques were available and if character-property relationships could be established then the degree to which ceramics are not uniform, reproducible, and reliable could be determined.

In attempting to specify which elements of character may influence specific properties, it should be recognized that a considerable amount of interplay exists between the various character features. For example, tensile strength measurements on ceramic bodies having rough and heavily damaged surfaces would not be expected to show a large dependence of strength on grain size or porosity. However, as the quality of the surface is improved the strength may be increased until it is influenced by the grain size utilized and a grain size affect is observed. As the grain size is altered to effect higher strength, the surface condition or some other factor may become limiting. In addition to these factors it should be pointed out that as the grain size of a body is changed by altering the thermal treatment, the extent of segregation of impurities to the grain boundaries may cause significant property variations quite unrelated to the grain size itself. Thus, before judging that a certain factor does or does not significantly influence some property, it must be established that another factor is not obscuring the test results. This also emphasizes that when one factor is judged, the state of several other potentially limiting factors must be specified.

A. Grain Size and Porosity

Binns and Popper [6] reported transverse strength, average grain diameter, and density for a wide range of alumina ceramics obtained from a number of manufacturers. These compositions varied from 87 to 99.9 per cent Al_2O_3. The data were obtained from bars of round and square cross sections one cm in diameter or one cm on a side, broken in three point loading over a 10 cm span. Figure 1 shows the transverse strength plotted as a function
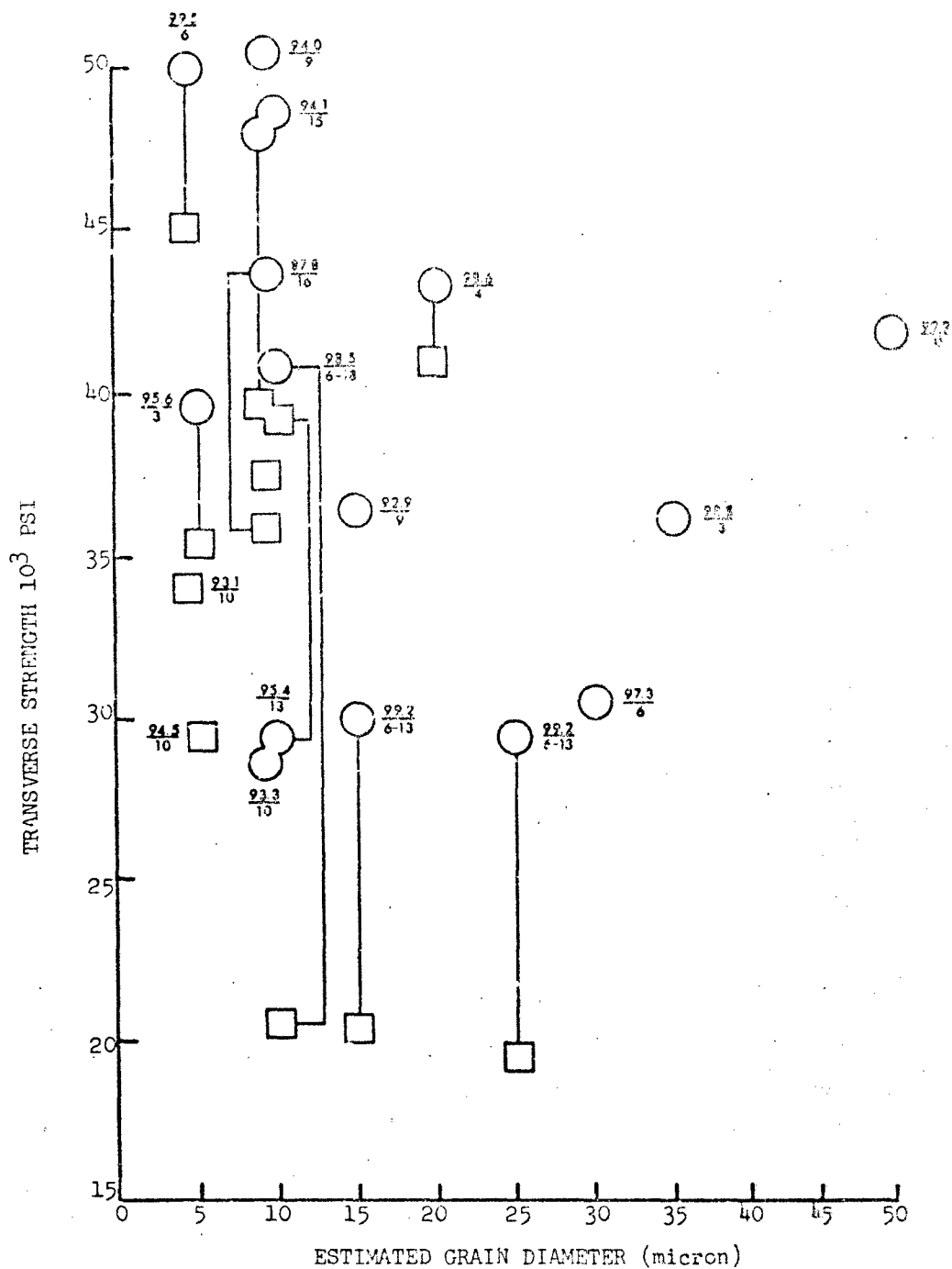
Figure 1.   Transverse Strength (3-point loading) vs Grain Diameter for Round and Square Cross Sectional Bars of 87-99.9% Al_2O_3, 0-18% Porosity.

of grain diameter. The round and square data points are for round and square bars respectively. Lines connect points where both types of bars were broken for the same compositions. The numbers beside the data points are per cent Al_2O_3 over the per cent porosity. These data show that Al_2O_3 ceramics may exhibit transverse strengths from 20,000 to 50,000 psi depending upon composition, test bar shape, and porosity. It is interesting to look at the data for the specimens of a nominal 10 micron particle size and note that for the round bars with a composition of 93 - 94 per cent Al_2O_3 and 9 - 10 per cent porosity that the transverse strength ranges from 28,000 and 50,000 psi. This suggests that the strength might vary by a factor of almost two for a rather narrow range of particle size, composition, and porosity. Comparison of strength data from round and square bars shows that, with one exception, square bars give lower values, sometimes considerably lower than the round ones. Binns and Popper suggested that this might be due either to purely geometrical factors, such as sensitivity to misalignment during testing, or to material factors, such as the frequency of flaws in the sharp edges of square specimens. However, since only limited characterization was performed, it would be impossible to assign any significance to the data. These data are included in this discussion to illustrate the typical use of the "Conventional Characterization" such as porosity, average grain size, and chemical composition.

Many investigators have observed a strength-grain size relationship when the composition, porosity, surface finish, and heat treatment have been carefully controlled and where all processing has been within one organization. Such work is typified by that reported by Spriggs, Mitchell, and Vasilos [7]. An example of their data is shown in Figure 2. Spriggs, et al. also reported that at a grain size of 2 micron the transverse strength decreased from 70,000 psi to 55,000 psi when the porosity was increased from three to six per cent. From these data it can be seen that there is a definite relationship between strength and grain size and porosity at this level of purity when all other parameters are adequately controlled. Although such data substantiate the fact that pores (including microcracks) effect the strength of ceramics, it appears that the size, shape, location, and distribution of these defects may be more important than quantity as far as influencing scatter in data.

As in the case of pores and defects it may be that variations of grain size and geometry within the structure are more important as a source of scatter of data than average grain size. Pears [8] reported a study of a polycrystalline alumina of 98 to 99.5 per cent of theoretical density and a 1-3 micron average particle diameter that provided tensile strength values that ranged from 20,000 psi to 50,000 psi. Fractography revealed the strength differences were probably more related to grain size variations within a specimen and other microstructure anomolies than to slight changes in total density and average grain size.

B. Surface Finish

The condition of the surface of a brittle material has a major influence on the strength of the specimen. This is particularly true when the specimen is stressed in tension or flexure. Therefore, any variability
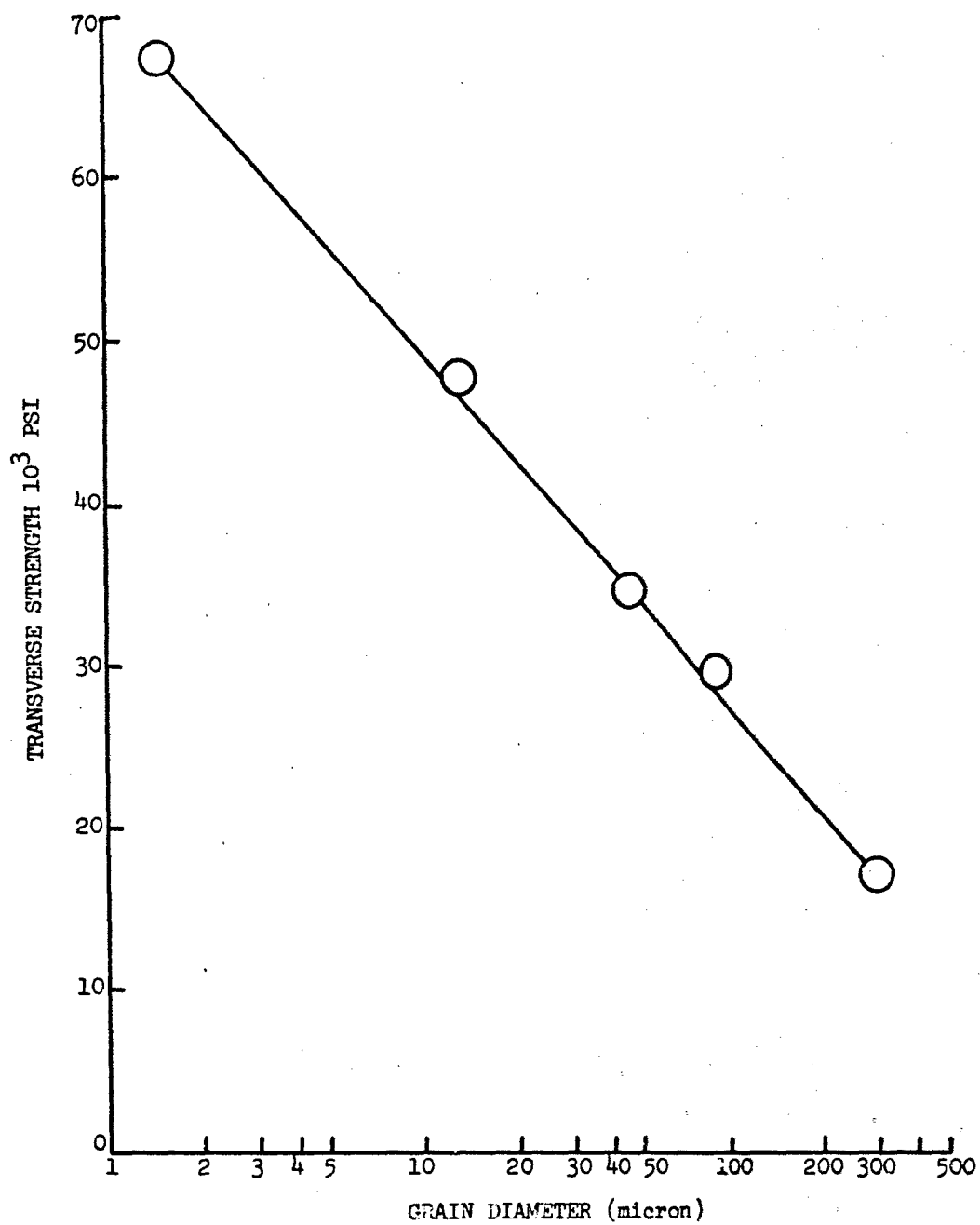
Figure 2. Transverse Strength (4 point loading) vs Grain Diameter for 99.9 Al$_2$O$_3$ - 3% Porosity.

in surface finish, surface flaw concentration, or distribution, would be expected to have a direct effect on the scatter of data.

The need for a high quality (low rms) surface finish can be compared to the need for high quality testing methods. Both are mandatory if the data are to be indicative of the true strength of the material. A poor surface finish does not necessarily yield scatter in data, but will result in lower apparent strength values. However, if the surface finish is not uniformly "poor," scatter in data would result. It might be expected that surface finish variations would be more critical with respect to scatter of data as the average surface finish becomes of higher quality. Figure 3 shows this effect from data presented by Pears 8/ for a particular alumina composition which he studied. It can be seen that the tensile strength dropped from 37,000 psi to 32,000 psi with a change in surface finish from 20 to 35 rms. A change in surface finish from 120 rms to 300 rms resulted only in a change in strength from 25,000 psi to 23,000 psi. Also, a poor surface finish can often mask other effects. For example, Figure 4 presents data reported by Pears which illustrates the influence that surface finish exerts on the temperature-tensile strength behavior of a particular aluminum oxide. A definite temperature effect was observed at a surface finish of 20 rms which was essentially eliminated when the surface finish was 120 rms.

It should be emphasized that the use of root mean square surface finish indices at best provide only a control of surface consistency for comparative purposes. They do not describe the integrity of the surface with respect to its ability to withstand stresses, or identify surface or subsurface micro-cracks or cracks. These flaws would be expected to be a major source of scatter of data, and are not easily detected by current characterization tech-niques. Their contribution to the scatter of data can vary depending upon the size of the specimen and the size of the flaw. Figure 5 by Pears 8/ illustrates that microflaws in the form of 1/64 to 1/32-inch cracks reduced the tensile strength of 1/8-inch diameter specimens of a hot pressed alumina body by about 9,000 psi, but the same defects reduced the strength of 3/4-inch diameter specimens of the same body by only about 1,000 psi.

TEST METHODS

The brittle nature of ceramic materials prevents load redistribution under conditions of testing as well as in actual use. This unforgiving physical character of ceramics must be considered in the interpretation of the numbers obtained from testing, in that the number can be influenced by condi-tions peculiar to the test itself. That is, the number, which suppcsedly represents a real material property may be so influenced by the "conditions of the test" that a real material property is not successfully measured.

It is the purpose of this section to review the results of a state of the art survey concerning the testing of ceramics, primarily regarding their tensile fracture strengths. This survey brought into focus two areas which must be considered when obtaining property data for ceramics. First, the recognition that the behavior of ceramic materials to a given test is a function of the test and the test specimen, and that material inhomogeneity
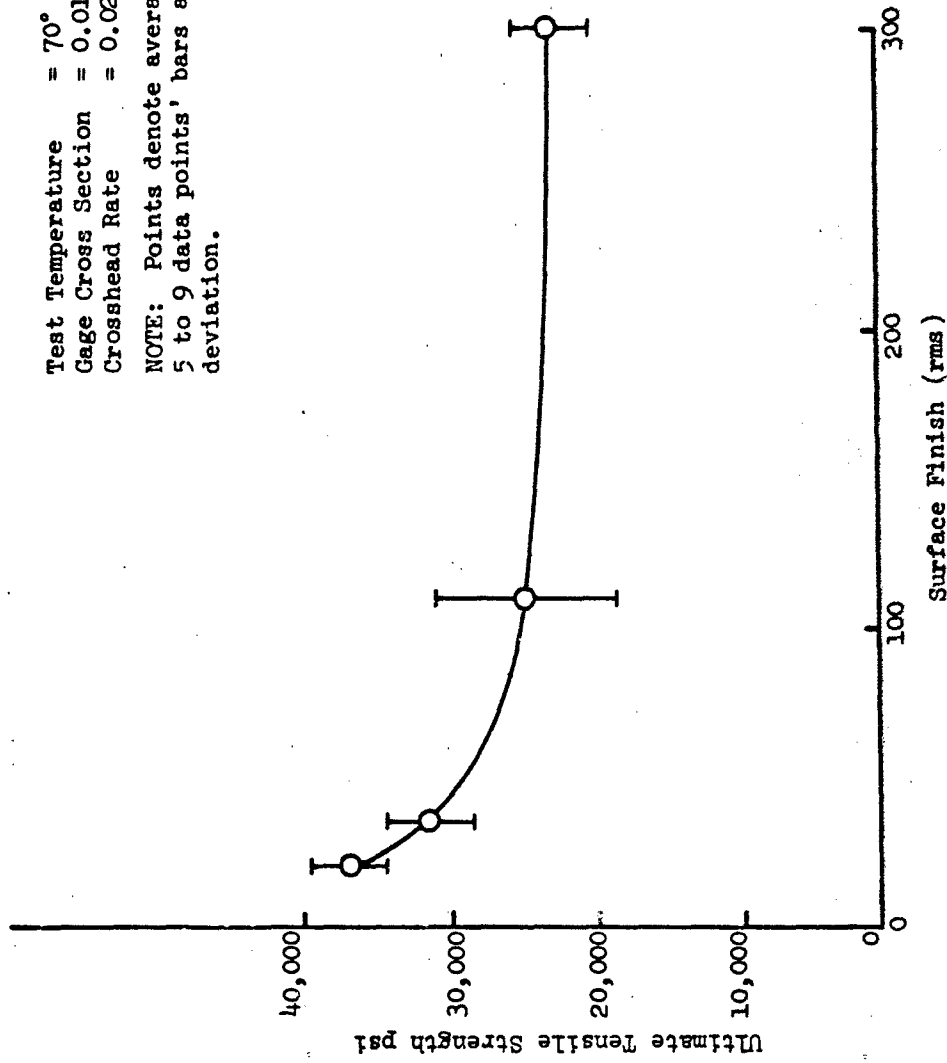
Figure 3. The Effect of Surface Finish on the Ultimate Tensile Strength of Unnotched Alumina at 70° F and One Stress Rate
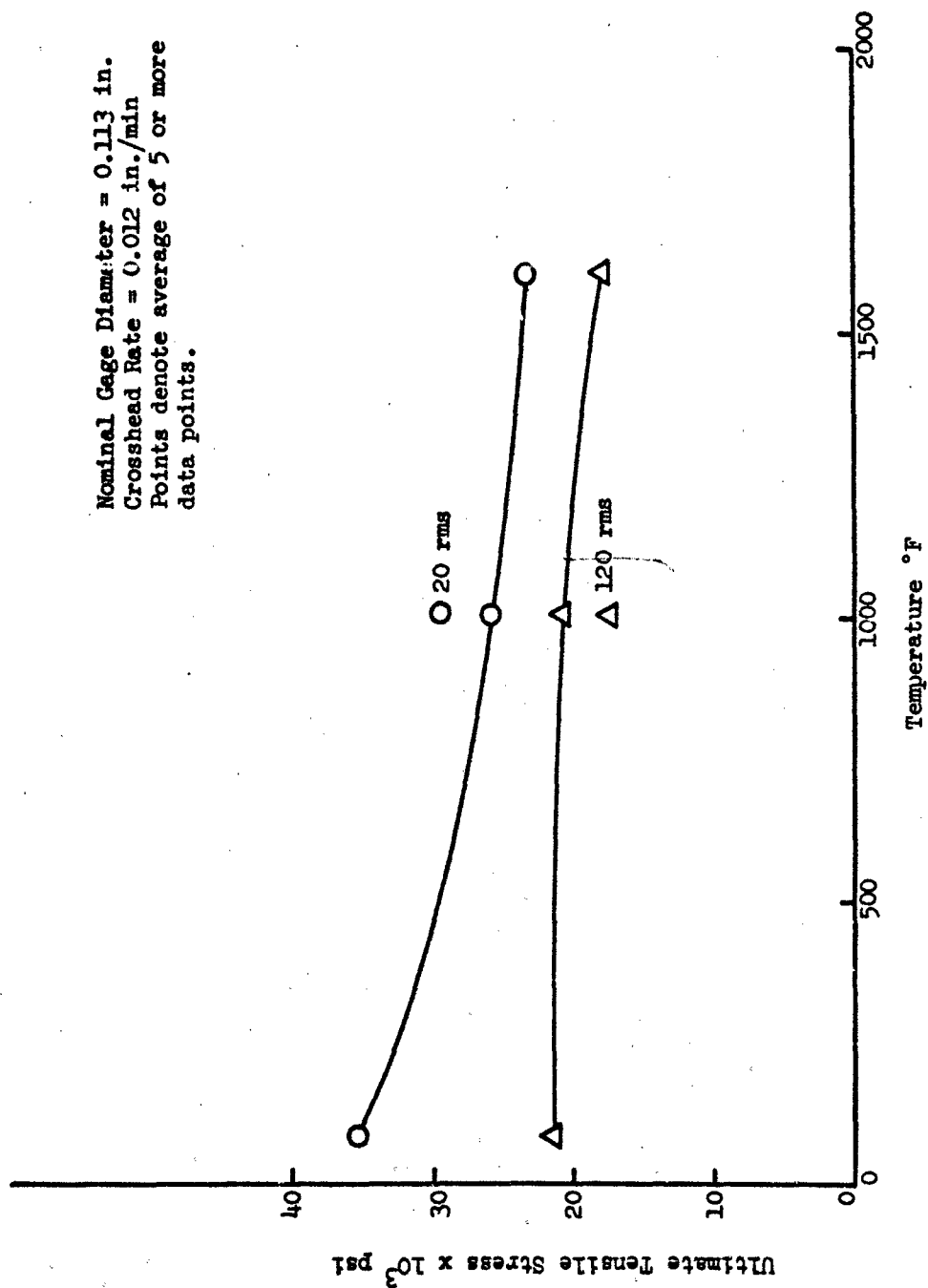
201

Figure 4. Influence of Surface Finish on Strength of Pressed and Fired Alumina as a Function of Temperature.
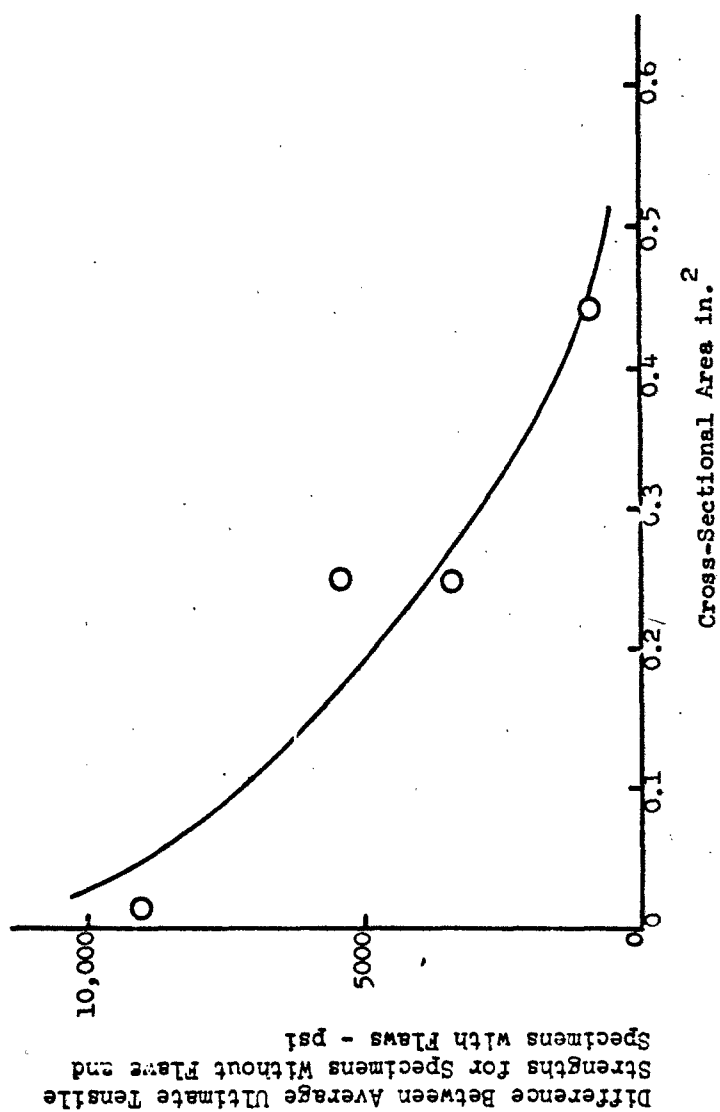
202

Figure 5. Influence of Visual Macrocracks on Strength of Different Volume Specimens of a Hot Pressed Alumina.

contributes significantly to data scatter. Second, the accurate determination of tensile fracture strengths depends upon test methods which introduce a minimum of parasitic stress and a maximum definition of test conditions.

A real material property is one which results solely from some constitutive material response per se, unperturbed by the response of the specimen and the test conditions. In order to attach physical significance to material changes, the difference in a material property must be greater than the influence of specimen and test conditions, while the test employed must allow the accurate observation of the material change.

Once the properties and conditions of interest are defined, the problem remains of selecting a suitable test method. Because of the stringent requirements introduced by the nature of ceramics, this selection demands extreme care and demands further that the tester be oriented to the total problem. There is no single, simple test that can be recommended for all properties under all conditions. The chances are that there is no single value for any property but that each is a function of the "conditions" of the test.

Some of these conditions which should be controlled or at least recognized as influencing the property data obtained are (1) uniformity of the imposed strain, (2) temperature, (3) strain rate, (4) specimen geometry, (5) surface finish, (6) method of loading, etc. Temperature and surface finish have been previously illustrated.

The amount of undesirable bending stress that might be realized in the usual apparatus used to determine the tensile strength of ceramics has been studied by Barnett and McGuire 9/. They instrumented a single ceramic dogbone tension specimen to study the percentage of bending introduced into the specimen through the grips. The dogbone was placed carefully in a set of grips, loaded to some level, and the total stress was compared to the nominal tensile stress. The specimen was then removed from the grips and carefully replaced again to repeat the procedure. The resulting rectangular distribution of "per cent bending stress" is shown in Figure 6. We observe that bending stresses are obtained which are greater than 90 per cent of the uniform tensile stresses and that they are just as likely to occur as the lower stress values. In view of these parasitic bending stresses, it is not surprising that the simple tension test has fallen into disuse as a means of determining statistical fracture strength parameters.

The strength of ceramics does vary with stress rate at room temperature and even more dramatically at higher temperatures. Pears 10,11/ showed in Figure 7 that for a 20 rms surface finish, the influence of stress rate over the small range investigated was quite small at 70° F but significant at 1000° F and 1600° F. Other work on the same material 11/ and shown in Figure 8 indicated that a much larger range of stress rates could introduce a range in fracture strength of from 24,000 to 34,000 psi. Here again, stress rate is a significant controlled condition in the mechanical response of brittle materials and, therefore, must be controlled in studies of behaviors.
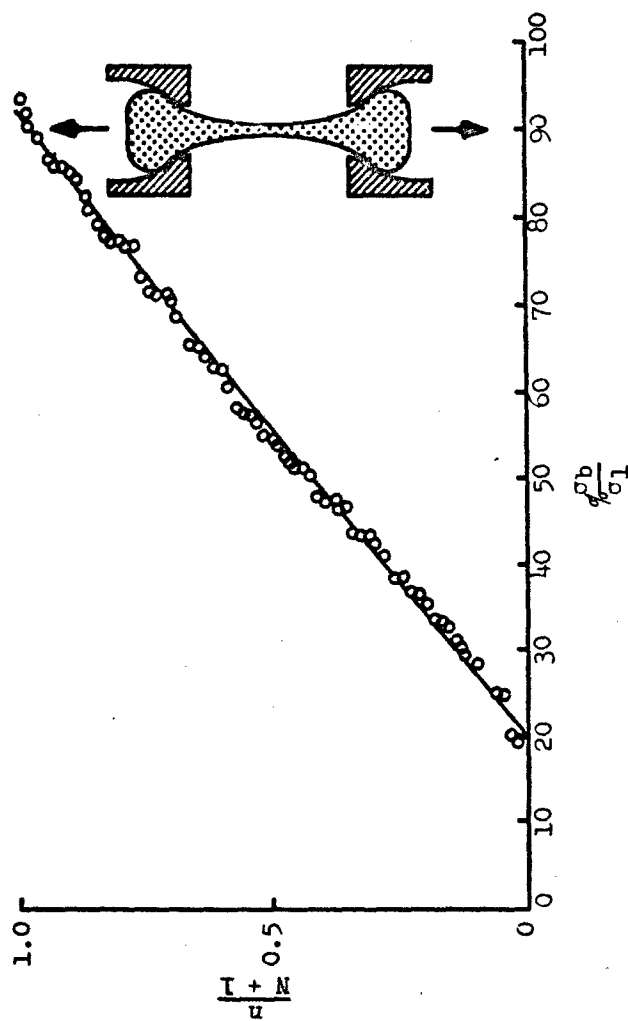
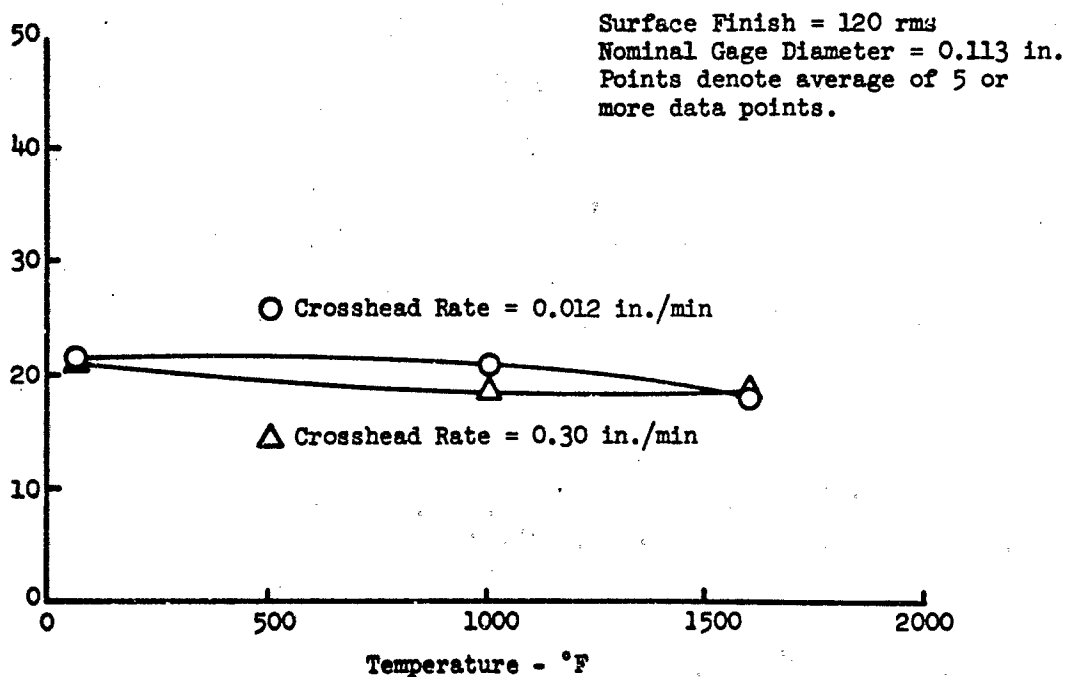Figure 6. Cumulative Distribution of Bending Stress in a Tension Specimen.
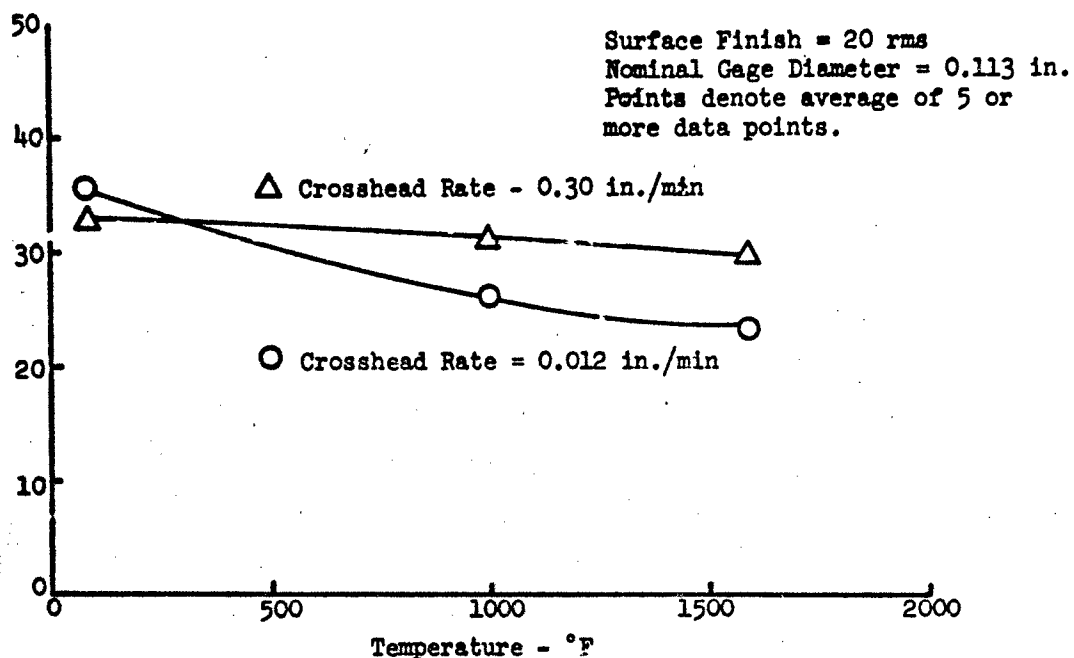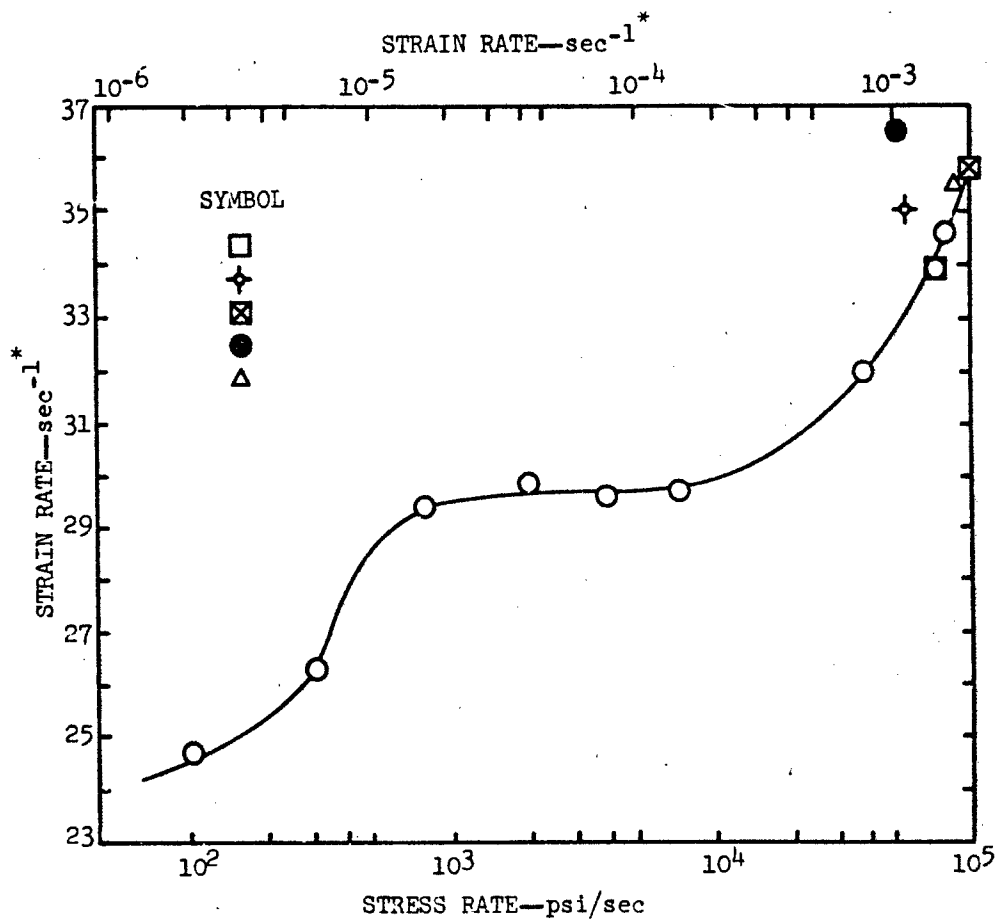
Figure 7. Influence of Strain Rate on Strength of Pressed and Fired Alumina as a Function of Temperature for Two Different Surface Finishes

Figure 8. Effect of Stress Rate and Gage Volume on Ultimate Tensile Strength of Alumina.

From the previous discussion it is evident that "conditions" associated with any test must be accounted for in any program to establish property-character relationships. For tensile strength data the test apparatus should provide a uniform and predictable stress distribution in the gauge volume of the specimen. Two types of tensile test apparatus will be discussed as being capable of providing a homogeneous state of stress.

A. Gas Bearing 12/

The purpose of the gas-bearings is to eliminate parasitic stresses in the specimen by (1) accommodating the misalignments that usually occur as the crosshead moves, and (2) permit detection and elimination of "kinks" in the load train by virtue of the ability to rotate the load train before each run and check its "run out" with dial indicators. The precision of the strain measurement is to 0.000020-inch and the parasitic stress introduced in a tensile specimen is about 0.1 per cent. This apparatus is shown schematically in Figure 9.

B. Pressurized Ring 13/

The pressurized ring has been developed over recent years for the purpose of avoiding, in tensile testing of brittle materials, the generation of parasitic stresses caused by misalignment, gripping, and various other stress concentration factors. Figure 10 shows the pressurized ring apparatus.

The method takes advantage of the intrinsic properties of hydrostatic pressure in that the internal force is always normal to the confining surface and absolutely uniform at every point of contact. The test specimen is a short, thin-walled cylinder against whose inner wall hydrostatic pressure is applied through a rubber bulb. This pressure, exerted radially, creates in the wall of the specimen a tangential tensile stress whose magnitude can be computed exactly from the value of hydrostatic pressure applied and the geometry of the specimen.

Another type of internally pressurized ring is possible in which the cylinder specimen is floated between two conical end pieces that permit a controlled gas leakage out the gap between the specimen and end pieces. The advantage of the floated specimen is that it permits the possibility of operation at high temperatures since an internal bladder is not required.

MATERIAL PROCESSING

Before concluding this discussion, some attention must be given to the materials processor since it is his product which will be used for these critical applications. His ability to provide a uniform, reproducible and reliable product depends not only upon his control of raw materials and process but upon his knowing when his product is deficient with respect to uniformity, reproducibility or reliability. This, of course, depends upon the ability to characterize his product.

Graphite or Steel Pull Rod

Mating Surface Flat and Perpendicular to 0.005"

3-Piece Split Ring

Compression Nut

True, Concentric, and Parallel to 0.005"

Specimen

Grips

Positioning Crosshead

Gas Exit

Gas Pressure

Precision Load Cell

Furnace

Tensile Specimen

Power Crosshead

Mechanical Screw Load Application

Upper Spherical Gas-Bearing

Optical Strain Analyzer
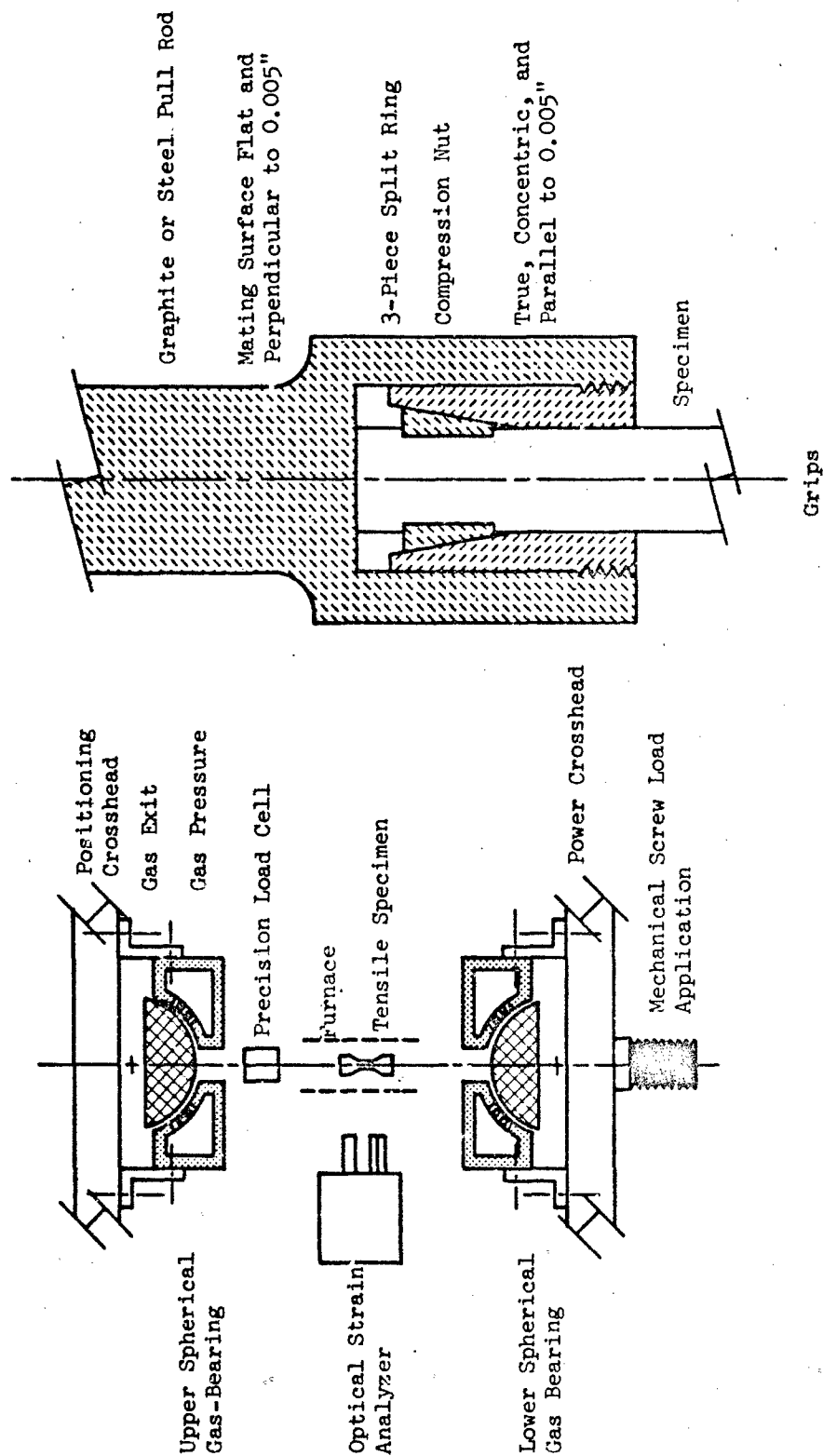
Lower Spherical Gas Bearing

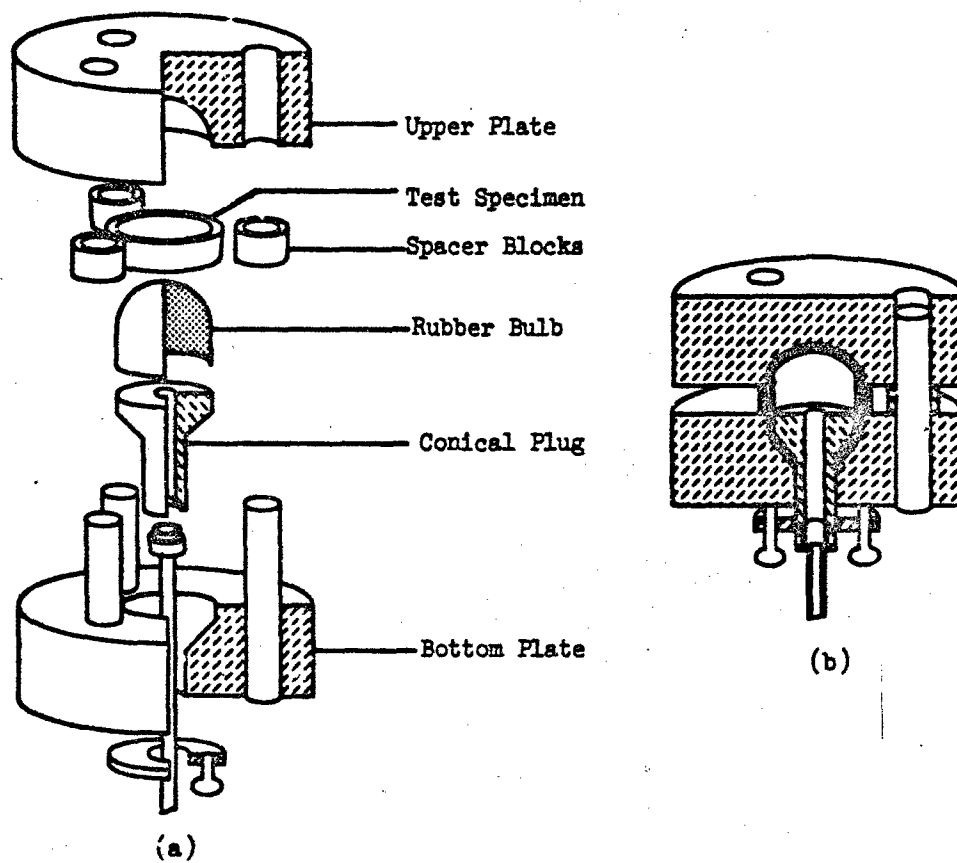Figure 9. Schematic Arrangement of Gas-Bearing Universals, Specimen, Load Train, and Grips.

Figure 10.   Tensile Test Specimen Holder (a) Exploded View, (b) Assembled Unit

Only a few programs have been found in the literature in which sufficient characterization of the material was performed and care in testing was exercised that confidence could be placed on the property data obtained and where the scatter in data might be related to variability in the material. This was possible only in a few cases where the test apparatus was of high quality and properly used, and the test specimens were properly prepared, machined, and surface finished. The results of these programs have shown that the ceramic processor tended to overestimate his ability to provide the same product from day to day and batch to batch. This was observed with respect to research processors as well as production processors. This appears to be based on the assumption that he is aware of the ceramic process parameters that determine the character of his product, and that he has these under adequate control. However, as a result of sophisticated testing of certain of these products it has been possible to uncover character features that were not controlled, and as a result were directly responsible for variability in property data. Therefore, one of the objectives of this paper is to communicate the need for adequate characterization and precisely controlled testing to reduce a major source of variability and therefore aid in developing wider use of brittle materials for critical structural applications.

CONCLUSIONS

The complexity of the problem of establishing quantitative character-property relationships has been emphasized in this discussion. This was done to draw attention to the fact that the current state of the art of material characterization and property measurements is one that might be described as an emerging technology. The vast majority of the work to date has been extremely nieve. Most of the published data upon which character-property relationships have been based were obtained under conditions where neither the test technique used nor the material was adequately described or characterized. Even less attention has been given to material characterization with respect to the abundance of mechanical property data for brittle materials which fills the literature. The problem facing us now is one of communicating to the radome designer the critical role that material characterization and mechanical testing techniques play in determining the behavior of ceramic radome materials and to encourage him to take these factors into account when using published mechanical property data in designing ceramic radomes.

REFERENCES

1. Robert J. Stokes, "Correlation of Mechanical Properties with Micro-structures" <u>Microstructure of Ceramic Materials Proceedings of an</u> American Ceramic Society Symposium, Pittsburgh, Pa., April 27-28, 1963.

2. J. B. Wachtman, "Mechanical Properties of Ceramics An Introductory Survey" Presented at the "Symposium on Ceramic Materials and Their Properties," National Bureau of Standards, Gaithersburg, Md., October 14, 1966.

3. R. M. Spriggs, "Microstructure and Its Influence on Strength" <u>Strengthening Mechanisms-Metals and Ceramics</u> Syracuse University Press, Syracuse, New York, Chapter 7, pp 181-218, 1966.

4. S. C. Carniglia, "Grain Boundry and Surface Influence on Mechanical Behavior of Refractory Oxides - Experimental and Deductive Evidence," <u>Materials Science Research</u> Vol. 3, Plenum Press, Chapter 24, pp 425-471, 1966.

5. W. D. Kingery and R. L. Cable, "A Review of the Effect of Microstructure on Mechanical Behavior of Polycrystalline Ceramics," <u>Mechanical Behavior of Crystalline Solids</u>, Proceedings of an American Ceramic Society Symposium, New York, N. Y., April 28-29, 1962.

6. D. B. Binns and P. Popper, "Mechanical Properties of Some Commercial Alumina Ceramics," <u>Proceedings of the British Ceramic Society</u>, No. 6, 71-82, June 1966.

7. R. M. Spriggs, J. B. Mitchell and T. Vasilos, "Mechanical Properties of Pure Dense Alumina Oxide as a Function of Temperature and Grain Size," <u>J. Am. Ceram. Soc.</u> 47 (α) 323-27 July 1964.

8. C. D. Pears and H. S. Starrett, "An Experimental Study of the Weibul Volume Theory," AFML-TR-66-228, June 1966.

9. R. L. Barnett and R. L. McGuire, "Statistical Approach to Analysis and Design of Ceramic Structures" <u>Bulletin of the American Ceramic Society</u>, Vol. 45, No. 6, pp 595-602, June 1966.

10. C. D. Pearsand F. J. Digesu, et al., "Evaluation of Tensile Data for Brittle Materials Obtained with Gas-Bearing Concentricity," ASD-TRD-63-245.

11. "C. D. Pears and F. J. Digesu, "The True Stress-Strain Properties of Brittle Materials to 5000° F," AEC ORO 461, 1961, and subsequent Southern Research Reports 5511-1190 (1962), 6387-1190 (1963), and 6995-1190 (1964) all to the Atomic Energy Commission.

12. N. M. Parikh, et al., "Studies of the Brittle Behavior of Ceramic Materials, Parts I, II, and III, ASD-TR-61-628.

13. R. Sedlacek, "Tensile Strength of Brittle Materials," AFML-TR-65-129.

PRECISION MEASUREMENT OF RADOME PERFORMANCE

Bernard Rolsma
McMillan Radiation Labs, Inc.
Ipswich, Massachusetts   01938

ABSTRACT

This paper presents a simple measurement system which provides accurate performance data on radomes. The system has been used and the results have been correlated with computer analysis.

INTRODUCTION

The classic measurement methods of obtaining radome window performance are not accurate enough to determine if the window which was fabricated is what was designed. The measurement techniques, as typified by MIL-R-7705, will provide results which cannot be accurately tied back to window laminate parameters.

The wide band reflection measurement technique or ARCH measurement used at McMillan does provide an accurate picture of what the window is doing and its output data can be used to analyze window laminate parameters. The ARCH measurement is a bistatic reflectivity range which uses a sweep oscillator, a broadband detector and an oscilloscope analyzer.

MEASUREMENT SYSTEM

The ARCH measurement system is an updated version of the Naval Research Laboratory (NRL) reflectivity arch system originally used for measuring absorber reflectivity. The signal source is a sweep oscillator, the detector is broadband, and the display is an oscilloscope analyzer which provides a sweep in frequency versus db.

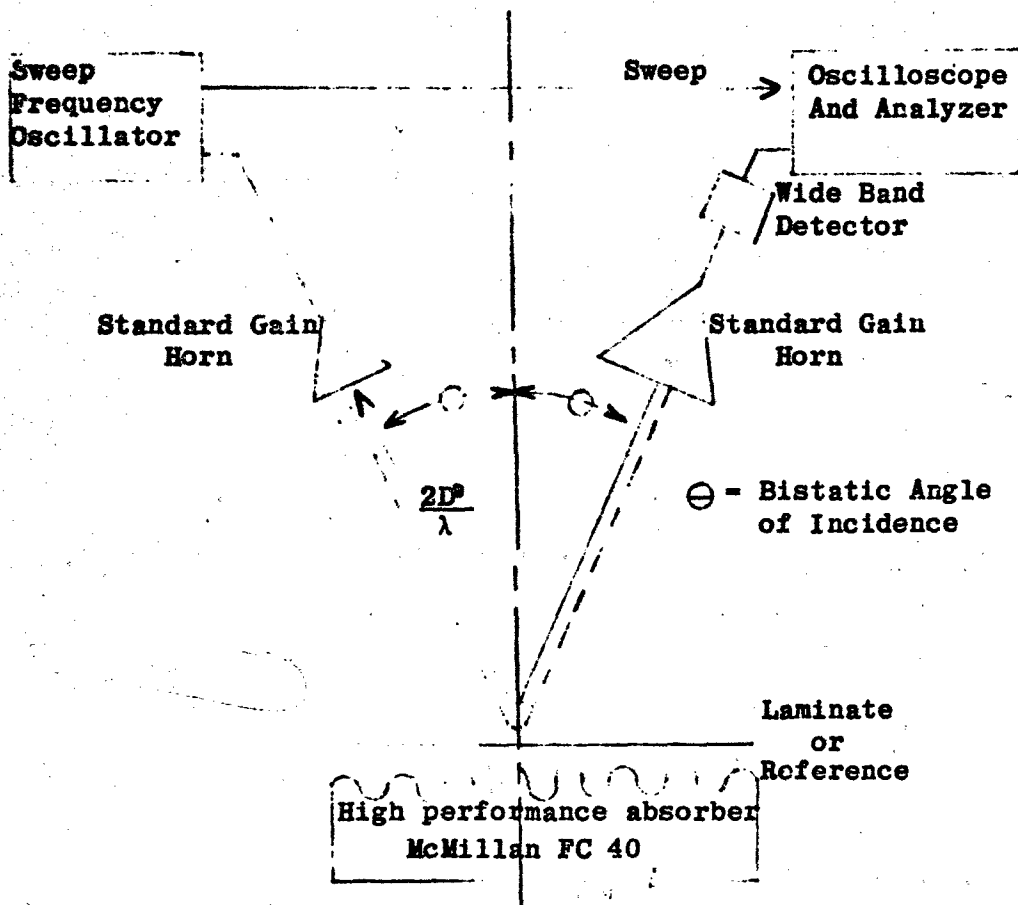Figure I is a diagram of the Reflection Meter.

FIGURE I

The reflection method of obtaining performance relies
on the fact that a low loss laminate will exhibit minimum
reflection at the frequency where the wall is an electrical
half-wave.   The balanced A sandwich and multilayer
sandwiches also exhibit this property of a point of minimum
reflection. The curve of reflection is sharper in contour
over a broad frequency range than is the curve of transmission
which accounts for the method's ability to provide accurate
data.

Figure II is a scope picture of an A sandwich with
.038 skins and a .126 core. Frequency is from right to
left starting at 12.4 GHz and stopping at 17.4 GHz. The
three (3) markers are set at 13.250, 13.575 and 13.790 GHz.
The center marker was set at the curve minimum. The top
horizontal line is the reference from a metal plate. The
reflection from the A sandwich was approximately 38 db down.

0 db

-10 db

-20 db

-30 db

-40 db

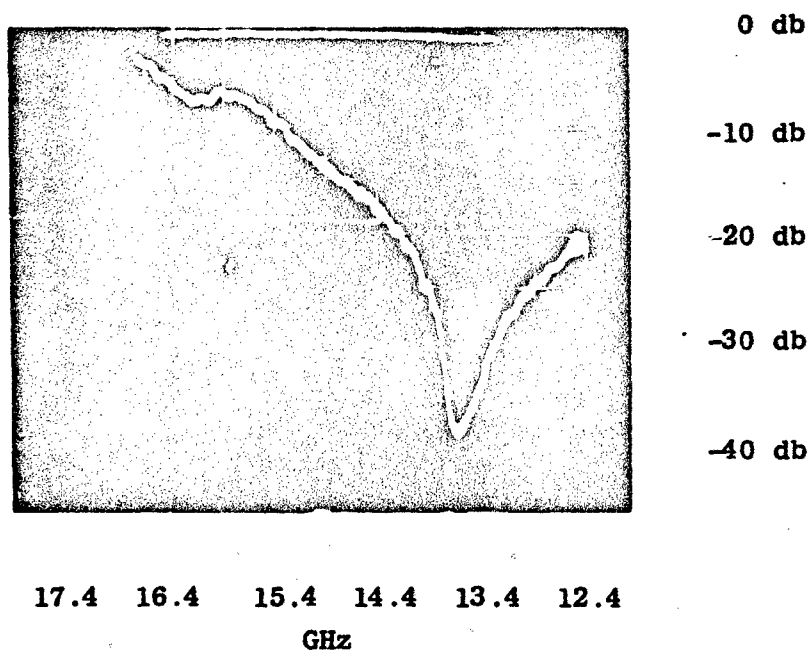17.4   16.4   15.4   14.4   13.4   12.4

GHz

FIGURE II

Figure III is the result of a computer run of the
A sandwich (assuming the lossless case). The computer
input data accuracy at McMillan has been greatly enhanced
by the use of the null measurement on the arch. Sandwich
unbalance, such as caused by uneven bulking or excess paint
on one side, will show up by a filling in of the null. The
ARCH test has also shown the benefits derived from painting
both sides of a radome to maintain a low reflection. Another
fact concerning a balanced sandwich or a solid laminate radome
is: A radome designed at f_1 for a maximum transmission
efficiency (Minimum Reflection) at an angle of incidence other
than the test angle θ of Figure I will have a minimum reflec-
tion (Maximum transmission efficiency) at a frequency f_2 at
the test angle θ. The relationship of frequency and θ is
readily obtainable by using standard transmission equations.
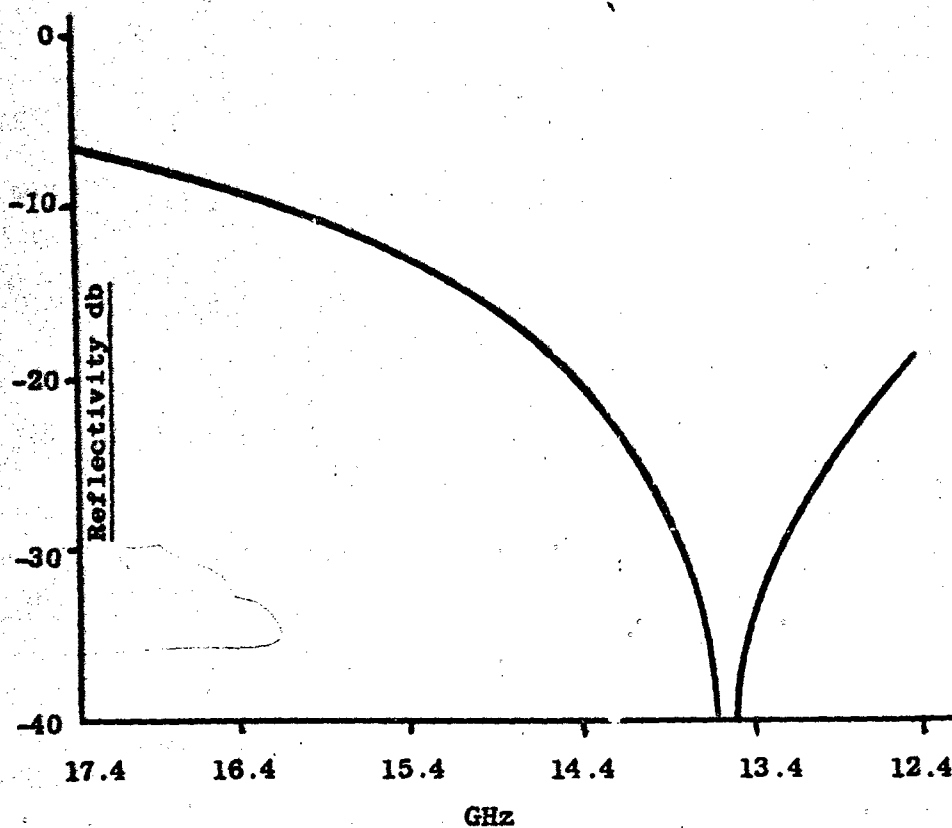
COMPUTER RUNOFF OF A SANDWICH 0.038 SKINS, 0.126 CORE

FIGURE III

216

Figure IV shows the relationship of where the null occurs in frequency for various angles of incidence θ. The sharpness of this curve illustrates the need for the accurate measurement of θ. The ARCH measurement can be made at any angle θ up to the point where coupling between horns affects the measurement, usually below 40°.

This measurement technique has been used to excellent advantage as a production check, and when correlated with the radar system radome performance has permitted a reduction in the amount of testing usually required on the system test range.
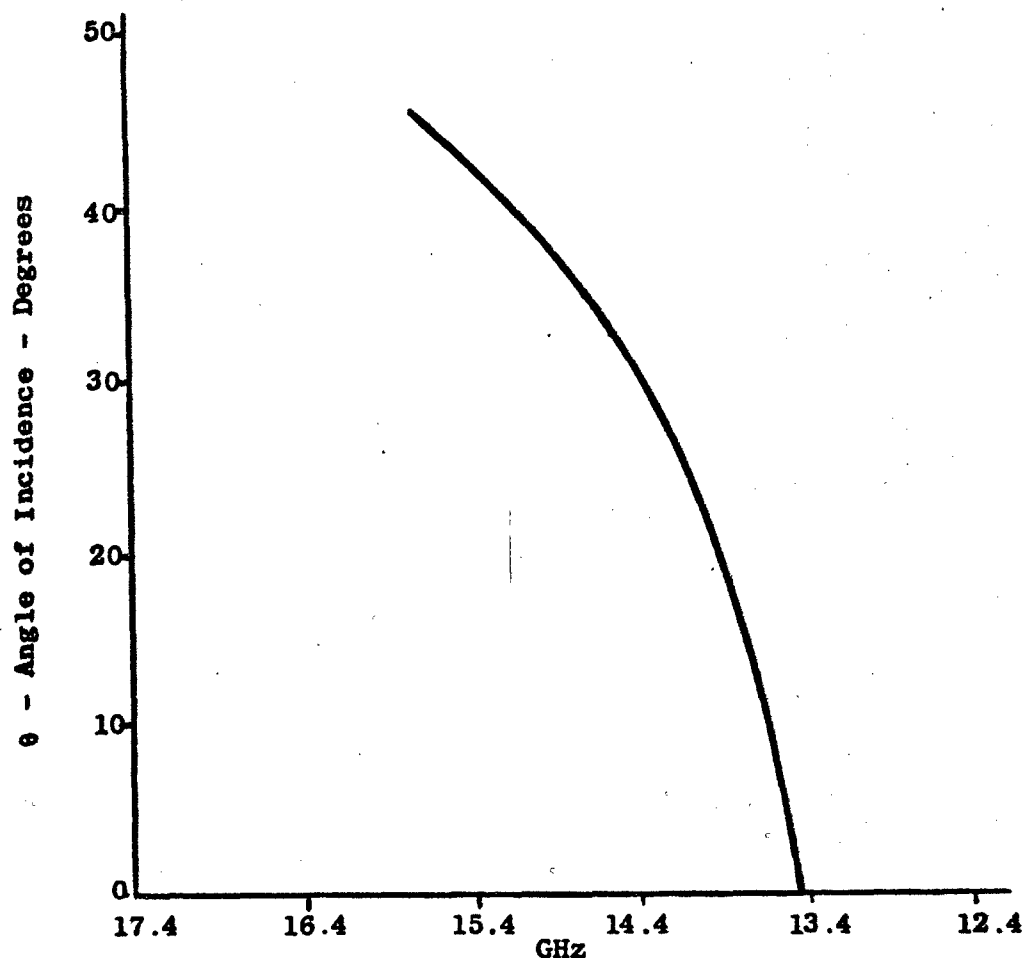
ANGLE OF INCIDENCE VERSUS FREQUENCY OF MINIMUM REFLECTION FOR AN A SANDWICH WITH 0.038"SKINS AND 0.126"CORE (PERP.POLARIZATION)

FIGURE IV
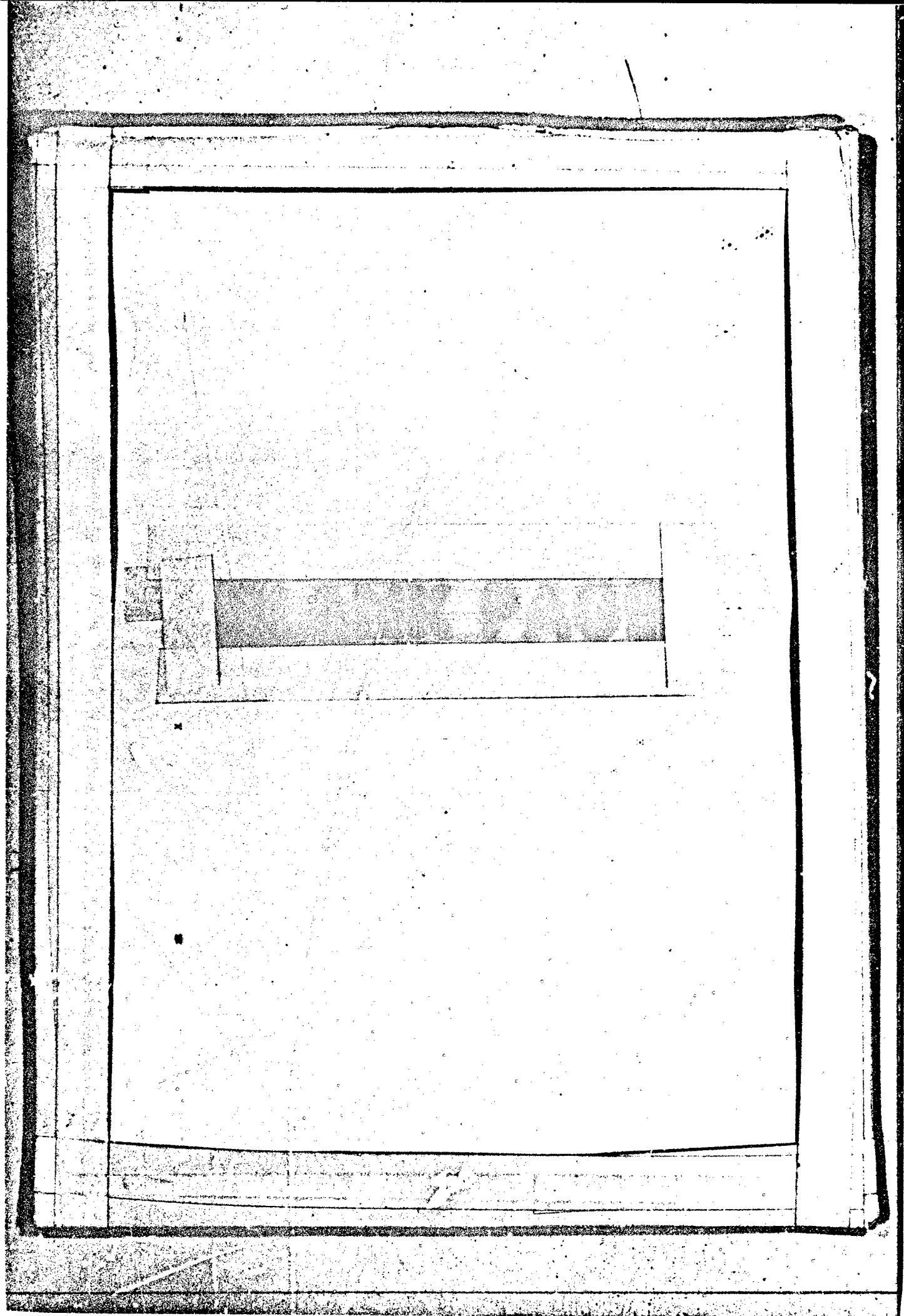
DEVELOPMENT OF THE RADOME FOR THE
CONCORDE PROTOTYPE AIRCRAFT

G.F. Meades and S. Powis
British Aircraft Corporation (Operating) Ltd.
Guided Weapons Division
Stevenage Works
Stevenage, Hertfordshire, England.

ACKNOWLEDGEMENTS

ABSTRACT

The operating conditions of the supersonic transport are more akin to those applicable to the latest military aircraft than to past civil aircraft. Experience gained at B.A.C. on radomes for guided missiles and military aircraft has enabled a radome for the Concorde to be designed which is within our present technology. A solid, half-wave epoxy laminate was chosen for the basic radome. Economic considerations led to the use of matched moulds for radome manufacture.

The basic design is for low transmission losses. However, the presence of a large boom, various services and lightning conductor strips degrade the performance.

This paper examines the various items leading to the chosen radome form giving some indication of the problems encountered and the progress to date.

INTRODUCTION

In mid-1963 the Guided Weapons Division of the British Aircraft Corporation was charged with the problem of producing a nose radome for the Concorde super-sonic transport. The division has a great deal of experience in the design, development and production of radomes for supersonic flight. Large numbers of radomes were designed and produced for Bloodhound and Thunderbird guided missiles at B.A.C., while the radome for the supersonic fighter, the Lightning, was designed by the guided weapons division. The radome for the T.S.R.2 strike aircraft had also been under development within the division before concellation of the project.

It was felt that the experience gained on these projects would be directly applicable to the Concorde as its specification is quite unlike that of previous civil aircraft but more like that of a military aircraft but with even greater emphasis placed on safety, life and cost.

SPECIFICATION

The original specification covered a wide field of properties and also laid down stringent mechanical and electrical performance requirements. The significant features of the specification are as follows:-

1. **Basic Radome Laminate**

   1.1 The Ultimate Tensile strength was to be greater than 10,000 p.s.i. at 130°C following 4000 hrs. soak at 130°C.

   1.2 Young's Modulus was to be greater than 0.4×10^6 lbs/sq. in. at 130°C following 4000 hrs soak at 130°C.

   1.3 Physical properties such as the coefficient of expansion and thermal conductivity were specified together with a heat distortion temperature of the resin system of greater than 200°C.

2. **Moulded Radome Environment and Life**

   2.1 The Radome was to be suitable for world-wide operation.

   2.2 Climatic conditions specified levels of humidity, rain and ambient temperatures of -50°C to +90°C.

   2.3 Operational temperatures against time for a typical flight were specified (figure 1) and the radome was to withstand short periods of exposure at 190°C at the radome tip and 150°C at the rear attachment ring.

   2.4 Target service life was to be 45,000 hrs. of flying, subject to periodic visual inspection.

3. **Electrical Performance**

   3.1 Operating frequency range of 9.314 to 9.405 G.Hz.

   3.2 Attenuation shall not exceed 1.5 dB peak or 0.75 dB averaged over $\pm 60°$ in the plane of the radome axis.

   3.3 Aberration shall not be greater than 1° in the azimuth plane and 0.5° in the pitch plane.

   3.4 The presence of the radome shall not increase any sidelobe level by more than 3 dB at any look angle.

   3.5 The V.S.W.R. shall not be greater than 1.1 : 1 when seen by a matched antenna.

220

3.6   All the above figures shall apply when the radome is measured with
        the correct antenna.

SELECTION OF MATERIAL AND TYPE OF CONSTRUCTION

The selection of a suitable resin system, reinforcement, and type of con-
struction for a radome is an involved problem embracing many parameters such
as physical properties, tooling and cost, and the Concorde is no exception. As was
noted above the specification for the Concorde radome is in many respects like that
of a guided missile. B.A.C. experience with half-wave solid laminate radomes led
one to expect that less risk would be involved with this form of construction than
with any other for the prototype aircraft.

A major advantage of the half-wavelength design is that the radome is over-
strength (though this is paid for by increased weight). This results in a design
flexibility which allows a choice of reinforcement form. Production experience on
missile radomes has shown that knitted glass stockings give a product which is
more economic than woven shapes in initial price, tooling and assembly on the
mould.

An investigation into resin systems quickly narrowed the field to the polyester
and epoxy groups. The final choice for the prototypes fell on the C.I.B.A. 33/1020
resin with HY906 hardener. It was felt that this system had the best all round
strength retention characteristics both with temperature and age, and good
electrical consistency at elevated temperatures.

METHOD OF MOULDING

Two methods of making a half wavelength solid wall radome are by hand lay-
up on a male mould, and by moulding between matched tools. The first technique is
often used for prototypes and experimental work, though this is felt to be a false
economy where a production requirement exists. It is considered that the hand
lay-up method will eventually cost more than laying down production type tools in
the first instance and the testing involved would institute undesirably long production
lead times.

The design of the mould is in principle very simple but due to the size and
shape manufacturing problems have been encountered. The radome is a straight
cone of circular cross section, 91 ins. from tip to base and 44 ins. base diameter
(pre-production radomes will have an elliptical cross-section). Cast aluminium
was used for the construction of the moulds as this gave a relatively light, rigid
construction which could be heated as an aid to curing of the resin. Heating was
accomplished by the use of Isopad heating jackets. These jackets are fitted to the
inside of the male mould and the outside of the female mould. They were divided
into 18 zones, each accurately controlled by thermocouples.

Handling equipment had to be designed which could give easy access to the
male mould, mould assembly, inversion, moulding and final positive ejection of the
radome. Figure 2 shows the assembled mould mounted within the handling frame.
The total mould weight is approximately $3\frac{1}{2}$ tons.

221

Figure 3 shows the basic moulding layout. Following surface preparation of the male mould the knitted glass stockings are laid-up and fastend with metal hooks to the steel ring on the mould. The female mould is then positioned over the lay-up and clamped down. The mould is then inverted and the glass reinforcement dried at 70°C by the use of the heating pads. Following the drying operation the mould temperature is reduced and stabilised at 50°C. Air is then removed from the mould and the vacuum adjusted to 25 ins. of mercury. The resin is then fed into the mould at a pressure of 40 lbs/sq. in. The mould takes about 7 hours to fill. The moulding is then cured for 72 hours at 50° and the allowed to cool to room temperature. Ejection is then carried out using hydraulic jacks under the steel ring which encircles the base. After ejection the moulding is subjected to a gradual post cure schedule. The moulding technique has been completely established on three radomes. Thermal cycling tests, and trial installations have been carried out, and to date no further modifications to the build have been required.

ELECTRICAL TESTS

The prototype Concorde radome is fitted with a large boom 48 ins. long and about $1\frac{1}{2}$ ins. in diameter. This boom is attached to the radome by an assembly 4 ins. in diameter. The boom supports incidence vanes and pitot tube. Along the length of the radome lie three pipes carrying various services and two lightning conductor strips.

The specified attenuation of 1.5 dB peak is for the complete assembly. Measurements give a figure of 2.5 dB. The greater part of the remainder of this paper is concerned with investigating the discrepancy.

The attenuation investigation has been broken down to cover four main regions namely:-

   i.   wall thickness

   ii.   nose hardware and pitot tube

   iii.   three service tubes and

   iv.   lightning conductors.

CLEAN RADOME

The present nominal radome wall thickness is a calculated figure based upon a measured dielectric constant of 3.68. It is known that a taper exists on the wall thickness of prototype radomes. This taper leads to an average radome wall thickness that is thinner than desired. Thus an optimum frequency will exist in practice which is a little higher than the design figure and the optimum will not be as good as predicted by theory.

The peak attenuation, which occurs on-axis, has been measured over the frequency range 9.2 G.Hz to 9.6 G.Hz. This showed an optimum as expected a little above 9.6 G.Hz. The measured value is about 0.1 dB above that predicted for a wall thickness corresponding to a design frequency of 9.6 G.Hz, a dielectric constant of 3.68 and a loss tangent of 0.015. The difference of 0.1 dB is probably

222

due to the taper of the radome wall thickness. It was therefore concluded that a clean radome of constant thickness could be designed to give 0.7 dB attenuation at 9.375 G.Hz.

NOSE HARDWARE AND PITOT

The nose hardware and pitot were then added to the clean radome and the extra attenuation measured. This came to approximately 0.9 dB which is mainly due to the nose hardware. Calculations of aperture blocking showed that the measured value is about twice that expected from theory. This could be due to other scattering mechansims existing caused by the length of the obstruction and its proximity to a dielectric skin. This was checked by replacing the nose hardware with a metal disc of the same diameter. The attenuation was measured as 0.5 dB.

SERVICE TUBES

These tubes consist of two, $\frac{3}{8}$ ins. diameter, mounted together on one side of the radome and a third, $\frac{7}{8}$ ins. diameter mounted on the other. When mounted at opposite sides the peak attenuation due to the tubes is 1.0 dB. As the tubes are brought together this attenuation decreased to about 0.3 dB when all three tubes are together and crossed to the E vector.

LIGHTNING CONDUCTORS

The conductors are two strips, $1\frac{1}{4}$ ins wide, 138° apart and almost in line with the E vector. Under these conditions a loss of 0.5 dB results. An investigation was carried out into the effect of varying the strip widths as well as position. A peak in the attenuation occurs when each strip is about $\frac{3}{4}$ ins. wide. This is assumed to be due to the normal width resonance modified by the presence of the dielectric surface (The wavelength in the dielectric is 0.65 ins.). Minimum loss also occured when the two strips were brought together and crossed to the E vector.

COMPLETE RADOME WITH FITTINGS

As a final measurement all the fittings were put into their normal places. In this condition the services are shaddowed by the lightning conductors which run on the outside surface of the radome. The peak loss measured at 9.4 G.Hz was 2.5 dB. Summing the individual losses of 0.9 dB for the clean radome, 0.9 dB for the nose hardware and pitot and 0.9 dB for the lightning conductor strips and shaddowed services, we obtain a figure of 2.7 dB.

This shows that the total improvement expected can be obtained by summation of the individual improvements.

SUMMARY OF ATTENUATION PERFORMANCE

No single modification can be made which will reduce peak losses to the specified 1.5 dB level.

i. Wall thickness. At present this is slightly non optimum. When optimised and with no taper a figure of 0.7 dB may be achieved. A lower figure will only be obtained if the basic resin were changed for a lower loss material.

ii. Nose hardware. The pitot tube itself is assumed to be unchangeable and only contributes 0.1 dB. If the nose hardware were to be redesigned a performance approaching that of a flat metal disc might be achieved, say 0.6 dB plus 0.1 dB for the pitot tube.

iii. Lightning strips plus services. It is clear from the experiments that for best electrical performance the strips and services should be mounted in the H plane of the radome i.e. at the top of the radome. Whilst this might be possible for the services the efficiency of the lightning strips may be impaired. A compromise may be struck by moving the lightning strips to a separation of 80°, giving a loss of about 0.5 dB.

ABERRATION

This is measured by noting the change in direction of the polar diagram main beam peak response when the radome is fitted. Although an inaccurate method it is still sufficient for the purposes of this measurement. Aberrations measured are well within the specification.

SIDELOBE DEGREDATION AND V.S.W.R.

Measurements of polar diagrams with and without the radome showed that sidelobe degredation and V.S.W.R. are greater than specified. In view of the relatively high transmission loss caused through blockage and scattering by nose, strips etc. it is not surprising that the sidelobe and V.S.W.R. performances are degraded. However, an improvement in loss will result in an improvement in sidelobes and V.S.W.R. and should enable the specification to be met.

CONCLUSION

The manufacturing techniques for making a pressure injection moulding of the size of this radome have been established and a number of radomes made. Radomes have been subjected to thermal cycling, strength, and trial installation tests, and have met the requirements. The electrical performance is below the prototype specification but the reasons are known and modifications are in hand to improve the situation. The knowledge obtained by our test programmes will now ensure full performance on the pre-production and production radomes which differ physically from the prototype discussed in this paper.
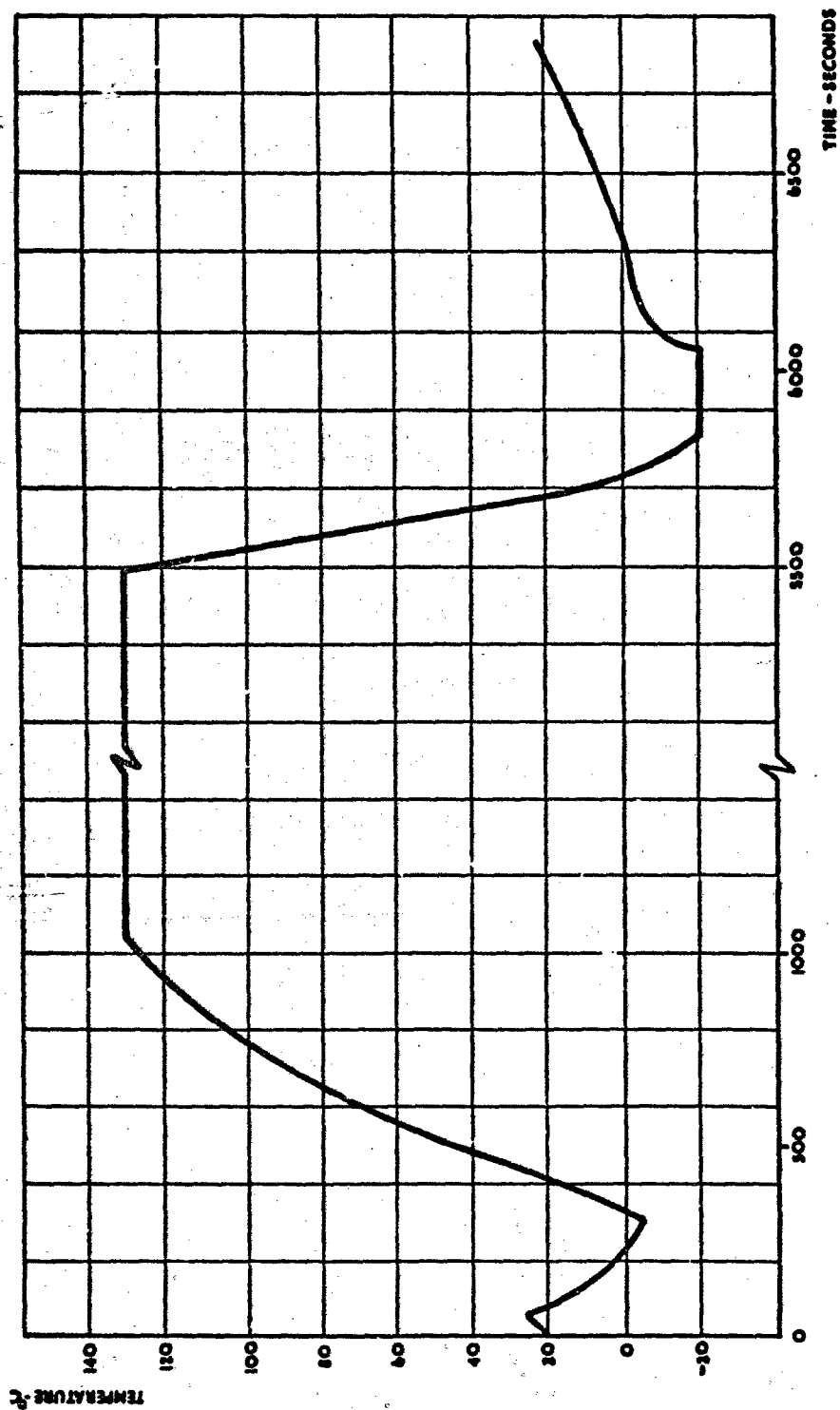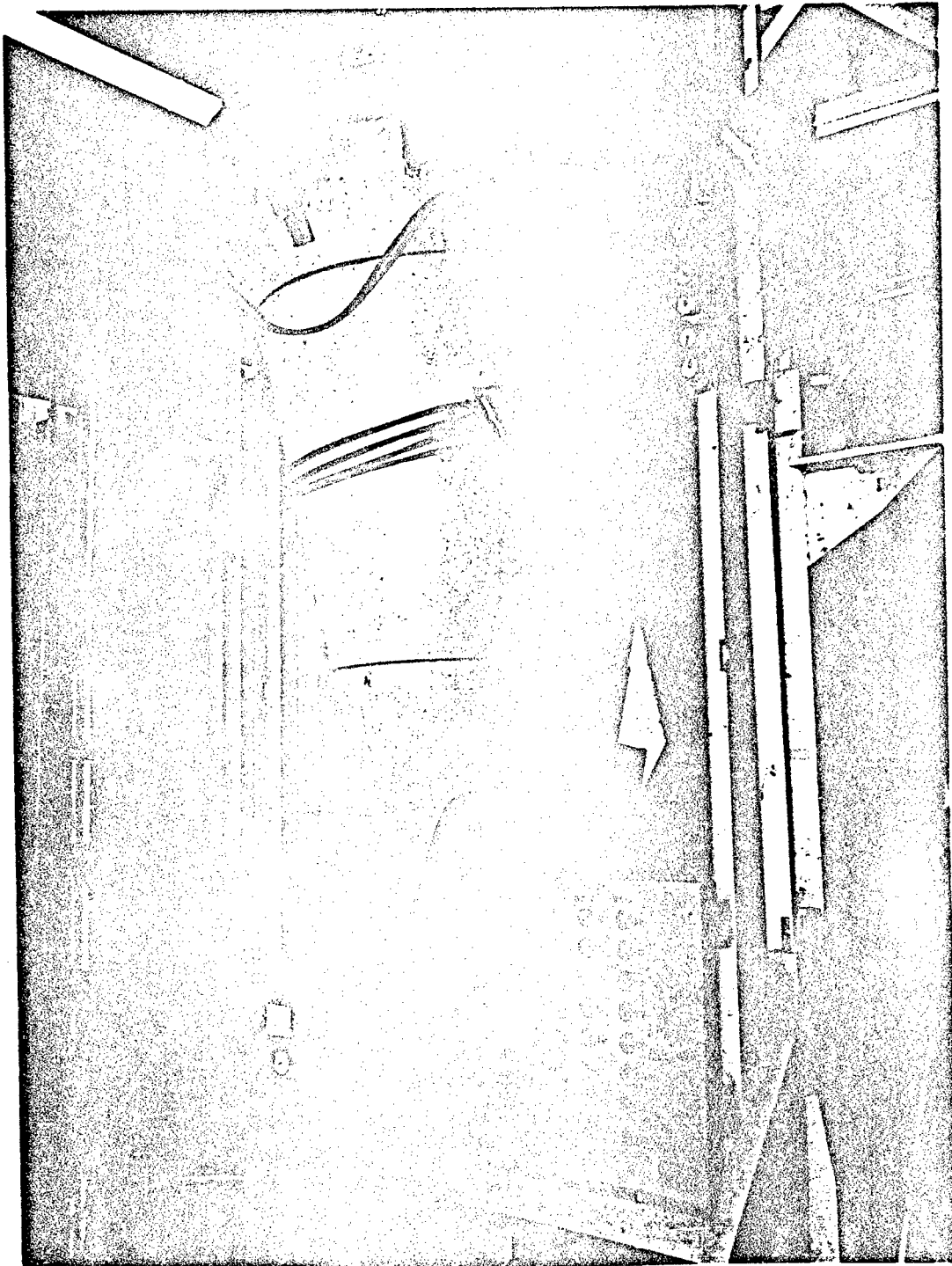
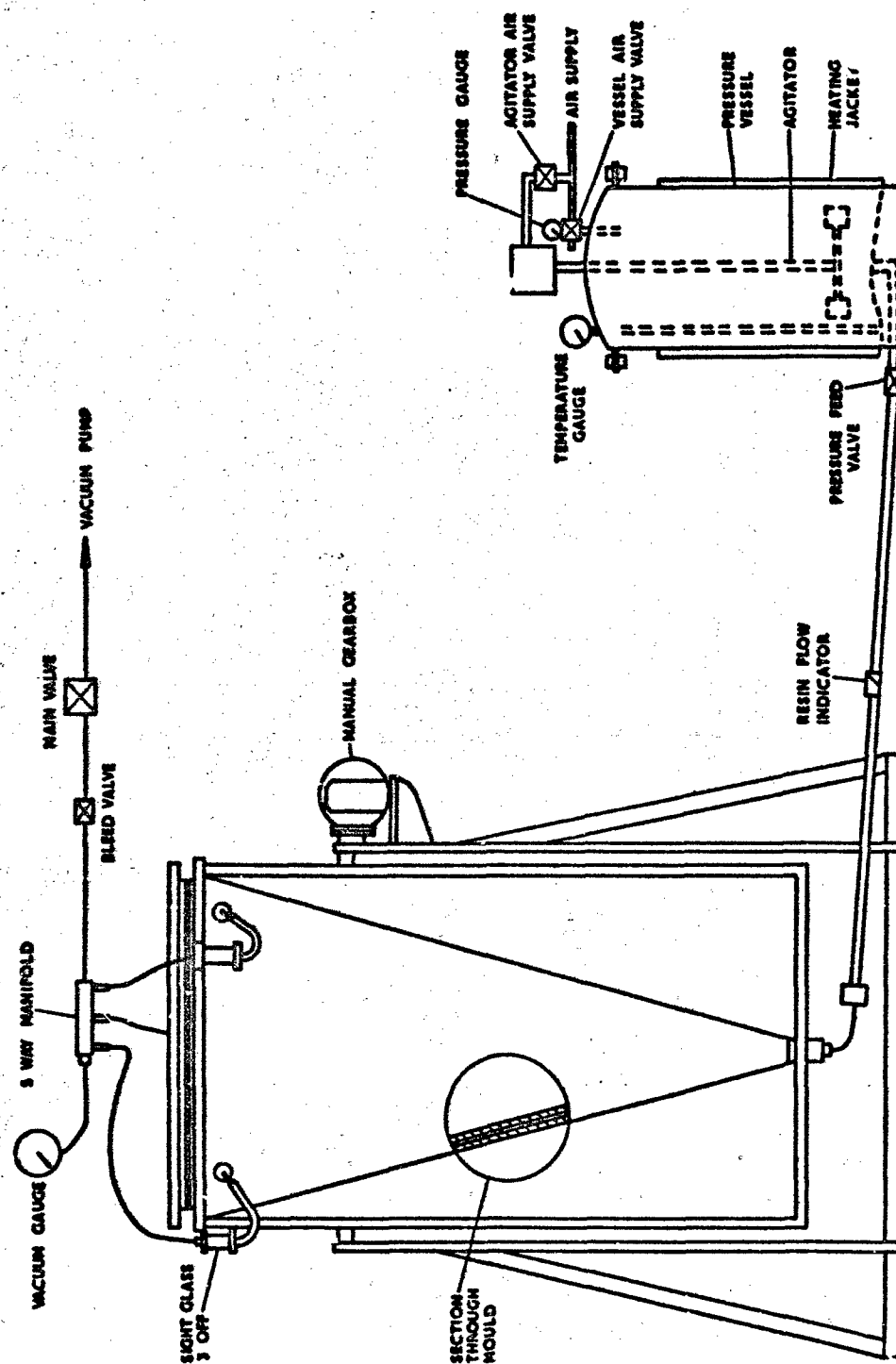Figure 1. Variation of Adiabatic Wall Temperature.

Figure 2. Assembled Mould.

Figure 3. Basic Moulding Layout for Concord Radome.

X-BAND DIELECTRIC CONSTANT OF SLIP CAST FUSED SILICA

B. Fellows
HITCO
Gardena, California

1.0 INTRODUCTION

Slip cast fused silica is being used and considered for a wide range of electromagnetic window applications. Among the properties of special importance to the design and performance of such a window is the dielectric constant.

The dielectric constant of any material in general, but in particular SCFS, is influenced by the composition, micro-structure, and density.

2.0 THEORETICAL CONSIDERATIONS

A SCFS EM window can be considered as a distribution of porosity and impurities in the silica matrix. For the case of isotropically dispersed phases in the silica matrix the logarithmic mixutre rule gives:[1]

$$\log K = \Sigma V_i \log K_i \qquad (1)$$

where

K_i = dielectric constant of phase i

V_i = volume fraction of phase i

The major phases present in SCFS are: (1) fused silica containing impurities in solution, (2) cristobalite, and (3) air in the form of porosity. Thus equation (1) can be written:

$$\log K = V_{fs} \log K_{fs} + V_{cr} \log K_{cr} + V_p \log K_p \qquad (2)$$

The literature reports a dielectric constant of 3.78 for pure clear fused silica at 10^{10} cps. A value for the cristobalite phase has not been obtained. It is felt that it would be higher since cristobalite is more dense than fused silica.

Over the narrow density range involved, equation (1) is closely approximated by a straight line.

---

[1]Kingery, Introduction to Ceramics, p. 720

3.0 EXPERIMENTAL PROGRAM

3.1 Sample Preparation

Samples of fused silica slip were cast into rods or disks, dried, and then fired at 2200°F. for times ranging from 1-1/2 to 5 hours. Test samples were then machined from these blanks by grinding with diamond tools using water cooling. Following machining, the samples were dried at 1500°F. for 1 hour. The prepared samples were stored in sealed plastic bags.

3.2 Dielectric Constant Test Method

The shorted-line method of dielectric constant measurement in a rectangular wave guide was used. Calibration with a 3.00 standard to within $\pm$ 1% agreement was maintained. Measurement techniques and equations described by von Hippel[2] were used. Correction for fit in the wave guide were not felt to be required since the fit was generally good to within 0.001 inch.

3.3 Sample Characterization

The sample composition, density, and cristobalite constant were measured. The density of each sample was accurately determined by measuring and weighing the rectangular test samples. The cristobalite content of randomly selected samples of different densities was measured on a General Electric XRD X-ray diffraction unit. The cristobalite contents reported are relative, compared to the Georgia Tech A-10 standard.

3.4 Results

The dielectric constant versus bulk density data is presented in Figure 1. It should be noted that the three lots of material tested cover a considerable range of densities which are due to differences between lots in slip properties, as well as deliberate variations in the sintering cycle.

The cristobalite content for randomly selected samples is compared to the density and dielectric constant data in Table I.

The Furlilca-10 SCFS is 99.6 - 99.7% SiO_2 while the Aero-Ceram 50 is 99.9% SiO_2. The major impurity is Al_2O_3.

4.0 DISCUSSION OF RESULTS

The dielectric constant data in Figure I fits a straight line reasonably well over the entire range. By inspection, the line shown was drawn through the points and its equation obtained as:

---

[2]von Hippel, A.R. Dielectric Materials Applications, Wiley 1954

also see - Handbook of Microwave Measurements, Chapter 9, Polytechnic Institute of Brooklyn, 1963

$$K^1 = 1.61\rho + 0.183$$

$$= 1.61\rho + 0.183 \qquad (3)$$

The influences of the changes in purity and cristobalite content appear to be quite small and unnoticeable compared to the effect of density.

The data suggest and practice has confirmed that it is possible to adjust the dielectric constant within limits over the range reported by judicious selection of raw material and sintering schedule. Selected values have been reproduced as closely as ± 0.03 with acceptable rejection rates, although ± 0.05 is a more reasonable tolerance from a manufacturing viewpoint.

It should be noted that because of variations from batch to batch of material that are difficult to control, close regulation of the dielectric constant is often obtained only at the expense of other properties (such as modulus of rupture).

5.0 CONCLUSIONS

5.1 The dielectric constant of SCFS is primarily a linear function of the bulk density of the material and is not appreciably changed by minor changes in purity or cristobalite content.

5.2 The dielectric constant can be varied over a limited range as desired and held within close tolerances.

TABLE I

SELECTED CRISTOBALITE CONTENT DATA

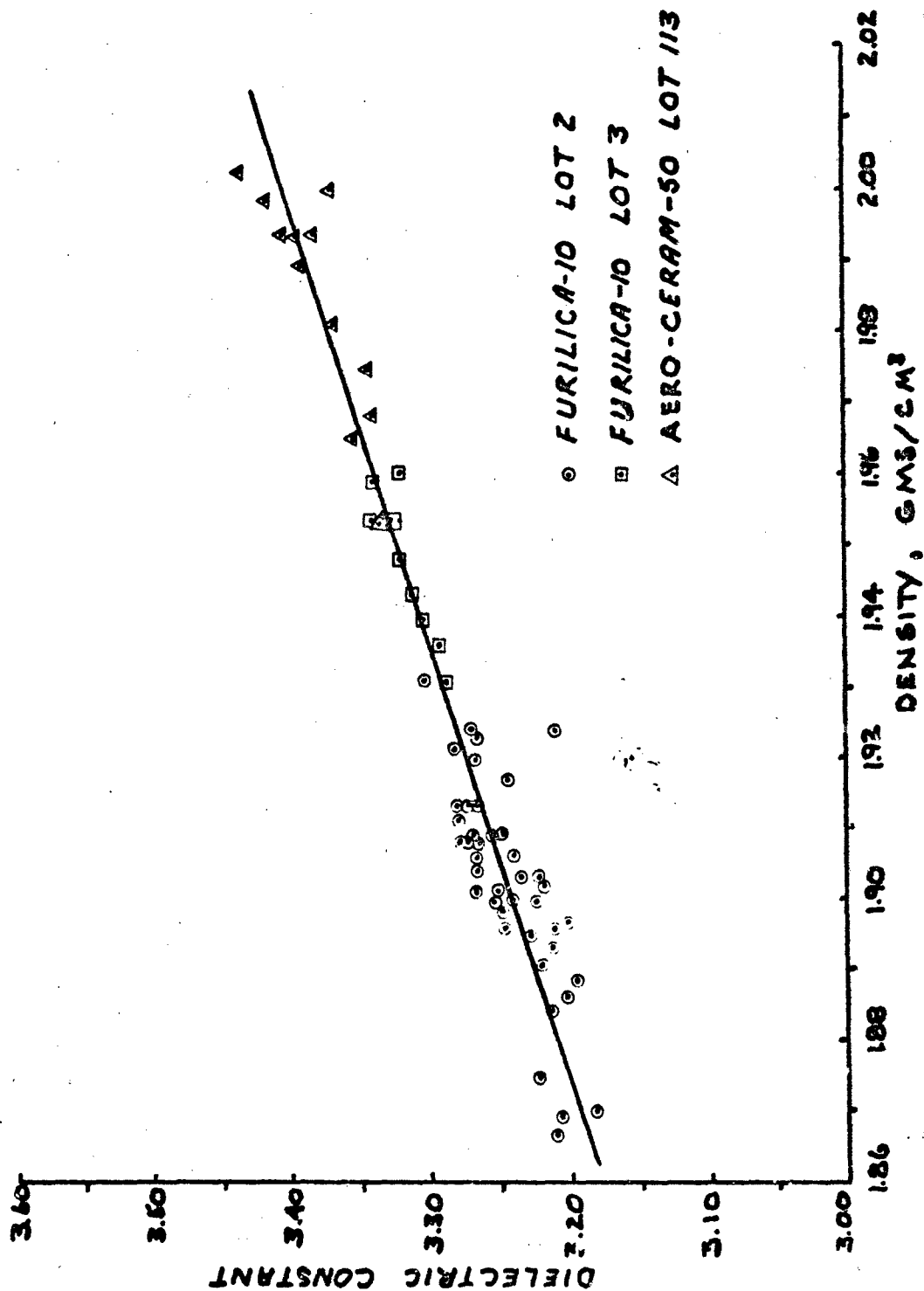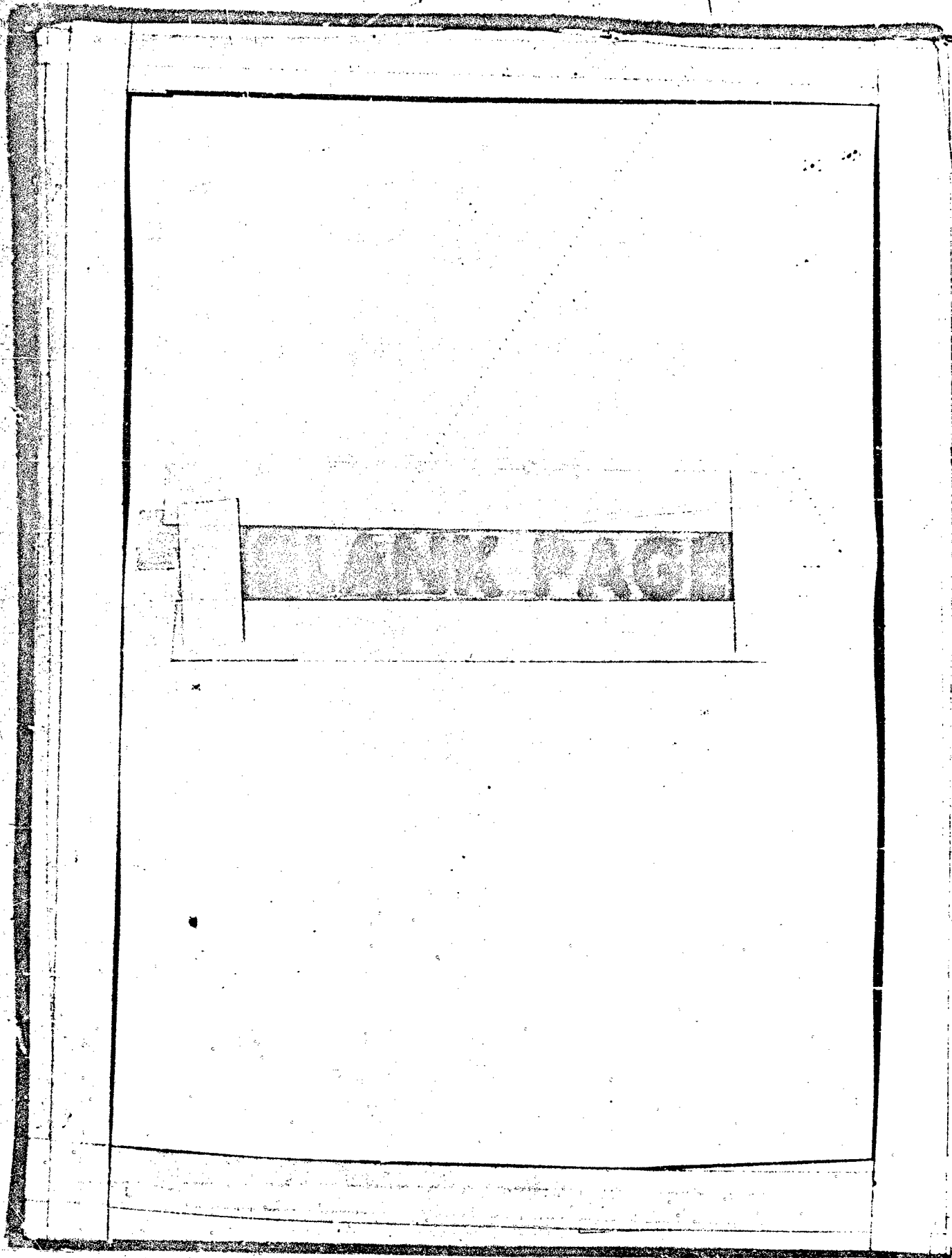| Sample	Density	Dielectric Constant	Volume % Cristobalite
Furilica-10, Lot 2	1.869	3.193	2.2
	1.873	3.196	1.2
	1.891	3.227	1.3
	1.903	3.247	4.4
	1.914	3.265	6.0
	1.931	3.292	6.7
Aero-Ceram-50, Lot 113	1.954	3.335	0.2
	1.968	3.350	<0.1
	1.975	3.362	0.6
	1.981	3.373	<0.1
	1.994	3.394	1.0
	1.998	3.400	0.2
	2.012	3.420	0.9

Figure 1. SCFS Dielectric Constant vs. Density.

233

BLANK PAGE

CHARACTERIZATION OF FUSED SILICA SLIPS

C. A Murphy

High Temperature Materials Division
Materials Application Branch
Engineering Experiment Station
Georgia Institute of Technology
Atlanta, Georgia 30332

ACKNOWLEDGMENTS

ABSTRACT

Commercial fused silica slips were evaluated according to a set of characterization parameters which were formulated to provide a basis for selection of fused silica slips for the fabrication of test radomes under Contract N00017-67-C-0053. This work on the characterization of the commercial fused silica slips is presented as a special report to furnish users and potential users of fused silica slip with a source for preparing engineering specifications and/or for making comparisons to data generated during the course of laboratory investigations or hardware fabrication programs.

INTRODUCTION

The state-of-the-art of slip-cast fused silica (SCFS) has advanced to the stage where precision SCFS radomes have been fabricated and have been successfully flown on a Navy Missile. SCFS has also been successfully flown as a portion of the cylindrical missile body which serves as the EM window on an Air Force missile. These flights are considered most noteworthy, and with their success, interest in utilizing SCFS for experimental and operational hardware has accelerated among a number of organizations. However, the lack of well defined process control parameters could result in the production by some organizations having little or no previous background in SCFS, of SCFS radomes and EM windows with inferior physical properties.

At the present time there are three independent commercial sources which supply fused silica slip. These slips often exhibit different characteristics from batch to batch as well as between sources. Experience has indicated that significantly different physical properties are obtained in the sintered SCFS when the same processing parameters are used. Unlike most ceramics, the parameters of sintering time and temperature alone are not adequate to characterize the processing of SCFS. Variances in the physical properties of SCFS are not produced solely by the degree of sintering densification obtained during processing. Rather, they result from a balance between sintering densification and the degree of devitrification of the fused silica. Since the devitrification rate of fused silica is so dependent upon such factors as impurity content,

particle size, residual crystallinity, and furnace atmosphere, simple processing controls such as sintering time and temperature can not solely be used to obtain desired physical properties in a fabricated component. Therefore, it soon became apparent during this program under Contract N00017-67-C-0053 that there was a critical need to develop the technology which could be used to assist in developing reliability in the production of SCFS flight hardware from one organization to another. Three areas which were considered and which were investigated to provide this technology were: (1) characterization of commercially available fused silica slips, (2) definition of time-temperature-thickness relationships for uniform sintering, and (3) determination of the influence of grinding on the particle distribution, time-temperature-cristobalie behavior and the physical properties of slipcast bodies. This report covers the work in the area of commercial fused silica slip characterization.

EXPERIMENTAL ACCOMPLISHMENTS

The need for establishing the property data which would allow a decision to be made on the suitability of a given fused silica slip for the production of flight hardware has been recognized for many years. In earlier work, a number of tests had been used, but allowable limits had not been established, and fused silica slip acceptability had been determined more or less by trial. To improve this situation, parameters were established which implement the characterization of fused silica slips. These are presented in Table I. The fused silica slips that were required under this and other research programs at Georgia Tech during 1967 were evaluated according to these measurements. Also, other fused silica slip samples were obtained from the manufacturers and examined using these measurement techniques. The measured data are shown in Table II and in Figures 1 through 4.

As histories were compiled, a pattern began to develop which, on the basis of two measurements, appeared to allow a decision to be reached concerning the suitability of a particular fused silica slip for the fabrication of hardware. These measurements were: (1) cristobalite content in 3/4-inch diameter specimens after sintering for 3-1/3 hours at 2200° F, and (2) apparent viscosity as a function of spindle speed (using the Brookfield Viscometer with a number 2 spindle). It was found that this approach was not entirely satisfactory because some fused silica slips were not stable (even though the viscosity was in a certain range) and had a high tendency towards particle sedimentation. This is strongly influenced by the weight per cent solids but is not well defined since the rheology is controlled by a balance between pH, per cent solids and particle size distribution. For example, slip number 13 settled excessively as shown in Figure 5; the pH and per cent solids are within acceptable bounds. This settling manifests itself as "thick" sediment in containers during the casting operation as "thick" sediment in the mold cavity (this, however, can be compensated for in a somewhat unsatisfactory manner by allowing the sediment to build-up on a surface not having any function in the formation of the hardware, i.e. on the closure plate of a radome mold by casting with the radome tip "up") and as "plugged" delivery lines (sediment in some cases completely filled delivery lines terminating the casting operation). It was clear that a simple test to observe the settling was necessary as a third observation on the fused silica

TABLE I

PARAMETERS USED TO CHARACTERIZE FUSED SILICA SLIP

Parameter	Method of Measurement
pH	Line voltage pH meter
Weight per cent solids	Weight loss (volatiles) at 350° F
Particle size distribution (mass and count bases)	Coulter Counter® 1/
Apparent viscosity	Brookfield Synchro-Lectric Model LVF Viscometer
Residual crystalline phases	X-ray diffraction 2/
Impurities	Spectrographic analysis
Cristobalite content in slip-cast, 3/4-inch diameter test bars vs time at 2200° F	X-ray diffraction 2/
Young's modulus of slip-cast, 3/4-inch diameter test bars vs time at 2200° F	Sonic 3/
Modulus of rupture of slip-cast, 3/4-inch diameter test bars after sintering for 3-1/3 hours at 2200° F	Four point, quarter point loading 4/
Young's modulus of slip-cast, 3/4-inch diameter test bars after sintering for 3-1/3 hours at 2200° F	Sonic 3/
Cristobalite content of slip-cast, 3/4-inch diameter test bars after sintering for 3-1/3 hours at 2200° F	X-ray diffraction 2/
Porosity, bulk density and theoretical density of slip-cast, 3/4-inch diameter test bars after sintering for 3-1/3 hours at 2200° F	Air displacement 5/

TABLE II

CHARACTERIZATION DATA ON FUSED SILICA SLIPS

Measurement	Values for Slip Number					
	1	2	3	4	5	6
pH	4.1	4.4	6.5	4.6	4.5	4.2
Weight Per Cent Solids	82.1	82.6	82.2	82.2	83.1	82.1
Particle's Size Distributions	Figures 1 and 2	Figures 1 and 2	Figures 1 and 2	Figures 1 and 2	Figures 1 and 2	---
Apparent Viscosity[1] in Centipoise at -						
60 rpm	104	117	10	106	114	108
30 rpm	102	115	49	105	113	109
12 rpm	22	135	308	101	135	165
6 rpm	10	165	1200	130	150	160
Residual Crystalline Phases (other than cristobalite)	None	None	α-quartz tridymite	None	None	α-quartz
Residual Cristobalite (Volume Per Cent)	0.6	---	0.2	0.6	1.7	0.5
Spectrographic Analysis Parts per million of -						
Mg	---	---	20-100	n.d. (n.d.)	n.d. (2-25)	---
Fe	---	---	20-100	100-500 (20-50)	3-50 (5-25)	---
Al	---	---	20-100	2-3 (2-20)	2-20 (2-20)	---
Ti	---	---	n.d.	100-500 (10-25)	100-500 (25-50)	---
Ca	---	---	n.d.	20-50 (n.d.)	20-50 (n.d.)	---

NOTE: n.d. = not detected.

[1]Measured with Brookfield Synchro-Lectric Model LVF using No. 2 spindle.

(Continued)

238

TABLE II (Continued)

CHARACTERIZATION DATA ON FUSED SILICA SLIPS

Measurement	Values for Slip Number					
	1	2	3	4	5	6
Cristobalite Content vs Time at 2200° F	Figure 3	Figure 3	Figure 3	Figure 3	Figure 3	---
Elastic Modulus vs Time at 2200° F	Figure 4	Figure 4	Figure 4	Figure 4	Figure 4	---
Modulus of Rupture - sintered for 3-1/3 hours at 2200° F (lb/in^2)	3382 ± 468[2]	5612 ± 500	4426 ± 713	3600 ± 346	4738 ± 228	2442 ± 582
Elastic Modulus - sintered for 3-1/3 hours at 2200° F $(10^6 \; lb/in^2)$	2.44 ± 0.23[2]	4.84 ± 0.05	6.11 ± 0.10	3.93 ± 0.14	4.33 ± 0.06	2.53 ± 0.10
Other Properties - sintered for 3-1/3 hours at 2200° F						
a. Porosity (Volume Per Cent)	14.24 ± 0.14[2]	11.75 ± 0.15	11.06 ± 0.46	13.78 ± 0.13	14.12 ± 0.14	13.45 ± 0.32
b. Bulk Density (gm/cc)	1.957 ± 0.002[2]	1.978 ± 0.004	1.974 ± 0.017	1.900 ± 0.007	1.902 ± 0.004	1.932 ± 0.006
c. Theoretical Density (gm/cc)	2.285 ± 0.005[2]	2.241	2.219 ± 0.010	2.203 ± 0.007	2.217 ± 0.005	2.232 ± 0.005
Cristobalite Content - sintered for 3-1/3 hours at 2200° F (Volume Per Cent)	39.7 ± 3.9[3]	---	11.0 ± 0.3	11.8 ± 1.2	8.9 ± 0.06	29.2 ± 1.2

[2] Confidence Interval at 95 per cent level based on ten specimens.

[3] Confidence Interval at 95 per cent level based on three determinations.

(Continued)

239

TABLE II (Continued)

CHARACTERIZATION DATA ON FUSED SILICA SLIPS

Measurement	Values for Slip Number					
	7	8	9	10	11	12
pH	4.7	4.7	4.6	---	5.9	5.0
Weight Per Cent Solids	82.8	82.3	81.4	---	82.6	82.8
Particle Size Distributions	---	---	Figures 1 and 2	Figures 1 and 2	Figures 1 and 2	Figures 1 and 2
Apparent Viscosity[1] in Centipoise at -						
60 rpm	134	234	89		120	160
30 rpm	132	128	91		110	150
12 rpm	160	135	109		109	150
6 rpm	205	165	125		50	170
Residual Crystalline Phases (other than cristobalite)	None		None	None	None	None
Residual Cristobalite (Volume Per Cent)	1.0	0.3	0.1	0.5	0.3	0.3
Spectrographic Analysis Parts per million of -						
Mg	---	---	2-5	2-5	---	20-100 (n.d.)
Fe	---	---	50-200	5-20	---	20-100 (5-25)
Al	---	---	20-100	2-10	---	2-20 (n.d.)
Ti	---	---	50-100	20-50	---	100-500 (25-50)
Ca	---	---	n.d.	n.d.	---	n.d. (n.d.)

NOTE: n.d. = not detected.

[1] Measured with Brookfield Synchro-Lectric Model LVF using No. 2 spindle.

(Continued)

240

TABLE II (Continued)

CHARACTERIZATION DATA ON FUSED SILICA SLIPS

Measurement	Values for Slip Number					
	7	3	9	10	11	12
Cristobalite Content vs Time at 2200°F	---	Figure 3	Figure 3	Figure 3	Figure 3	Figure 3
Elastic Modulus vs Time at 2200°F	---	---	Figure 4	Figure 4	Figure 4	Figure 4
Modulus of Rupture - sintered for 3-1/3 hours at 2200°F (lb/in²)	2832 ± 434[2]	2176 ± 120	5405 ± 175	3251 ± 424	4567 ± 807	3566 ± 630
Elastic Modulus - sintered for 3-1/3 hours at 2200°F (10^6 lb/in²)	2.71 ± 0.05[2]	1.63 ± 0.02	4.54 ± 0.09	3.30 ± 0.05	4.26 ± 0.04	4.01 ± 0.10
Other Properties - sintered for 3-1/3 hours at 2200°F						
a. Porosity (Volume Per Cent)	12.92 ± 0.32[2]	14.48 ± 0.24	13.61 ± 0.14	---	12.85 ± 0.51	13.03 ± 0.16
b. Bulk Density (gm/cc)	1.962 ± 0.009[2]	2.002 ± 0.009	1.942 ± 0.004	---	1.952 ± 0.005	1.959 ± 0.006
c. Theoretical Density (gm/cc)	2.252 ± 0.007[2]	2.364 ± 0.014	2.248	---	2.240 ± 0.017	2.252 ± 0.005
Cristobalite Content - sintered for 3-1/3 hours at 2200°F	33.3 ± 3.1[3]	90.2 ± 2.8	---	13.9 ± 0.3	20.3 ± 1.1	26.4 ± 0.8

[2] Confidence Interval at 95 per cent level based on ten specimens.

[3] Confidence Interval at 95 per cent level based on three determinations.

(Continued)

TABLE II (Continued)

CHARACTERIZATION DATA ON FUSED SILICA SLIPS

Measurement	Values for Slip Number		
	13	14	15
pH	5.1	5.7	3.8
Weight Per Cent Solids	82.0	82.3	83.8
Particle Size Distributions	Figures 1 and 2	Figures 1 and 2	Figures 1 and 2
Apparent Viscosity[1] in Centipoise at -			
60 rpm	108	175	132
30 rpm	100	135	138
12 rpm	140	135	160
6 rpm	200	140	170
Residual Crystalline Phases (other than cristobalite)	None	None	None
Residual Cristobalite (Volume Per Cent)	---	0.5	0.6
Spectrographic Analysis Parts per million of -			
Mg	2-5	2-5	10-50 (n.d.)
Fe	5-20	5-20	20-50 (n.d.)
Al	n.d.	2-10	2-200 (2-10)
Ti	< 10	< 10	n.d. (n.d.)
Ca	n.d.	n.d.	5-50 (n.d.)
Cristobalite Content vs Time at 2200° F	---	Figure 3	Figure 3
Elastic Modulus vs Time at 2200° F	---	Figure 4	Figure 4
Modulus of Rupture - sintered for 3-1/3 hours at 2200° F (lb/in²)	4301 ± 564[2]	3252 ± 453	2369 ± 218[4]

NOTE: n.d. = not detected.

[1] Measured with Brookfield Synchro-Letric Model LVF using No. 2 spindle.

[2] Confidence Interval at 95 per cent level based on ten specimens.

[4] Sintered for 15 hours at 2200° F.

(Continued)

TABLE II (Concluded)

CHARACTERIZATION DATA ON FUSED SILICA SLIPS

Measurement	Values for Slip Number		
	13	14	15
Elastic Modulus vs Time at 2200° F	---	Figure 4	Figure 4
Modulus of Rupture - sintered for 3-1/3 hours at 2200° F (lb/in^2)	4301 ± 564[2]	3252 ± 453	2369 ± 218[4]
Elastic Modulus - sintered for 3-1/2 hours at 2200° F (10^6 lb/in^2)	4.24 ± 0.09	3.44 ± 0.38	8.45 ± 0.25[4]
Other Properties - sintered for 3-1/3 hours at 2200° F			
a. Porosity (Volume Per Cent)	---	12.87 ± 0.25[2]	10.08 ± 0.04
b. Bulk Density (gm/cc)	---	1.901 ± 0.004[2]	1.987 ± 0.009
c. Theoretical Density (gm/cc)	---	2.207 ± 0.007[2]	2.210 ± 0.018
Cristobalite Content - sintered for 3-1/3 hours at 2200° F	8.8 ± 1.6[3]	---	---

[2] Confidence Interval at 95 per cent level based on ten specimens.

[3] Confidence Interval at 95 per cent level based on three determinations.

[4] Sintered for 15 hours at 2200° F.
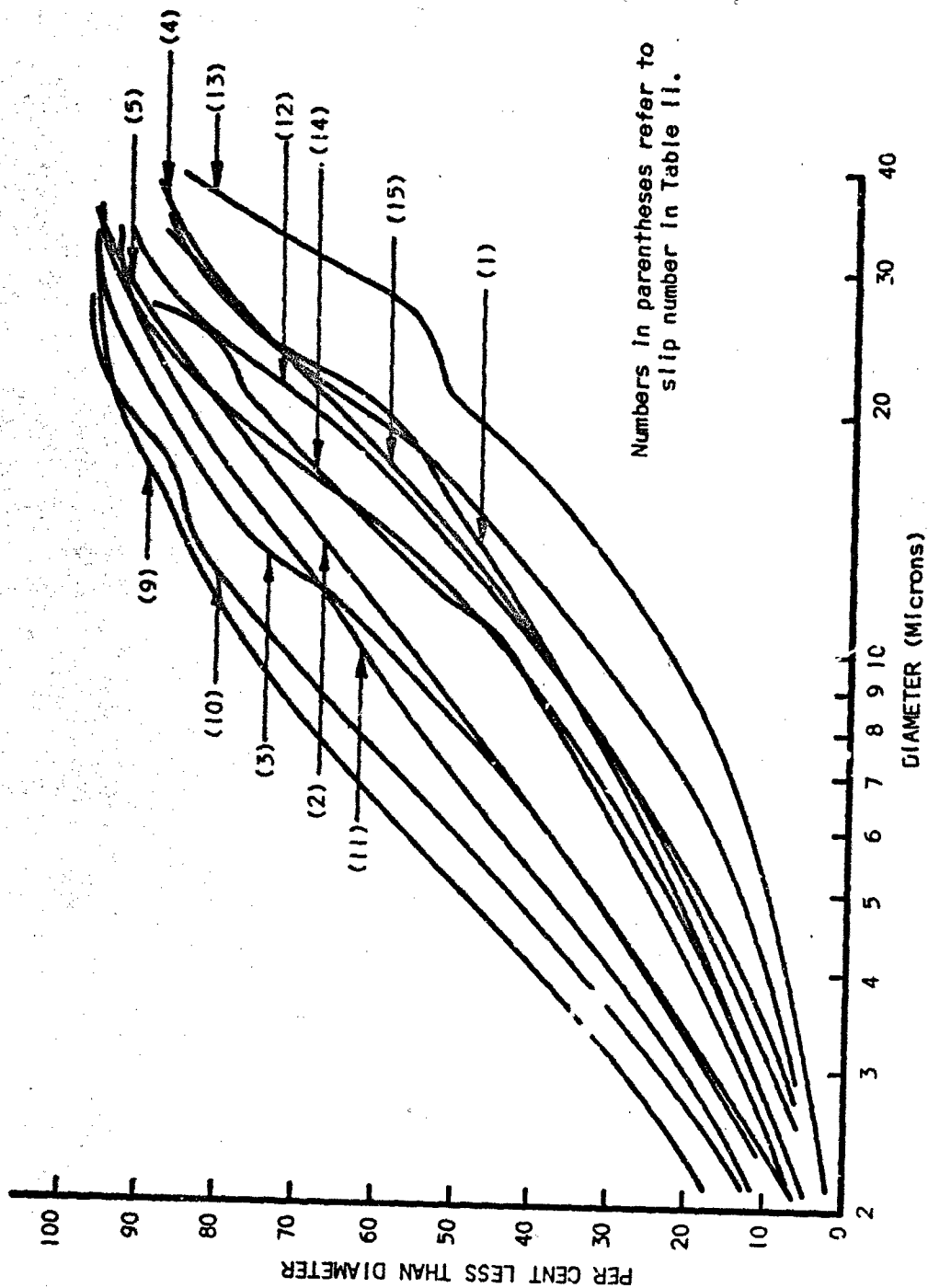
Figure 1. Particle Size Distributions of Fused Silica Slips on Mass Basis as Determined Using a Coulter Counter® with a 100 Micron Aperture.

244
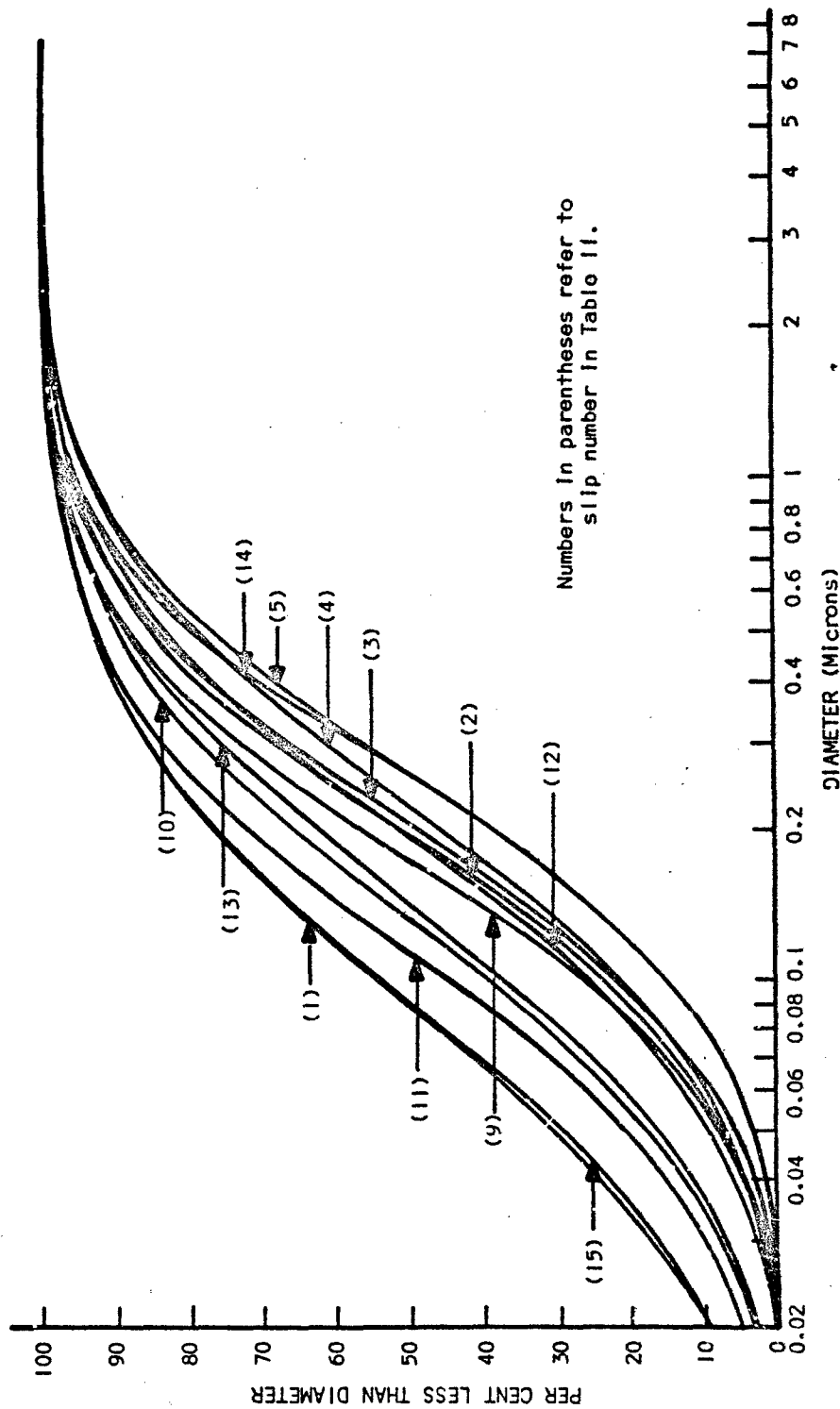
Figure 2. Particle Size Distributions of Fused Silica Slips on Count Basis as Determined Using a Coulter Counter® with a 100 Micron Aperture.
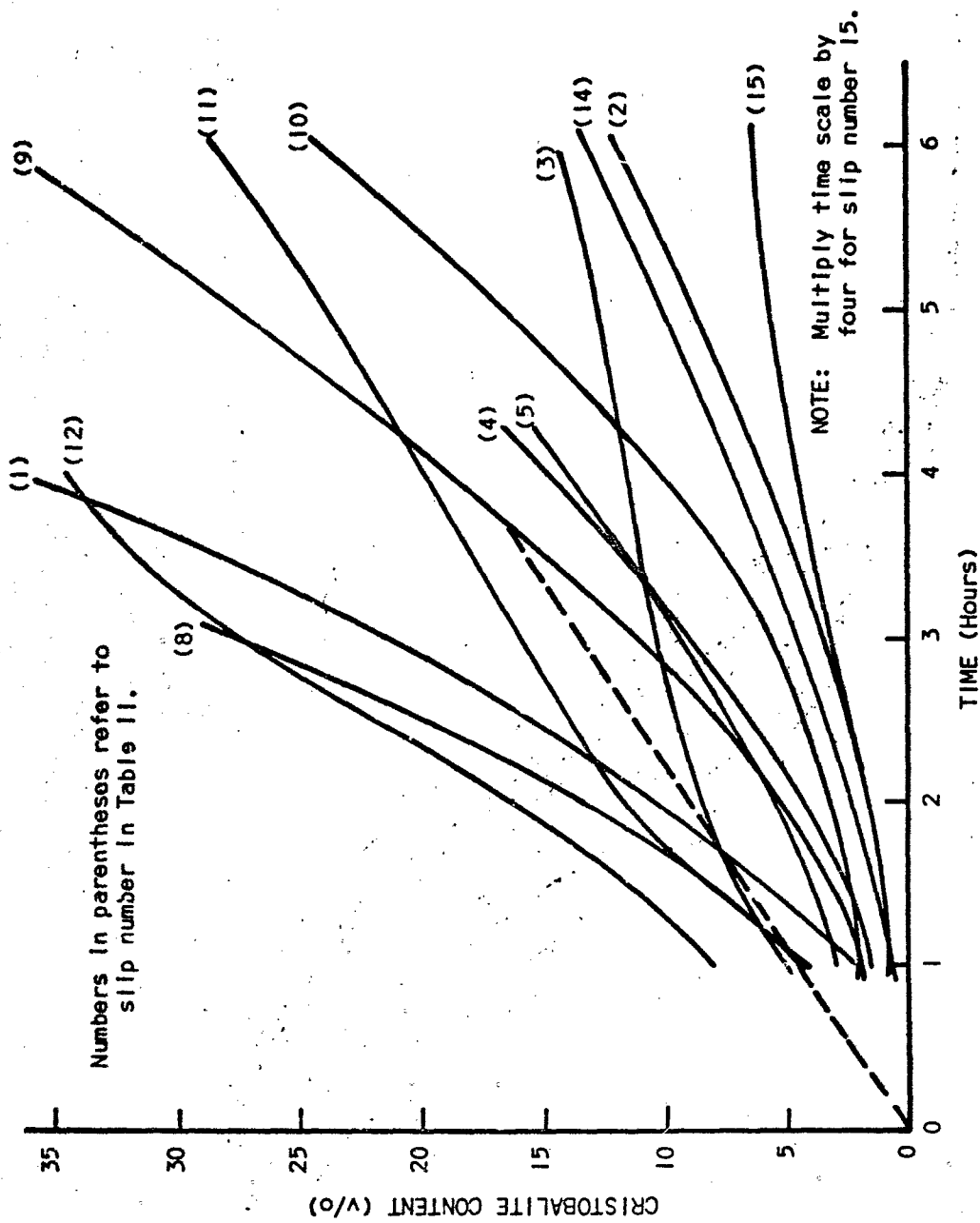
Figure 3.   Cristobalite Content Vs Sintering Time at 2200° F.
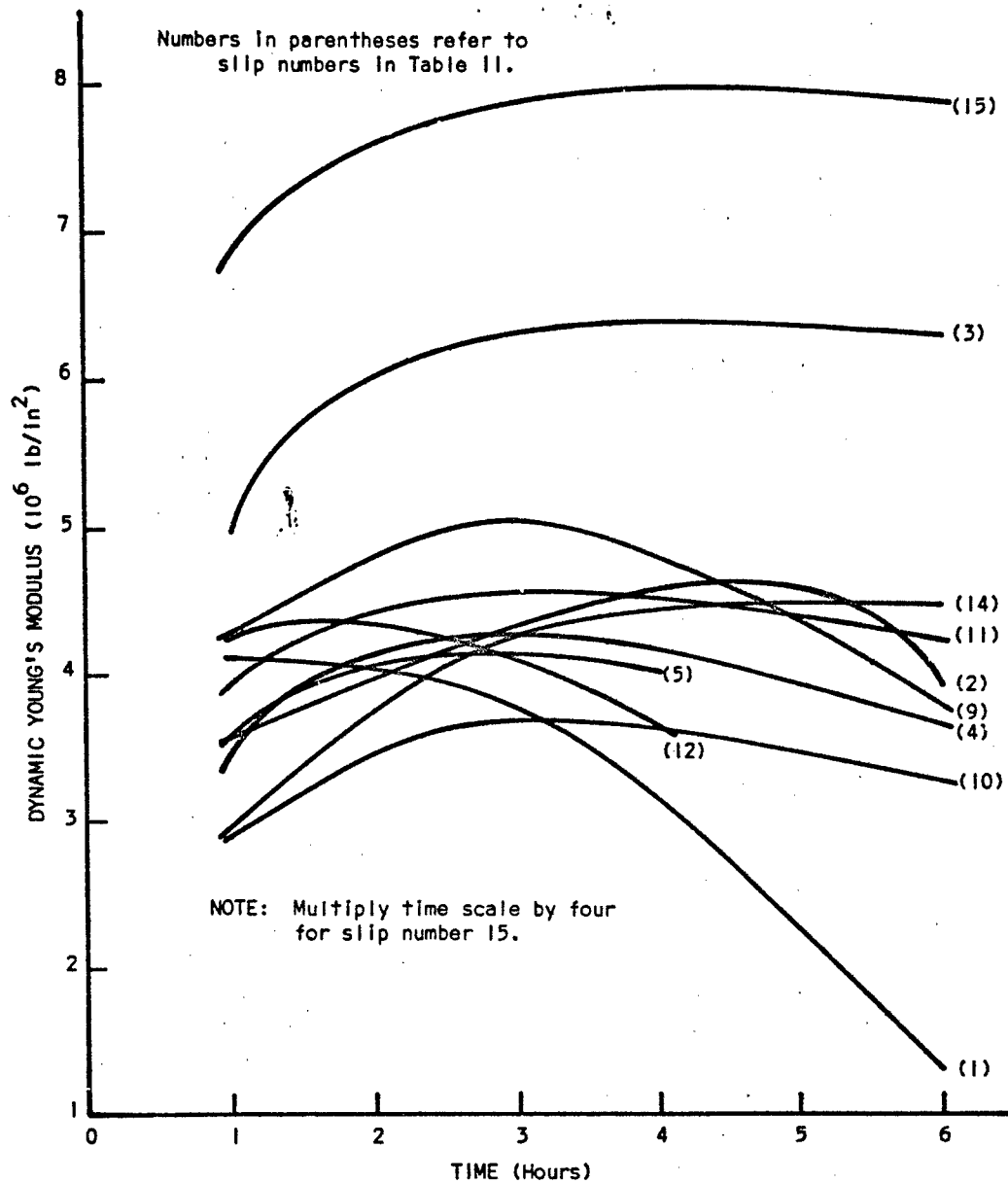
Figure 4. Young's Modulus Vs Sintering Time at 2200° F.

slip under consideration. For this test, one liter graduated cylinders were satisfactory and a procedure was adopted which provides a representation of slip stability by direct measurement of settling amount as a function of time (or perhaps, as more data is acquired, a simple, one-time measurement will be satisfactory; 6 hours should be sufficient). Measurements of settling were made on three fused silica slips (Figure 5).

Using the three measurements stated above* as indicators is thought to be satisfactory for making a decision on the suitability for purchase of a particular fused silica slip and for the fabrication of hardware. The three measurements do not, however, provide a complete and sufficient characterization of the fused silica slip. It is strongly recommended that, for any fused silica slip used for hardware fabrication, a characterization at least to the extent of the measurements listed in Table I should be accomplished, including settling measurements, so that any question of acceptability could be examined for merit. In the detailed characterization, observations of the particle(s) size-shape should be made using light and electron microscopy to obtain a measure of the particle shape factor for computation of specific surface area using the particle size distribution data. An electron micrograph showing the typical particulate character of slip number 5 is presented in Figure 6. From this figure, and others, an estimate was made of the shape factor, i.e. the ratio of the true surface area to the area of a sphere having the same volume. The value was determined to be 3.3 which, when used to determine the specific surface area of the particles making up slip number 5, gave a value of 5.8 square meters per gram. This agrees well with the measurements reported by Fleming for dried fused silica slip 6/**.

From the overall viewpoint, the characterization of the fused silica slips reported herein is thought to be very revealing, particularly as the characterization relates to the effective use and selection of commercial fused silica slips. The processing of the slip-cast fused silica is also demonstrated to be very importantly related to the behavioral characteristics illustrated by the aggregate data. For example, those slips having cristobalite growth vs sintering time at 2200° F curves below the dotted line in Figure 3 meet the criteria of less than 15 v/o cristobalite after 3-1/3 hours (nos. 2,3,4,5,9,10,14, and 15). Examination of the data in Figure 4 shows that test bars from each of these slips exhibited "plateeus" in their Young's modulus vs sintering time at 2200° F behavior, suggesting that processing time control would be easily accomplished. From these data, the correct time for sintering at 2200° F can be estimated since the failure strain

---

*NOTE: For these measurements, less than 15 v/o cristobalite after 3-1/3 hours at 2200° F, a viscosity of 120 ± 35 centipoise and a sediment thickness of less than 2 mm in 6 hours are considered satisfacfactory.

**NOTE: As determined by B.E.T. low temperature nitrogen adsorption, Fleming reported a value of 5.4 square meters per gram for dried fused silica slip and a value of 5.2 square meters per gram for slip-cast and dried material. Values for sintered slip-cast fused silica are also reported.
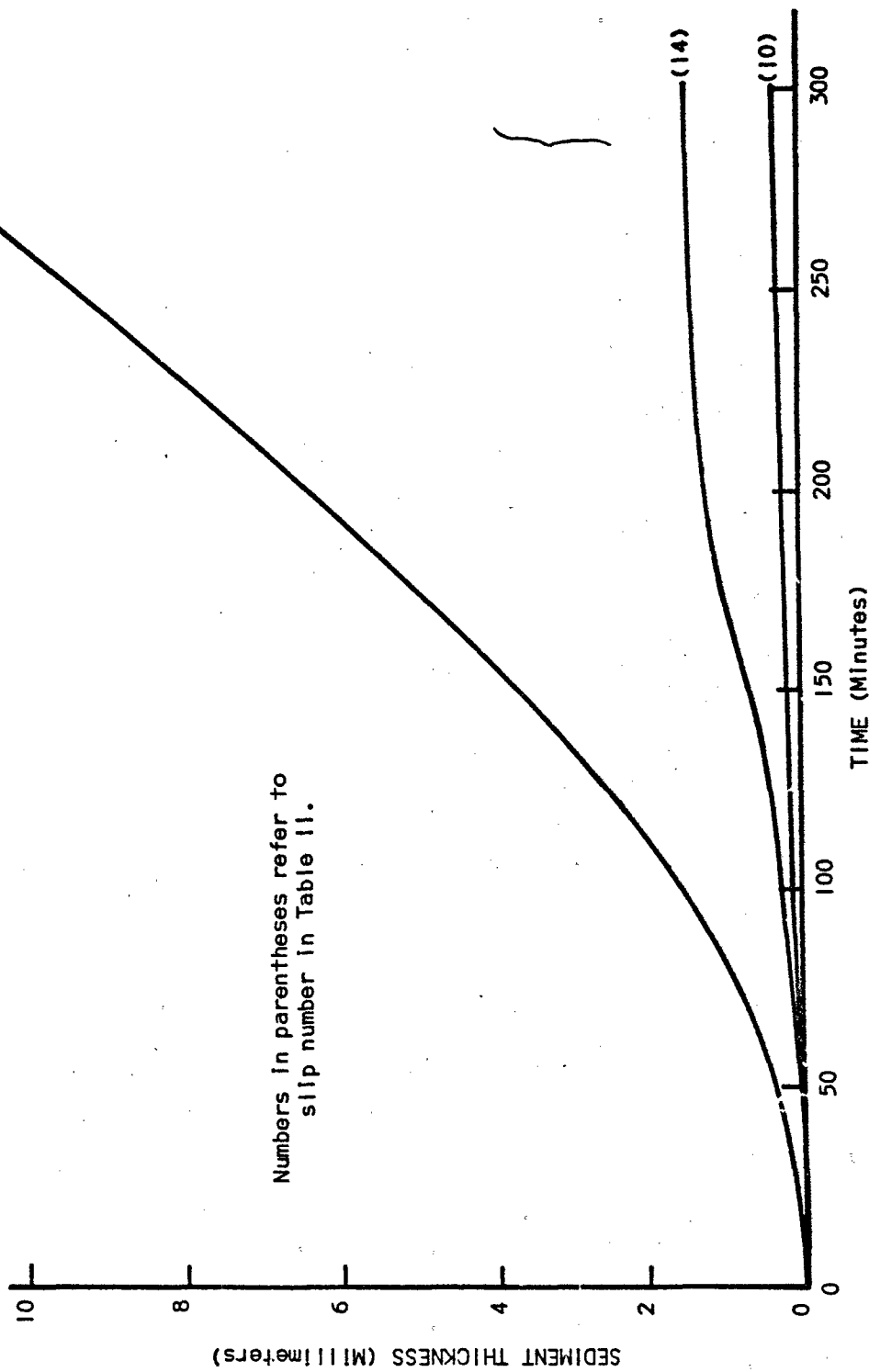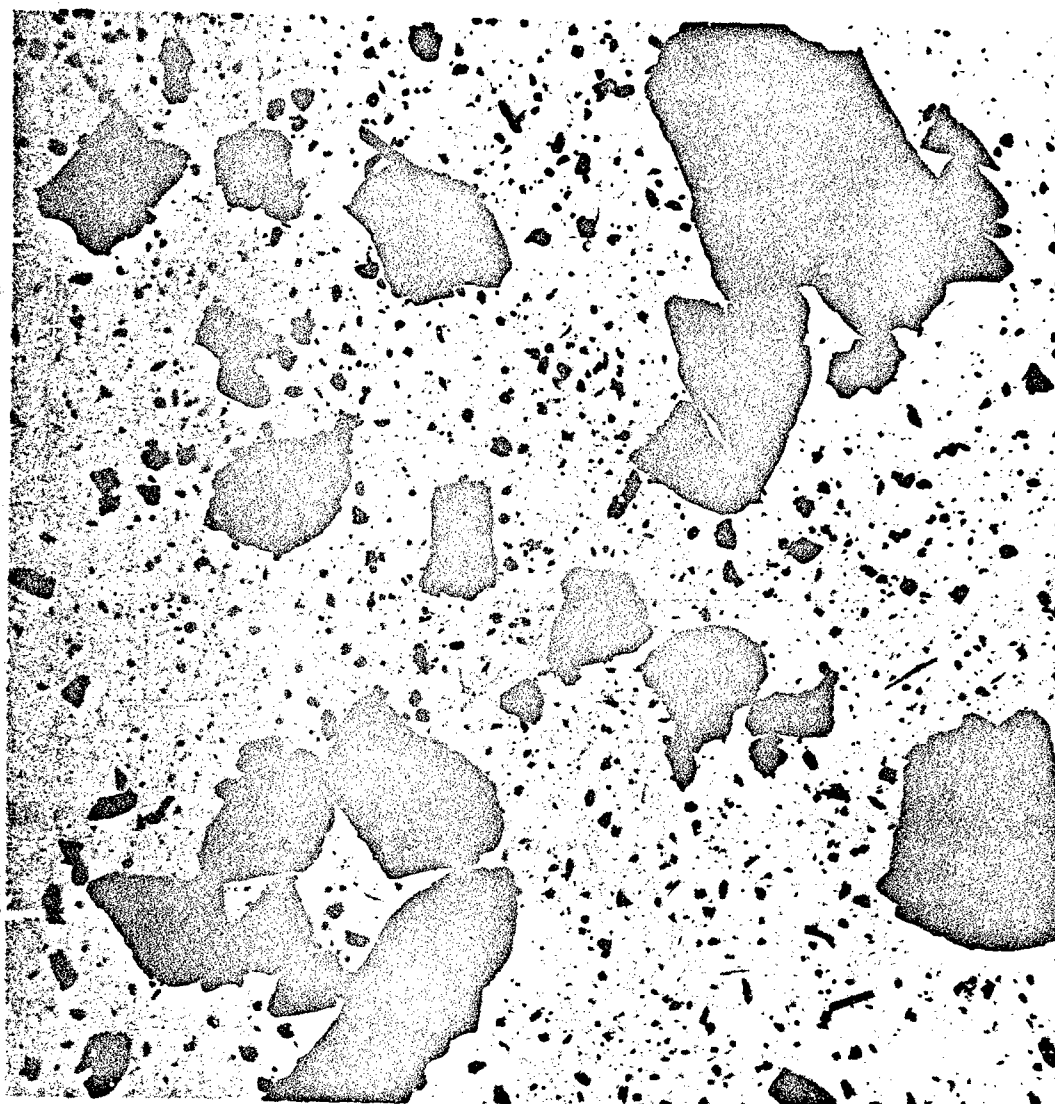
Numbers in parentheses refer to slip number in Table II.

Figure 5. Sediment Thickness Vs Time for Three Fused Silica Slips.

1μ

(8,337x)

Figure 6. Electron Micrograph Illustrating Typical Particle Character of Fused Silica Slip.

is almost a constant value. That is, from the data of Figure 4, a sintering
time of 3-1/3 hours appears reasonable for hardware fabricated from slips
numbers 3, 4, 5, 10, and 11 (in view of the fact that the maximum modulus
occurs at this time). That this may be almost the case is demonstrated by the
data in Table II. For numbers 4, 5, 10, and 11, the calculated critical
failure strain* of sintered test bars is almost constant, ranging from a low
of 0.92×10^{-3} in/in to a high of 1.09×10^{-3} in/in. However, in the case
of the test bars from slip number 3, the critical failure strain was
0.72×10^{-3} in/in; a low value compared to the others. Examination of the
data for the remaining slips, excluding number 15, shows values of the critical
failure strain from a low of 0.94×10^{-3} in/in to a high of 1.33×10^{-3} in/in
for a sintering time of 3-1/3 hours at 2200° F and 0.28×10^{-3} in/in for
number 15 for a sintering time of 15 hours** (the time which appears to give
a maximum Young's Modulus). Therefore, with numbers 3 and 15 excluded, the
selection of processing time from the determination of Young's Modulus as a
function of sintering time, is quite reasonable. From experience, a sintering
time slightly less than the time of maximum modulus is necessary; the order of
10 to 15 per cent less. Further study may show that the optimum sintering time
may occur at the point where the slope of the Young's Modulus vs sintering
curve is near a value of one. This remains to be demonstrated, however.

Up to this point the discussion has emphasized the behavior as associated
with measured viscosities, settling rates, and cristobalite growths, since
these are most important in relation to purchase acceptability of the fused
silica slip and to the processing of hardware fabricated from fused silica
slips. On a more basic level, many questions arise with regard to why there
were wide differences in behavior from one batch of fused silica slip to
another batch. Questions such as (1) why did the maximum Young's Modulus of
the sintered material vary from a low of about 3.5×10^6 psi (slip no. 10) to
a high of about 8.0×10^6 psi (slip no. 15), (2) why did the average cristo-
balite growth rate vary from a low of approximately 0.25 per cent per hour
(slip no. 15) to a high of 30 per cent per hour (slip no. 8), (3) why did the
mean particle size on a mass basis vary from a low of 5 microns (slip no. 9)
to a high of 20 microns (slip no. 13), (4) why should the viscosity show a
strong increase with increasing shearing rate in one case (slip no. 1) and a
sharp decrease with increasing shearing rate in another case (slip no. 3),
and (5) why should there be evidence of crystalline phases other than
cristobalite in some slips (nos. 3 and 6) and not in others (nos. 1,2,4,5,9,
10,11,12,14, and 15)?

The answers to these questions are evident in some cases and not in
others. They are intimately interrelated in the overall characterization

---

*Critical failure strain is estimated from the simple Hookean relationship,
$\sigma = E\epsilon$ where σ = failure stress, E = Young's Modulus, and ϵ = the critical
failure strain.

**This is an extremely low calculated critical strain, as compared to the
nominal value of 1×10^{-3} in/in for sintered slip-cast fused silica. This
may be due to a very high cristobalite concentration on the surface of the
specimens which results in a low failure stress level.

and are, in some cases, dependent on a single factor not accounted for during the manufacturing process. For example, the occurrence of crystalline phases other than cristobalite is apparently due to insufficient fusion of the starting quartz and/or incomplete separation of the fused material from unfused material during subsequent processing. The viscosity of a given slip is affected by pH (the measure of hydrogen ion activity, which is associated with the adsorbed species on the surface of the particles; the region associated with the chemically attached ions is referred to as the micellous region) and the effect is associated with the distribution of particle sizes making up the slip. Unfortunately, from the data in Table II and in Figures 1 and 2 a correlation is not evident and thus no conclusion can be arrived at which would provide a plausible explanation for the viscosity variation in slips numbers 1 and 3 (neither of these slips was used for the fabrication of hardware under this or any other program). Attempts to correlate the cristobalite formation with impurity levels in the dried slip was fruitless. The cristobalite growth behavior could not be related to the individual impurity level or to total impurity levels. Also, as shown by the "re-runs" on slips numbers 4, 5, 12, and 15 (values in parentheses in Table II), the spectrographic analyses are not absolute since the impurity levels between determinations varied by more than an order of magnitude. This is probably due to a "sampling problem" since from a theoretical viewpoint the impurity content of a single particle could cause large differences between determinations[*].

The variation in cristobalite growth rates exhibited by the fused silica slips examined is large; two orders of magnitude between the lowest rate and the highest rate[**]. It is apparent that such differences are not acceptable for routine purchase and use of fused silica slips and careful measurements of the cristobalite growth should be conducted on any slip used for hardware fabrication since the optimum ultimate strength and the porosity are so strongly related to the cristobalite growth during sintering.

The advantage to be gained by low cristobalite growth rate is demonstrated by the data in Table II for slip number 15. The high value of Young's Modulus, 8.45×10^6 psi, and the low porosity, 10.08 per cent, make this fused silica slip appear attractive for hardware fabrication. At the present time, however, this fused silica slip is not available. A representative of the manufacturer has stated that the company would quote on fabricated items using this slip. The reported strength data in Table II for sintered test bars of slip number 15 is not considered to be indicative of the strength level that is possible by increased densification. The low apparent strength of the sintered test bars, 2369 psi, is, as stated earlier, thought to be the result of a surface condition associated with high cristobalite concentrations at the surface (the result of mold contamination) since machining the surface with diamond tooling will increase the mean strength and, if the surface is polished, the strength will be increased to 6000 to 7000 psi. Further work with high-density sintered slip-cast fused silica is to be accomplished to determine the effect of surface condition on the strength 7/.

---

[*]Spectrographic analysis is performed on a small sample of dried slip.

[**]This is the extreme variation. Excluding slip number 15, which is stated to be a special aerospace grade, the difference is one order of magnitude.

From the histories presented here, a composite "picture" of a "satis-factory" standard commercial fused silica slip could be created. Such a slip would have the "best" features of a number of the fused silica slips investi-gated in this work. The composite fused silica slip characterized by such an approach, however, would at this time present a formidable objective for the manufacturers of fused silica slip. In fact, it is doubtful that an "ideal" or a "composite" fused silica slip is necessary, although having consistent target goals during manufacture is desirable.

As it stands at the present time, the selection of a commercial fused silica slip for hardware fabrication is based on measurements to provide information concerning the slip stability (settling behavior and apparent viscosity), devitrification rate (cristobalite growth in test bars sintered at 2200° F for 3-1/3 hours) and strength (Modulus of Rupture and Young's Modulus of test bars sintered at 2200° F for 3-1/3 hours). These measurements serve the purpose of establishing whether the particular batch of slip should be purchased; a complete characterization is accomplished on slips after they have been purchased. The manufacturers of the fused silica slips cooperate with this approach by furnishing a sample of fused silica slip from a particular production lot and agree to hold a sufficiently large quantity of that batch of fused silica slip until the initial measurements can be accomplished, usually two to three days. That this is not the most efficient method is obvious, and the implementation of tests of a similar or identical nature on each batch of slip provided and certification of the results by the manufacturers of the fused silica slips will be necessary in the future.

Bounds which describe the acceptable range of values for each parameter and which probably apply to more than 90 per cent of the acceptable standard commercial fused silica slips can be abstracted from the data on the fused silica slips examined in this work. Such a treatment of the data is as follows:

Measurement	Range of Values
pH	4.0 to 5.4
Particle Size Distribution	Normal grinding mill comminution to a mean diameter of 7 to 11 microns as determined by Coulter Counter® on mass basis.
Apparent Viscosity	90 to 140 centipoise
Residual Crystalline Phases other than Cristobalite	None
Residual Cristobalite	0 to 1 volume per cent
Spectrographic Analysis	< 1000 ppm total impurities
Cristobalite vs Time at 2200° F	< 15 v/o after 3-1/3 hours

Measurement	Range of Values
Elastic Modulus vs Time at 2200° F	Broad range, nearly constant between 1-1/2 and 5 hours sintering time at 2200° F; range of values 3.5×10^6 psi to 5.5×10^6 psi.
Modulus of Rupture	3000 psi to 5000 psi after sintering for 3-1/3 hours at 2200° F; critical strain 1×10^{-3} in/in.
Other Properties - Sintered for 3-1/3 hours at 2200° F	
a. Porosity	11.0 to 14.0 per cent
b. Bulk Density	1.9 to 2.0 gm/cc
c. Theoretical	2.20 to 2.22 gm/cc

This summary of property values and ranges is presented to serve as a guide in the preparation of engineering specifications on fused silica slips. It is expected that the majority of the fused silica slips that have properties which are within these bounds will be acceptable for hardware fabrication.

CONCLUSIONS

This work demonstrates the necessity of imposing specifications on the commercial fused silica slips used for aerospace hardware fabrication. Particular importance has been given to identifying the least number of measurements required to assure the suitability of a particular batch of fused silica slip for the production of hardware and bounds have been placed on the values arrived at from the measurements. Further, the ranges of property values for fifteen commercial fused silica slips and for sintered test specimens fabricated from the slips have been identified. From this work, it is apparent at this time that preliminary measurements should be accomplished on a sample from a particular batch of fused silica slip prior to purchasing the slip for hardware fabrication, or, arrangements should be made to return the slip to the vendor if it does not meet certain criteria.

REFERENCES

1. Boland, P., <u>Computer Analysis/Data Reduction of Particle Size Data From Electronic Sensing Zone Device,</u> Contract N00017-67-C-0053, Georgia Institute of Technology, Engineering Experiment Station, Special Technical Report, Project A-994, to be published May 1968.

2. Harris, J. N., Sales, A. T., Corbett, W. J., et al., <u>Filament Wound Silica Radome Techniques,</u> Contract AF-33(615)-3330, with the Air Force Avionics Laboratory, Georgia Institute of Technology, Engineering Experiment Station, Technical Report AFAL-TR-67-65, April 1967.

3. Spinner, S., and Tefft, W. E., "A Method for Determining Mechanical Resonance and for Calculating Elastic Moduli From These Frequencies," <u>A.S.T.M. Proc</u>. 61, 1221-1238 (1961).

4. Poulos, N. E., Murphy, C. A. and Harris, J. N., <u>Design and Development of An Electromagnetic Window for Air Lift Reentry Vehicles,</u> Contract AF-33(657)-11504 with the Air Force Avionics Laboratory, Georgia Institute of Technology, Engineering Experiment Station, Technical Report AFAL-TR-66-34, March 1966.

5. Fleming, J. D., Boland, Paul, and Harris, J. N., "Porosity Measurements by Air Displacement," Materials Research and Standards, 3, 20-24, Jan. 1963.

6. Fleming, J. D., <u>Fused Silica Manual,</u> Contract No. AT-(40-1)-2483 with the U. S. Atomic Energy Commission, Georgia Institute of Technology, Engineering Experiment Station, Final Report, 1 September 1964.

7. Harris, J. N., Bomar, S. H., Jr., and Poulos, N. E. <u>High Strength, Broadband, Lightweight Silicon Oxide Radome Techniques,</u> Contract F33615-67-C-1594, Georgia Institute of Technology, Engineering Experiment Station, Summary Technical Report No. 1, 1 March 1968.

BLANK PAGE

DEVELOPMENT OF HIGH-PURITY FUSED SILICA RADOME STRUCTURES

Joe N. Harris and Steve H. Bomar, Jr.
Engineering Experiment Station
Georgia Institute of Technology
Atlanta, Georgia 30332

ACKNOWLEDGMENTS

ABSTRACT

Development of low and high density, high strength, silica components for construction of A-sandwich radomes is described. Design goals for materials in this application are discussed. Techniques are described for forming low density structures by slip-casting of honeycomb structures and foaming of ultra-high purity amorphous silica. High density structures were slip-cast from a high-purity slip prepared by consolidation and ball milling of Cab-O-Sil®, a synthetic, colloidal silica. After sintering, densities of 98 per cent of theoretical and elastic moduli of 9×10^6 psi were achieved. The new materials significantly improve the performance capabilities of fused silica A-sandwich radome structures.

INTRODUCTION

One method of achieving broadbandedness in a ceramic radome is the A-sandwich concept. A fused silica A-sandwich radome has the advantage over a monolithic slip-cast fused silica radome of a greater transmission efficiency over a wide frequency range. However, it has not been possible, using commercially available fused silica slips and foams prepared from arc fused quartz sand, to produce an A-sandwich radome having lower weight and greater strength than a monolithic radome having the same size and design center frequency. Previous work under U. S. Air Force Contract AF 33(615)-3445 on developing A-sandwich radomes from commercial fused silica foams and fused silica slips indicated that the strength of the skins would have to be doubled and the strength of the core increased by a factor of four to bring the mechanical performance up to that attainable with current state-of-the-art monolithic structures.

The tensile strength of transparent fused silica exceeds that of commercial slip-cast fused silica by a factor of 3 to 3.5. The Young's modulus of transparent fused silica is of the order of 2.5 times that of slip-cast fused silica. The density of commercial slip-cast fused silica is only 85 per cent of that of transparent fused silica.

The reasons for the slip-cast material's lower modulus, strength, and density are found in the sintering process. The formation of the crystalline phase cristobalite inhibits the continual sintering of the body. Because of

the volume expansion on inversion of the cristobalite, the amount of cristobalite that can be tolerated without causing thermal shock problems is of the order of 10 volume per cent. The maximum strength and modulus of a body cast from commercial fused silica is usually achieved at this level of cristobalite. Higher levels of cristobalite result in microcracking of the body and a resulting decline in the mechanical properties.

The rate of formation of cristobalite at sintering temperatures is markedly influenced by impurities in the silica; particularly by alkali impurities. If the impurity content of the silica is reduced, longer sintering times and/or higher sintering temperatures can be used to produce higher density and stronger slip-cast fused silica bodies. Other approaches such as the incorporation of fibers, either continuous or discontinuous, into the silica body can be used to increase the strength of slip-cast fused silica but it is the intent of this paper only to discuss radomes developed from high purity silicas.

EXPERIMENTAL PROGRAM

The experimental program to develop high purity slip-cast fused silica A-sandwich radomes was divided into two phases: (1) the development of high-density, high strength structures for use as the A-sandwich skins, and (2) the development of low-density, high strength structures for use as the A-sandwich core. In both cases initial work was conducted on material development.

1. Methods of Obtaining Materials for Production of High Purity Fused Silica Slips

Two primary sources of high purity fused silica materials were considered.

a. Pure amorphous silica produced by the steam pyrolysis of silicon tetrachloride (synthetic silica).

b. Fused silica produced from very pure quartz deposits such as the material used in production of high quality transparent fused silica components.

Several sources of high purity amorphous silica materials are available which originate from the steam pyrolysis of silicon tetrachloride. One source provides these pure materials in a wide range of particle size distributions. Unfortunately, however, the present price of these materials are in excess of thirty dollars per pound. Another source of high purity amorphous silica material, prices its product at approximately eighty cents per pound, and this product is manufactured in quantities on the order of 5 to 10 million pounds per year. However, it is an extremely finely divided material which is essentially a monofraction with a mean particle diameter of 0.012 micron. The particles are essentially spherical and form sponge like (porous) agglomerates. Total impurities found in this material by spectrographic analysis were of the order of 27 parts per million. This is an order of magnitude less than the impurity level in common commercial fused silica slips.

In order to use this material in a casting slip it is necessary to have a log-normal particle size distribution ranging downward from 50 microns. To obtain such a distribution the finely divided powder must be consolidated into particles about 0.1-inch in diameter and then wet ball milled to the proper size distribution.

Seven different methods were considered for densifying and coalescing the material to obtain larger particle diameters but, only two of these methods met with any degree of success. These were:

    a. Dry pressing and subsequent sintering

    b. Extrusion from a water paste with subsequent sintering.

The dry pressing operation was conducted by placing the finely divided powder in plastic bags to avoid contamination. The bags were then loaded in steel dies and pressed to about 3200 psig. After pressing the plastic bag was stripped away and the silica recovered in thin sheets or laminae, one to two millimeters in thickness. The laminations occurred because of entrapped air in the pressing operation. The pressed material was dried at low temperature to remove mechanical water and then fired at 2200° F for 3-1/2 hours. The resulting mill feed was in the form of translucent platelets, approaching theoretical density. These platelets typically have a cristobalite level of 0.0 to 0.6 v/o.

Extrusion of a silica "spaghetti" is the second method which can produce a satisfactory ball mill feed. Considerable effort was devoted to development of this method because it offers the possibility of being readily scaled up to quantity production. The optimum composition of the extrusion mixture was found to be 30 w/o of the finely divided silica and 70 w/o distilled water. No wetting agents or other adulterants were used, since high purity of the extruded mixture was a major objective. Test quantities of "spaghetti" were dried, then fired at 2200° F for 3-1/3 hours to achieve densification. The resulting mill feed was in the form of short cylinders, about one millimeter in diameter, very much like rice in appearance. Typical cristobalite content of this material after firing was 0.0 to 0.6 v/o.

Materials that are suitable for comminution by ball milling to fused silica slips can be produced by both the extrusion and dry pressing methods. Both processes can be scaled up to pilot quantity and ultimately to production quantity levels without prohibitive expense and difficulty.

Experimental quantities of high purity fused silica slip were made by grinding the feed in one gallon ball mills. The mill and grinding media were usually 99.6 per cent alumina. Alumina has a higher hardness than conventional mullite type mills and grinding balls; it was therefore preferentially used to avoid contaminating the slip with crystalline silica abraded from the mill and balls.

Five experimental batches of high purity silica slip were prepared from dry pressed and fired mill feed and characterization studies were conducted. The first three experimental slips were ground in alumina mills. These slips

were intended to define a suitable grinding time and to demonstrate that slips with satisfactory reproducibility could be made. Grinding times of 18, 24, amd 27 hours were used. The slips had properties similar to conventional fused silica slips and could be cast by conventional techniques without difficulty. Pertinent properties are shown in Table I, along with those of a good batch of commercial fused silica slip.

Experimental Slip No. 4 was prepared in a mullite ball mill, but otherwise was similar to those just described. The slip obtained had the expected particle size, viscosity, and pH characteristics. The devitrification rate of slip ground in the mullite mill was found to be somewhat higher than for slip ground in high-alumina mills. This effect was expected since the less tough mullite mill should wear more than the alumina mill and thereby yield some contamination of the slip. Since large batches of silica slip are generally ground in mullite mills, Slip No. 4 was intended to determine whether significant deterioration in fired properties would result from such grinding.

A second material obtained from the same commercial source was identical to the previous finely divided amorphous silica except that it had been partially agglomerated to a bulk density of about twice that of the original material. A slip was prepared from this material and designated Slip No. 5. All other factors being the same, the second material would be preferred because its higher bulk density facilitates consolidation into mill feed.

Particle size distributions on a mass basis are shown in Figure 1. In these and subsequent figures, data representing the aforementioned commercial fused silica slip are shown for comparison. Details of the particle measure-rent technique have been described elsewhere [1].

Firing studies were conducted on the experimental slips. In these studies two 3/4-inch diameter bars were cast from each slip and dried. The bars were fired together in an electric furnace at 2200° F for 2 hours; then volume per cent cristobalite, and modulus of elasticity were measured. The bars were then fired under the same conditions for another increment of time, and the measurements repeated. This procedure was carried on until the bars broke up from excessive devitrification, and yielded an extensive body of data as a function of firing time at 2200° F. This temperature is used in most fused silica firing studies at Georgia Tech because it gives a convenient compromise between a fast sintering rate and adequate control. These data are shown in Figures 2 and 3 for the experimental slips and the commercial fused silica slip mentioned previously.

The elastic modulus versus sintering time at 2200° F shown in Figure 3 was measured by a sonic technique [2]. The elastic modulus curve for the commercial fused silica slip is typical of a large number of conventional slips investigated by this method. The experimental slips reached a maximum elastic modulus of about 8 to 9.6 million psi, higher by a factor of two or more than conventional slips. Slip No. 5 showed exceptionally low rates of sintering and cristobalite formation. After 60 hours of firing at 2200° F, its elastic modulus reached a value of 7.7×10^6 psi at a cristobalite content of only 4 per cent. The peaks are rather broad so that further improvement might be achieved by adjustment of sintering temperature.

TABLE 5

PROPERTIES OF SEVERAL FUSED SILICA SLIPS

Slip	pH	Apparent Viscosity (cp)	Per Cent Solids (w/o)	Grinding Time (hr)	Residual Cristobalite (v/o)
1	3.75	121	79.3	27	0-0.6*
2	3.86	110	80.1	24	0-0.6
3	4.05	105	77.8	24	0-0.6
4**	4.10	74	77.6	18	0-0.6
5***	3.70	159	71.8	18	0-0.6
6****	6.80	81	80.7	---	0
7*****	3.80	132	83.8	---	0-0.6
561-B+	4.50	114	83.1	---	1.5-2.0

*Cristobalite content of mill feed.

**Feed prepared from synthetic silica powder and ground in mullite mill.

***Feed prepared from higher density synthetic silica powder and ground in alumina mill.

****High-Purity Fused Silica Cullet ground in alumina mill.

*****Proprietary Commercial High-Purity Slip.

+Common Commercial Slip.

The second method of preparing high-purity silica slips is to start with a high purity fused silica prepared from pure Brazilian quartz crystals. This material is purchased as glass cullet from a manufacturer of lamp glass and is cleaned by leaching in hydrochloric acid before milling in high alumina ball mills. The slips prepared from this material were evaluated in the same manner as the previous slips and the data obtained are shown in Figures 2 and 3. This material labeled 6 in the figures compares favorably with the slips using the finely divided synthetic starting material.

A third material was obtained from a commercial vendor who makes a specialty high-purity fused silica slip for fabrication of high quality fused silica parts. This slip is not marketed by the vendor but the vendor will fabricate fused silica parts from the material on order. The properties of this slip are also included in Figures 2 and 3 for comparison of properties with the high-purity fused silica slips prepared at Georgia Tech. These curves are labeled 7 and compare well with the other materials. The method of preparing this high-purity fused silica slip is proprietary with the company manufacturing it.

2. Preparation of Dense Skins for Fused Silica A-Sandwich Radomes

From the data in Figure 1, slips 2, 4, 5, 6, and 7 along with the commercial slip labeled 361-B should be satisfactory for slip-casting thin sections of fused silica. Slips 1 and 3 were overground and are too fine; excessive shrinkage and cracking problems would occur using these slips. Slips 6 and 7 were actually selected because of the availability of material. The skins can be prepared by slip-casting alone to the required thickness for skins between 50 and 100 mils. However, the preferred method is to slip-cast some thickness over 100 mils then to machine by grinding with diamond tooling to the final thickness.

3. Preparation of Foamed Cores for Fused Silica A-Sandwich Radomes

A foam was prepared from slip number 6 using the following procedure.

(1) Foam Formulation:

    1000 cc of fused silica slip
      35 cc of 1.5 N hydrochloric acid
    12.5 cc water
    12.5 cc non-ionic detergent

(2) Foaming Procedure:

The water and acid were added with slow mixing. The detergent was added and high speed agitation provided with an electric mixer. The resultant foam was dried in a paper mold and fired for 6 hours at 2200° F. The resultant foam had an approximate density of 25 lb/ft^3.

optimum strength, specimens were fired at 2200° F at
intervals of 2 hours. After each interval, measurements were made
for elastic modulus, bulk density, and cristobalite content. Over the 41 hour
firing cycle bulk density of the foam increased from 23 to 27.5 pounds per
cubic foot. Plots of cristobalite content versus firing time and elastic
modulus versus firing time are shown in Figure 4. Data for a conventional
commercial foam are also included for comparative purposes.

A second foam sample was prepared from slip No. 7. The same foaming
procedure as described for the nominally 25 lb/ft3 foam was used except beating
time was shorter, thereby producing a foam of nominally 45 lb/ft3 density.
This foam was fired initially for 10 hours then in 4 hour increments for a
total of 78 hours. Plots of cristobalite content versus firing time and
elastic modulus versus firing time are shown in Figure 5. Again the values
for a commercial foam of the same nominal density have been included for
comparative purposes. A comparison of the properties of the high purity
and commercial foams in Figures 4 and 5 shows the improvement achieved in
elastic modulus with the higher purity foams. Although it is possible to
achieve an elastic modulus in the commercial foams equivalent to that
achieved in the high purity foams, the sintering time where this maximum
modulus is achieved is very short and the elastic modulus drops rapidly with
increasing time at temperature.

Foam of this type are cast roughly to shape and given final shape by
machining. The A-sandwich radomes are then assembled using a fused silica
cement which upon reheating provides a strong adhesive bond.

4. Other Core Materials

The use of a honeycomb cast structure rather than a foam has been
considered briefly. The honeycomb or oriented pore structure is attractive
because of the much higher strengths and better control of dielectric properties
that can be obtained with oriented pore structures. Honeycomb fused silica
planar sections are relatively easy to fabricate by slip-casting. An example
is shown in Figure 6. However, to fabricate radome core sections with changing
orientation of pores along the length of the core is a much more difficult
problem and is beyond the scope of the present study.

CONCLUSIONS

In both conventional and high-purity slip-cast fused silicas, the elastic
modulus reaches a maximum at a cristobalite content of about 5 to 11 volume
per cent. The high-purity silicas reach a maximum elastic modulus about twice
that of conventional slip-cast silica, however. If the surface effects which
ordinarily control strength measurements in brittle materials are temporarily
disregarded, elastic modulus can be considered roughly analogous to strength.
Thus it is observed that considerable improvement in physical properties can
be achieved by reducing the level of impurities in silica slips; these improved
properties are believed to result from suppression of the nucleation and growth
of cristobalite during sintering of the cast bodies.

After casting, the "green" bodies are fired at high temperatures (typically 2200° F) to fuse together particles in the packed structure. This operation develops strength by joining many small particles into a continuous piece, with a resulting decrease in porosity. However, cristobalite, a crystalline phase of silica, forms simultaneously at sintering temperatures, and upon cooling the cristobalite shrinks and causes microcracked flaws in the structure. Thus, the suppression of cristobalite growth reduces microcracking and the loss of strength associated with it. High-purity slips can be sintered much longer before reaching a particular cristobalite content, so that more complete sintering occurs with these slips before the detrimental effects of cristobalite become important.

The molecular structure of vitreous silica is still the subject of debate, but is probably very similar to most of the crystalline phases of silica 3/. That is, the basic structural unit consists of four oxygen atoms located at the corners of an imaginary tetrahedron, with a silicon atom at the center of the tetrahedron. The important difference between the vitreous and crystalline states is the orientation of the tetrahedra in space; vitreous silica is a continuous network of interconnected silicon and oxygen atoms, but lacks the parallel planes of similar atoms which characterize a crystal. Interatomic distances may be expected to fluctuate over wider ranges than are found in crystalline phases also, but the vitreous and crystalline structures are really not radically different.

The devitrification of vitreous silica during sintering begins with nucleation, or the assembly of two or more SiO_4 tetrahedra into an orderly unit which can continue to grow by addition of similar units, forming a stable crystalline phase. At sintering temperatures, this crystallization process, in which cristobalite is the stable phase, will proceed until no vitreous silica remains if given sufficient time. Its speed is increased by increasing temperature and the presence of certain foreign materials, especially alkali metals and water vapor. Whether these foreign materials promote nucleation or catalyze crystallization after it starts is not yet understood. However, the substantial reduction in impurity level achieved in this study has been shown to lead to dramatically improved properties in slip-cast fused silica structural components.

REFERENCES

1. C. A. Murphy, P. Boland and C. W. Gorton, "Ceramic Systems for Missile Structural Applications," Quarterly Report No. 2, Contract N00017-67-C-0053, Georgia Tech Engineering Experiment Station, June 1967, Appendix III.

2. S. Spinner and W. E. Tefft, "A Method for Determining Mechanical Resonance Frequencies and for Calculating Elastic Moduli from These Frequencies," A.S.T.M. Proc. 61, 1221-1238 (1961).

3. R. B. Sosman, The Phases of Silica, Rutgers University Press: New Brunswick, N. J., 1965, Chap. 14.
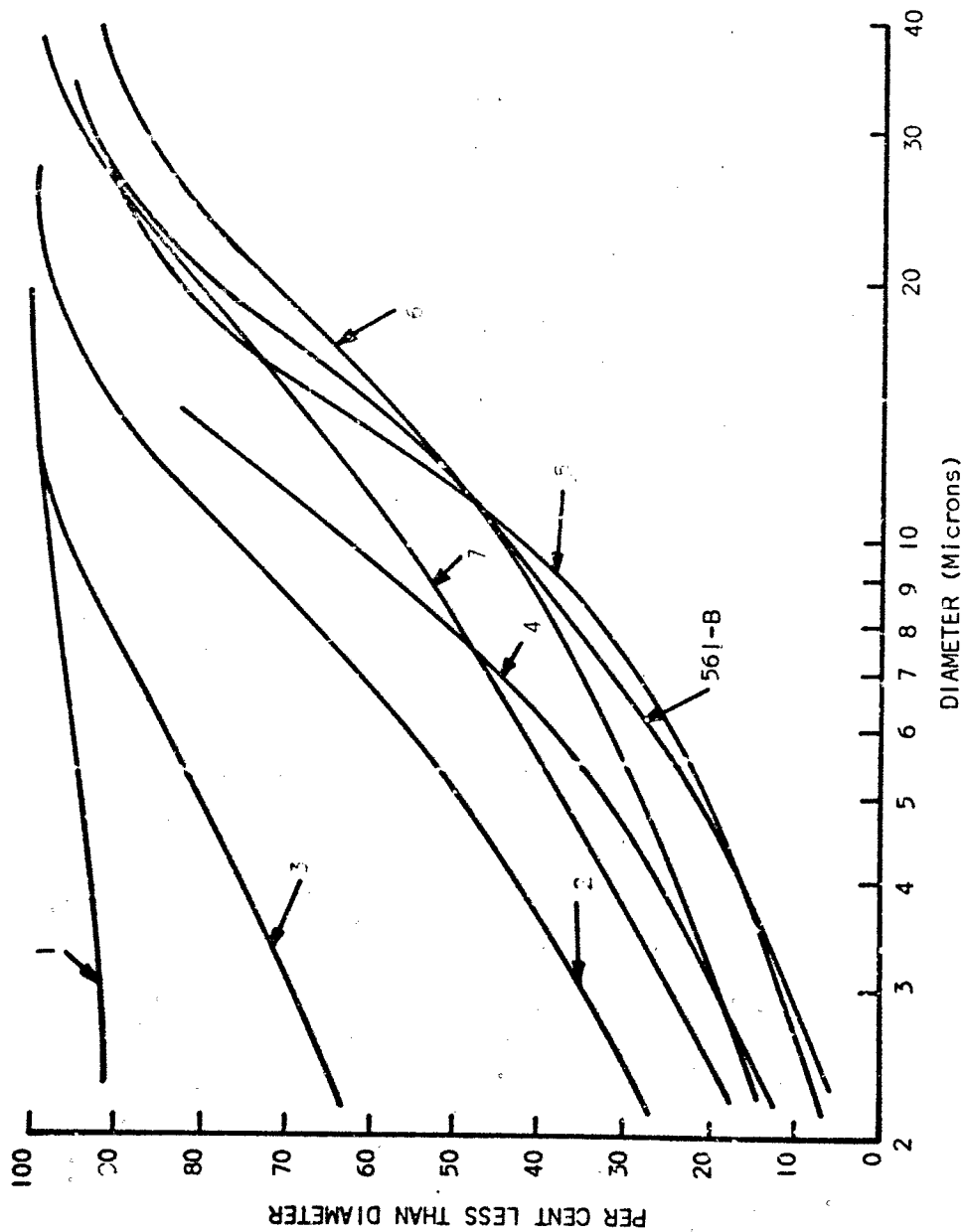
Figure 1. Mass Basis Particle Size Distributions of Glasrock®561-B Slip and Six Experimental Cab-O-Sil® Slips.
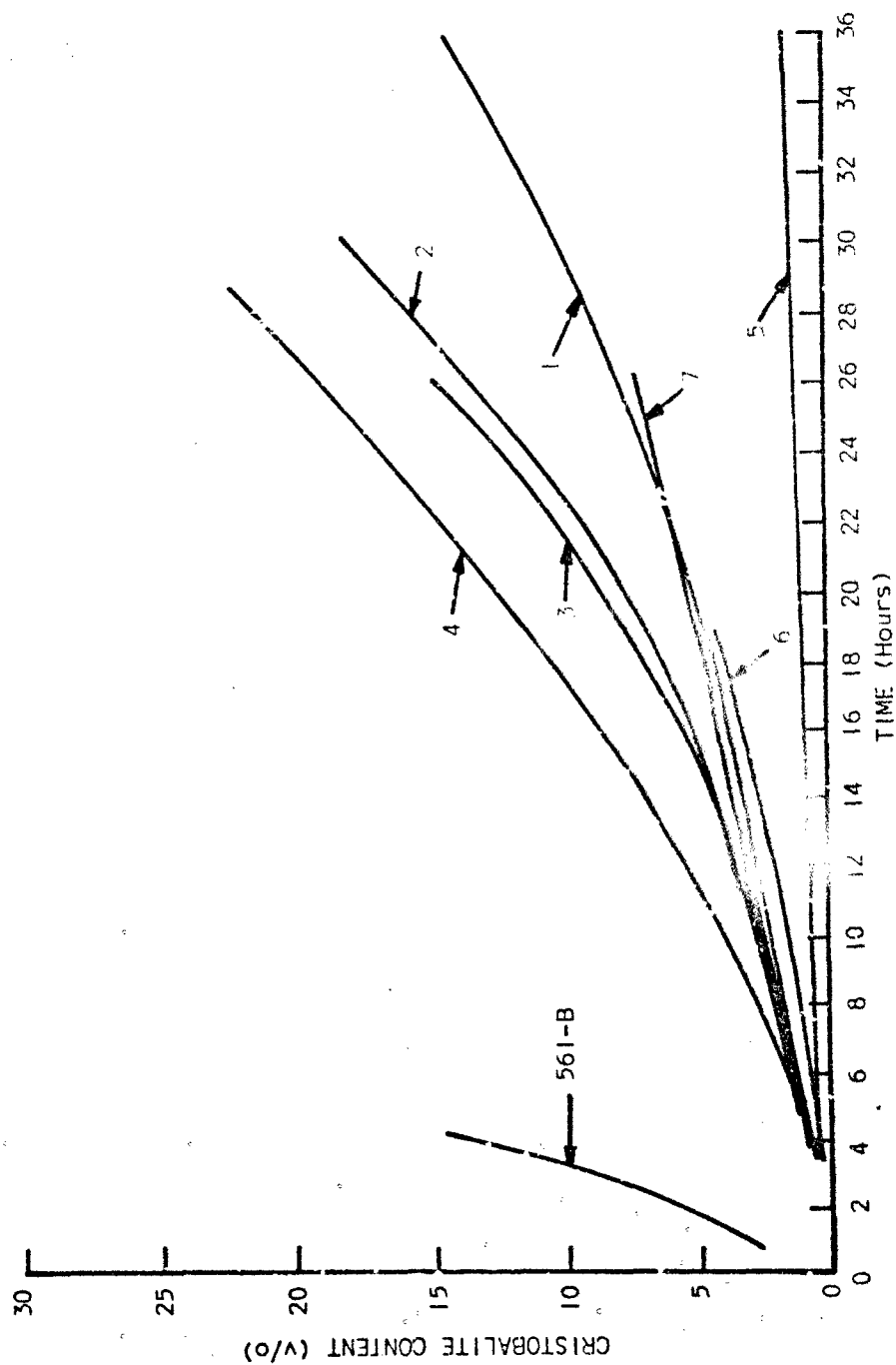
Figure 2. Cristobalite Content vs Sintering Time at 2200° F for Experimental Fused Silica Slips.
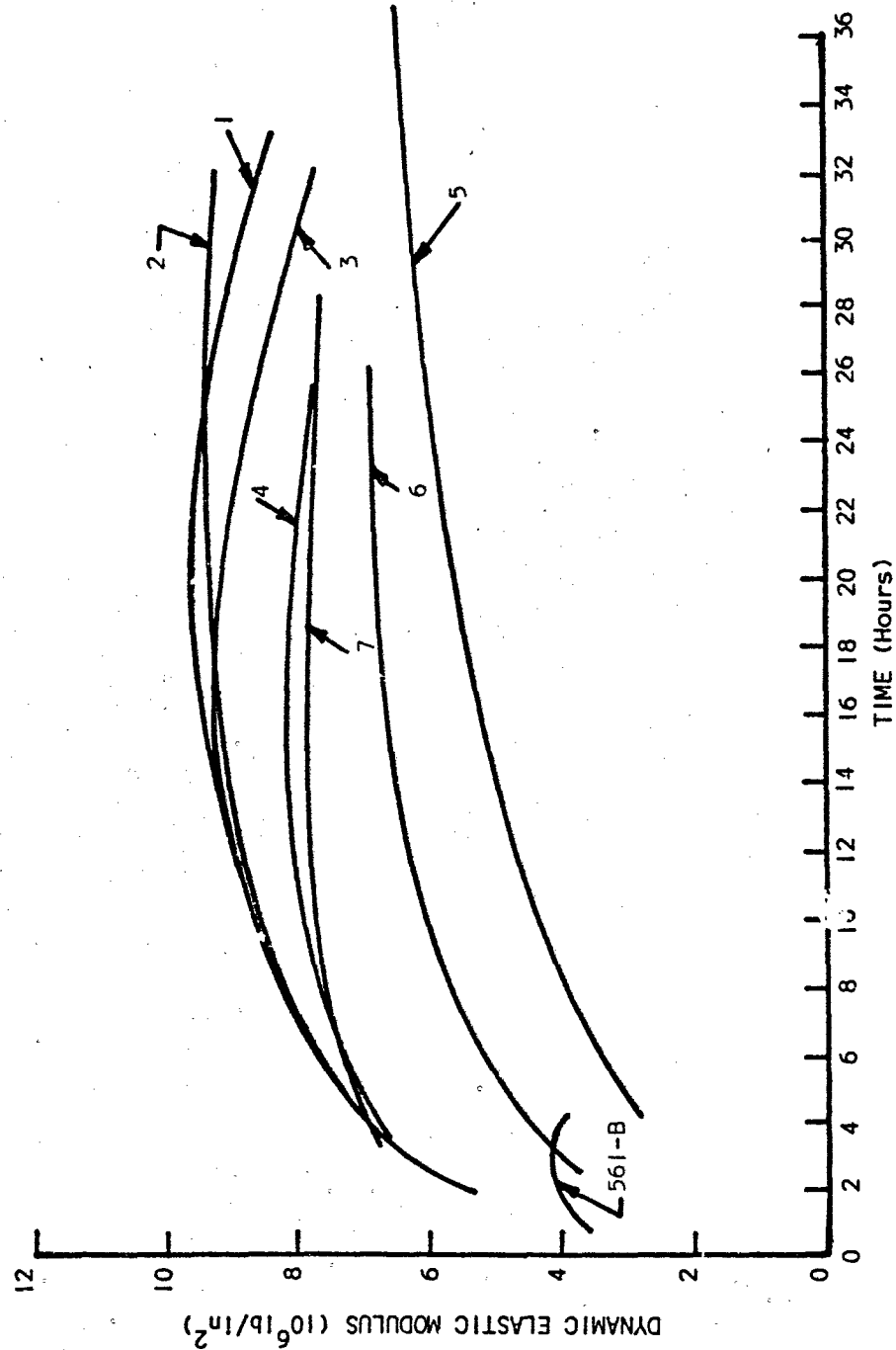
Figure 3. Elastic Modulus vs Sintering Time at 2200° F for Experimental Fused Silica Slips.

TIME (Hours)

DYNAMIC ELASTIC MODULUS (10^6 lb/in^2)

561-B
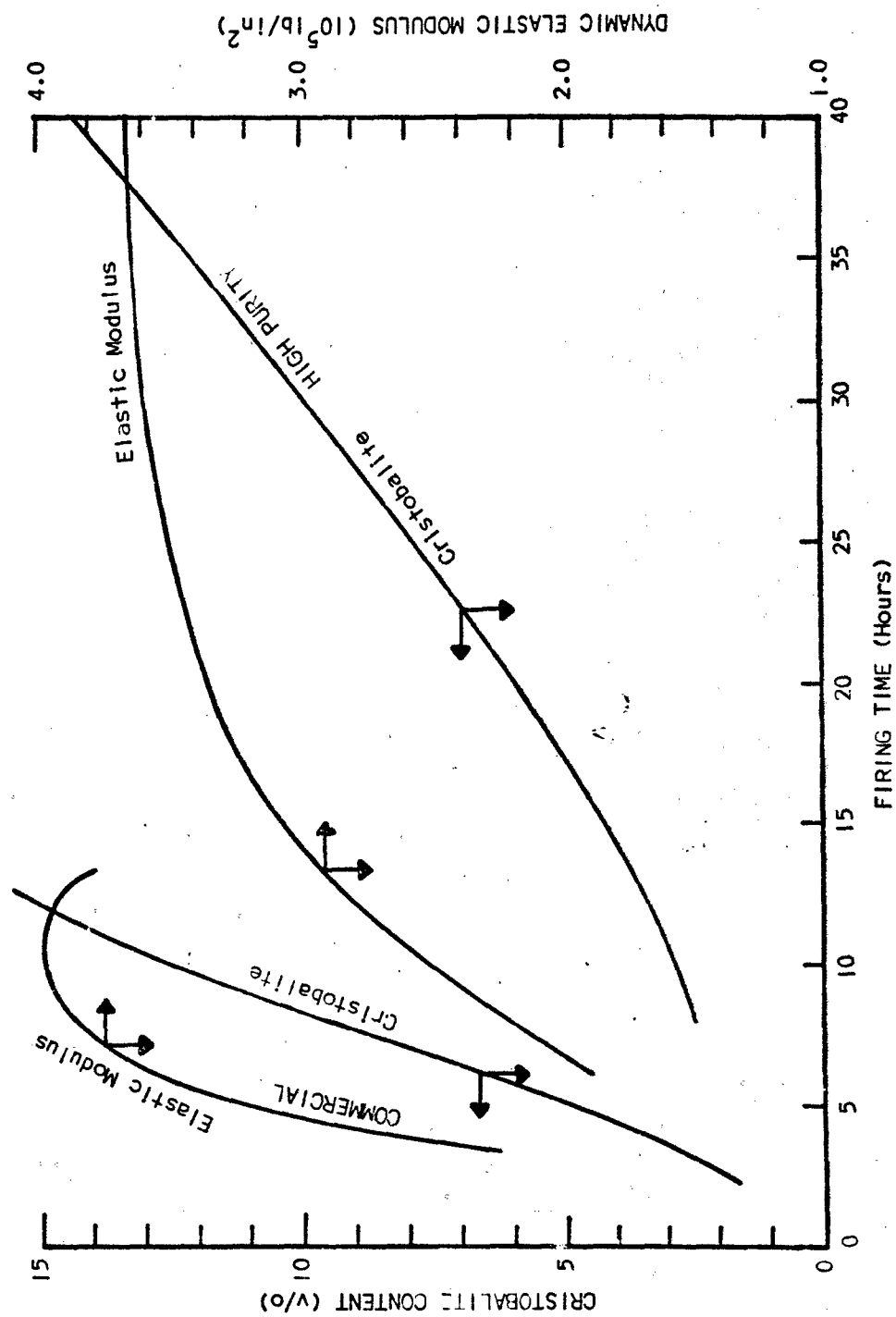
Figure 4. Cristobalite Content and Dynamic Elastic Modulus vs Time at 2200° F for High Purity and Commercial Fused Silica Foam of Nominal 25 lb/ft³ Density.
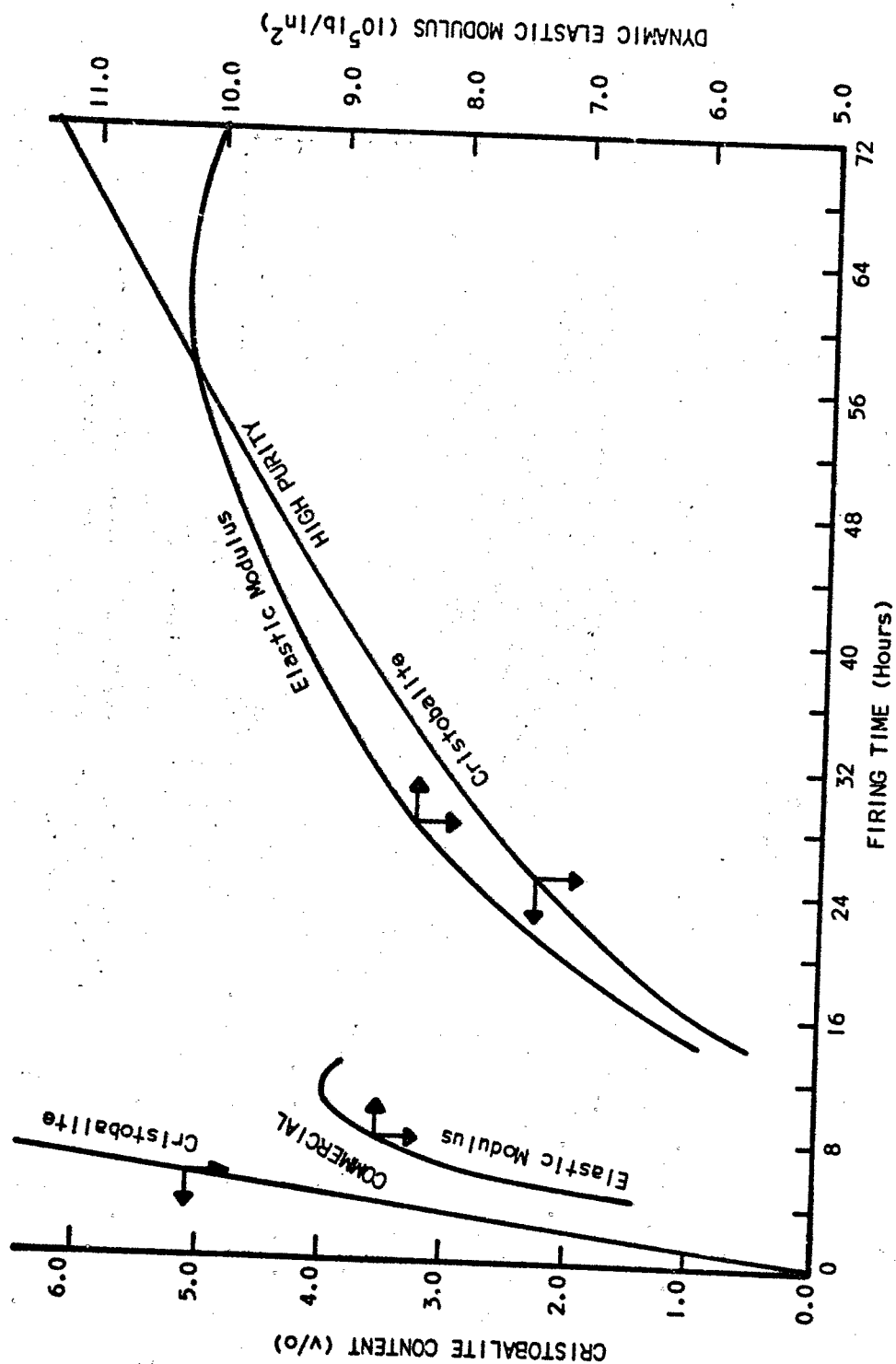
Figure 5. Cristobalite Content and Dynamic Elastic Modulus vs Time at 2200° F for High Purity and Commercial Fused Silica Foam of Nominal 45 lb/ft³ Density.
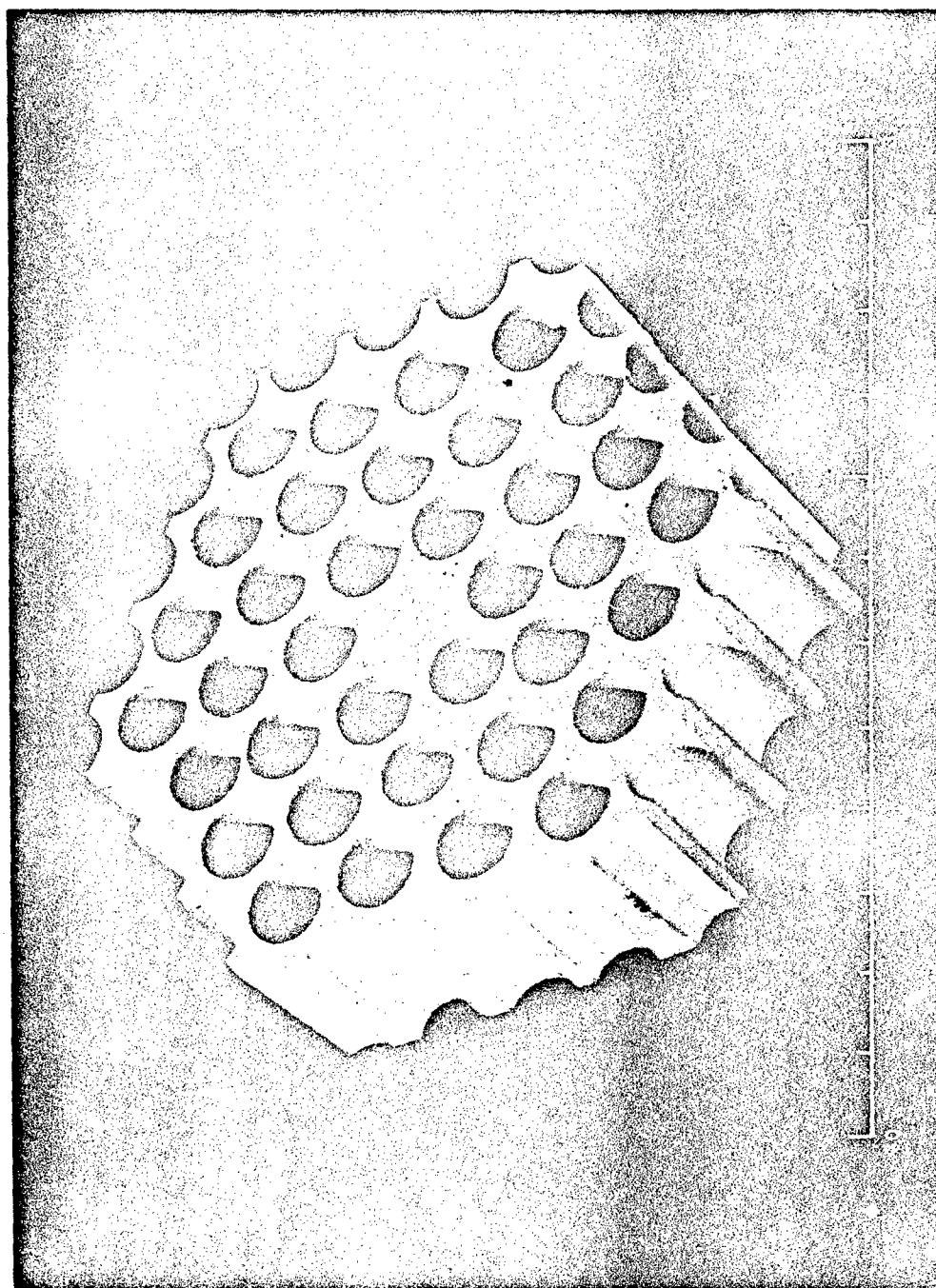
Figure 6. Section of Slip-Cast Fused Silica Honeycomb.

APPENDIX I

TABLE OF CONTENTS - VOLUME II

SESSION III

ELECTRICAL THEORY AND DESIGN

SESSION IV

RADANT AND OTHER TECHNIQUES

PAPERS NOT PRESENTED

TABLE OF CONTENTS - VOLUME III

SESSION V

ENVIRONMENTAL SIMULATION

SESSION VI

RADOMES FOR ADVANCED WEAPONS SYSTEMS

Paper No.

APPENDIX II

AUTHOR INDEX

AUTHOR INDEX

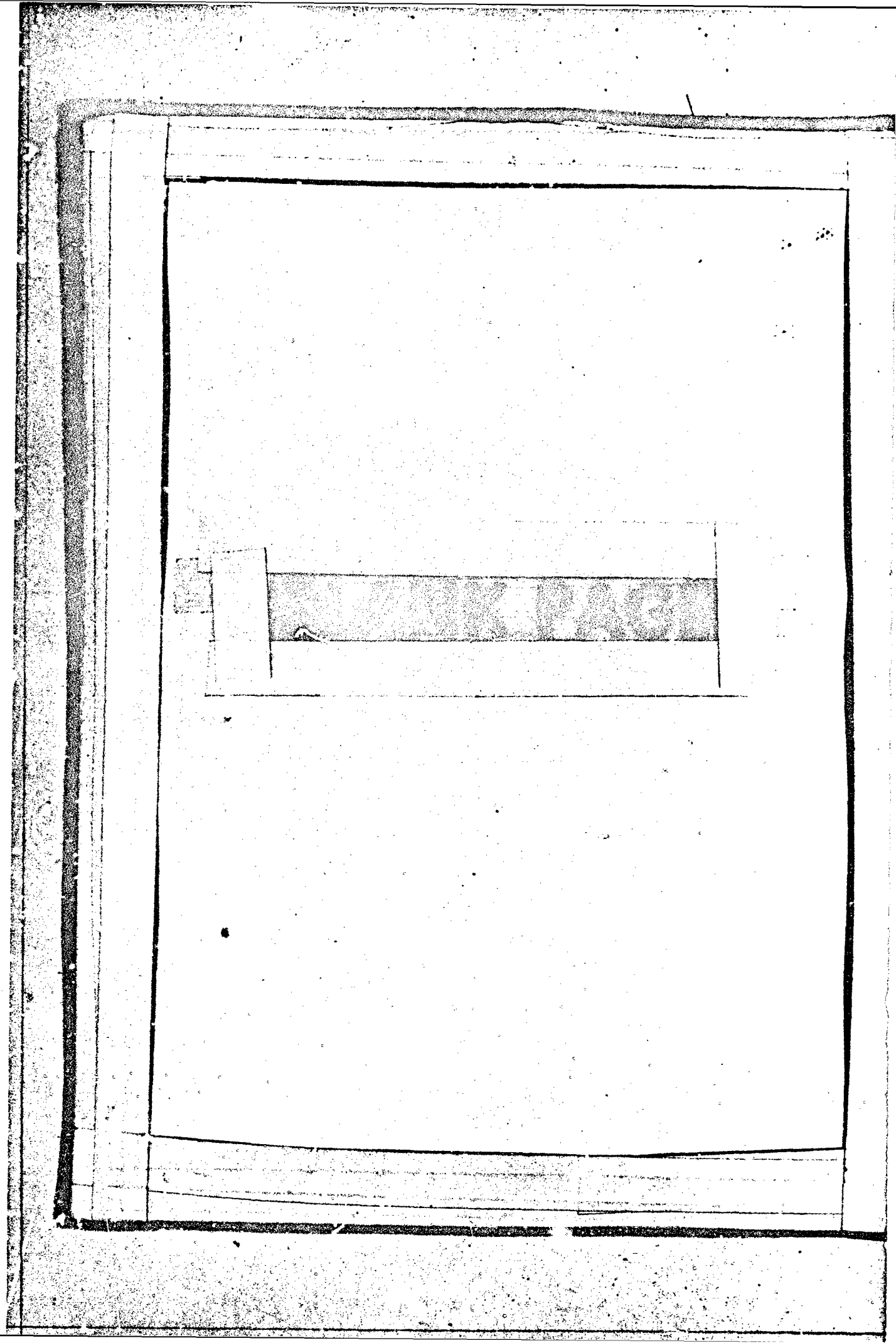|	Vol.		Vol.
C. J. Bahun	I	J. J. Krochmal	I
D. Beeler	I	A. C. Lind	II
A. Bennett	I	C. D. Lunden	II
P. Boland	III, IV	J. W. Maurer	II
S. H. Bomar	I	R. J. McHenry	I
J. J. Boyle	III	P. W. McMillan	I
R. C. Buggeln	I, IV	G. F. Meades	I
K. H. Breeden	II	R. A. Miller	I
J. R. Brown	I	C. A. Murphy	I, III
E. W. Carpenter	II	J. E. Nicholson	IV
V. D. Celentano	III	G. Partridge	I
W. K. Cetaruk	III	A. J. Patrick, Jr.	I
V. Chase	I	C. C. Post	IV
S. C. Colburn	I	B. Poulin	I
D. A. Conti	II	S. Powis	I
R. Copeland	I	C. L. Price	IV
A. J. DeCecco	III	C. L. Purinton	II
W. D. Delany	II	B. L. Reynolds	III
R. Eastridge	I	R. D. Rocke	I
R. S. Ebert	II	B. Rolsma	I
W. A. Elliott	III	E. L. Rope	II
J. L. Entrekin	IV	A. J. Russo	II
B. Fellows	I	A. T. Sales	IV
T. E. Fiscus	II	G. F. Schmitt, Jr.	I
A. C. Francisco	III	D. R. Stewart	III
A. A. Fyall	I	A. W. Straiton	II
L. E. Gates, Jr.	I	C. J. Swafford	III
C. W. Gorton	III	A. J. Thompson	I
R. M. Hale	IV	R. Timms	II
J. N. Harris	I	C. W. Tolbert	II
D. L. Hollinger	II	G. P. Tricoles	II
R. O. Howe	II	R. E. VanDoeren	II
H. S. Jones	IV	R. C. VanWagoner	II
K. R. Kilcoyne	II	J. D. Walton	I
C. H. King	II	P. R. Zuzolo	III
J. Kmetzo	II		

APPENDIX III

ATTENDEES TO THE USAF AVIONICS LABORATORY-GEORGIA INSTITUTE OF TECHNOLOGY
SYMPOSIUM ON ELECTROMAGNETIC WINDOWS

Arthur B. Abeling
Senior Research Engineer
Georgia Institute of Technology
Engineering Experiment Station
Atlanta, Georgia 30332

Edwin F. Abrams
Senior Scientist
General Technologies Corporation
1821 Michael Faraday Drive
Reston, Virginia 22070

Richard H. Adams
Program Manager
Mithras, Division of Sanders
    Associates, Inc.
701 Concord Avenue
Cambridge, Massachusetts 02138

Dallas L. Addis
Sr. Electronics Engineer
Brunswick Corporation
Technical Products Division
325 Brunswick Lane
Marion, Virginia 24354

F. W. Addis
Sr. Engineer/Scientist
Douglas Aircraft
3000 Ocean Park Blvd.
Santa Monica, California 90403

George Angeletti
Assistant Manager
Market Development
The Brush Beryllium Company
17876 St. Clair Avenue
Cleveland, Ohio 44110

Gerard F. Aubin
Senior Development Engineer
Societe L. DESMARQUEST et Cie
B. P. 20 - 92 Sevres - FRANCE

Richard J. Bailey
Member of Technical Staff
North American Rockwell Corporation
4300 E. Fifth Avenue
Columbus, Ohio 43216

Harold L. Bassett
Research Engineer
Georgia Institute of Technology
Engineering Experiment Station
Atlanta, Georgia 30332

Robert M. Beasley
Staff Scientist
Lockheed Missiles & Space Company
P. O. Box 504
Sunnyvale, California 94088

David R. Beeler
Material Development Engineer
Brunswick Corporation
Marion, Virginia 24354

Bruce J. Benedict
Project Engineer
USAF - Air Force Weapons
    Laboratory
Kirtland AFB, New Mexico 87117

A. Bertagna
Ingenieur
S.T.T.A.
241 Rue de la Convention
Paris, FRANCE

August H. Bickel
Marketing Engineer
Brunswick Corporation
2683 Kathy Lee Ct.
Dayton, Ohio 45416

Henry R. Blecha
Mechanical Engineer
U.S. Naval Weapon Center
Code 5531
China Lake, California 93555

Paul Boland
Head, Evaluation & Analysis Branch
Engineering Experiment Station
Georgia Tech
Atlanta, Georgia

Phillip N. Bolinger
Supervising Engineer
General Electric Company
P. O. Box 8555
Philadelphia, Pennsylvania 19101

Steve H. Bomar, Jr.
Research Engineer
Engineering Experiment Station
Georgia Tech
Atlanta, Georgia

John J. Boyle
Eng/Sci-Spec
Douglas Missile & Space Systems
    Division
3000 Ocean Park Boulevard
Santa Monica, California 90406

Kenneth H. Breeden
Research Engineer
Georgia Institute of Technology
Engineering Experiment Station
Atlanta, Georgia 30332

Thomas W. Brock
Owens-Illinois, Inc.
P. O. Box 1035
Toledo, Ohio 43601

Richard J. Budin
Project Engineer
Owens-Illinois, Inc.
1020 N. Westwood Avenue
Toledo, Ohio 43607

Lt. Richard C. Buggeln
Project Engineer
Air Force Weapons Laboratory
Kirtland AFB, New Mexico 87117

Rudolf H. Buhlmann
Design Engineer
The Boeing Company
P. O. Box 3707
Seattle, Washington 98124

Jack E. Burroughs
Senior Design Engineer
General Dynamics
P. O. Box 748
Fort Worth, Texas 76101

George H. Burson, Jr.
Project Engineer
Hayes International Corporation
P. O. Box 2287
Birmingham, Alabama 35201

Howard E. Bussey
Physicist
National Bureau of Standards
Division 251.03
Boulder, Colorado 80302

Paul E. Butzien
MTS
Bell Labs
Whippany, New Jersey 07981

Elmer Cain
Engrg. Spec.
Northrop-Norair
3901 West Broadway
Hawthorne, California 90250

Stanley A. Casazza
Senior Engineer
Raytheon Company
Hartwell Road
Bedford, Massachusetts 01730

Vincent Dominic Celentano
Development Chemist
Plastics Technology
General Electric Company
P. O. Box 8555
VFSTC, Rm. U-7026
Philadelphia, Pennsylvania 19101

Walter K. Cetaruk
Engineering Assistant
The MITRE Corporation
P. O. Box 208
Bedford, Massachusetts 01730

Huel H. Chandler
Staff Engineer
Martin Marietta Corporation
Sand Lake Road
Orlando, Florida

V. A. Chase
Matr. & Process Dev. Manager
Brunswick Corporation
Marion, Virginia 24354

Albert Cohen
President
Electronic Space Structures Corporation
Old Powder Mill Road
W. Concord, Massachusetts 01781

S. C. Colburn
Senior Research Engineer
General Dynamics
P. O. Box 2507
Pomona, California 91766

Norman Stanley Corney
Principal Scientific Officer
Ministry of Technology
Materials Branch
St. Giles Court
London W.C.2 GREAT BRITAIN

William B. Daniel
Procurement/Technical
WRAMA
Robins Air Force Base
Warner Robins, Georgia

W. D. Delany
Antenna Engineer
Admiralty Surface Weapons
   Establishment
Hambrook, Chichester
SUSSEX, U.K.

R. S. Ebert
Senior EE
Lockheed-Georgia Company
86 South Cobb Drive
Marietta, Georgia 30060

A. B. Eisenberg
Marketing Manager
Douglas Aircraft Company
3000 Ocean Park Blvd.
Santa Monica, California 90406

Warren A. Elliott
Senior Engineer
Wheller Labs, Inc.
Box 561
Smithtown, New York

Wilfred T. Engelke
Research Engineer
Southern Research Institute
2000 Ninth Avenue South
Birmingham, Alabama 35205

Joe L. Entrekin
Staff Assistant Technical
Division 1425
Sandia Corporation
Box 5800
Albuquerque, New Mexico

P. R. Erickson
Senior Elect. Engineer
General Dynamics (Convair Division)
P. O. Box 1128
San Diego, Califronia 92112

Ben Fellows
Technical Manager
Aero-Ceramics, Inc.
(A Subsidiary of HITCO, Inc.)
1600 W. 135th
Gardena, California 90249

Bernig Fink
Product Manager
HITCO
1600 West 135th Street
Gardena, California 90247

283

J. M. Fiskin
Sr. Engr./Sc.
McDonnell Douglas Corp.
3855 Lakewood
Long Beach, California

Ken Fitzgerald
Engineer
General Electric
24400 Highland Road
Richmond Hts., Ohio 44143

Capt. Richard J. Flaherty
Project Engineer
Air Force Weapons Laboratory
Kirtland Air Force Base, New Mexico

P. L. Fleischner
Research Scientist
National Beryllia Corp.
First Avenue
Haskell, New Jersey

Robert D. Force
Associate Engineer
The Boeing Company
P. O. Box 3733
Seattle, Washington 98124

Allen C. Francisco
Research Specialist
The Boeing Company
P. O. Box 3996
Seattle, Washington 98124

Robert Kelly Frazer
Associate Engineer
Applied Physics Lab
Johns Hopkins
9621 Georgia Avenue
Silver Springs, Maryland 20902

William G. D. Frederick
Tech Area Manager for Electronics
AF Materials Lab
ATTN: MAYE
Wright Patterson AFB, Ohio 45433

Hugo R. Fulmer
Product Line Manager
Scientific-Atlanta, Inc.
P. O. Box 13654
Atlanta, Georgia 30324

A. A. Fyall
Principal Scientific Officer
Royal Aircraft Establishment
Farnborough
Hants, ENGLAND

Bobby G. Gamble
Material Development Engineer
Brunswick Corporation
Marion, Virginia 24354

Norman L. Gamble
Plastics Engineering
Goodyear Aerospace Corporation
Plastics Engineering
Department 481-C
Akron, Ohio 44315

L. E. Gates, Jr.
Technical Staff
Hughes Aircraft Company
Centinels & Teale
Culver City, California 90230

Dan Graves
PENAIDS
AFAL
WPAFB
Dayton, Ohio 45433

Robert M. Hale
Senior Scientist
Aeronutronic Div.--Philco-Ford
Ford Road
Newport Beach, California 92663

Richard C. Hall
Research Chief
Martin-Marietta Corporation
Orlando, Florida 32805

Crawford W. Hallett
IPSEN Industries
Box 500
Rockford, Illinois 61105

Robert L. Hallse
Member, Technical Staff
Aerospace Corporation
1111 E. Mill Street
San Bernardino, California 92402

Bernard H. Hamling
Product Manager
Union Carbide Corporation
P. O. Box 324
Tuxedo, New York 10987

Virgil L. Harrington
Supervisor
Philco-Ford Corporation
Ford Road
Newport Beach, California 92625

J. L. Harris
Aero. Res. Engr.
USAMICOM, R&DD, Adv. Sys. Lab
Headquarters, U.S. Army Missile Command
ATTN: AMSMI-RDC
Redstone Arsenal, Alabama 35809

Joe N. Harris
Head, Processes & Fabrications Branch
Engineering Experiment Station
Georgia Tech
Atlanta, Georgia

Richard S. Hassard
Sr. Dev. Engr.
Goodyear Aerospace Corporation
Litchfield Park, Arizona 85340

R. L. Heestand
Associate Division Chief
Battelle Memorial Inst.
505 King Avenue
Columbus, Ohio 43201

M. Henika
Market Development
Union Carbide Corporation
Carbon Products Division
270 Park Avenue
New York, New York 10017

Edward C. Henry
Consulting Engineer
General Electric Company
P. O. Box 8555
Philadelphia, Pennsylvania 19101

Travis G. Hickman
Research Engineer
Scientific Atlanta, Inc.
Box 13654
Atlanta, Georgia 30324

James J. Higgins, Jr.
Marketing Representative
Scientific-Atlanta, Inc.
Route 27 Parsonage Road
Edison, New Jersey 08817

Maurice A. Hill
AFAL
APAFB, Ohio 45433

Chandler K. Hom
Engineer
Fairchild Hiller Corporation
Farmingdale
Long Island, New York 11735

Leonard E. Hoots
Section Chief, Electronics
Brunswick Corporation
Technical Products Division
325 Brunswick Lane
Marion, Virginia 24354

Milton B. Hoover
Design Engineer
Goodyear Aerospace
Litchfield Park, Arizona 85340

Alan R. Honig
Section Head
Norden Division, United Aircraft
Helen Street
Norwalk, Conn.

Ron Horner
Fuzing Officer
Naval Plant Representative Office
P. O. Box 504
Sunnyvale, California 94088

R. O. Howe
Physics Branch Manager
Raytheon Company
Missile Systems Division
Hartwell Road
Bedford, Massachusetts 01730

Donald P. Hutchison
Research Engineer
The Boeing Company
3801 S. Oliver
Wichita, Kansas 67210

Arthur Johnson
Group Leader
Grumman Aircraft Engr. Corp.
South Oyster Bay Road
Bethpage, New York

John Oscar Johnson
Engineering Specialist
Vought Aeronautics Division
LTV Aerospace Corporation
P. O. Box 5907
Dallas, Texas 75222

Howard S. Jones, Jr.
Supervisory Electronic Engineer
Harry Diamond Laboratories
Washington, D. C. 20438

George S. Kandrach
Sales Representative
Corning Glass Works
Corning, New York 14830

J. F. Kauffman
Research Engineer
Corning Glass Works
Electronic Research Laboratory
Raleigh, North Carolina 27604

Neil R. Kilcoyne
Research Associate
O.S.U. ElectroScience Laboratory
1320 Kinnear Road
Columbus, Ohio 43212

Charles H. King
Research Engineer
Boeing Company
P. O. Box 707
Renton, Washington 98055

Henry P. Kirchner
President
Ceramic Finishing Company (Linden Labs)
P. O. Box 498
State College, Pennsylvania 16801

Aare Kivi
Maxson Electronics Division
Sunrise Hwy.
Great River, New York

John L. Kmetzo
Engineer
Sperry-Rand Corporation
Sperry Gyroscope Division
Great Neck, New York 11020

Karl Knauerhase
AEG - TELEFUNKEN
Steinhoft 9
2 Hamburg 11
Deutschland 2 11 105

Lester H. Kosowsky
Sr. Systems Eng.
Norden, UAC
Helen Street
Norwalk, Connecticut 00850

Allan H. Krabill
Development Engineer
AF Materials Lab
AFML (MANE)
Wright-Patterson AFB
Ohio 45433

H. Kraenzler
Ing. Aero
French Navy
Toulon - FRANCE

Jerome J. Krochmal
Senior Project Officer
Air Force Materials Laboratory
Wright-Patterson AF Base, Ohio 45433

E. A. Kuhlman
Senior Engineer
McDonnel Douglas Corporation
Box 516
St. Louis, Missouri 63166

Helmuth H. Laue
Sr. E.E.
General Dynamics/Convair
5001 Kearney Villa Road
San Diego, California 92112

H. Leggett
Section Chief
Composites Branch, MR&PM
Missile And Space Systems Division
Douglas Aircraft Company
3000 Ocean Park Boulevard
Santa Monica, California 90406

Arthur C. Lind
Senior Engineer
McDonnell Astronautics
Department 413, Building 102
P. O. Box 516
St. Louis, Missouri 63166

Thomas E. Little
Graduate Research Assistant
Ga. Tech, High Temperature
    Materials Division
Atlanta, Georgia 30313

Nicholas D. LoBue
Engineer
North American Rockwell Corporation
5701 W. Imperial Highway
Los Angeles, California 90009

Donald L. Loyet
Project Engineer
Hughes Aircraft Company
Missile Systems Division
Canoga Park, California 91304

Clifford R. Lundquist
Electronic Engineer
Naval Weapons Center Corona Lab.
Corona, California 91720

Thurman Judson Lyon
Manager, Electromagnetic Studies
Scientific-Atlanta, Inc.
3845 Pleasantdale Road
Doraville, Georgia 30040

Edward B. McMillan
Research Director
Resources Development Institute
P. O. Box 86
Greenlawn, New York 11740

Robert J. McNish
Manufacturing Manager
Koppers Company, Inc.
400 Commonwealth Avenue
Bristol, Virginia 24201

John W. Maurer
Proj. Engr.
General Electric Company
One River Road
Schenectady, New York 12305

E. B. Mellette
Engineer
Robins AFB (WRNEBG)
Georgia

C. A. Murphy
Head, Material Applications Branch
Georgia Institute of Technology
Engineering Experiment Station
Atlanta, Georgia 30332

Hubert A. Myers
Radome Development Engineer
HITCO
1600 West 135th Street
Gardena, California

H. Nadeau
Missile Systems Division
Raytheon Company
Hartwell Road
Bedford, Massachusetts 01730

Glen B. Nicholas
Aerospace Engineer
SAM-D Project Off.
Missile Command
Radstone Arsenal, Alabama 35809

James E. Nicholson
Mithras, Division of Sanders
    Associates, Inc.
701 Concord Avenue
Cambridge, Masschusetts 02138

T. Larry Worin
Research Engineer
The Boeing Company
P. O. Box 3996
Seattle, Washington 98124

Dean E. Norris
Mechanical Engineer
MOTOROLA INC.
Gov't. Electronics Division
Aerospace Center, 8201 E. McDowell Rd.
Scottsdale, Arizona 85252

Otis H. Ogburn
Electronic Engineer
U.S. Air Force
Rogins Air Force Base
Warner Robins, Georgia 31093

Samuel S. Oleesky
Sr. Engineer/Scientist
Douglas Aircraft Company
Missile & Space Systems Division
3000 Ocean Park Boulevard
Santa Monica, California

James D. Ott
Sr. Mechanical Engineer
MOTOROLA INC., Gov't. Electronics Div.
Aerospace Center
8201 E. McDowell Road
Scottsdale, Arizona 85252

R. L. Overholt
Mgr., Special Products
ESSCO
West Concord, Massachusetts 01781

Lionel Pasiuk
Aerospace Engineer
Naval Ordnance Systems Command
Department of the Navy
Washington, D.C. 20360

Alexander J. Patrick
Group Leader - Dielectric Materials
Avco Corporation
Lowell Industrial Park
Lowell, Massachusetts 01851

Maurice A. Pennisi
Senior Radome Engineer
McMillan Radiation Labs, Inc.
Brownville Avenue
Ipswich, Massachusetts 01938

Theron P. Place
Mechanical Engineer
MOTOROLA INC., Gov't. Electronics Div.
Aerospace Center
8201 E. McDowell Road
Scottsdale, Arizona 85252

Cecil C. Post
Physical Science Laboratory
New Mexico State University
University Park, New Mexico 88001

Nick E. Poulos
Associate Chief
High Temperature Materials Division
Georgia Tech
Atlanta, Georgia

Walter E. Powell, Jr.
Engineer
RCA
Building 101-208
Moorestown, New Jersey 08057

Thomas Stanley Powis
Assistant Chief Electronics Engineer
British Aircraft Corporation, Ltd.
Six Hills Way
Stevenage, Hertfordshire ENGLAND

Clay L. Price, Jr.
Project Aerosystems Engineer
General Dynamics
P. O. Box 748
Fort Worth, Texas 76101

Donald L. Purinton
Research Engineer for Radome &
    Antennas
Texas Instruments
MS327
Dallas, Texas 75222

E. L. Radell
Design Engineer
Beech Aircraft Corporation
9709 E. Central Avenue
Wichita, Kansas 67201

Byron L. Reynolds
Manager of R&D
AERONCA, Inc.
1712 Germantown Road
Middletown, Ohio 45042

Richard D. Rocke
Staff Engineer
Hughes Aircraft Company
P. O. Box 3310
Fullerton, California 92634

James Richard Rogers
Sr. Engineer
McDonnell Douglas
Box 516
St. Louis, Missouri 63166

Eugene Lowell Rope
Engineer
General Dynamics
Electronics Division
3090 Pacific Highway
P. O. Box 127
San Diego, California 92112

Anthony J. Russo
Research Engineer
Sandia Laboratory
Albuquerque, New Mexico

Arthur T. Sales
Research Engineer
Engineering Experiment Station
Georgia Tech
Atlanta, Georgia

Arthur H. Schaufelberger
Engineering Staff Consultant
Sperry Microwave Electronics Division
Box 4648
Clearwater, Florida 33518

George F. Schmitt, Jr.
Materials Engineer
Air Force Materials Laboratory
CODE: MANE
Wright-Patterson AFB, Ohio 45433

Michael Schmitt
Physicist
Naval Weapons Center
Corona Laboratories
Corona, California 91720

Oscar Seidman
Director, Weapons Dynamics Division
Naval Ordnance Systems Command
Department of the Navy
Washington, D. C. 20360

A. P. Sheppard
Head, Special Techniques Group
Engineering Experiment Station
Georgia Institute of Technology
Atlanta, Georgia   30332

Lloyd G. Shipley
Engineering Specialist
LTV Aerospace Corporation
Vought Aeronautics Division
P. O. Box 5907
Dallas, Texas   75222

William A. Slippy, Jr.
Marketing Representative
Sperry Electronic Tube Division
Waldo Road
Gainesville, Florida   32601

Kenneth M. Smith
Consultant Cer. Eng.
A.P.L. of J. Hop. Univ.
8621 Ga. Avenue
Silver Springs, Maryland

Adam P. Smolski
Electronic Space Structures Corp.
Old Powder Mill Road
West Concord, Massachusetts   01781

Donald D. Stephens
Antenna Research Specialist
Lockheed California Company
P.O. Box 551
Burbank, California   91503

John B. Styron
Manager of Electronics
Brunswick Corporation
325 Brunswick Lane
Marion, Virginia   24354

Richard J. Sudin
Engineer
Gov't. Prod. & Serv
Owens-Illinois, Inc.
1020 N. Westwood
Toledo, Ohio   43607

C. J. Swafford
Principal Lab Mech.
Georgia Tech Research
North Avenue
Atlanta, Georgia

Raymond B. Sylvain
Manager, Materials Engineering
McMillan Radiation Labs, Inc.
Brownville Avenue
Ipswich, Massachusetts   01938

Gene Tarrants
Radome Project Engineer
AFAL/AVWE
Wright-Patterson AF Base, Ohio   45433

George J. Tatnall
Supv. Radome Sec.
U. S. Naval Air Dev. Center
Warminster, Pennsylvania   18974

Arthur J. Thompson
Sr. Electronics Engineer
Brunswick Corporation
325 Brunswick Lane
Marion, Virginia   24354

Robert J. Timms
Research Section Head
Sperry Gyroscope Division-
   Sperry-Rand Corporation
Great Neck, New York

R. Rodriguez Torrent
Research Scientist
Martin-Marietta Corporation
P. O. Box 5837
Orlando, Florida   32805

Gus Peter Tricoles
Design Specialist
General Dynamics
Electronics Division
3090 Pacific Highway
P. O. Box 127
San Diego, California   92112

Edwin M. Turner
Air Force Avionics Laboratory
AVWE-3
Wright-Patterson AFB, Ohio 45433

W. Vance
Material & Process Engineer
McDonnell Douglas
P. O. Box 516
St. Louis, Missouri 63166

Richard E. Van Doeren
Research Associate
Ohio State University
1320 Kinnear Road
Columbus, Ohio 43221

Richard C. Van Wagoner
Technical Consultant
Radiation Systems, Inc.
1755 Old Meadow Road
McLean, Virginia 22101

Peter G. Verhoeven
Product Technical Representative
Goodyear Aerospace Corporation
Litchfield Park, Arizona 85340

Norman E. Wahl
Principal Scientist
Bell Aerosystems Company
Post Office Box One
Buffalo, New York 14240

Jesse D. Walton, Jr.
Chief
High Temperature Materials Division
Georgia Institute of Technology
Atlanta, Georgia 30332

D. M. Watters
General Engineer
Naval Weapons Center Corona Labs.
Corona, California 91720

Kenneth B. Wear
Research Engineer
Georgia Institute of Technology
Engineering Experiment Station (PSD)
Atlanta, Georgia 30332

L. B. Weckesser
Engineer
Johns Hopkins University
Applied Physics Lab.
8621 Georgia Avenue
Silver Springs, Maryland 20910

Hadley W. Wellborn, Jr.
Assistant Research Engineer
Georgia Tech Engineering Experiment
    Station
Atlanta, Georgia 30332

Earle A. Welsh
Assistant Research Engineer
Engineering Experiment Station
Georgia Institute of Technology
Atlanta, Georgia 30332

Robert E. Westlund
Supervisory Mechanical Engineer
U.S. Army Harry Diamond Labs
Conn. & Van Ness Sts., N.W.
Washington, D.C. 20438

John M. White
Manager of Materials, Processes and
    Standards Lab
Sperry Electronic Tube Division
Waldo Road
Gainesville, Florida 32601

P. G. Whitmore
Director
Staff Marketing Research
3M Company
3M Center
St. Paul, Minnesota 55101

Arthur C. Woodard
Product Planner
General Electric
Lamp Glass Department
24400 Highland Road
Richmond Hts., Ohio 44143

Charles S. Young
Senior Engineer
Scientific-Atlanta, Inc.
3845 Pleasantdale Road
Doraville, Georgia 30046

Peter R. Zuzolo
Engineering Supervisor
Farichild Hiller Corporation
Republic Aviation Division
Farmingdale, New York 11735

Philip S. DiPiazza
Development Eng.
Norden Division of U.A.C.
Helen Street
Norwalk, Connecticut 06850

DOCUMENT CONTROL DATA - R & D

(Security classification of title, body of abstract and indexing annotation must be entered when the overall report is classified)

1. ORIGINATING ACTIVITY (Corporate author)	2a. REPORT SECURITY CLASSIFICATION
Engineering Experiment Station Georgia Institute of Technology Atlanta, Georgia 30332	Unclassified
	2b. GROUP

3. REPORT TITLE

USAF Avionics Laboratory/Georgia Institute of Technology Symposium on Electromagnetic Windows   Volumes I, II, III.

4. DESCRIPTIVE NOTES (Type of report and inclusive dates)

5. AUTHOR(S) (First name, middle initial, last name)

N. E. Poulos, Editor

6. REPORT DATE	7a. TOTAL NO. OF PAGES	7b. NO. OF REFS
June 12-14, 1968		

8a. CONTRACT OR GRANT NO.	9a. ORIGINATOR'S REPORT NUMBER(S)
F33615-67-C-1594	
b. PROJECT NO.	AFAL-TR-68-97
4161	
c. Task No. 416103	9b. OTHER REPORT NO(S) (Any other numbers that may be assigned this report)
d. BPSN 7-63416103	

10. DISTRIBUTION STATEMENT

This document is subject to special export controls and each transmittal to foreign governments or foreign nationals may be made only with prior approval of AFAL (AVWE), Wright-Patterson Air Force Base, Ohio

11. SUPPLEMENTARY NOTES	12. SPONSORING MILITARY ACTIVITY
	United States Air Force Air Force Avionics Laboratory Wright-Patterson Air Force Base, Ohio

13. ABSTRACT

The proceedings are contained in four volumes, three of which are unclassified and one classified Confidential. The papers presented in these volumes were submitted for the USAF Avionics Laboratory/Georgia Institute of Technology Symposium on Electromagnetic Windows held on the Georgia Tech Campus, Atlanta, Georgia, 12, 13, and 14 June 1968. These papers were compiled by Nick E. Poulos, Engineering Experiment Station, Georgia Institute of Technology under USAF Contract No. F33615-67-C-1594.

DD FORM 1 NOV 65 1473   (PAGE 1)

14. KEY WORDS	LINK A		LINK B		LINK C	
	ROLE	WT	ROLE	WT	ROLE	WT
Electromagnetic Windows						
Materials Research						
Development						
Testing						
Evaluation						
Electrical Theory and Design						
Radomes						
Environmental Simulation						